

Mechanisms of the Heterogeneously Catalyzed Reaction of CO₂ Hydrogenation on Transition Metal Surfaces

Présentée le 16 juin 2020

à la Faculté des sciences de base
Laboratoire des matériaux pour les énergies renouvelables
Programme doctoral en chimie et génie chimique

pour l'obtention du grade de Docteur ès Sciences

par

Kun ZHAO

Acceptée sur proposition du jury

Prof. B. Smit, président du jury
Prof. A. Züttel, directeur de thèse
Prof. C. Müller, rapporteur
Prof. S. Garcia Lopez, rapporteuse
Prof. K. Sivula, rapporteur

Acknowledgements

I thank very much my supervisor, Prof. Züttel, whom we call chef often, for supporting me the PhD studies. I appreciate very much for his great tolerance and generosity for my not practiced English expression and slow outcome at the beginning, and the cultural differences. He is really a profound professor who always provides critical ideas and solutions, and improves the article incisively. Talking with Prof. Züttel every time, no matter for the work or out of work, nurtures my view of the research, life, cultures, and societies. Moreover, he is a so kind professor who does not present himself as someone at the position high above us. Instead, he has lunch with us, often talks with us, organizes group hiking in the summer and group ski in the winter, shows us generously the beautiful Swiss Alps and life, invites us for dinner at his place, and even cooks for us. He keeps encouraging me in all senses, educating me not only to be successful in PhD, but also a “princess” – elegant, generous, and confident in life. His joyful laugh is a typical sign of LMER. I had doubted if there was something wrong, because I felt too equal and relaxed in front of the professor.

I thank very much Dr. Marco Calizzi, Dr. Emanuele Moioli, and Dr. Wen Luo for guiding me in the work. Marco as my co-advisor did corrections for every of my articles and the thesis; Emanuele always gave incisive suggestions and revised my manuscripts promptly; Wen was always available for discussion and giving fast and efficient solutions. They pushed me into the success of my PhD. I thank the other members too. Heena was gentle and kind for caring people and used to cook Korean food for us. Loris is such a joyful Swiss Alpine boy and easygoing with everyone in the lab, making the heavy atmosphere of the work delighting. He is industrious person who not only works hard on his own project but also did frequently the services in the lab, for example, filling up the public necessities and emptying and replacing the trash bins. He is also a helpful person who always ready for offering helps for both work and life. Jie is always helping in time, sharing his knowledge, and talking with us. Alexandre arrives recently, but he already did the XPS measurements with Mo and Wen for my published work. Mo works most of the time in the NAP-XPS room, known as a life enjoying person comparing to the most of Chinese. Youngdon joins in the group the most recently, and presents as a very kind and hard-working person. I appreciate that we PhDs sat in the same office, sharing our work and breaks. I also thank our previous and current administrative secretaries, Constance, Miriam, and Ivana, who solved the issues in our work and living in Switzerland so efficiently that we could work smoothly. Especially, Ivana is our mom in the lab who takes well care of everyone. Additionally, I thank the former members, Dr. Mariana Spodaryk and Dr. Robin Mutschler. I

had worked with Marina for two years. The big benefits to work with her was to learn her excellent communication, being helped by her in communication and work. Robin was the first full PhD here in Sion and just finished his defense last autumn. The first year when we were the only two PhD students in the lab, we had many good activities. Also, I thank his kindness and sharing in the work.

Specially, I thank Prof. Daniel Auerbach who is an enthusiastic and honest scientist. He gave very important helps at my most depressed time of the work, including discussing carefully with me about my work and revising fully my manuscripts. For my first article, Daniel revised comprehensively, meanwhile taught me writing sentence by sentence. He even asked Prof. Rainer Beck for helping advise me and showed me new techniques of molecular beam in that lab. What was more, he helped me the research plan of my application of postdoc, provided me information of potential postdoc positions in USA, and wrote me strong recommendation letter. He participated importantly in my success. I cannot be more thankful to his helps and enlightenments on me.

I also appreciate a lot from my friends, Zhiyong Zhang, Shiqi Huang, Valentina Waller, Constance Visser Witman, Chongqi Yu, Wei Liu, for their friendship with me, cares of me, and helped me in talk and in life.

Finally, I would like to thank my family, who supports me all the way and let me free in choice of the studies. I did not have many contacts with my family, influenced by the previous “one child” policy and the poverty of China at that time. I was unfortunately the second child and a girl, disappointed the family terribly. I did not have chance to stay with the parents. But without their insists in my schools and supports on all my school and university fees in China, I would not be able to come to the stage today. Especially my grandma, she brought me up and she is 85 years old. She waits me every year to return. I feel sorry that I could not tell her the truth that I have my journey to accomplish for more years oversea.

Abstract

Renewable energy supply and energy storage in a closed materials cycle are the urgent global challenges of the 21st century. Carbon dioxide (CO₂) hydrogenation over catalysts is a method to produce synthetic fuels from renewable energy in a CO₂ neutral cycle. Numerous catalysts from pristine to novel materials have been investigated to achieve high CO₂ conversion and selective hydrocarbon. Ahead of developing innovatively active catalyst with a high selectivity, it is crucial to understand the active sites and the related reaction mechanisms. Despite the fact that CO₂ + H₂ is a rather simple chemical equation, many reaction paths on a solid catalyst are possible. However, the proposed mechanisms from literatures have been controversial due to two main difficulties in 1) evidently identifying the reaction species, especially some vital transient species on the pathway of carbon hydrogenation and C-C coupling, and 2) proving the relation between surface structure of the catalysts and the reactivities. To address these difficulties, we built a new instrumental setup and developed an analysis program in order to investigate the catalyst surface and analyze the reaction mechanism in operando.

We built up a diffuse reflectance infrared Fourier transform spectroscopy-mass spectroscopy-gas chromatography (DRIFTS-MS-GC) instrument for an operando study of the surface, gas, and liquid products using DRIFTS, MS, GC, and ex situ NMR. A bilevel evolutionary Gaussian fitting (BEGF) program was developed for dataset treatment including peak deconvolution and kinetic plot. Standard chemicals like carbonates, bicarbonates, formic acid, acetic acid, methanol, and ethanol, and isotopic spectra using ¹³CO₂ and D₂ in the reactions were employed for supporting peak assignments. Based on these infrastructures, CO₂ adsorption and hydrogenation reactions on pristine metals (Fe, Co, Ni, and Cu), metal hydride alloy (LaNi₄Cu), and metal-oxide (Co-CoO) were studied. We found out pure Fe, Co, Ni, Cu and LaNi₄Cu metals are not efficient for CO₂ hydrogenation, and have no detectable adsorption species on the surface. High conversion (> 90%) of CO₂ on Co-CoO surface emphasized the importance of oxide for CO₂ chemisorption and for the observations of the surface species. The following investigation on oxide supported metal catalyst Ru/Al₂O₃ via an in situ control of the individual formation and hydrogenation of each adsorption species demonstrates that the oxide assists CO₂ initial activation. CO₂ methanation starts at the interface of the metal and the oxide and passes through the steps of CO₂ → HCO₃⁻* (and/or HCOO⁻* in CO₂+H₂ co-adsorption condition) → CO* → CH₄. We further explored the relationship between metal/(metal+oxide) ratio and their reactivities. We synthesized Co/(Co+CoO) catalysts in the DRIFTS-MS-GC instrument, and

investigated the CO₂ hydrogenation reaction on site. The results reveal that high concentration of the oxide in the catalyst boosts CO₂ methanation, because the CO₂ binding is moderate and the adsorption is enhanced when the oxide concentration increased.

In short, we established equipment for an operando study of CO₂ hydrogenation on catalyst surfaces, unraveled the surface reaction mechanisms and the active sites, developed a highly active catalyst, as well as initiated an efficient data analysis program.

Keywords

CO₂ hydrogenation, heterogeneous catalysis, methanation, reaction mechanism, surface adsorption, adsorbates, catalyst, metal oxide, IR spectra, data analysis, in situ, operando, DRIFTS-MS-GC

Résumé

L'approvisionnement en énergie renouvelable et le stockage de l'énergie dans un cycle de matériaux clos sont les défis mondiaux urgents du 21^{ème} siècle. L'hydrogénation du dioxyde de carbone (CO_2) sur des catalyseurs est une méthode de production de carburants synthétiques à partir d'énergies renouvelables dans un cycle neutre en CO_2 . De nombreux catalyseurs allant des matériaux vierges aux matériaux nouveaux ont été étudiés pour obtenir une conversion élevée en CO_2 et des hydrocarbures sélectifs. Avant de développer un catalyseur innovant et actif avec une sélectivité élevée, il est essentiel de comprendre les sites actifs et les mécanismes de réaction associés. Malgré le fait que $\text{CO}_2 + \text{H}_2$ est une équation chimique assez simple, de nombreuses voies de réaction sur un catalyseur solide sont possibles. Cependant, les mécanismes proposés dans les littératures ont été controversés en raison de deux difficultés principales: 1) identifier clairement les espèces réactionnelles, en particulier certaines espèces transitoires vitales sur la voie de l'hydrogénation du carbone et du couplage C-C, et 2) prouver le lien entre la structure de surface des catalyseurs et des réactivités. Pour résoudre ces difficultés, nous avons planifié la recherche de cette thèse en partant de la construction du programme de configuration instrumentale + analyse, puis de la conception du catalyseur + du mécanisme de la réaction.

Nous avons d'abord construit un instrument DRIFTS-MS-GC pour une étude opératoire de la catalyse hétérogène. Les produits de surface, gazeux et liquides ont été analysés par DRIFTS, MS, GC et ex situ NMR, respectivement. Un programme de bilevel evolutionary Gaussian fitting (BEGF) a été mis au point pour le traitement des ensembles de données, notamment la déconvolution des pics et le tracé cinétique. Des produits chimiques standard tels que les carbonates, les bicarbonates, l'acide formique, l'acide acétique, le méthanol et l'ethanol, ainsi que les spectres isotopiques utilisant le $^{13}\text{CO}_2$ et le D_2 dans les réactions ont été utilisés pour soutenir les assignations de pointe. Sur la base de ces infrastructures, des réactions d'adsorption et d'hydrogénation de CO_2 sur des métaux purs (Fe, Co, Ni et Cu), un alliage hydrure métallique (LaNi_4Cu) et un oxyde métallique (Co-CoO) ont été étudiées. Nous avons découvert que les métaux purs Fe, Co, Ni, Cu et LaNi_4Cu ne sont pas efficaces pour l'hydrogénation du CO_2 et n'ont aucune espèce d'adsorption détectable à la surface. En outre, l'hydrure de métal LaNi_4Cu réduit le CO_2 à une température beaucoup plus élevée que celle des métaux Co et Ni purs et de la désorption de H_2 , ce qui indique que l'adsorption de H_2 ne pourrait pas être le facteur clé de la réduction de la barrière énergétique de l'hydrogénation du CO_2 . La conversion élevée (> 90%) de CO_2 sur la surface de Co-CoO a mis en évidence l'importance de l'oxyde pour la chimisorption du CO_2 et l'obversement des étapes réactionnelles. Les recherches suivantes sur le

catalyseur métallique Ru/Al₂O₃ supporté sur un oxyde via un contrôle in situ de la formation individuelle et une hydrogénation de chaque espèce d'adsorption démontrent que l'oxyde contribue à l'activation initiale du CO₂. La méthanisation du CO₂ commence à l'interface du métal et de l'oxyde et passe par les étapes CO₂ → HCO₃⁻* (et / ou HCOO⁻* dans les conditions de co-adsorption CO₂ + H₂) → CO* → CH₄. Nous avons exploré la relation entre le rapport métal / (métal + oxyde) (Co / (Co + CoO)) et leurs réactivités dans la réaction d'hydrogénation du CO₂ révèle qu'une concentration élevée d'oxyde dans le catalyseur stimule la méthanation du CO₂, car la liaison au CO₂ est modérée et l'adsorption est améliorée sur le site d'oxyde.

En bref, nous avons mis en place des équipements pour une étude opérationnelle de l'hydrogénation du CO₂ sur les surfaces des catalyseurs, démêlé les mécanismes de réaction de surface et les sites actifs, développé un catalyseur très actif et lancé un programme efficace d'analyse des données.

Mots-clés

Hydrogénation du CO₂, catalyse hétérogène, méthanisation, mécanisme de réaction, adsorption de surface, adsorbats, catalyseur, oxyde métallique, spectres IR, analyse de données, in situ, operando, DRIFTS-MS-GC

Contents

Acknowledgements.....	ii
Abstract	iv
Résumé.....	vi
Contents.....	viii
List of Figures.....	xi
List of Tables.....	xv
Chapter 1 Introduction.....	16
1.1 World Energy Requirement	16
1.2 Synthetic Hydrocarbons from CO ₂ Conversion.....	18
1.2.1 CO ₂ properties	18
1.2.2 CO ₂ interaction with solid surface	20
1.3 Heterogeneous Catalysts for CO ₂ hydrogenation	24
1.3.1 Pristine metals	24
1.3.2 Supported metals	24
1.3.3 Bimetals	25
1.3.4 Single atom.....	26
1.3.5 Bifunctional.....	27
1.4 Structure-Activity Relationships	28
1.4.1 Size effect.....	28
1.4.2 Interface	29
1.4.3 Specific surface sites.....	29
1.5 Instrumental Methods	30
1.5.1 DRIFTS.....	30
1.5.2 MS, GC, NMR and other Methods	32
1.6 Challenges in this Field and Objectives of this Thesis.....	33
1.7 Overview of the Research Wok in this Thesis.....	33
References	35
Chapter 2 A Combined Diffuse Reflectance Infrared Fourier Transform Spectroscopy–Mass Spectroscopy–Gas Chromatography for the Operando Study of the Heterogeneously Catalyzed CO ₂ Hydrogenation over Transition Metal-Based Catalysts.....	41

Abstract	42
2.1 Introduction.....	43
2.2 Experimental	45
2.2.1 Setup	45
2.2.2 Experiments.....	46
2.2.3 Determinations of rate constant and activation energy.....	47
2.3 Results and Discussions.....	50
2.3.1 CO ₂ adsorption and hydrogenation reactions on the pristine metal surfaces	50
2.3.2 CO ₂ hydrogenation reaction on the metal hydride surface	52
2.3.3 CO ₂ hydrogenation reaction on the Co-CoO surface	53
2.3.4 Kinetic comparison of the CO ₂ methanation reaction on the pristine and alloyed metals, and the Co-CoO surface	57
2.4 Conclusions.....	58
Reference.....	59
Chapter 3 Identifying Reaction Species by Evolutionary Fitting and Kinetic Analysis: an Example of CO₂ Hydrogenation in DRIFTS.....	62
Abstract	63
3.1 Introduction.....	64
3.2 Fitting and Experimental Methods	65
3.2.1 Bilevel evolutionary Gaussian fitting (BEGF) procedure	65
3.2.2 Experimental methods.....	68
3.3 Results and Discussions.....	68
3.3.1 BEGF analysis of spectra of ex-situ-HCOO* hydrogenation.....	68
3.3.2 BEGF analysis of spectra of CO ₂ hydrogenation.....	72
3.4 Conclusions.....	80
References	82
Supporting Information	84
Chapter 4 In Situ Control of the Adsorption Species in CO₂ Hydrogenation: Determination of Intermediates and Byproducts	96
Abstract	97
4.1 Introduction.....	98
4.2 Experimental Section.....	99

4.3	Results and Discussions.....	100
4.3.1	Correlations of coexisting adsorption species in the CO ₂ hydrogenation reaction.....	100
4.3.2	Unraveling the roles of individual species using in situ control	102
4.4	Conclusions.....	109
	References	111
	Supporting Information	114
Chapter 5	Unraveling and Optimizing the Metal-Metal Oxide Synergistic Effect in a Highly Active Co _x (CoO) _{1-x} Catalyst for CO ₂ Hydrogenation.....	123
	Abstract	124
5.1	Introduction.....	125
5.2	Experimental Methods.....	127
5.2.1	Sample preparations.....	127
5.2.2	Characterization.....	128
5.2.3	CO ₂ hydrogenation	129
5.2.4	CO ₂ + H ₂ adsorption	129
5.3	Results and Discussion	130
5.3.1	Sample synthesis and characterization.....	130
5.3.2	Activity in the CO ₂ conversion.....	133
5.3.3	Sample stability during hydrogenation.....	136
5.3.4	Surface reaction mechanisms	137
5.3.5	Surface electronic structure	142
5.4	Conclusions.....	144
	References	146
	Supporting Information	149
	Conclusions	160
	Perspectives.....	163
	Apendix – BEGF Program	164
	Life Story.....	172
	Curriculum Vitae	176

List of Figures

Figure 1.1. (a) Total world energy consumption by primary energy source. (b) Each primary energy source contributing in the world energy consumption. (c) Majority of world CO ₂ emission by the primary energy source. (d) Total world CO ₂ emission contributed by energy source. Reproduced from references.	16
Figure 1.2. World GDP (purchasing power parity, 2011 dollars) is growing relative to energy consumption and CO ₂ emissions. Reproduced from references.	17
Figure 1.3. Schematic representation of the closed carbon and synthetic fuel cycle. Hydrogen is obtained from water splitting by renewable energy. CO ₂ captured from air is reduced by hydrogen to hydrocarbons. Reproduced from reference.	18
Figure 1.4. Standard formation enthalpy, entropy, and free energy of linear alkanes (n-alkanes) at 300 K as a function of the number of carbon atoms from CO ₂ reduction by H ₂ . The phases of C ₅₊ are considered as liquid.	19
Figure 1.5. Three possible structures of bent CO ₂ on Ni surface.	20
Figure 1.6. CO ₂ adsorption at 298 K on (a) Cu(111) with subsurface oxygen, (b) Cu(111) with subsurface oxygen and H ₂ O, (c) Ag(111) surface with surface oxygen, and (d) Ag(111) surface with surface oxygen and H ₂ O. Reproduced from reference.	22
Figure 1.7. Equilibrium concentration of CO, CH ₄ , CH ₃ OH production from CO ₂ hydrogenation as function of temperature.	23
Figure 1.8. The distinct geometric and electronic structures of nanoparticles bulk, nanoclusters and single atom. Reproduced from reference.	26
Figure 1.9. (a) Pure CO ₂ adsorption on KBr at pressure from 50 to 300 mbar. (b) 200 mbar CO ₂ adsorption on KBr at temperature from 50 to 300 °C.	32
Figure 2.1. Schematic of the DRIFTS-MS-GC instrument utilized in this study.	46
Figure 2.2. (a) IR spectra for 1 bar CO ₂ adsorption on Fe, Co, Ni, and Cu surfaces at 400°C. (b) CH ₄ yields from the CO ₂ hydrogenation reactions on the Fe, Co, Ni, and Cu surfaces at 200°C.	51
Figure 2.3. (a) IR spectra for the CO ₂ hydrogenation reaction on LaNi ₄ Cu surface at elevating temperatures. (b) The integrated IR absorbance of gaseous reactant of CO ₂ and gaseous products of CO and CH ₄ . CO ₂ intensity was divided by five times.	53

Figure 2.4. (a) CO ₂ and CH ₄ conversion from CO ₂ hydrogenation on Co-CoO surface analyzed using MS data. (b) The calculated yields of C ₂ H ₆ and CO gas products using GC data. (c) Very small quantities of CH ₃ OH, C ₂ H ₅ OH, and CH ₃ COOH liquid products collected using the inline deionized water and measured using NMR.	55
Figure 2.5. (a) IR spectra for the CO ₂ hydrogenation reaction on Co-CoO surface. (b) Development of the adsorbed formate and carbonate with IR peaks at 1620 and 1520 cm ⁻¹ , respectively.	56
Figure 2.6. Reaction rate constants k' at 200 °C (left axis) and activation energies E_a of CO ₂ methanation (right axis). Activation energies of CO ₂ methanation on Co and Ni were taken from the reference.	58
Figure 3.1. The developed bilevel evolutionary Gaussian fitting algorithm.	67
Figure 3.2. (a) The error evolution approaching convergence as a function of time and (b) the average time of iteration for the fitting in the range of 1800–1500 cm ⁻¹ from 20–220 °C by BEGF.	69
Figure 3.3 (a) The experimental spectra of ex-situ-HCOO ^{-*} hydrogenation on Ru/Al ₂ O ₃ (black circles) with fitted peaks (colored lines) in the ranges of 1770–1538 and 1440–1360 cm ⁻¹ . The fitting result of the evolution of (b) Bi-HCOO ^{-*} -Al ₂ O ₃ , (c) HCOO ^{-*} -MSI, (d) Br-HCOO ^{-*} -Ru during the reaction of ex-situ-HCOO ^{-*} hydrogenation.	71
Figure 3.4. The spectra of CO ₂ hydrogenation on Ru/Al ₂ O ₃ (black circles) with fitted Gaussian peaks (colored lines) in the ranges 2100–1840, 1780–1535 and 1530–1480 cm ⁻¹ . The vibrations in the range of 2100–1840 cm ⁻¹ are C≡O asymmetric stretching, and in 1780–1535 cm ⁻¹ are O-C-O asymmetric stretching of Bi-HCOO ^{-*} -Al ₂ O ₃ (green peak), HCOO ^{-*} -MSI (blue peak), Br-HCOO ^{-*} -Ru (yellow peak), HCO ₃ ^{-*} (red peak), and CO ₃ ^{2-*} (magenta).	74
Figure 3.5. The full infrared spectra of (a) ¹³ CO ₂ hydrogenation by mixing 200 mbar ¹³ CO ₂ and 800 mbar H ₂ , after which heated from 20 to 300 °C by 1 °C/min, (c) ¹² CO ₂ deuteration in pure D ₂ by mixing 200 mbar ¹² CO ₂ and 800 mbar D ₂ , after which heated from 20 to 300 °C by 1 °C/min. The extracted spectra in the wavenumber range between 1800 to 1200 cm ⁻¹ from (b) ¹³ CO ₂ hydrogenation and (d) ¹² CO ₂ deuteration.	76
Figure 3.6. The fitting result of the evolution of (a) Bi-HCOO ^{-*} -Al ₂ O ₃ , (b) HCOO ^{-*} -MSI, (c) Br-HCOO ^{-*} -Ru during the CO ₂ hydrogenation.	78
Figure 3.7. The fitting result of the evolution of (a) HCO ₃ ^{-*} and (b) CO ₃ ^{2-*} during CO ₂ hydrogenation.	79
Figure 3.8. The fitting result of the evolution of (a) linear-CO* and (b) bridged-CO* during the reaction. ..	80

Figure 4.1. (a) Infrared absorbance spectra with the insertion of CO ₂ to CH ₄ conversion during CO ₂ hydrogenation (Exp. I). And evolution of adsorption species of (b) HCO ₃ ^{-*} with peak at 1650 cm ⁻¹ and CO ₃ ^{2-*} with peak at 1450 cm ⁻¹ located at MSI, (c) R-CO* on Ru, (d) Bi-HCOO* on Ru, Br- and Br-HCOO* on Ru, and Bi-HCOO* on Al ₂ O ₃ . In (b)-(d), circles are the original data of integrated peak intensity from Gaussian fittings, and the lines are the non-linear fittings of those original data.	101
Figure 4.2. (a) HCO ₃ ^{-*} and CO ₃ ^{2-*} , (b) R-CO*, (c) three structural HCOO ^{-*} during CO ₂ adsorption reaction (Exp. II); (d) HCO ₃ ^{-*} and CO ₃ ^{2-*} , (e) R-CO* during HCO ₃ ^{-*} decomposition (Exp. III). The peak positions were the same as in Figure 4.1. The circles are the original data of integrated peak intensity from Gaussian fittings, and the lines are the non-linear fittings of those original data.	103
Figure 4.3. (a) Production of CH ₄ and (b) reduction of CO* during R-CO* hydrogenation (Exp. IV). Evolution of (c) HCO ₃ ^{-*} and CO ₃ ^{2-*} , (d) R-CO*, (e) three structural HCOO ^{-*} , (f) CH ₄ during HCO ₃ ^{-*} hydrogenation (Exp. V). The peak positions were the same as in Figure 1. The circles are the original data of integrated peak intensity from Gaussian fittings, and the lines are the non-linear fittings of those original data.	105
Figure 4.4 Schema of the hydrogenation steps of CO ₂ on Ru/Al ₂ O ₃	107
Figure 5.1. Mass loss of Co ₃ O ₄ sample when reduced in H ₂ /He flow with a heating rate of 2 °C min ⁻¹ in a microbalance.	130
Figure 5.2. XPS of Co 2p _{3/2} and 2p _{1/2} peaks of synthesized samples. Black, blue and red lines represent the deconvoluted signals of Co ₃ O ₄ , CoO and Co states, respectively. Gray and gray dash lines are the total fitted spectra and baseline, respectively. The peaks were fitted by using the standard spectra of Co ₃ O ₄ , CoO and Co.	132
Figure 5.3. TEM of prepared samples. (a) Co ₃ O ₄ , (b) Co _{0.2} , (c) Co _{0.5} , (d) Co _{0.8}	133
Figure 5.4. (a) CO ₂ conversion as a function of temperature, (b) onset temperature of 2% CO ₂ conversion, (c) CO ₂ conversion at 180, 200, and 220 °C, and (d) CH ₄ production rate at 180, 200, and 220 °C over the Co ₃ O ₄ , Co _{0.2} , Co _{0.5} and Co _{0.8} samples.	135
Figure 5.5. Arrhenius plot of CH ₄ formation in the CO ₂ conversion range of 2%–30% for Co _{0.2} , Co _{0.5} , Co _{0.8} , and Co ₃ O ₄ samples. The corresponding temperature ranges are 160–220 °C for Co _{0.2} sample, 180–231 °C for Co _{0.5} sample, 202–260 °C for Co _{0.8} sample, and 283–313 °C for Co ₃ O ₄ sample. ...	136
Figure 5.6. (a) DRIFTS spectra during CO ₂ + H ₂ co-adsorption at 100 °C, revealing the presence of formate and carbonate species. (b) CO ₂ desorption measured using TPD-MS (m/z = 44) from CO ₂ + H ₂ co-	

adsorption with a heating rate of $15\text{ }^{\circ}\text{C min}^{-1}$, and the intensities are normalized with He intensity. 139

Figure 5.7. The evolution of adsorbed species and CO_2 to CH_4 conversions during CO_2 hydrogenation on (a) $\text{Co}_{0.5}$, (b) $\text{Co}_{0.2}$, (c) Co_3O_4 . Left panels were data from DRIFTS, and right panels were data from MS. 141

Figure 5.8. (a) Core-level XPS and (b) valence band of the partially reduced sample (58% Co and 42% CoO) prepared and measured in NAP-XPS. The black line which is crossed at 1.15 eV of x-axis shows the onset of the edge of the valence band of CoO. Fermi level (E_f) is at 0 eV. 143

Note: figures from supporting information or supplementary data are not listed here

List of Tables

Table 1.1. Bond strength ²¹	21
Table 3.1. Vibrational modes and infrared peak positions (cm ⁻¹) of formate, bicarbonate and carbonate from CO ₂ hydrogenation.	70
Table 3.2. Vibrational modes and infrared peak positions (cm ⁻¹) of ¹³ C-formate, -bicarbonate and -carbonate from ¹³ CO ₂ hydrogenation.	76
Table 3.3. Vibrational modes and infrared peak positions (cm ⁻¹) of D-formate, -bicarbonate and -carbonate from CO ₂ hydrogenation in pure D ₂	77
Table 4.1. Vibrational modes and infrared peak positions (cm ⁻¹) of the reference samples and the reaction species from this work.	108
Table 4.2 Vibrational modes and infrared peak positions (cm ⁻¹) of CO* from this work.	109
Table 5.1. H ₂ reduction conditions, metal ratio and specific surface area of Co _x (CoO) _(1-x) samples.	131
Table 5. 2. Activation energies of CH ₄ formation ($E_a^f(CH_4)$), CO ₂ desorption from CO ₂ + H ₂ co-adsorption ($E_a^{d1}(CO_2)$ and $E_a^{d2}(CO_2)$), the main adsorption products on the sample surfaces and the corresponding main infrared peaks, i.e., O–C–O asymmetric stretching ($\nu_{as}(O-C-O)$). $E_a^{d1}(CO_2)$ and $E_a^{d2}(CO_2)$ refer to the first and second peak in the TPD spectrum, respectively.	137

Note: tables from supporting information or supplementary data are not listed here

Chapter 1 Introduction

1.1 World Energy Requirement

The annual world energy supply from primary sources such as oil, coal, natural gas, renewables, etc. increased from 11.6 terawatt (TW) in 1990 to 18.5 TW in 2017 (Figure 1.1(a)-(b)). This equals to 58% increase in total.¹ Simultaneously, the CO₂ emission increased from 20.5 gigatons (Gt) in 1990 to 32.8 Gt in 2017 with 43% increasing in total. The atmospheric CO₂ concentration increased from approximately 280 ppm in the early 1800s to 407 ppm now (Figure 1.1(c)-(d)).^{2,3} The increase of CO₂ emission contributes to the global climate change.⁴ However, the energy consumption and climate change is driven by economic and population growth. As shown in Figure 1.2, the world GDP growth links directly to the energy consumption and CO₂ emission.⁵ It is predicted that the fossil fuels such as coal, petroleum, and natural gas will continue to supply more than three-fourths of world energy demand in 2040, and the atmospheric CO₂ concentration will reach nearly 600 ppm in 2100.^{1-4,6}

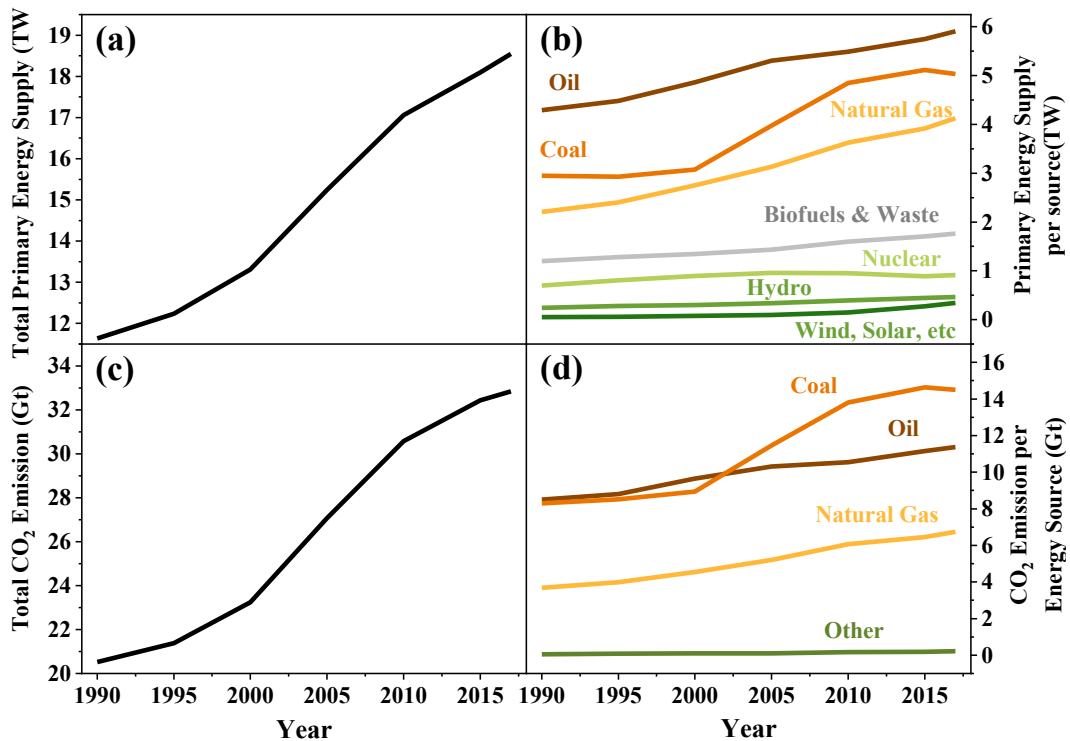


Figure 1.1. (a) Total world energy consumption by primary energy source. (b) Each primary energy source contributing in the world energy consumption. (c) Majority of world CO₂ emission by the primary energy source. (d) Total world CO₂ emission contributed by energy source. Reproduced from references.^{1,2}

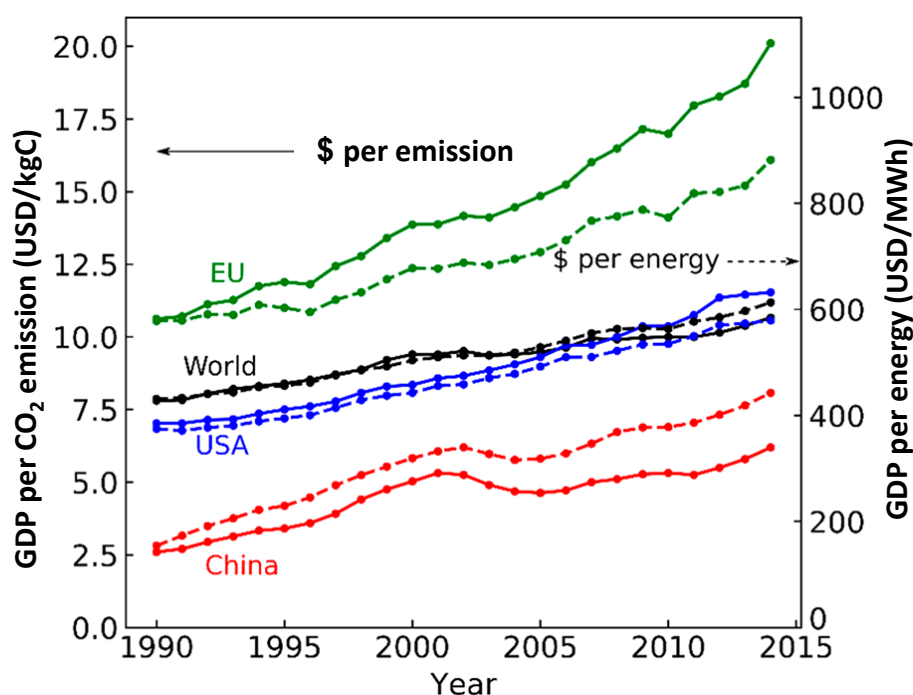


Figure 1.2. World GDP (purchasing power parity, 2011 dollars) is growing relative to energy consumption and CO₂ emissions. Reproduced from references.⁴

The continuously increasing consumption of the unsustainable fossil fuels motivates the society to search sustainable and clean energy supplies. Hydropower, wind, solar, geothermal, and biomass are exploited and promising to replace the majority of role of fossil fuels. According to the 30-year statistics of these renewable energies development, they are predicted to contribute roughly the same quantity as natural gas and coal in global net electricity generation until 2040.^{7,8} Nevertheless, the renewables face a problem of time- and location-dependent energy fluxes, restricting their energy supply. Energy storage is thus required in order to balance the short term (day/night) fluctuations and seasonal variations. Therefore, an energy carrier has to be produced from heat or electricity. The energy density is crucial for transport and mobile applications. Hydrogen, which can be produced from electricity and heat by means of electrolysis of water, offers the highest gravimetric energy density of all combustibles with 39 kWh/kg. Current hydrogen storage density reaches max. 20 mass% in borohydrides. Without taking into account the stability and cyclability problems of this material, an energy density of 7.8 kWh/kg could be achieved. However, this is 60% of the energy density of hydrocarbon fuels, e.g. diesel (12.8 kWh/kg). In order to overcome the limitation of the energy density of hydrides, hydrogen can be utilized to reduce CO₂ to hydrocarbons, i.e. a synthetic fuel as shown in Figure 1.3.

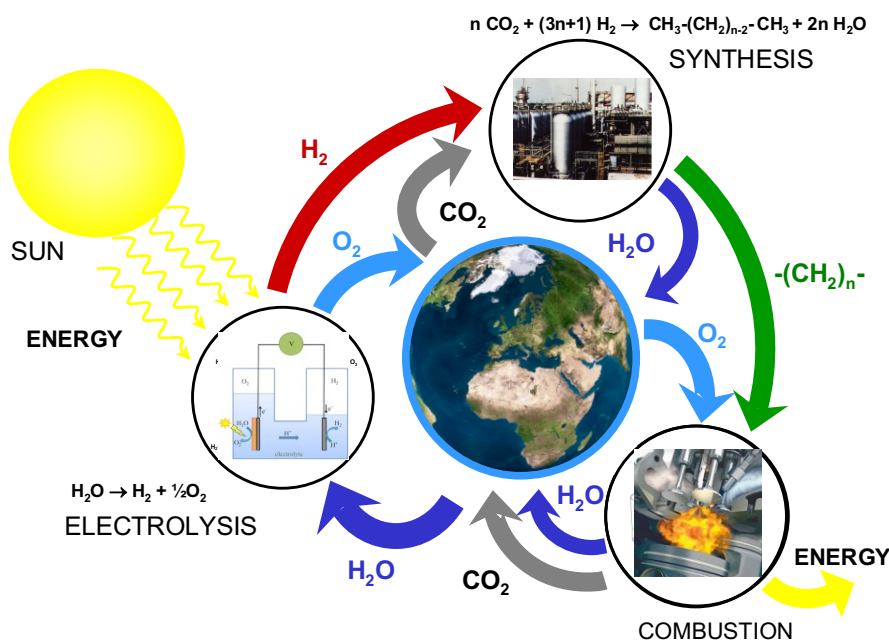


Figure 1.3. Schematic representation of the closed carbon and synthetic fuel cycle. Hydrogen is obtained from water splitting by renewable energy. CO₂ captured from air is reduced by hydrogen to hydrocarbons. Reproduced from reference.⁹

1.2 Synthetic Hydrocarbons from CO₂ Conversion

Converting CO₂ to synthetic hydrocarbons using H₂ and catalyst can close carbon cycle and meet the energy demand. Therefore, investigation of reaction mechanism of CO₂ hydrogenation over gas/solid interface is the subject of this thesis.

1.2.1 CO₂ properties

CO₂ is a stable molecule ($\Delta G_f^0 = -394.4 \text{ kJ mol}^{-1}$, Eq.1.1). However, it can be activated via catalytic reaction. The reaction of CO₂ with H₂ to hydrocarbons is exothermic (Eq.1.2, Figure 1.4). The thermal catalysis for this process is either based on indirect routes: Sabatier reaction (Eq.1.3), or the reverse water gas shift (RWGS) reaction (Eq.1.4) combined with the Fischer-Tropsch (FT) reaction (Eq.1.5) at high temperature and under high pressure, or methanol production (Eq.1.6) at the first stage and olefin productions from CH₃OH at a separated stage over transition metal based catalysts.¹⁰⁻¹³

$$\text{C} + \text{O}_2 \rightarrow \text{CO}_2, \Delta H_f^0 = -393.51 \text{ kJ mol}^{-1}, \Delta S_f^0 = 2.86 \text{ J K}^{-1} \text{ mol}^{-1}, \Delta G_f^0 = -394.36 \text{ kJ mol}^{-1}. \quad \text{Eq. 1.1}$$

$$n\text{CO}_2 + (3n+1)\text{H}_2 \rightarrow \text{C}_n\text{H}_{n+2} + 2n\text{H}_2\text{O}. \quad \text{Eq. 1.2}$$

$$\text{CO}_2 + 4\text{H}_2 \rightarrow \text{CH}_4 + 2\text{H}_2\text{O}, \Delta H_f^0 = -165 \text{ kJ mol}^{-1}, \Delta S^0 = -172.6 \text{ JK}^{-1}\text{mol}^{-1}, \Delta G_f^0(300 \text{ K}) = -113.2 \text{ kJ mol}^{-1}. \quad \text{Eq. 1.3}$$

$$(\text{CO}_2 + \text{H}_2 \rightarrow \text{CO} + \text{H}_2\text{O}, \Delta H_f^0 = 41.17 \text{ kJ mol}^{-1}, \Delta S^0 = 42.26 \text{ JK}^{-1}\text{mol}^{-1}, \Delta G_f^0(298 \text{ K}) = 28.58 \text{ kJ mol}^{-1}). \quad \text{Eq. 1.4}$$

$$n\text{CO} + (2n+1)\text{H}_2 \rightarrow \text{C}_n\text{H}_{2n+2} + n\text{H}_2\text{O}. \quad \text{Eq. 1.5}$$

$$\text{CO}_2 + 3\text{H}_2 \rightarrow \text{CH}_3\text{OH} + \text{H}_2\text{O}, \Delta H_f^0 = -130.7 \text{ kJ mol}^{-1}, \Delta S^0 = -408.7 \text{ JK}^{-1}\text{mol}^{-1}, \Delta G_f^0(300 \text{ K}) = -8.1 \text{ kJ mol}^{-1}. \quad \text{Eq. 1.6}$$

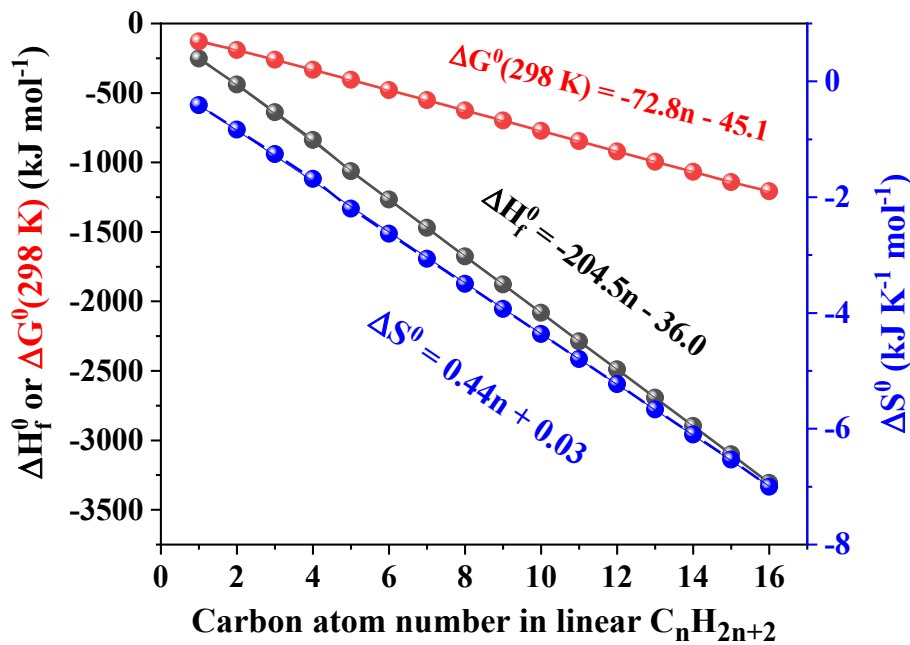


Figure 1.4. Standard formation enthalpy (ΔH_f^0), entropy (ΔS^0), and free energy (ΔG^0) of linear alkanes (n-alkanes) at 300 K as a function of the number of carbon atoms from CO_2 reduction by H_2 . The phases of C_{5+} are considered as liquid.

Although the overall Gibbs energy of the CO_2 hydrogenation reaction is negative at room temperature, the reactions do not take place at room temperature due to high energy barrier. Generally, heating enables faster interactions between the molecules. However, the high temperature is not favorable to the exothermic reaction. Therefore, metal-based catalysts are used to lower down the activation energy of the CO_2 hydrogenation reaction.

1.2.2 CO₂ interaction with solid surface

1.2.2.1 CO₂ activation

CO₂ reduction processes initiate from CO₂ chemisorption and activation. Chemisorbed species normally sit on defect sites, such as step, kink, and unsaturated coordinate sites, where induce the electron transfer between CO₂ and catalyst surface.^{14,15} The specific adsorption orientations remain enigmatic. The three possible coordinative structures have been reported as (a) bridge on without confirmation of the bond angle, (b) side on with one carbon and one oxygen atoms, and (c) end on with the carbon atom or one oxygen atom (Figure 1.5).^{16,17} The different adsorption structures could not only lead to different reaction intermediates, e.g. *HCOO or *CO, but also to different explanations for the electron-transfer mechanisms, i.e. outer-sphere, inter-sphere, proton-coupled electron transfer (PCET), and decoupled proton-electron transfer.¹⁸ Comparing the bond strength of metal-C and metal-O bonds, the metal-O bond is much stronger than its metal-C bond (refer to metal-CH₃ bonds, Table 1).¹⁹ This indicates that CO₂ adsorbed on the surface with metal-O form would be stronger than that with the metal-C form. Besides, the metal-O bonds become stronger from Cu to Fe in the first row of transition metals in the periodic table, while the metal-CH₃ bond follows the opposite trend, implying that Fe is more easily oxidized by oxygen than the heavier transition metals on the same period, while CH₃ is more strongly fixed on Cu than that on Fe, Co or Ni.

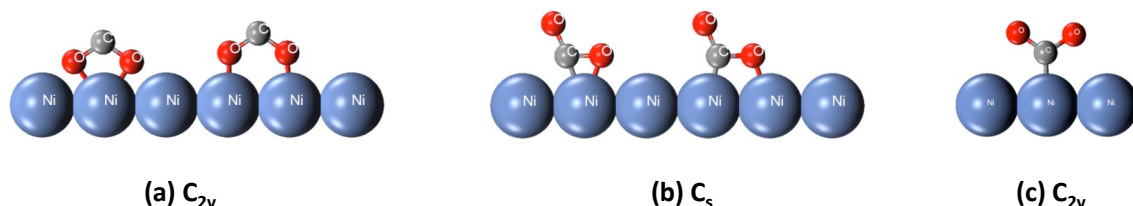


Figure 1.5. Three possible structures of bent CO₂ on Ni surface.¹⁶

Freund found in some early work that CO₂ adsorbed on Ni(110) surface forms CO₂⁻ anion by observing work function change.¹⁶ CO₂⁻ anion has bond order of 1.5 and elongated and bent bond length of 1.25 Å. For comparison, the C=O bond of gaseous CO₂ has bond order of 2 and bond length of 1.17 Å. The formation of CO₂⁻ anion is an energetically favored process (CO₂⁻ → CO₂ + e⁻, E_a = 0.4 eV) at 80~130 K. CO₂⁻ anion is relatively stable with the lifetime of 60~90 μs. This bent CO₂⁻ shows IR peak of O-C-O asymmetric stretching at around 1600 cm⁻¹, and is a precursor of dissociated CO + O.^{16,20} Dissociation of CO₂ occurs in the temperature range of 220~470 K.^{21,22}

Table 1.1. Bond strength²¹

Bond strength (kJ/mol)	C	H	O	Fe	Co	Ni	Cu
C	348	439 (CH ₄)	804 (O ₂) 1072 (CO)	364 (Fe-CH ₂) 135 (Fe-CH ₃)	331 (Co-CH ₂) 178 (Co-CH ₃)	208 (Ni-CH ₃)	25 (Cu-CO) 223 (Cu-CH ₃)
H		436	430	148	245	240	255
O			498	407	397	366	293
Fe				118			
Co					< 127		
Ni						204	
Cu							182

CO₂ adsorbed on oxide surface forms carbonate species, and its co-adsorption with H produces formate.²³ Surface alkali atoms and adsorbed H₂O molecules promote CO₂ chemisorption.^{24–26} Paul found that on all alkali promoted and hydrogen deficient surfaces, CO₂ forms oxalate anion C₂O₄²⁻.²⁷ The C₂O₄²⁻ is stable from cryogenic temperature to room temperature. A low coordinated C₂O₄²⁻ can be found at 2310 and 1710 cm⁻¹, and a high coordinated C₂O₄²⁻ can be detected at 1650~1700 cm⁻¹. Decomposition of this species gives either CO₃²⁻ + CO or C + O, depending on the metals. Recent X-ray spectroscopy investigations using synchrotron radiation discovered that surface oxidation state and adsorbed H₂O molecule can stabilize chemisorbed CO₂ at room temperature. For instance, on Cu surface, the surface Cu⁺ atom stabilizes chemisorbed linear CO₂ and the neighbor adsorbed H₂O interacts with CO₂ to stabilize the bent CO₂ through a hydrogen bond at 298 K (Figure 1.6(a)-(b)). On Ag surface, linear CO₂ is not stable. However, CO₂ reacts strongly with surface oxygen to form a carbonic acid structure (Figure 1.6(c)). This species can connect one to four adsorbed H₂O through hydrogen bonding. Bent CO₂ can also be stabilized by a pair of surface adsorbed H₂O via forming hydrogen bonds with each O of bent CO₂ (Figure 1.6(d)).^{28,29}

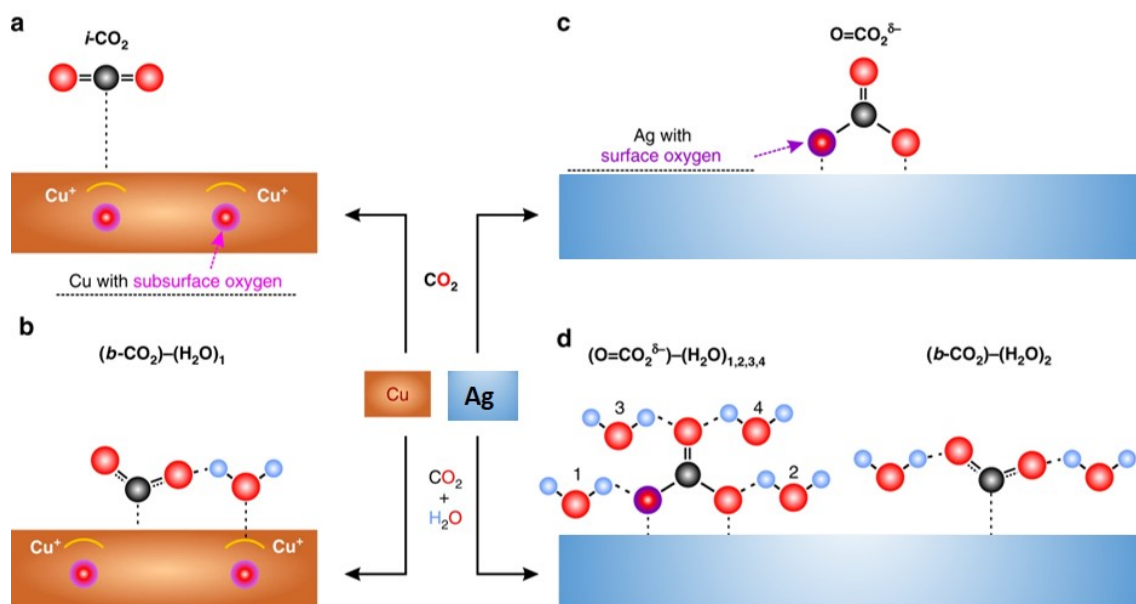


Figure 1.6. CO₂ adsorption at 298 K on (a) Cu(111) with subsurface oxygen, (b) Cu(111) with subsurface oxygen and H₂O, (c) Ag(111) surface with surface oxygen, and (d) Ag(111) surface with surface oxygen and H₂O. Reproduced from reference.³⁰

1.2.2.2 Hydrogenation

CO₂ conversion to fuels has drawn enormous attention in the recent three decades for its potential to reduce atmospheric greenhouse effect and to store large quantities of renewable energy. Apart from the indirect methods as mentioned in Section 1.1, it is also possible to have direct CO₂ hydrogenation through various heterogeneously catalytic approaches such as thermal, electrochemical and photocatalysis. However, the direct CO₂ hydrogenation gives rise to only gaseous products, i.e., C₁–C₄.³⁰

C₁ products such as CH₄ and CO are usually the most common products under atmospheric pressure through Sabatier and RWGS reactions, respectively. CH₃OH as another valuable product is obtained under high pressure and on Cu-based catalysts, e.g. Cu/ZnO/Al₂O₃, Cu/ZrO₂, CeO_x/Cu *etc.*^{31–33} According to the reaction equilibrium, CO production starts from high temperature compared to the hydrocarbons products (Figure 1.7). Increasing temperature augments the CO yield. CH₄ has high yield in wide temperature range of 200 – 800 °C. CH₃OH can be produced at lower temperature between 100 – 300 °C, but generally this happens at pressure of more than 20 bar.

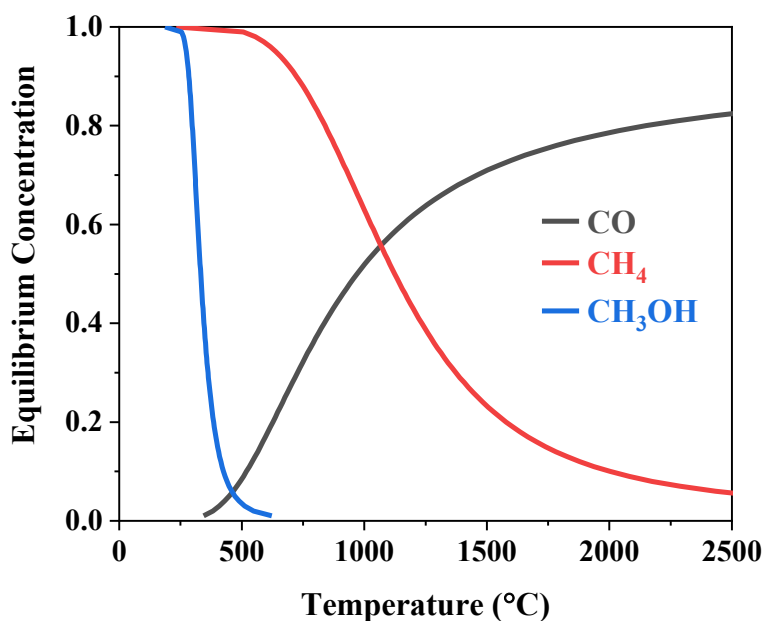


Figure 1.7. Equilibrium concentration of CO, CH₄, CH₃OH production from CO₂ hydrogenation as function of temperature.

C₂₊ products from direct CO₂ hydrogenation are limited in the range of C₂-C₄ on a tandem or bifunctional catalyst.^{34,35} To produce C₂₊ hydrocarbons involved the C-C bond coupling mechanisms, which is strongly limited probably by the transfer kinetics of massive electrons and atoms. The current speculations of carbon chain growth in thermal catalysis are mostly based on FT reaction with the carbide or CO insertion mechanisms.^{36,37} Hensen's group found that the formation of σ bonds such as C-H bond is structure-insensitive, hence taking place likely on planar sites.³⁸ In contrast, carbon chain growth on stepped sites via CH_x monomer, hence requires a certain particle size.^{39,40} For the same size of the cobalt particle, higher CO pressure gives less active sites, therefore lowers the CO consumption rate and enhances the chain growth; lower CO pressure gives more active sites, therefore accelerates the CO consumption rate and lessens the chain growth.³⁹

Tremendous assembling and modifications, including size minimizing, depositing on supports, bi-functionalizing and alloying of the metal catalysts have been made to improve the activity and/or selectivity based on the transition metals. In order to understand the relationships between materials and CO₂ hydrogenation in the heterogeneous catalysis, the following two sections have been distributed to the novel catalyst design and active site studies.

1.3 Heterogeneous Catalysts for CO₂ hydrogenation

Based on the compositions of the catalysts, we will introduce the materials from the simplest pristine transition metals to novel optimized materials.

1.3.1 Pristine metals

A summarized and systematic research has been represented by Mutschler, *et al* recently about CO₂ hydrogenation in a flow gas feed condition under ambient pressure on unsupported pristine Fe, Co, Ni, and Cu metal powders with particle size of around 1 μm .⁴¹ A commercial 0.5wt%Ru/Al₂O₃ was studied simultaneously for reference. A comparison of reactivity of those metals showed Co, Ni and Ru/Al₂O₃ are principally active in Sabatier reaction to produce CH₄ with similar activation energies of 77, 74 and 73 kJ/mol, respectively. The maximal CH₄ yields found on Co, Ni and Ru/Al₂O₃ were 70.2% at 661 K 43.8% at 786 K and 73.4% at 652 K, respectively. At higher temperature, the endothermic RWGS reaction dominates to produce CO, leading to a maximum CO yield of 6.9% at 817 K on Co, 18.2% at 829 K on Ni, and 26.2% at 813 K on Ru/Al₂O₃. Fe is favorable for RWGS reaction to produce CO with activation energy of 50 kJ/mol and with a maximum CO yield of 22.4% at 813 K. In all these four catalysts, C₂₊ production is less than 1%. Cu is inactive toward CO₂ conversion. These results are consistent with the old report by Bartholomew, *et al.* in the 1980s about the silica-supported metals for CO₂ hydrogenation.⁴²

1.3.2 Supported metals

Supported metals have been widely studied as the supports are used to stabilize the active metal nanoparticles. The systematical studies could be dated back to 1980s by Bartholomew *et al.*^{42–45} Bartholomew *et al.* studied CO₂ and CO hydrogenation on supported nickel systematically in terms of various kinetic factors including gas hourly space velocity and partial pressure of the feed gases, as well as the effects of the supports. CO₂ turnover number increases with increasing space velocity from 5000 to 50000 h⁻¹, but the selectivity to CH₄ is on the opposite. When the partial pressures of CO₂ (< 2%) and H₂ are low (< 10%), the reaction rate is moderately dependent on CO₂ and H₂ concentrations; while at higher partial pressure, CH₄ turnover number tends to be independent of the reactant concentrations. When the total pressure increases, CO₂ conversion is invariant, whereas CH₄ turnover number and yield increase, simultaneously CO production rate and yield decrease. When comparing CO₂ and CO hydrogenation, CO₂ conversion shows nearly same rate as CO hydrogenation between 500-575 K, but slower above 575 K. The activation energy of CO₂ hydrogenation (80

kJ/mol) is lower than that of CO (96 kJ/mol). When adding CO into CO₂ and H₂, CO₂ conversion and CH₄ production are inhibited at CO concentration exceeding 0.012% 525 K. The inhibition effect of CO becomes less strong when increasing the temperature, e.g., this inhibition occurs when CO concentration exceeds 0.12% at 600 K. As for the support effect, the activity and CH₄ selectivity shows a trend of Ni/SiO₂ < unsupported Ni < Ni/Al₂O₃ < Ni/TiO₂ due to the increasing degree of metal-support interaction which leads to increasing CO₂/H and CO/H adsorption ratios.

In addition, Bartholomew, *et al.* had a benchmark investigation of the specific activities and selectivity of CO₂ hydrogenation on silica-supported group VIII metals (Fe, Co, Ni, Ru).^{42–45} In the condition of 450–650 K, 140–1030 kPa, and space velocities of 4000–50000 h⁻¹, the specific activity of CO₂ hydrogenation showed the order of Co/SiO₂ > Ru/SiO₂ > Ni/SiO₂ > Fe/SiO₂; the selectivity toward CH₄ production showed the order of Ru/SiO₂ > Ni/SiO₂ > Co/SiO₂ > Fe/SiO₂. CO is produced significantly on Ni/SiO₂ and Co/SiO₂, and is the primary product on Fe/SiO₂. Visible amounts, low compared to CH₄, of C₂–C₅ hydrocarbons are produced on Fe/SiO₂ and Co/SiO₂, with an active order of Fe/SiO₂ > Co/SiO₂ > Ru/SiO₂.

1.3.3 Bimetals

The main advantage of alloys is to provide multiple binding sites for the reactants and intermediates. When integrating the quantum confinement and alloy effect for the nanosized metals, the d-band reconstructs through charge transfer between different metals.^{46,47} Therefore, alloy could exhibit altered reactivity comparing to the single metals. Ni₃Fe alloy supported on Al₂O₃ shows improved CO₂ conversion and CH₄ selectivity with regard to commercial Ni/Al₂O₃.⁴⁸ Ni-Co nanoalloy enhances the higher alcohol synthesis by increasing the amount of the non-dissociated CO on the catalyst surface for CO insertion.⁴⁹ When unpromoted Fe-based catalyst exhibits low selectivity of C₂–C₄⁼ olefins and C₅+, Cu doped Fe-based nanoparticles shows a decreased selectivity of C₂–C₄⁼ olefins but increased selectivity toward C₅+, because of the strong interaction between Cu and Fe.⁵⁰ For Pd-Cu bimetal, DFT calculations show that Pd-Cu bimetal enhances methanol formation by exposing unsaturated Pd atoms on top of stepped PdCu(111). A complementary experimental result confirms that SiO₂-supported PdCu alloy has higher selectivity to CH₃OH than PdCu₃.⁵¹ Another alloy, Pt₃Co, shows octapod shape. This particular shape presents “sharp-tip” effect and combines with alloy effect to accumulate negative charges to activate CO₂ and accordingly enhanced the catalytic activity towards CO₂ hydrogenation to methanol. Pt₃Co octapods display superior catalytic activity with TOF of 758 h⁻¹, and is 2.2, 6.1, and 6.6 times higher than those of Pt₃Co nanocubes, Pt octapods, and Pt

nanocubes, respectively.⁴⁷ In addition, during the hydrogenation of CO₂ into methanol, the catalytic activity of Rh₇₅W₂₅ nanosheets was 5.9, 4.0, and 1.7 times as high as that of Rh nanoparticles, Rh nanosheets, and Rh₇₃W₂₇ nanoparticles, respectively. Mechanistic studies reveal that the remarkable activity of Rh₇₅W₂₅ nanosheets is owing to the integration of quantum confinement and alloy effect.⁵²

1.3.4 Single atom

Single-atom catalysts are similar to the concept of doping material where a foreign atom substitutes the crystal atom. Notwithstanding, single atom is more homogenous on the up surface of 2D sheets than the general doping. The methods for synthesizing single-atom catalysts include physical deposition, metal leaching, wet chemistry, *etc.* The details of the preparation methods have been summarized in the references.^{53,54} Single-atom catalysts are stable owing to strong metal-support interaction. What is more, they possess significant efficiency per active center due to the unsaturated coordination of metal atoms.⁵⁵ In fact, when the nanoparticle size (>2nm) reduces to nanoclusters (~1nm), the continuous energy bands become discrete levels like molecular orbitals; when the size further reduces to single atom level, the quantum size effects occur that confined electron states are formed around the Fermi level (Figure 1.8). Single atom will fill the additional electrons in the valence shell.⁵⁴ However, the high active electrons could be stabilized through the charge transfer between the metal and the support to reach equilibrium.⁵⁶ Therefore, the particular electronic structures enable single-atom catalyst to deliver high activity and selectivity in the reactions.

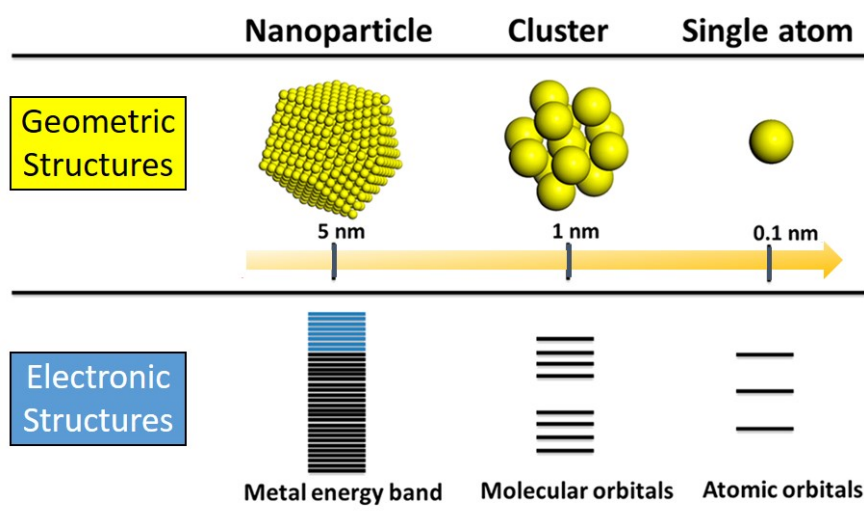


Figure 1.8. The distinct geometric and electronic structures of nanoparticles bulk, nanoclusters and single atom. Reproduced from reference.⁵⁶

Bell and Head-Gordon have investigated twenty-eight single-atom doping the host metal surface to form “single-atom bimetallic” alloys for CO₂ electrochemical reduction by DFT simulation.⁵⁷ They conduct the CO₂ hydrogenation by two steps: 1) CO₂ conversion to CO and 2) CO to CH₄ or CH₃OH. They selected useful single-atom alloys such as Cu, Ni, Pd, Pt, Co, Rh and Ir substituting the host surface Au or Ag. They found CO₂ reduction to CO takes place on the host Au or Ag via proton reduction, while the further reduction of CO occurs on the substitution atoms because those substitution atoms bind *CO selectively. Different host, Au or Ag, alters the elementary pathways of CO₂ to CH₄. In detail, on Rh@Au(100), *CO is hydrogenated through H adding on carbon atom step where *CH_x is the intermediates, whereas on Rh@Ag(100), CO* is hydrogenated by keeping the C-O bond so that methoxyl group *OCH₃ is the intermediates.

1.3.5 Bifunctional

The so-called bifunctional catalysts are normally composed by mixing two different materials. These two materials provide different activities for subsequent steps of CO₂ conversion, for instance, convert CO₂ to CO on one surface, then convert the obtained CO to hydrocarbons. Recent articles were reported a Na-Fe₃O₄/HZSM-5 and In₂O₃/HZSM-5 nano catalyst converted CO₂ to gasoline (C₅-C₁₁) with a robust selectivity as high as 78% through the indirect pathways of passing CO and CH₃OH intermediates, respectively at 350 °C and 3 MPa. The sample was prepared by physical mixing of one-pot synthesized Na-Fe₃O₄ nano catalyst and the commercial/hydrothermal synthesized nanocrystalline zeolite. Zeolite helped increase the selectivity to gasoline-range isoparaffins and aromatics enormously, at the same time the opposite function for C₁-C₄.^{58,59} Based on these results, another bifunctional catalyst, indium–zirconium composite oxide mixed with SAPO-34 zeolite (In-Zr/SAPO-34), was prepared by similar way but realized a direct conversion of CO₂ to C₂-C₄.³⁴ High selectivity of low olefins and low paraffins reach 80% and 93%, respectively at 360 °C. The metal oxide and the zeolite were responsible for the CO₂ activation and C-C coupling, respectively. A tandem catalyst designed with two metal/metal oxide interfaces has also been announced to convert CO₂ to C₂-C₄ with selectivity up to 60% among all hydrocarbon products.³⁵ The catalyst was composed by a CeO₂–Pt core and a mesoporous silica shell which was further decorated with cobalt nanoparticles. The CeO₂/Pt interface converts CO₂ and H₂ into CO through the RWGS reaction, and the Co/mSiO₂ interface subsequently converts CO to C₂-C₄ through FT process.

1.4 Structure-Activity Relationships

Understanding the relationships between catalyst structures and their reactivities is the key to optimize the catalyst and therefore to tune the catalytic activity.

1.4.1 Size effect

Minimizing the particle size is a way of optimize the use of precious metal catalysts. More importantly in fundamental science, when the particle size reduces to nanosized, the specific surface area increases to enable enhanced adsorption of the reactants, thus enhance the conversion. When the particle size reduces to single nanometer, not just the specific surface area increases, but the electronic and surface atomic structures of the particles present different properties due to the low coordination and high chemical potential.^{60–62} Vogt, *et al.* found that decreasing particle size of Ni from 7 to 1 nm lead to a decreasing CO adsorption strength during CO₂ hydrogenation. The rate-determining step of CO₂ hydrogenation was hypothesized to be the process of hydrogenation of intermediate CO.⁶³ Single dispersed Ru agglomerates to form Ru clusters and even nanoparticles during CO₂ hydrogenation reaction at 350 °C. However, the activity of CO₂ conversion and the selectivity of CH₄ over CO increase gradually.⁶⁴ This indicates dynamic of the reconstruction plays positive role in the activity.

Size effect has been especially widely investigated in FT reaction especially on cobalt.^{65,66} De Jong's group has found that the cobalt particle size did not affect the reaction in terms of turnover frequency (TOF), selectivity and activity for CO hydrogenation until 6 nm at 1 bar or 8 nm at 35 bar.^{67,68} When the cobalt particle size was reduced to 2.6 nm, the TOF decreased about 16 times and the C₅₊ selectivity decreased 1.6 times at 35 bar compared to those on 16 nm particles. The lower TOF of Co particles <6 nm is caused by both blocking of edge/corner sites and a lower intrinsic activity at the small terraces because irreversible CO coverage was found to be increased on the smaller particles. The higher methane selectivity of small Co particles is mainly brought about by their higher hydrogen coverages. Besides, the particle size effects facilitate the reversibly bonding of CH_x and OH_x intermediates, whereas inhibit reversible CO coverage for small Co particles (<6 nm). These were attributed to the low-coordinated surface sites of cobalt based on the observation of a decrease of the cobalt coordination number under reaction conditions in extended X-ray absorption fine structure (EXAFS) spectroscopy.

1.4.2 Interface

The metals have been considered to be the reactive centers, while the supports were used for dispersing and stabilizing the metal nanoparticles and even for deactivation function.^{69–71} Burch and co-workers clearly summarized the hypotheses about the synergistic interactions between copper and zinc oxide into six categories as follows: (a) the formation of Cu^+ ions in ZnO; (b) electronic interactions between Cu and ZnO; (c) Schottky Junction effects at the Cu/ZnO interface; (d) the formation of a Cu/Zn pair; (e) a specific reaction at the Cu/ZnO interface; (f) stabilization of Cu in a morphologically active form by ZnO. Surprisingly, they concluded that direct contact between the active sites and support is not necessary for higher activity.⁷² Liu's and Guang's group proved the highly active ZnCu alloy formed by partial reduction of ZnO or a decoration of Cu with metallic Zn.^{33,73} Moreover, Liu's group found that the selectivity to CO or CH_4 in CO_2 hydrogenation on supported bimetallic PtCo can be tuned, *i.e.* CeO_2 or ZrO_2 supported PtCo shows high selectivity of CH_4 production through $^*\text{HCOO}/^*\text{HOCO}$ and/or $^*\text{CH}_3\text{O}$ intermediate steps, while TiO_2 support favors CO formation via $^*\text{HCOO}/^*\text{HOCO}$ intermediates. The intrinsic reason was explained by DFT calculation that the interface has selectivity toward C,O-bound and O-bound species.⁷⁴

Overall, the interfacial effect arises from the strong metal-support interaction. The strong metal-support interaction could be determined by the adhesion energy of the supported metal atoms. The adhesion energy increases when the heat of formation of the oxide is high, the enthalpy of the reduction of the oxide is low, and the density of surface oxygen atoms on the oxide is high. The adsorbates sit on the support site of the interface because the support usually acts as acidic site with anionic vacancy or with hydroxyl group to host the CO_2 or CO molecules.^{75,76}

1.4.3 Specific surface sites

Besides those “detectable” active sites described above, some more micro-structures of the surface are also proposed to be the key active sites for catalytic reaction. Those include surface defects such as step, edge, corner, oxygen vacancies, and B5 center (e.g. five Ru atoms at the step of hcp-crystals).^{77–81} As characterizations of those sites require restrict conditions, for instance, single crystalline surface, ultrahigh vacuum, and relies on special instrument, a direct detection of those atomic structures under reaction condition is a case-by-case challenge. Therefore, we do not expand the discussion of this part.

1.5 Instrumental Methods

The investigation methods often include spectroscopic analyses, such as diffuse infrared reflectance infrared Fourier transform spectroscopy (DRIFTS)⁸², mass spectroscopy (MS), x-ray photoelectron spectroscopy (XPS), nuclear magnetic resonance (NMR), and gas and liquid chromatography (GC and LC, respectively). These instruments are generally used in situ, which is to use these methods independently. Here below is the brief introduction of each technique in this operando method.

1.5.1 DRIFTS

DRIFTS monitors both the gaseous molecules and the surface species due to the molecular spectrum of the bond vibrations are in the IR spectra region. It is the core part in the setup used in this thesis and mainly used for the surface species analysis.

The molecular spectrum originates from the molecular motions which can be expressed by several motion modes:

$$\varepsilon_i = \varepsilon_i^T + \varepsilon_i^R + \varepsilon_i^V + \varepsilon_i^E, \quad \text{Eq. 1.7}$$

where ε_i^T , ε_i^R , ε_i^V , and ε_i^E are the translational, rotational, vibrational, and electronic energy, respectively. The first three terms come from nuclear motion and the fourth term is electron motion. The energy levels are discrete according to quantum theory but with different gaps between the energy levels. The energy range of each motion, calculated by statistical thermodynamic methods, is different and follows the order $\varepsilon_i^T < \varepsilon_i^R < \varepsilon_i^V < \varepsilon_i^E$.¹⁴ This explains why ε_i^R and ε_i^V can be excited by far~middle and middle~near infrared (IR), respectively. Therefore, we utilize the rotational-vibrational spectrum of IR absorption to study the CO₂ chemistry in this thesis. One of the difficulties of IR spectroscopy is the assignment of the bond vibrations of each species (molecules or adsorbates). Because one species could possess multiple stretching and bending modes due to the molecular symmetry, the IR peak of the bond vibrations could couple and disturb the discerning especially for similar species, for example, carbonate (CO₃²⁻), bicarbonate (HCO₃⁻), and formate (HCOO⁻) which could be formed from CO₂ chemisorption.

The CO₂ molecule has four fundamental vibrational degrees of freedom (3N-5 for linear molecules where N is the number of the atoms in the molecule). They are symmetric stretching mode ν_1 at around 1380 cm⁻¹, two identical bending modes ν_2 including in plane and out of plane bending at 667 cm⁻¹, and asymmetric mode ν_3 at 2349 cm⁻¹. The ν_2 and ν_3 are IR active as they have dipole

moment change ($\mu = \mathbf{q} \cdot \mathbf{r}$), while ν_1 is Raman active as the symmetric stretching does not have dipole moment change but polarizability change. In addition, there are two combinational peaks, i.e. $\nu_3 + 2\nu_2$ at 3610 cm^{-1} , and $\nu_3 + \nu_1$ at 3710 cm^{-1} which are IR active, and ν_1 is split to a doublet peak at 1288 and 1389 cm^{-1} which are caused by Fermi resonance of ν_1 and $2\nu_2$ and are Raman active.¹⁵

CO_2 adsorbed on the surface leads to a weakened C=O bond by electrostatic interaction or surface- CO_2 chemical bond formation. Bent CO_2 could be formed when the interaction is strong. This appears as a redshift of the peak on the IR spectrum, which is used to justify physisorption or chemisorption of CO_2 .¹⁶ When CO_2 dissociates or forms other compound on the surface, usually like CO_3^{2-} , HCO_3^- , HCOO^- , carbon monoxide (CO), oxygenate (C_2O_4^-), and so on, new IR peaks that are completely different from CO_2 peaks will emerge. This is used for defining the products of CO_2 chemisorption reaction on the surface.

DRIFTS is a feasible method for studying the reaction mechanisms from both the surface and gas phase in the catalyzed CO_2 hydrogenation process. Some specific issues about the DRIFTS instrument need to be figured out first, for example, avoiding the interference from the atmospheric gas in IR spectra, optimizing measurement parameters of scanning speed and resolution, the IR peak assignments, etc. Herein, we studied the CO_2 peak intensity in the IR spectra varying with the pressure and temperature first to find the proper measurement parameters and to understand the CO_2 IR spectra. It is of importance to keep the DRIFTS instrument flushing in N_2 gas to blow away the atmospheric gases in the IR beam pathways. At least 500 NL/h N_2 flow for 1 h is required before the first measurement. Longer flush time is needed for very low concentration gas or vacuum surface measurement. As shown in Figure 1.9, pure CO_2 was filled in the DRIFTS chamber which is loaded by KBr powder sample. CO_2 presents as free gas molecule with the asymmetric stretching centered at 2349 cm^{-1} , because the low-energy rotational motion consists the IR peak. 2360, 2341, and 2310 are the R branch ($\Delta J = +1$, ground state), P branch ($\Delta J = -1$, excited state), and hot band of rotational spectra, respectively.⁸⁴ When pressure increases, the whole rotational-vibrational peaks increase correspondingly (Figure 1.9(a)). When the temperature increases, the P branch and hot band are enhanced obviously.

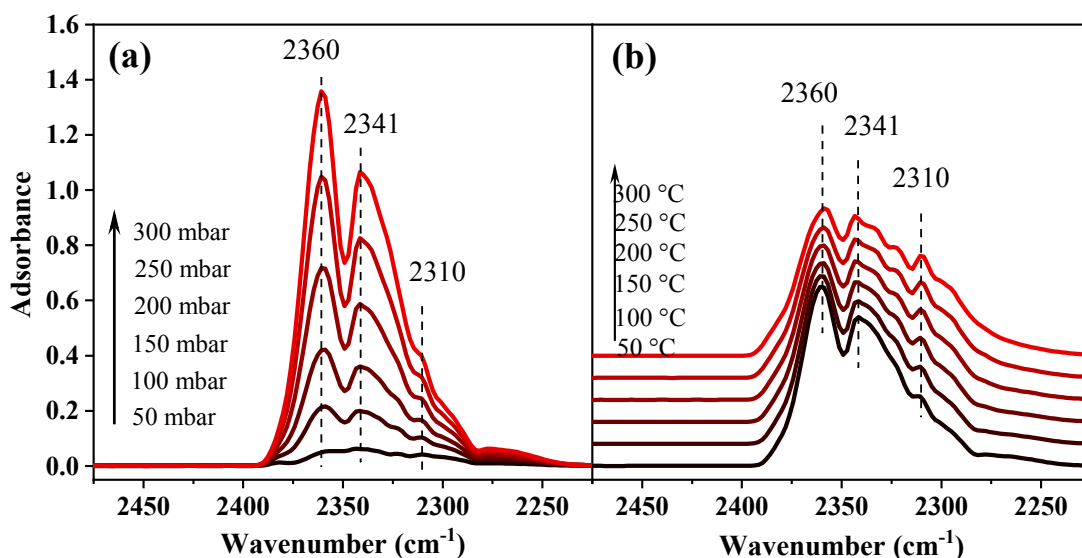


Figure 1.9. (a) Pure CO₂ adsorption on KBr at pressure from 50 to 300 mbar. (b) 200 mbar CO₂ adsorption on KBr at temperature from 50 to 300 °C.

1.5.2 MS, GC, NMR and other Methods

MS measures the mass-to-charge (m/z) ratio of the gas fragments which are ionized by the electrons at 1 kV. MS can be used for quantitative analysis of the gas components in the reactants and products in the gas flow when the ion current intensities of the CO₂, H₂, and CH₄ gases are calibrated at different gas concentrations. MS has fast response of the sample scan, which can be programmed in a few hundred milliseconds for a full scan. Therefore, MS data analysis facilitates the kinetic parameters of the reactions.

GC measures the retention time of the gases passing through the stationary phase with a specific column filling. The gases interact with the stationary phase differently and exit the column at different time due to the different chemical and physical properties of the gases. GC has advantages of separation of the gases that have overlapped signals in MS, for example, the abundance of $m/z = 28$ from both CO and CO₂ gases, and can detect low concentration of a dozen ppm precisely. However, GC has long measuring time (~15 minutes) for one-time detection comparing to the fast response in DRIFTS and MS. Therefore, GC can be used for a supplementary gas analysis method in addition to MS.

NMR measures the chemical shift of the resonance frequencies of the nuclear spins of the sample molecules, which are dissolved in the reference solvent, in a magnetic field. NMR can supplement

the analysis of the liquid or dissolvable reaction products, such as alcohols and acids. Moreover, NMR can detect low concentration of the samples down to a few ppm.

Other methods, such as X-ray photoelectron spectroscopy (XPS), transmission electron microscopy (TEM), X-ray diffraction (XRD), and BET surface area via N₂ adsorption, are generally used for sample characterizations.

1.6 Challenges in this Field and Objectives of this Thesis

CO₂ hydrogenation has been investigated over a century. But the reaction mechanisms and effective (high activity and selectivity) catalysts are still under research. There are four frontier questions highlighted here. Starting from the instrumental methods, the majority of the current investigations are using in situ equipment, for instance, in situ DRIFTS or in situ MS. However, using these equipments independently leads to either inconsistent experimental conditions or incomplete information. Secondly, the data analysis part is onerous but vital, for example, the deconvolution of the IR peaks from the strongly overlapped spectra, the quantification of the reaction components, the kinetic analysis, etc. Thirdly, the relation between the reactivity and the catalysts, such as the active sites for the reaction, is always ambiguous. Fourthly, the grasp of the reaction intermediates in the experiment is disturbed by the complex of the reaction, e.g. mixing with byproducts and rapid conversion.

Therefore, to address these issues, we set the objectives of this thesis as developing instrument for an operando study, developing data analysis methods for both DRIFTS and MS, identifying the reaction intermediates and explain the reaction mechanisms, developing novel and efficient catalyst and finding out the relation between the reactivity and the catalyst structure.

1.7 Overview of the Research Wok in this Thesis

We build an operando platform for investigating the catalytic process of one experiment stream using multiple detect methods. On the basis of the developed instrument, we create an analysis program for resolving spectral dataset. Apart from the instrumental side, we studied variously transition metal-based catalysts and the mechanisms of CO₂ adsorption and reduction reactions over those catalysts. Finally, we designed a novel catalyst according to what we have discovered to optimize the catalytic reactivity and to further understand the relationship between the catalyst surface and the CO₂ hydrogenation. Following is the brief introduction of each chapter.

In Chapter 2, an operando method, DRIFTS-MS-GC, is developed, aiming at analyzing the gas components and the surface adsorbed species simultaneously in the reaction stream. The details of this setup, the fundamental research on CO₂ interaction with pure metal, alloy, and metal-oxide, the quantification of the gas amounts, and the kinetic determinations are described in depth.

In Chapter 3, we developed an efficiently automatic program, bilevel evolutionary Gaussian Fitting (BEGF) program, for analyzing the spectral sets of the CO₂ hydrogenation experiments. The BEGF program searches the deconvolution results by genetic algorithm and fitting the peaks by Gaussian function. The analyzed results show the correct deconvoluted and kinetics of the peaks. Therein, we showed the results of IR peak assignments of gas and adsorbates from CO₂ hydrogenation reaction and from isotopic ¹³CO₂+H₂ and CO₂+D₂ reactions over Ru/Al₂O₃ surface.

Continuing the establishment above, in Chapter 4, we investigated the surface reaction mechanisms of CO₂ hydrogenation on Ru/Al₂O₃ in DRIFTS via controlling the formation and hydrogenation of each adsorbed species. The development of each adsorbed species verified which are intermediates and which are byproducts. Therein, the CO₂ hydrogenation steps were elaborated. Moreover, the oxide support, Al₂O₃, is not inert, but participates in CO₂ activation. The initial hydrogenation takes place on the interface of Ru and Al₂O₃.

Learning from above results that the catalyst requires oxide to facilitate CO₂ hydrogenation reaction, we suspect there could be a relationship between the ratio of metal/oxide and the reactivity. Therefore, in Chapter 5, we designed Co_x(CoO)_{1-x} catalyst from an in situ reduction methods in the DRIFTS-MS-GC instrument. The results showed high concentration of CoO in the catalyst is the key to achieve high CO₂ conversion. This not because CoO provides new catalytical center but because CoO enhanced the CO₂ adsorption.

Conclusions and perspective of this thesis are organized after the last chapter.

References

- (1) Source: IEA World Energy Balances **2019**. <https://webstore.iea.org/world-energy-balances-2019>. All rights reserved.
- (2) Source: IEA CO₂ Emissions from Fuel Combustion. **2019**. <https://www.iea.org/subscribe-to-data-services/co2-emissions-statistics>. All rights reserved.
- (3) Zhang, L.; Zhao, Z. J.; Gong, J. L. Nanostructured Materials for Heterogeneous Electrocatalytic CO₂ Reduction and Their Related Reaction Mechanisms. *Angew. Chem. Int. Ed.* **2017**, *56*, 11326–11353.
- (4) Nitopi, S.; Bertheussen, E.; Scott, S. B.; Liu, X.; Engstfeld, A. K.; Horch, S.; Seger, B.; Stephens, I. E. L.; Chan, K.; Hahn, C.; et al. Progress and Perspectives of Electrochemical CO₂ Reduction on Copper in Aqueous Electrolyte. *Chem. Rev.* **2019**, *119* (12), 7610–7672.
- (5) GDP per unit of energy use (PPP \$ per kg of oil equivalent). Data <https://data.worldbank.org/indicator/EG.GDP.PUSE.KO.PP?contextual=default&locations=US-CN-EU-1W>.
- (6) Haegel, N. M.; Margolis, R.; Buonassisi, T.; Feldman, D.; Froitzheim, A.; Garabedian, R.; Green, M.; Glunz, S.; Henning, H.-M.; Holder, B.; et al. Terawatt-Scale Photovoltaics: Trajectories and Challenges. *Science* **2017**, *356*, 141–143.
- (7) World Energy Demand and Economic Outlook. *EIA*. **2016**.
- (8) Züttel, A.; Gallandat, N.; Schlapbach, L. Net-Zero Emission System for Switzerland. **2019**, *in preparation*.
- (9) Züttel, A.; Mauron, P.; Kato, S.; Callini, E.; Holzer, M.; Huang, J. Storage of Renewable Energy by Reduction of CO₂ with Hydrogen. *Chimia* **2015**, *69*, 264–268.
- (10) Che, M. Nobel Prize in Chemistry 1912 to Sabatier: Organic Chemistry or Catalysis? *Catal. Today* **2013**, *218–219*, 162–171.
- (11) Schulz, H. Short History and Present Trends of Fischer–Tropsch Synthesis. *Appl. Catal. A: General* **1999**, *186*, 3–12.
- (12) Centi, G.; Quadrelli, E. A.; Perathoner, S. Catalysis for CO₂ Conversion: A Key Technology for Rapid Introduction of Renewable Energy in the Value Chain of Chemical Industries. *Energy Environ. Sci.* **2013**, *6*, 1711–1731.
- (13) Torres Galvis, H. M.; de Jong, K. P. Catalysts for Production of Lower Olefins from Synthesis Gas: A Review. *ACS Catal.* **2013**, *3*, 2130–2149.
- (14) Freund, H. J.; Roberts, M. W. Surface Chemistry of Carbon Dioxide. *Surf. Sci. Rep.*, **1996**, *25*, 225–273.
- (15) Pacchioni, G.; Freund, H. Electron Transfer at Oxide Surfaces. The MgO Paradigm: From Defects to Ultrathin Films. *Chem. Rev.* **2013**, *113*, 4035–4072.
- (16) Volkenshtein, V. F. Electronic Processes in Chemisorption. *Russ. Chem. Bull.* **1953**, *2*, 865–870.
- (17) Bendavid, L. I.; Carter, E. A. CO₂ Adsorption on Cu₂O(111): A DFT+U and DFT-D Study. *J. Phys. Chem. C* **2013**, *117*, 26048–26059.

-
- (18) White, J. L.; Baruch, M. F.; Pander III, J. E.; Hu, Y.; Fortmeyer, I. C.; Park, J. E.; Zhang, T.; Liao, K.; Gu, J.; Yan, Y.; et al. Light-Driven Heterogeneous Reduction of Carbon Dioxide: Photocatalysts and Photoelectrodes. *Chem. Rev.* **2015**, *115*, 12888–12935.
- (19) Luo, Y.-R. *Comprehensive Handbook of Chemical Bond Energies*; CRC Press, **2007**.
- (20) Bartos, B.; Freund, H. J.; Kuhlenbeck, H.; Neumann, M.; Lindner, H.; Müller, K. Adsorption and Reaction of CO₂ and CO₂/O CO-Adsorption on Ni(110): Angle Resolved Photoemission (ARUPS) and Electron Energy Loss (HREELS) Studies. *Surf. Sci.* **1987**, *179*, 59–89.
- (21) Burghaus, U. Surface Chemistry of CO₂ – Adsorption of Carbon Dioxide on Clean Surfaces at Ultrahigh Vacuum. *Prog. Surf. Sci.* **2014**, *89*, 161–217.
- (22) Wambach, J.; Illing, G.; Freund, H. J. CO₂ Activation and Reaction with Hydrogen on Ni(110): Formate Formation. *Chem. Phys. Lett.* **1991**, *184*, 239–244.
- (23) Peng, G.; Sibener, S. J.; Schatz, G. C.; Ceyer, S. T.; Mavrikakis, M. CO₂ Hydrogenation to Formic Acid on Ni(111). *J. Phys. Chem. C* **2012**, *116*, 3001–3006.
- (24) Sandford, S. A.; Allamandola, L. J. The Physical and Infrared Spectral Properties of CO₂ in Astrophysical Ice Analogs. *Astrophys. J.* **1990**, *355*, 357–372.
- (25) Wohlrab, S.; Ehrlich, D.; Wambach, J.; Kuhlenbeck, H.; Freund, H.-J. Promoter Action of Alkali in the Activation of CO₂ on Pd(111): A HREELS Case Study. *Surf. Sci.* **1989**, *220*, 243–252.
- (26) Ge, Q. Chapter 3 - Mechanistic Understanding of Catalytic CO₂ Activation from First Principles Theory A2 - Suib, Steven L. In *New and Future Developments in Catalysis*; Elsevier: Amsterdam, 2013; pp 49–79.
- (27) Paul, J.; Hoffmann, F. M. CO₂ Conversion and Oxalate Stability on Alkali Promoted Metal Surfaces: Sodium Modified Al(100). *Catal. Lett.* **1988**, *1*, 445–455.
- (28) Ye, Y.; Yang, H.; Qian, J.; Su, H.; Lee, K.-J.; Cheng, T.; Xiao, H.; Yano, J.; Goddard, W. A.; Crumlin, E. J. Dramatic Differences in Carbon Dioxide Adsorption and Initial Steps of Reduction between Silver and Copper. *Nat. Commun.* **2019**, *10*, 1875.
- (29) Favaro, M.; Xiao, H.; Cheng, T.; Goddard, W. A.; Yano, J.; Crumlin, E. J. Subsurface Oxide Plays a Critical Role in CO₂ Activation by Cu(111) Surfaces to Form Chemisorbed CO₂, the First Step in Reduction of CO₂. *Proc. Natl. Acad. Sci.* **2017**, *2017*, *114*, 6706–6711.
- (30) Melaet, G.; Ralston, W. T.; Li, C.-S.; Alayoglu, S.; An, K.; Musselwhite, N.; Kalkan, B.; Somorjai, G. A. Evidence of Highly Active Cobalt Oxide Catalyst for the Fischer–Tropsch Synthesis and CO₂ Hydrogenation. *J. Am. Chem. Soc.* **2014**, *136*, 2260–2263.
- (31) Behrens, M.; Studt, F.; Kasatkin, I.; Kühl, S.; Hävecker, M.; Abild-Pedersen, F.; Zander, S.; Girgsdies, F.; Kurr, P.; Kniep, B.-L.; et al. The Active Site of Methanol Synthesis over Cu/ZnO/Al₂O₃ Industrial Catalysts. *Science* **2012**, *336*, 893–897.

-
- (32) Larmier, K.; Liao, W.-C.; Tada, S.; Lam, E.; Verel, R.; Bansode, A.; Urakawa, A.; Comas-Vives, A.; Copéret, C. CO₂-to-Methanol Hydrogenation on Zirconia-Supported Copper Nanoparticles: Reaction Intermediates and the Role of the Metal–Support Interface. *Angew. Chem. Int. Ed.* **2017**, *56*, 2318–2323.
- (33) Kattel, S.; Ramírez, P. J.; Chen, J. G.; Rodriguez, J. A.; Liu, P. Active Sites for CO₂ Hydrogenation to Methanol on Cu/ZnO Catalysts. *Science* **2017**, *355*, 1296–1299.
- (34) Gao, P.; Dang, S.; Li, S.; Bu, X.; Liu, Z.; Qiu, M.; Yang, C.; Wang, H.; Zhong, L.; Han, Y.; et al. Direct Production of Lower Olefins from CO₂ Conversion via Bifunctional Catalysis. *ACS Catal.* **2018**, *8*, 571–578.
- (35) Xie, C.; Chen, C.; Yu, Y.; Su, J.; Li, Y.; Somorjai, G. A.; Yang, P. Tandem Catalysis for CO₂ Hydrogenation to C₂–C₄ Hydrocarbons. *Nano lett.* **2017**, *17*, 3798–3802.
- (36) van Santen, R. A.; Markvoort, A. J.; Filot, I. A.; Ghouri, M. M.; Hensen, E. J. Mechanism and Microkinetics of the Fischer–Tropsch Reaction. *Phys. Chem. Chem. Phys.* **2013**, *15*, 17038–17063.
- (37) Fischer–Tropsch synthesis revisited; efficiency and selectivity benefits from imposing temporal and/or spatial structure in the reactor, TU Delft Research Information Portal, Wageningen : Ponsen & Looijen BV, 2004. 159 p.
- (38) Pestman, R.; Chen, W.; Hensen, E. Insight into the Rate-Determining Step and Active Sites in the Fischer–Tropsch Reaction over Cobalt Catalysts. *ACS Catal.* **2019**, *9*, 4189–4195.
- (39) Chen, W.; Filot, I. A. W.; Pestman, R.; Hensen, E. J. M. Mechanism of Cobalt-Catalyzed CO Hydrogenation: 2. Fischer–Tropsch Synthesis. *ACS Catal.* **2017**, *7*, 8061–8071.
- (40) Filot, I. A. W.; van Santen, R. A.; Hensen, E. J. M. The Optimally Performing Fischer–Tropsch Catalyst. *Angew. Chem.* **2014**, *126*, 12960–12964.
- (41) Mutschler, R.; Moiola, E.; Luo, W.; Gallandat, N.; Züttel, A. CO₂ Hydrogenation Reaction over Pristine Fe, Co, Ni, Cu and Al₂O₃ Supported Ru: Comparison and Determination of the Activation Energies. *J. Catal.* **2018**, *366*, 139–149.
- (42) Weatherbee, G. D.; Bartholomew, C. H. Hydrogenation of CO₂ on Group VIII Metals: IV. Specific Activities and Selectivities of Silica-Supported Co, Fe, and Ru. *J. Catal.* **1984**, *87*, 352–362.
- (43) Weatherbee, G. D.; Bartholomew, C. H. Hydrogenation of CO₂ on Group VIII Metals. *J. Catal.* **1981**, *68*, 67–76.
- (44) Weatherbee, G. D.; Bartholomew, C. H. Hydrogenation of CO₂ on Group VIII Metals. *J. Catal.* **1982**, *77*, 460–472.
- (45) Vance, C. K.; Bartholomew, C. H. Hydrogenation of Carbon Dioxide on Group Viii Metals. *Appl. Catal.* **1983**, *7*, 169–177.
- (46) Zhang, W.; Wang, L.; Liu, H.; Hao, Y.; Li, H.; Khan, M. U.; Zeng, J. Integration of Quantum Confinement and Alloy Effect to Modulate Electronic Properties of RhW Nanocrystals for Improved Catalytic Performance toward CO₂ Hydrogenation. *Nano lett.* **2017**, *17*, 788–793.
- (47) Khan, M. U.; Wang, L.; Liu, Z.; Gao, Z.; Wang, S.; Li, H.; Zhang, W.; Wang, M.; Wang, Z.; Ma, C.; et al. Pt₃Co Octapods as Superior Catalysts of CO₂ Hydrogenation. *Angew. Chem. Int. Ed.* **2016**, *55*, 9548–9552.

-
- (48) Mutz, B.; Belimov, M.; Wang, W.; Sprenger, P.; Serrer, M.-A.; Wang, D.; Pfeifer, P.; Kleist, W.; Grunwaldt, J.-D. Potential of an Alumina-Supported Ni₃Fe Catalyst in the Methanation of CO₂: Impact of Alloy Formation on Activity and Stability. *ACS Catal.* **2017**, *7*, 6802–6814.
- (49) Zhao, L.; Mu, X.; Liu, T.; Fang, K. Bimetallic Ni–Co Catalysts Supported on Mn–Al Oxide for Selective Catalytic CO Hydrogenation to Higher Alcohols. *Catal. Sci. Technol.* **2018**, *8*, 2066–2076.
- (50) Liu, J.; Zhang, A.; Jiang, X.; Liu, M.; Sun, Y.; Song, C.; Guo, X. Selective CO₂ Hydrogenation to Hydrocarbons on Cu-Promoted Fe-Based Catalysts: Dependence on Cu–Fe Interaction. *ACS Sustain. Chem. Eng.* **2018**, *6*, 10182–10190.
- (51) Nie, X.; Jiang, X.; Wang, H.; Luo, W.; Janik, M. J.; Chen, Y.; Guo, X.; Song, C. Mechanistic Understanding of Alloy Effect and Water Promotion for Pd-Cu Bimetallic Catalysts in CO₂ Hydrogenation to Methanol. *ACS Catal.* **2018**, *8*, 4873–4892.
- (52) Zhang, S. R.; Tang, Y.; Nguyen, L.; Zhao, Y. F.; Wu, Z. L.; Goh, T. W.; Liu, J. J. Y.; Li, Y. Y.; Zhu, T.; Huang, W. Y.; et al. Catalysis on Singly Dispersed Rh Atoms Anchored on an Inert Support. *ACS Catal.* **2018**, *8*, 110–121.
- (53) Liu, J. Catalysis by Supported Single Metal Atoms. *ACS Catal.* **2017**, *7*, 34–59.
- (54) Tyo, E. C.; Vajda, S. Catalysis by Clusters with Precise Numbers of Atoms. *Nat. Nano* **2015**, *10*, 577–588.
- (55) Jiang, K.; Siahrostami, S.; Zheng, T.; Hu, Y.; Hwang, S.; Stavitski, E.; Peng, Y.; Dynes, J.; Gangisetty, M.; Su, D.; et al. Isolated Ni Single Atoms in Graphene Nanosheets for High-Performance CO₂ Reduction. *Energy Environ. Sci.* **2018**, *11*, 893–903.
- (56) Liu, L.; Corma, A. Metal Catalysts for Heterogeneous Catalysis: From Single Atoms to Nanoclusters and Nanoparticles. *Chem. Rev.* **2018**, *118* (10), 4981–5079.
- (57) Cheng, M.-J.; Clark, E. L.; Pham, H. H.; Bell, A. T.; Head-Gordon, M. Quantum Mechanical Screening of Single-Atom Bimetallic Alloys for the Selective Reduction of CO₂ to C₁ Hydrocarbons. *ACS Catal.* **2016**, *6*, 7769–7777.
- (58) Wei, J.; Ge, Q.; Yao, R.; Wen, Z.; Fang, C.; Guo, L.; Xu, H.; Sun, J. Directly Converting CO₂ into a Gasoline Fuel. *Nat. Commun.* **2017**, *8*, 15174.
- (59) Gao, P.; Li, S.; Bu, X.; Dang, S.; Liu, Z.; Wang, H.; Zhong, L.; Qiu, M.; Yang, C.; Cai, J.; et al. Direct Conversion of CO₂ into Liquid Fuels with High Selectivity over a Bifunctional Catalyst. *Nat. Chem.* **2017**, *9*, 1019–1024.
- (60) Liu, L.; Corma, A. Metal Catalysts for Heterogeneous Catalysis: From Single Atoms to Nanoclusters and Nanoparticles. *Chem. Rev.* **2018**, *118*, 4981–5079.
- (61) Henry, C. R.; Chapon, C.; Giorgio, S.; Goyhenex, C. Size Effects in Heterogeneous Catalysis. In *Chemisorption and Reactivity on Supported Clusters and Thin Films: Towards an Understanding of Microscopic Processes in Catalysis*; Lambert, R. M., Pacchioni, G., Eds.; NATO ASI Series; Springer Netherlands: Dordrecht, **1997**; pp 117–152.
- (62) Quinson, J.; Inaba, M.; Neumann, S.; Swane, A. A.; Bucher, J.; Simonsen, S. B.; Theil Kuhn, L.; Kirkensgaard, J. J. K.; Jensen, K. M. Ø.; Oezaslan, M.; et al. Investigating Particle Size Effects in Catalysis by Applying a Size-Controlled and Surfactant-Free Synthesis of Colloidal Nanoparticles in Alkaline Ethylene Glycol: Case Study of the Oxygen Reduction Reaction on Pt. *ACS Catal.* **2018**, *8*, 6627–6635.

-
- (63) Vogt, C.; Groeneveld, E.; Kamsma, G.; Nachtegaal, M.; Lu, L.; Kiely, C. J.; Berben, P. H.; Meirer, F.; Weckhuysen, B. M. Unravelling Structure Sensitivity in CO₂ Hydrogenation over Nickel. *Nat. Catal.* **2018**, *1*, 127–134.
- (64) Kwak, J. H.; Kovarik, L.; Szanyi, J. CO₂ Reduction on Supported Ru/Al₂O₃ Catalysts: Cluster Size Dependence of Product Selectivity. *ACS Catalysis* **2013**, *3*, 2449–2455.
- (65) van Helden, P.; Ciobica, I. M.; Coetzer, R. L. J. The Size-Dependent Site Composition of FCC Cobalt Nanocrystals. *Catal. Today* **2016**, *261*, 48–59.
- (66) Herranz, T.; Deng, X.; Cabot, A.; Guo, J.; Salmeron, M. Influence of the Cobalt Particle Size in the CO Hydrogenation Reaction Studied by In Situ X-Ray Absorption Spectroscopy. *J. Phys. Chem. B* **2009**, *113*, 10721–10727.
- (67) Bezemer, G. L.; Bitter, J. H.; Kuipers, H. P. C. E.; Oosterbeek, H.; Holewijn, J. E.; Xu, X.; Kapteijn, F.; van Dillen, A. J.; de Jong, K. P. Cobalt Particle Size Effects in the Fischer–Tropsch Reaction Studied with Carbon Nanofiber Supported Catalysts. *J. Am. Chem. Soc.* **2006**, *128*, 3956–3964.
- (68) den Breejen, J. P.; Radstake, P. B.; Bezemer, G. L.; Bitter, J. H.; Frøseth, V.; Holmen, A.; Jong, K. P. de. On the Origin of the Cobalt Particle Size Effects in Fischer–Tropsch Catalysis. *J. Am. Chem. Soc.* **2009**, *131*, 7197–7203.
- (69) Kondratenko, E. V.; Mul, G.; Baltrusaitis, J.; Larrazabal, G. O.; Perez-Ramirez, J. Status and Perspectives of CO₂ Conversion into Fuels and Chemicals by Catalytic, Photocatalytic and Electrocatalytic Processes. *Energy Environ. Sci.* **2013**, *6*, 3112–3135.
- (70) Dorner, R. W.; Hardy, D. R.; Williams, F. W.; Willauer, H. D. Heterogeneous Catalytic CO₂ Conversion to Value-Added Hydrocarbons. *Energy Environ. Sci.* **2010**, *3*, 884–890.
- (71) Khodakov, A. Y.; Chu, W.; Fongarland, P. Advances in the Development of Novel Cobalt Fischer–Tropsch Catalysts for Synthesis of Long-Chain Hydrocarbons and Clean Fuels. *Chem. Rev.* **2007**, *107*, 1692–1744.
- (72) Liu, X.-M.; Lu, G. Q.; Yan, Z.-F.; Beltramini, J. Recent Advances in Catalysts for Methanol Synthesis via Hydrogenation of CO and CO₂. *Ind. Eng. Chem. Res.* **2003**, *42*, 6518–6530.
- (73) Kattel, S.; Yan, B.; Yang, Y.; Chen, J. G.; Liu, P. Optimizing Binding Energies of Key Intermediates for CO₂ Hydrogenation to Methanol over Oxide-Supported Copper. *J. Am. Chem. Soc.* **2016**, *138*, 12440–12450.
- (74) Kattel, S.; Yu, W.; Yang, X.; Yan, B.; Huang, Y.; Wan, W.; Liu, P.; Chen, J. G. CO₂ Hydrogenation over Oxide-Supported PtCo Catalysts: The Role of the Oxide Support in Determining the Product Selectivity. *Angew. Chem. Int. Ed.* **2016**, *55*, 7968–7973.
- (75) Boffa, A.; Lin, C.; Bell, A. T.; Somorjai, G. A. Promotion of CO and CO₂ Hydrogenation over Rh by Metal Oxides: The Influence of Oxide Lewis Acidity and Reducibility. *J. Catal.* **1994**, *149*, 149–158.
- (76) Payen, E.; Grimblot, J.; Lavalley, J. C.; Daturi, M.; Mauge, F. Vibrational Spectroscopy in the Study of Oxide (Excluding Zeolites) and Sulfide Catalysts. In *Handbook of Vibrational Spectroscopy*; American Cancer Society, **2006**.
- (77) Kim, Y.; Trung, T. S. B.; Yang, S.; Kim, S.; Lee, H. Mechanism of the Surface Hydrogen Induced Conversion of CO₂ to Methanol at Cu(111) Step Sites. *ACS Catal.* **2016**, *6*, 1037–1044.
- (78) Gutiérrez-González, A.; Torio, M. E.; Busnengo, H. F.; Beck, R. D. Site Selective Detection of Methane Dissociation on Stepped Pt Surfaces. *Top. Catal.* **2019**, *62*, 859–873.

-
- (79) Gutiérrez-González, A.; Crim, F. F.; Beck, R. D. Bond Selective Dissociation of Methane (CH_3D) on the Steps and Terraces of Pt(211). *J. Chem. Phys.* **2018**, *149*, 074701.
- (80) Calle-Vallejo, F.; Tymoczko, J.; Colic, V.; Vu, Q. H.; Pohl, M. D.; Morgenstern, K.; Loffreda, D.; Sautet, P.; Schuhmann, W.; Bandarenka, A. S. Finding Optimal Surface Sites on Heterogeneous Catalysts by Counting Nearest Neighbors. *Science* **2015**, *350*, 185–189.
- (81) Nørskov, J. K.; Bligaard, T.; Rossmeisl, J.; Christensen, C. H. Towards the Computational Design of Solid Catalysts. *Nat. Chem.* **2009**, *1*, 37–46.
- (82) Meunier, F. C. The Design and Testing of Kinetically-Appropriate Operando Spectroscopic Cells for Investigating Heterogeneous Catalytic Reactions. *Chem. Soc. Rev.* **2010**, *39*, 4602–4614.
- (83) Atkins, P.; Paula, J. de. *Atkins' Physical Chemistry*; OUP Oxford, **2010**.
- (84) Compton, R. N.; Duncan, M. A. Fermi Resonance in CO_2 . Oxford Scholarship Online, **2015**, 316–320.
- (85) Rinsland, C. P.; Benner, D. C.; Devi, V. M. Absolute Line Intensities in CO_2 Bands near 4.8 Mm. *Appl. Opt.*, **1986**, *25*, 1204–1214.

Chapter 2 A Combined Diffuse Reflectance Infrared Fourier Transform Spectroscopy–Mass Spectroscopy–Gas Chromatography for the Operando Study of the Heterogeneously Catalyzed CO₂ Hydrogenation over Transition Metal-Based Catalysts

Kun Zhao^{1,2*}, Jie Zhang^{1,2}, Wen Luo^{1,2*}, Mo Li^{1,2}, Emanuele Moiola^{1,2}, Mariana Spodaryk^{1,2}, Andreas Züttel^{1,2}

¹ Laboratory of Materials for Renewable Energy, Institute of Chemical Sciences and Engineering, École Polytechnique Fédérale de Lausanne (EPFL), 1951 Sion, Switzerland

² Swiss Federal Laboratories for Materials Science and Technology (EMPA), 8600 Dübendorf, Switzerland

*Corresponding Author: kun.zhao@epfl.ch, wen.luo@epfl.ch

Preprint version: preprint version of the manuscript submitted for publication on the scientific journal *Review of Scientific Instrument*.

Edit: caption numbers of figures, tables, and equations were edited to adapter the thesis chapter number.

Summary: this Chapter introduces the work of setup building, the first application tests, the explorations on different catalysts, and kinetic calculation models for CO₂ methanation reaction. The reactivities of pristine and alloyed metals and metal-metal oxide were compared. Metal oxide was found to be essential to enable the observation of adsorbed species on the surface using DRIFTS, and to improve the reactivity for CO₂ methanation.

Abstract

We built an inline diffuse reflectance infrared Fourier transform spectroscopy-mass spectroscopy-gas chromatography (DRIFTS-MS-GC) apparatus aiming at operando mechanistic study of the heterogeneous catalyzed CO₂ hydrogenation reaction. The multifunctional and accurate system enabled the simultaneous utilization of IR, MS, GC, and NMR techniques in one single device to analyze the surface, gas and liquid products formed during the reaction process. To assess the potential of the system, we compared the activity of pristine metals (Fe, Co, Ni, and Cu), metal alloys (LaNi₄Cu) and metal-metal oxides (Co-CoO) catalysts with respect to the interactions between gaseous CO₂ and the catalyst surfaces. For the quantitative comparison, the rate constants and activation energies of CO₂ hydrogenation were determined. The results showed a composition dependent reactivity of the metals. The metal oxide mixed with the metal is essentially important for the formation of observable of the surface species deriving from CO₂ adsorption and for the enhancement of the CO₂ conversion to CH₄.

2.1 Introduction

The conversion of CO₂ into synthetic hydrocarbons is becoming of increasing importance, due to the demand of the storage of the exponentially growing renewable and sustainable energy sources.¹⁻³ Multiple reaction pathways, including thermal, electrochemical, and photo(electro)chemical catalysis have been used to successfully explore the conversion processes.⁴⁻⁸ At the current state of the art, thermal catalysis is the method with the highest power density and the greatest potential for scaling up due to high activity of the catalysts employed to this scope.⁹⁻¹¹ However, the efficiency and selectivity of the synthetic processes are expected to be improved through the design of highly active and selective catalysts. Recent studies reported several novel catalysts for CO₂ hydrogenation reactions.^{12,13} Ru-, Rh-, and Pd-based catalysts were found to be especially active for the transformation of CO₂ to CH₄ through the Sabatier reaction. For this reaction, reactor based on the selected noble metal-based catalyst can succeed in reaching 99% conversion.¹⁴⁻¹⁷ However, the high cost of these elements limits the employment on a large scale. Nano sized metals on supports reduce the economic issues, as the total load can be reduced to a few weight percentage. Yet, large loading is necessary for improving activity and selectivity.¹⁸ Ni- and Co-based catalysts, which are less expensive, are also active and widely used for CO₂ methanation. However, these catalysts show lower yields and require higher reaction temperature compared with Ru/Al₂O₃.¹⁹⁻²¹ Numerous alteration of the active phase, such as doping,²² alloying,²³⁻²⁵ promoting,^{26,27} and nanosizing,^{28,29} have been attempted to increase their activity and selectivity. Yet, there is no systematical comparison of the catalysts with different structural design in experiment to give instructions of the choice of a specifically structured catalysts.

In order to correctly address the development of new, less expensive and more performing catalysts, suitable integrated investigation techniques are necessary. The experimental and analytical tools are two essential aspects to be addressed. The investigation methods for the CO₂ hydrogenation studies often include spectroscopic analysis, such as diffuse infrared reflectance infrared Fourier transform spectroscopy (DRIFTS)³⁰⁻³³, mass spectroscopy (MS), x-ray photoelectron spectroscopy (XPS), nuclear magnetic resonance (NMR), and gas and liquid chromatography (GC and LC, respectively). However, these detection methods are generally performed independently or *ex situ*, which leads to either inconsistent experimental conditions or incomplete information. An operando method facilitates the collection of coherent and complete information of the reaction in one single experiment. This consideration is the main motivation for the development of the system here described.

With regard to the selection of the catalysts, ahead of designing the new materials, a systematic understanding of the fundamental differences of the metals in the CO₂ hydrogenation reaction is of great interest and importance. Recently, our group has compared the activities of the pristine metals Fe, Co, Ni, Cu in the Sabatier reaction.²¹ The results showed that Co and Ni can convert 70% and 55% CO₂ to CH₄ at 390 and 520 °C, respectively. These two pristine metals show similar activation energies of around 75 kJ/mol. Fe converted CO₂ to CO mainly above 300 °C, through the reversed water gas shift reaction. Cu was inactive toward CO₂ conversion. These results are consistent with the report by Bartholomew, *et al.* in the 1980s about the silica-supported transition metals for CO₂ hydrogenation.³⁴ However, in these valuable studies, no information on the binding products on the surfaces during the CO₂ conversion process are provided, leaving an critical gap in the explanation of the reaction mechanisms. Theoretical simulations that calculate the elementary steps of CO₂ adsorption and hydrogenation reactions could address this issue. However, the calculations are normally performed using specified single crystalline facets and under ideal condition.³⁵ These stimulate the demand of the experimental evidences of the intermediates formed under real reaction conditions in addition to the observation of the final products.

Therefore, we built an inline analysis system consisting of a diffuse reflectance infrared Fourier transform spectroscopy (DRIFTS), a mass spectroscopy (MS), a gas chromatography (GC) analyzer. The deionized water (DIW) bottle for nuclear magnetic resonance (NMR) analysis was an optional connection. We simplified the name as DRIFTS-MS-GC. This infrastructure enables the detection of surface, gas, and liquid products during the CO₂ hydrogenation reaction over the catalyst operando. The careful integration of the three instruments gathers the advantages of the variously important analytical techniques, and synchronizes the coherent data, which is main innovation in the field of scientific instruments and opens the way to the investigation of reaction pathways operando. At the best of our knowledge, as of today no study reports such an integrated system in operation.

Thanks to this apparatus, we investigated systematically the catalysts in the CO₂ hydrogenation reaction. Aiming at developing new highly active and efficient catalysts, we selected the first-row group 8–11 transition metal-based catalysts, and designed three different forms of these metals as representative catalysts. We began with the pristine metals, aiming at understanding the fundamental distinctions of CO₂ interaction with these pure metal surfaces. Second, considering the activation of the CO₂ molecule is hydrogen assisted, we used an alloy form, LaNi₄Cu metal hydride which can adsorb 3.63 hydrogen atoms per formula unit,³⁶ in order to evaluate the effect of hydrogen pre-storage in the metals on the CO₂ hydrogenation. Based on the experiences on these pristine and alloyed

metals, we examined the metal oxide effect using cobalt-cobalt oxide (Co-CoO), because the metal oxide is reported to enhance the catalytic conversion of CO₂.³⁷

2.2 Experimental

2.2.1 Setup

The DRIFTS-MS-GC setup consists of five parts as shown in Figure 1. Part I, a gas flow controller connected to H₂, CO₂, and He gas lines, whose flows were controlled using mass flow controller (MFC) and Labview program. Part II, a DRIFTS chamber (HVC, Harrick Scientific) integrated with a Fourier transform infrared (FTIR, Tensor 27, Bruker) spectrometer using a mercury cadmium telluride (MCT) detector. Part III, a mass spectrometer (MS, Pfeiffer OmniStar 320) using a detector of Faraday cup. Part IV, a sealed bottle containing DIW for the collection of any liquid products, such as ethanol. Part V, gas chromatography (GC, SRI 8610C) using a flame ionization detector (FID). In addition, a branch connection to MS was included, to make temperature-programmed desorption-mass spectrometer (TPD-MS) measurements.

The operation conditions for each part are as follows. For part I, the max flow speed for H₂, CO₂, and He are 10, 10, and 73 mL/min, respectively. For part II, DRIFTS can be operated in the pressure range from 10⁻⁶ – 10⁶ mbar and in the temperature range from room temperature (RT) to 900 °C, with an optimized scan speed of 38 scan/min. In addition, the entire DRIFTS part is maintained in N₂ gas flush to eliminate interference from atmospheric H₂O and CO₂ whose vibrational signals are especially IR sensitive. For part III, the MS measurements were taken at pressure below 10⁻⁵ mbar with a scan speed of 200 ms/amu in a mass range of 0-50. For parts IV and V, the exhaust gas passes through DIW and GC at ambient pressure. The measurement time (retention time) was set as 9 minutes for GC measurement with an interval time of 4 minutes between each measurement. Note that a back-pressure regulator has been placed at the exhaust gas line of DRIFTS.

The function of each part is as follows. For part I, a gas flow controller is utilized to precisely control gas flows using digital commands. For part II, DRIFTS scans the surface adsorption species, in addition to detecting the gas phase. For part III, MS detects the gas-phase reactants and products. For part IV, DIW collects any liquid products for NMR analysis. For part V, GC detects the gas phase to complement the analysis of gas products which have overlapped signals in MS.

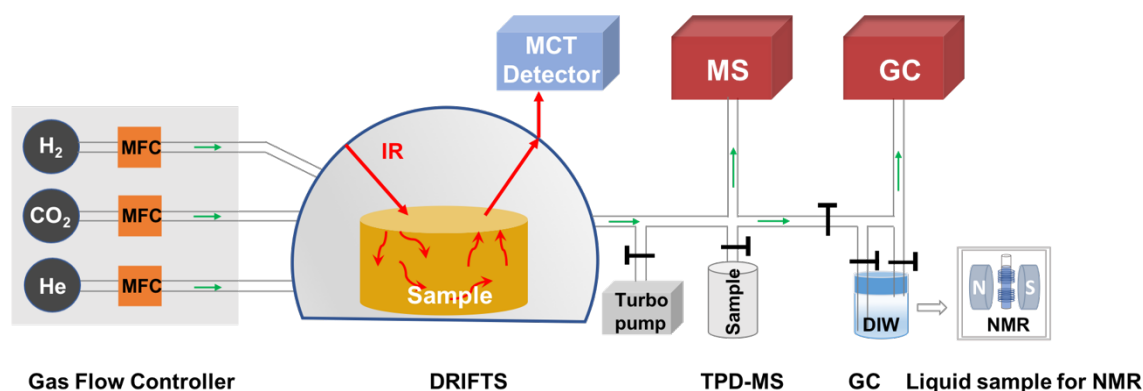


Figure 2.1. Schematic of the DRIFTS-MS-GC instrument utilized in this study

2.2.2 Experiments

2.2.2.1 Materials preparation

Fe, Co, Ni, and Cu powders (99%, max. particle size 60 μm , Goodfellow) were used as purchased, but compressed into soft pellets of the same size as the DRIFTS chamber (diameter, 6 mm; thickness 3.5 mm). Although the DRIFTS requires normally samples to not be pressurized, we observed that most of the intensity of the infrared (IR) signal was maintained over the soft pellet surface compared to powder surface. Moreover, pellet samples exhibit two important advantages compared to the powder samples. First, pellet samples have little problem of sample loss due to gas flow or pumping, which is particularly important for nanomaterials. Second, pellets have better thermal conductivity during the heating experiment.

LaNi₄Cu was synthesized through arc melting of La, Ni, and Cu metals under an Ar atmosphere. The details can be found in our previous work.³⁶ The LaNi₄Cu alloy was activated in pure H₂ gas at a pressure of 20 bar. The bulk alloy became a powder after H₂ activation. After releasing the high-pressure H₂, the sample was transferred to the DRIFTS chamber via an operation in the Ar gas-filled glovebox.

Co-CoO was synthesized by reducing Co₃O₄ nanoparticles in an H₂/He flow (6 mL/min / 4 mL/min) in the DRIFTS chamber at 250 $^{\circ}\text{C}$ for 4 h, with a heating rate of 2 $^{\circ}\text{C}/\text{min}$. Afterwards, the sample was cooled down in the same H₂/He flow. The Co₃O₄ nanoparticles were prepared by the calcination of Co(NO₃)₂·6H₂O (Sigma-Aldrich, 99%). The calcination program was set to 300 $^{\circ}\text{C}$ for 12 h and continuing heating to 400 $^{\circ}\text{C}$ for 2 h, using heating a rate of 2 $^{\circ}\text{C}/\text{min}$.

2.2.2.2 Reaction settings

CO₂ adsorption and hydrogenation reactions on pristine metals. The pristine Fe, Co, Ni, and Cu metal samples were loaded in the DRIFTS chamber and then evacuated to high vacuum at RT. The IR spectrum background was recorded on the metal surface at this high vacuum. CO₂ adsorption experiment was executed by filling this evacuated DRIFTS chamber with pure CO₂ gas of 1 bar. Afterwards, the samples were heated from RT to 500 °C with a heating rate of 5 °C/min. The spectra were taken at every 50 °C. The CO₂ hydrogenation reactions on Fe, Co, Ni, and Cu metals were performed also in the closed chamber condition. Again, the chamber was first pumped to high vacuum at RT. Afterwards, the samples were heated to 200 °C in the vacuum, and the IR backgrounds were taken. Then, 200 mbar CO₂ and 800 mbar H₂ were filled in the chamber. The spectra were taken every half an hour.

CO₂ hydrogenation reaction on metal hydride. The LaNi₄Cu alloy sample was loaded into the DRIFTS chamber through air-free operation. The chamber was then pumped to high vacuum at RT. The IR background was taken later on. Then 200 mbar CO₂ and 800 mbar H₂ were filled in the chamber. The sample was heated from RT to 450 °C with a heating rate of 2 °C/min, and the spectra were scanned continuously every 10 °C.

CO₂ hydrogenation on metal-metal oxide. The CO₂ hydrogenation reaction on the Co-CoO catalyst surface was carried out under continuous gas flow condition. After the Co-CoO catalyst was synthesized in the DRIFTS chamber, the IR background was taken. Then, CO₂ at 1.5 mL/min, H₂ at 6 mL/min, and He at 2.5 mL/min were allowed to flow through the whole DRIFTS-MS-GC system. Heating from RT to 350 °C with a ramp of 2 °C/min was applied to the sample. The IR spectra were taken every 20 °C. The MS measured the mass range of 0–50 amu, with a rate of 0.2 s per mass unit. The GC took 9 min to obtain each spectrum, with a cooling interval of 4 min between each measurement.

2.2.3 Determinations of rate constant and activation energy

The main reaction of CO₂ hydrogenation far before the reaction equilibrium is



Therefore, the kinetics of this reaction can be simplified as

$$\frac{d[CH_4]}{dt} = -k[CO_2]^m[H_2]^n, \quad \text{Eq. 2.2}$$

where $[CH_4]$, $[CO_2]$, and $[H_2]$ are the concentrations of CH_4 , CO_2 , and H_2 , respectively, at reaction time t , with units of mol/L. k is rate constant. m and n are the reaction orders of CO_2 and H_2 , respectively.

According to the stoichiometry, $[H_2]$ is four-fold $[CO_2]$. As we kept the gas feed of H_2 and CO_2 at ratio of 4:1, the $[H_2]$ can be replaced by $4 \cdot [CO_2]$. As for the reaction orders, the reaction order of CO_2 is reported to be less than 0.4, and that of H_2 is less than 0.9 at reaction temperatures lower than 250 °C.^{38–41} Therefore, we assume the overall reaction order is 1. Thence, the reaction kinetics is further simplified as

$$\frac{d[CH_4]}{dt} = -k'[CO_2]^{m+n}, \quad \text{Eq. 2.3}$$

where $m + n$ is 1 and k' is $4^n \cdot k$.

Therefore, to obtain k' , we only need to quantify the derivation of CH_4 quantity over the reaction time and the CO_2 quantity.

Note that Eq. 2.3 is the reaction rate of the overall reaction, which is from the beginning of dose of CO_2 to the end of the product of CH_4 . Therefore, the intermediate steps between CO_2 and CH_4 , i.e. $CO_2 \rightarrow$ surface reactive species $\rightarrow CH_4$, are incorporated. However, if the feeding ratio of H_2 / CO_2 is not 4 (nonstoichiometric), this simplification of Eq. 2.3 could not be used. Instead, the $[H_2]$, $[CO_2]$, m and n have to be quantified independently, and their real values have to be all used as described in the Eq. 2.2.

2.2.3.1 Determination of gas concentrations

We used two models of CO_2 hydrogenation reactions: constant volume without gas flow for the pristine and alloyed metals, and constant pressure with gas flow for the metal-metal oxide. Therefore, we used two different evaluation methods. For constant volume reaction, the pressure in the DRIFTS reaction chamber could be easily tracked by the pressure sensor, which is connected right before the reaction chamber. The quantity of each gas component is then calculated from the partial pressure. This calculation method was used for calculating the CH_4 yield over the four pure metals and the kinetic constant and activation energy over $LaNi_5Cu$.

For constant pressure (flow gas) reaction, the quantification is more challenging. The molar quantities of H₂, CO₂, CH₄, and He gases were determined using MS signals with m/z at 2, 44, 15, and 4, respectively. We mixed H₂/CO₂/He or CH₄/CO₂/He gases at different concentrations to obtain the correlation between the concentration and MS signal. He gas not only acted as carrier gas, but also the reference intensity of the MS signal. Herein, for H₂, CO₂ and CH₄ gases, we obtained

$$\frac{f(H_2)}{f(He)} = (3.98 \pm 0.18) \cdot \frac{I(H_2)}{I(He)}, \quad \text{Eq. 2.4}$$

$$\frac{f(CO_2)}{f(He)} = (2.57 \pm 0.04) \cdot \frac{I(CO_2)}{I(He)}, \quad \text{Eq. 2.5}$$

$$\frac{f(CH_4)}{f(He)} = (2.50 \pm 0.17) \cdot \frac{I(CH_4)}{I(He)}, \quad \text{Eq. 2.6}$$

where $f(H_2)$, $f(CO_2)$, $f(CH_4)$, and $f(He)$ (mL/min) are the flow rates of H₂, CO₂, CH₄, and He gases, respectively. $I(H_2)$, $I(CO_2)$, $I(CH_4)$, and $I(He)$ are the MS signal intensities with m/z at 2, 44, 15, and 2, respectively.

Combining Eq. 4–6, we can finally obtain the transient CO₂ and CH₄ molar numbers

$$n(CO_2) = \frac{f(CO_2)}{24.5}, \quad \text{Eq. 2.7}$$

$$n(CH_4) = \frac{f(CH_4)}{24.5}, \quad \text{Eq. 2.8}$$

where 24.5 (mL/mol) is the mole volume of idea gas at 25°C.

The Eq. 2.3 for calculating the kinetic constant can now be expressed as

$$\frac{dn(CH_4)}{dt} = -k'n(CO_2). \quad \text{Eq. 2.9}$$

The reaction time t is the gas passing time through the sample, which is calculated as

$$t = \frac{V_{sample}}{f_{total}}, \quad \text{Eq. 2.10}$$

where V_{sample} is the sample volume calculated from the size of the sample pellet. f_{total} is the total flow of the mixed gases which is 10 mL/min.

2.2.3.2 Determination of activation energy (E_a)

The correlation between k and E_a is determined using the Arrhenius equation

$$\ln k = \ln A - \frac{E_a}{R} \cdot \frac{1}{T}, \quad \text{Eq. 2.11}$$

where A is the pre-exponential factor, R is the gas constant, and T is reaction temperature.

Replacing k by k' , we obtain

$$\ln k' = \ln A' - \frac{E_a}{R} \cdot \frac{1}{T}, \quad \text{Eq. 2.12}$$

where the new pre-exponential factor A' is $4^n \cdot A$.

2.3 Results and Discussions

2.3.1 CO₂ adsorption and hydrogenation reactions on the pristine metal surfaces

CO₂ adsorption on the pristine Fe, Co, Ni, and Cu metal surfaces showed only gaseous CO₂ in the IR spectra with asymmetric stretching vibrations centered at 2349 cm⁻¹ (not shown). The derivative species, such as non-dissociated product carbonate and dissociated product CO*, were missing, indicating that CO₂ interacts very weakly on these pristine metal surfaces at RT. This is consistent with the reported low CO₂ binding energies (less than 40 kJ/mol) and with the desorption temperatures lower than RT on the single crystalline metal surfaces.^{42,43} To examine whether CO₂ molecules interacted stronger with the pure metal surfaces when increasing the temperature, we heated the surfaces up to 500 °C. As shown in Figure 2(a), CO gas, with rotational-vibrational modes in the range from 2230 to 2030 cm⁻¹, were produced on the Fe surface at 400 °C. Very low IR intensities of CO gas were also recorded on the Co and Ni surfaces at 400 °C. However, no products were detected on the Cu surface over the entire temperature range. Note that the small peak at 2070 cm⁻¹ represents the rotational bands of CO₂ gas.⁴⁴ Therefore, CO₂ gas interacts with pure Fe, Co, and Ni surfaces at high temperatures by dissociation into CO gas. Fe is the most active metal for the CO₂ dissociation reaction, whereas Cu is not active in the CO₂ adsorption reaction.

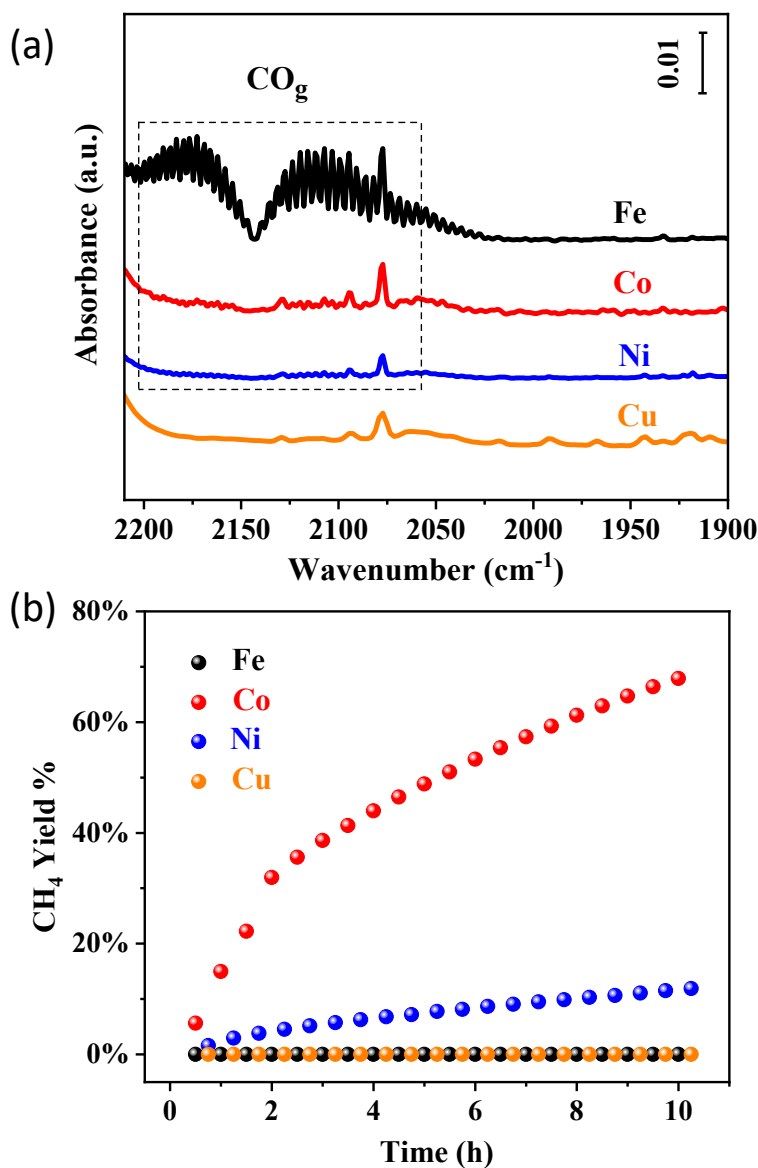


Figure 2.2. (a) IR spectra for 1 bar CO_2 adsorption on Fe, Co, Ni, and Cu surfaces at 400°C . (b) CH_4 yields from the CO_2 hydrogenation reactions on the Fe, Co, Ni, and Cu surfaces at 200°C .

CO_2 hydrogenation was subsequently investigated on these four pure metals. This reaction primarily produces CH_4 , which is known as the Sabatier reaction. The CH_4 yields at 200°C as a function of reaction time are shown in Figure 2(b). The highest CH_4 yield occurred on the Co surface, and second highest on the Ni surface. After 10 h of reaction, CH_4 yield on Co surface was seven-fold higher than that on Ni surface. No CH_4 was produced on the Fe and Cu surfaces in these conditions. Therefore, Co is the most reactive metal for the CO_2 methanation reaction, and Ni is the second most reactive. This is in line with the previous results from our group.²¹ These results suggest that Co is the most

promising catalyst for the efficient CO₂ conversion into synthetic methane. This inspires us to design Co-based materials for the further study of CO₂ hydrogenation, which is presented in the section 2.3.3.

2.3.2 CO₂ hydrogenation reaction on the metal hydride surface

In our previous study, we observed that adsorbed H₂ is a key component to weaken the C=O bond of CO₂ to form adsorbed formate or carbon monoxide.⁴⁵ Hence, we hypothesize that the poor performance of CO₂ hydrogenation observed for Fe, Ni, and Cu may be caused by insufficient H₂ on the surface. For this reason, we used LaNi₄Cu alloy for CO₂ reduction as this material represents a classic hydrogen storage material.^{36,46} As shown by the IR spectra in Figure 3(a), CO₂ was consumed, along with the production of CH₄ and CO gases when elevating the temperature. We integrated the absorbance of the reactant and product gases to understand the reaction kinetics. As shown in Figure 3(b), CH₄ and CO gases emerged above 350 °C. CH₄ production continued to increase until 450 °C, and CO production continued to increase until 410 °C. Above those temperatures, the intensities of these two products started to decrease. Nevertheless, the high onset temperature of the CO₂ hydrogenation reaction signifies that the LaNi₄Cu alloy did not help to lower down the reaction temperature, although the alloy was hydrogenated beforehand. Moreover, as the stored H₂ in the alloy remains stable until 100 °C,⁴⁶ the high onset temperature for CO₂ hydrogenation invalidated the advantages of H₂ pre-storage. In addition, no adsorbed species were observed from the IR spectra, similar to the cases for pristine metals, making it not possible to explain the intermediate catalyzed steps. Therefore, these pristine and alloyed metals are not suitable for reaction step study which is limited by the DRIFTS analysis, and we did not continue to study the reaction over these pure and alloyed metals using the rest of the methods such as MS, GC, and NMR.

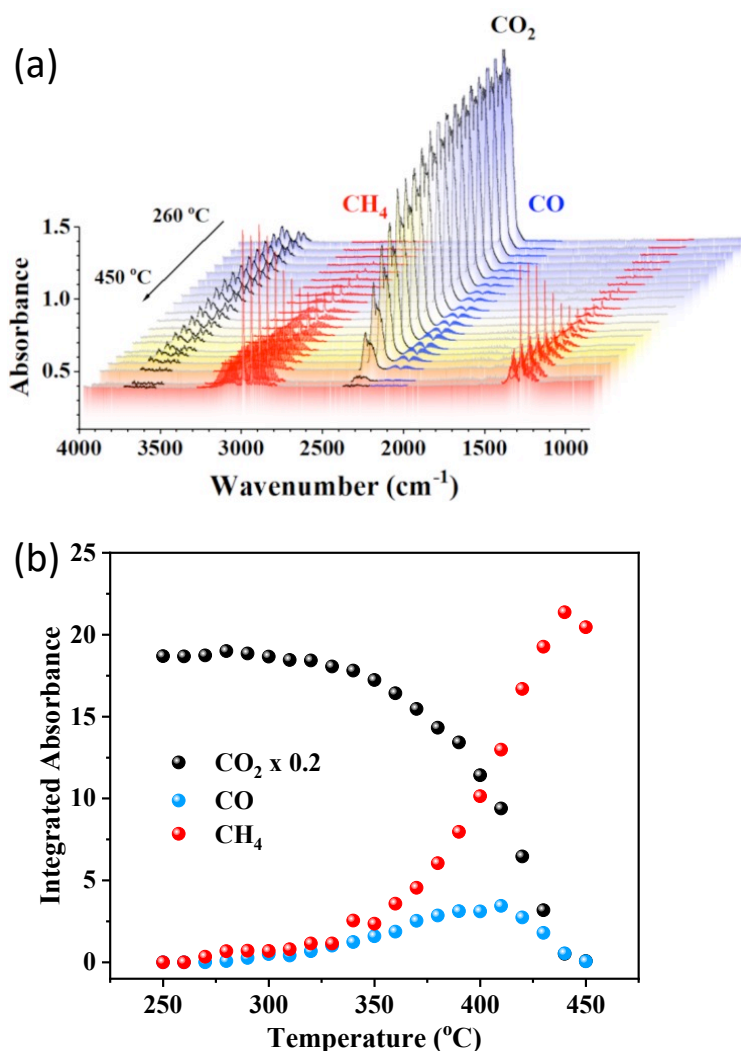


Figure 2.3. (a) IR spectra for the CO₂ hydrogenation reaction on LaNi₄Cu surface at elevating temperatures. (b) The integrated IR absorbance of gaseous reactant of CO₂ and gaseous products of CO and CH₄. CO₂ intensity was divided by five times.

2.3.3 CO₂ hydrogenation reaction on the Co-CoO surface

As we found that Co is the most reactive metal for CO₂ methanation among the transition metals tested, and based on the observation that metal oxides provide abundant adsorption sites in our previous study,^{45,47,48} we synthesized Co-CoO nanoparticles to investigate the gas, liquid, and surface products under flow gas conditions. The Co-CoO nanoparticles possessed a 20% molar concentration of metallic cobalt, as quantified by the consumed amount of H₂ gas measured using MS.

The CO₂ to CH₄ conversion were analyzed by means of MS. As shown in Figure 4(a), the CO₂ hydrogenation reaction on this Co-CoO catalyst began at approximately 160 °C. The primary and

main product was CH₄, with approximately 90% yield. Weak signals of the very small amounts of CO and C₂H₆ detected in MS overlapped with the signal of CO₂ fragments. Therefore, GC was employed to separate these gases. As shown in Figure 4(b), C₂H₆ and CO production have onset temperatures similar to CH₄ production, and show maximum yield of 0.15% and 0.024%, respectively, both at 270 °C. Above 270 °C, the observed amount of both C₂H₆ and CO decreased, indicating that high temperatures are not favorable for C₂₊ synthesis and reversed gas shift reactions on Co-CoO. A reason for this phenomenon could be that the intense methanation reaction produced large amount of H₂O at high conversion of CO₂, as we observed condensed water on the chamber window after long time reaction at high temperature. The produced H₂O competitively adsorbs on the surface and inhibits the reaction in the forward direction. Besides the gas products, traces of methanol, ethanol and acetic acid products were found using NMR, as shown in Figure 4(c). These latter species could be traced only by means of this analytical method. The overall yield of the non-methane products is less than 0.2%. However, the methods used in the study are able to collect information for all of the products.

After clarified the overall products of CO₂ conversion, we analyzed the intermediates on the surface during the reaction process. We tracked the surface adsorption species using the DRIFTS part. The IR spectra region between 1700 and 1200 cm⁻¹ contain information about the adsorption species (Figure 5(a)). These peaks formed upon CO₂ and H₂ co-adsorption at RT. A deconvolution using the bi-level evolutionary Gaussian fitting showed the development of the peaks. Please refer to our previous work for the peak deconvolution, assignment and identification.^{40,47} The peak at 1620 cm⁻¹ was ascribed to the O-C-O asymmetric stretching mode of formate on the metal-metal oxide interface, and the wide peak centered at 1520 cm⁻¹ was assigned to the adsorbed carbonate (CO₃^{2-*}).⁴⁵ The wide peak centered at 1385 cm⁻¹ was coupled by the C-H bending and O-C-O symmetric stretching of formate.⁴⁹⁻⁵² As shown in Figure 5(b), the formate consumed during the reaction, and the CO₃^{2-*} did not vary before 200 °C. Due to the strong interference of the IR spectra from H₂O, which was formed from the dominant CO₂ methanation reaction, the peaks after 200 °C could not be distinguished well. However, after CO₂ hydrogenation reaction and overnight flashing in He gas, the previously observed formate and carbonate species disappeared, as shown in the top green plot in Figure 5(a). This suggests that these species are completely consumed above 200 °C. However, new peaks at 1261, 1100, and 1020 cm⁻¹ remained on the surface after He flow.

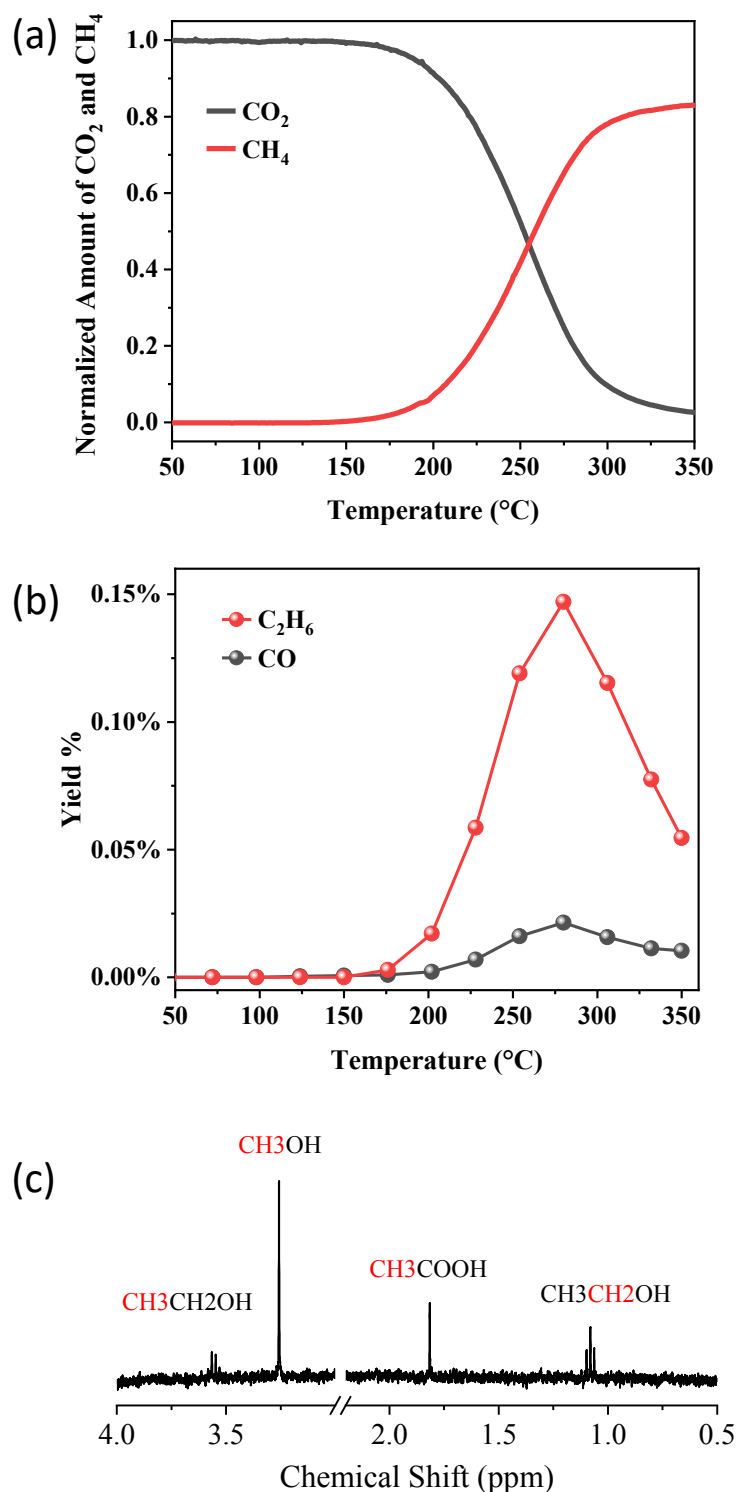


Figure 2.4. (a) CO_2 and CH_4 conversion from CO_2 hydrogenation on Co-CoO surface analyzed using MS data. (b) The calculated yields of C_2H_6 and CO gas products using GC data. (c) Very small quantities of CH_3OH , $\text{C}_2\text{H}_5\text{OH}$, and CH_3COOH liquid products collected using the inline deionized water and measured using NMR.

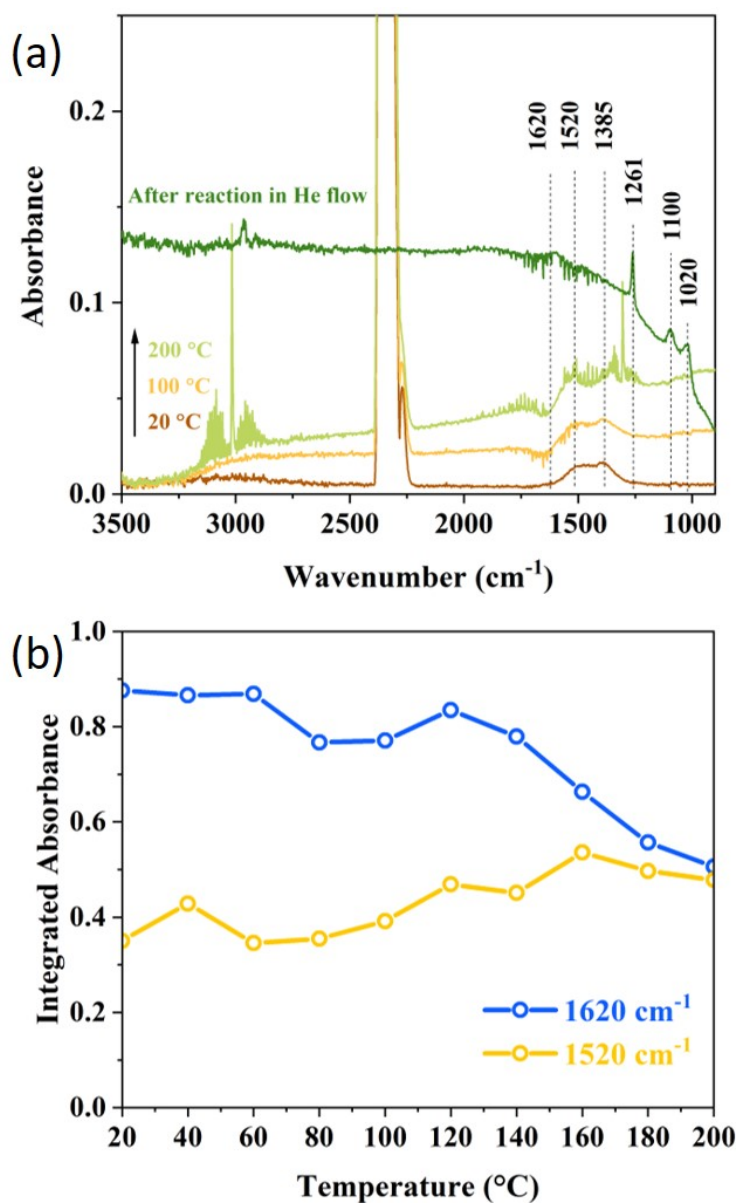


Figure 2.5. (a) IR spectra for the CO_2 hydrogenation reaction on Co-CoO surface. (b) Development of the adsorbed formate and carbonate with IR peaks at 1620 and 1520 cm^{-1} , respectively.

To identify the new peaks, we referred to the NMR results. We separately applied 1 μL of CH_3OH , $\text{C}_2\text{H}_5\text{OH}$, HCOOH , and CH_3COOH liquids to the resulting Co-CoO surface in the DRIFTS chamber in a glovebox. By comparing the IR peaks of the standard chemicals (spectra not shown), the peak at 1261 cm^{-1} was found to be fitted with the O-H bending mode of $\text{C}_2\text{H}_5\text{OH}$, the peak at 1100 cm^{-1} overlapped with the C-O stretching of HCOOH and $\text{C}_2\text{H}_5\text{OH}$, and the peak at 1020 cm^{-1} overlapped with the C-O stretching of CH_3OH and $\text{C}_2\text{H}_5\text{OH}$.⁵³ These species may have been retained on the

surface after CO₂ reduction. Yet, the retained species could also be strongly bound CO* and bidentate carbonate on the cobalt.⁵⁴

Consequently, the surface analysis provided the information that the formate at the metal-metal oxide interface and carbonate at the metal oxide formed upon CO₂ and H₂ co-adsorption. These two species were the intermediates of CH₄ formation. Some carbon oxides, either alcohol/acid or strongly bound CO*, were retained on the Co-CoO surface as byproducts.

Comparing to the invisible surface species on the pristine and alloyed metals, we speculate that the metal surfaces interact with CO₂ molecules weakly in the applied dry gas and clean surface condition, as the observations of CO₂ adsorption and desorption on metal surfaces are in ultrahigh vacuum and at low temperature (< 0 °C).^{55–57} However, on the oxide surface, CO₂ adsorption and desorption are usually above room temperature.^{42,58} Therefore, the physical properties of the material surface determines the CO₂ adsorption behavior and result in the invisible adsorbed species on the metal and visible adsorbed species on the metal oxide or the interface of the metal and metal oxide. Metal oxide is essentially important for the mechanism study of the surface reactions.

2.3.4 Kinetic comparison of the CO₂ methanation reaction on the pristine and alloyed metals, and the Co-CoO surface

As a final example of the capabilities of the instrumental set-up here developed, we calculated the kinetics of CO₂ methanation on the three types of catalysts studied to compare the activities of these catalysts. We calculated the kinetic constants at 200 °C using the Eq. 2.9. As shown in Figure 6 (left axis), Co-CoO exhibits tremendously higher kinetic constant than the pristine Co metal; Co metal possesses ten-fold higher kinetics than Ni; LaNi₄Cu is not reactive at 200 °C. These explained the high activity of the Co-CoO sample.

The activation energies (E_a) of CO₂ methanation were calculated using Eq. 2.12 for Co-CoO and LaNi₄Cu samples at their low CO₂ conversions of 2–40%. These low conversions related to temperature ranges of 166–236 °C for Co-CoO and 310–390 °C for LaNi₄Cu. The value of E_a on Co and Ni were taken from a previous work of our group.¹⁸ The results were demonstrated in Figure 6 (right axis). Co-CoO has higher activation energy than Co and Ni, indicating the kinetic constant change faster with temperature on Co-CoO than that on the Co and Ni. This coherent with the observations in Figure 2(b) and Figure 4(a). LaNi₄Cu has the highest activation energy, which is consistent with its less active at low temperature, and reflects the reaction rate changing fast at high temperature.

These are in line with the observations in Figure 2.3. These results emphasize the importance of the presence of metal oxide phase in the enhancement of the activity of the catalyst in the CO₂ methanation reaction.

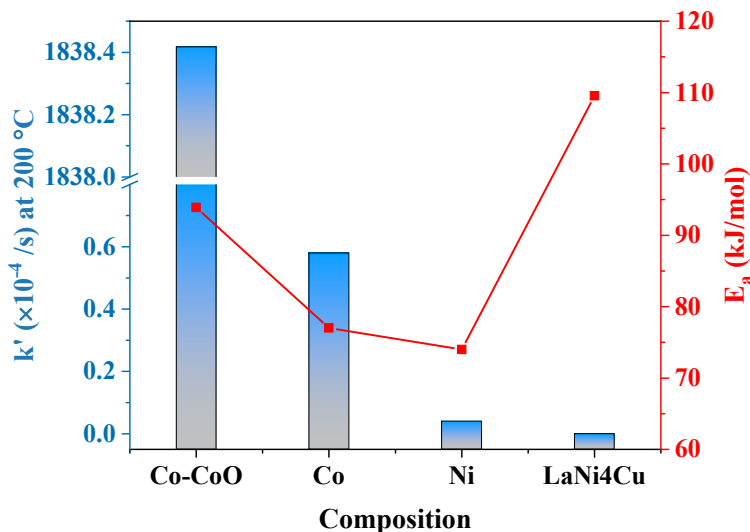


Figure 2.6. Reaction rate constants k' at 200 °C (left axis) and activation energies E_a of CO₂ methanation (right axis). Activation energies of CO₂ methanation on Co and Ni were taken from the reference²¹.

2.4 Conclusions

We built an inline DRIFTS-MS-GC apparatus to perform an operando study of the heterogeneously catalyzed CO₂ hydrogenation reaction. Pristine metals, metal hydride alloy, and metal-metal oxide materials were used as example materials to show the potential of the system and the related analytic methods including the calculation of the kinetic parameters of the reaction and the resolving of the complicated adsorption species. The results verified the reliability of the combined system and sensitivity of this apparatus for the simultaneous investigation of the gas, liquid, and surface products of CO₂ adsorption and hydrogenation reactions. Importantly, the observation of the adsorbed species on the catalyst surface requires the presence of a metal oxide phase in the catalyst. No adsorbed species but only gas phase was found on the purely metallic surfaces, such as pristine and alloyed metals.

In addition to the development of this special instrument and the correspondingly analytic method, this study shows the systematic understanding of the fundamental differences in the interaction of CO₂ with metals, and provides instructions of synthesizing highly active and efficient catalyst. Co is the most active metal to hydrogenate CO₂ to CH₄, while Fe is the most active to dissociate CO₂ to

CO gas. Pre-stored H₂ in metal hydride alloy does not assist the CO₂ hydrogenation. However, metal oxide mixed with metal facilitate the CO₂ hydrogenation, due to the adsorption of CO₂ at the metal oxide surface and the metal/metal oxide interface. As a result, the activity in the CO₂ methanation follows the order of Co-CoO > Co > Ni > LaNi₄Cu. This enlightens the importance of metal oxide phase in the design of the efficient catalyst to achieve high activity in CO₂ methanation.

Overall, the coupling of different analytic technique in a single experimental unit is therefore essential for the advancement of science in this complex field, enabling the contemporaneous understanding of different effects, which could not be revealed by means of the single individual tools.

ACKNOWLEDGMENTS

SCCER HeE, which is financially supported by Innosuisse, the Swiss Innovation Agency, is gratefully acknowledged. W.L acknowledges the financial support from SNSF (Ambizione Project PZ00P2_179989). M.L would like to thank the China Scholarship Council for the PhD grant (Grant No. 201506060156).

Reference

- ¹ N.S. Lewis and D.G. Nocera, *Proc. Natl. Acad. Sci.* **103**, 15729 (2006).
- ² M. Aresta and A. Dibenedetto, *Catal. Today* **98**, 455 (2004).
- ³ A. Züttel, P. Mauron, S. Kato, E. Callini, M. Holzer, and J. Huang, *Chimia* **69**, 264 (2015).
- ⁴ S. Gao, Y. Lin, X. Jiao, Y. Sun, Q. Luo, W. Zhang, D. Li, J. Yang, and Y. Xie, *Nature* **529**, 68 (2016).
- ⁵ W.-H. Wang, Y. Himeda, J.T. Muckerman, G.F. Manbeck, and E. Fujita, *Chem. Rev.* **115**, 12936 (2015).
- ⁶ R.W. Dörner, D.R. Hardy, F.W. Williams, and H.D. Willauer, *Energy Environ. Sci.* **3**, 884 (2010).
- ⁷ W.L. Vrijburg, E. Moiola, W. Chen, M. Zhang, B.J.P. Terlingen, B. Zijlstra, I.A.W. Filot, A. Züttel, E.A. Pidko, and E.J.M. Hensen, *ACS Catal.* **9**, 7823 (2019).
- ⁸ R. Mutschler, E. Moiola, K. Zhao, L. Lombardo, E. Oveisi, A. Porta, L. Falbo, C.G. Visconti, L. Lietti, and A. Züttel, *ACS Catal.* **10**, 1721 (2020).
- ⁹ E. Moiola, N. Gallandat, and A. Züttel, *Chem. Eng.* **375**, 121954 (2019).
- ¹⁰ E. Moiola, R. Mutschler, and A. Züttel, *Renew. Sust. Energy Rev.* **107**, 497 (2019).
- ¹¹ E. Moiola and A. Züttel, *Sustain. Energy Fuels* **4**, 1396 (2020).
- ¹² F. Marques Mota and D.H. Kim, *Chem. Soc. Rev.* (2019).

-
- ¹³ W. Li, H. Wang, X. Jiang, J. Zhu, Z. Liu, X. Guo, and C. Song, *RSC Adv.* **8**, 7651 (2018).
- ¹⁴ E. Moiolli, N. Gallandat, and A. Züttel, *React. Chem. Eng.* **4**, 100 (2018).
- ¹⁵ M. Jacquemin, A. Beuls, and P. Ruiz, *Catal. Today* **157**, 462 (2010).
- ¹⁶ J. Szanyi and J.H. Kwak, *Phys. Chem. Chem. Phys.* **16**, 15117 (2014).
- ¹⁷ M. Che, *Catal. Today* **218–219**, 162 (2013).
- ¹⁸ J.H. Kwak, L. Kovarik, and J. Szanyi, *ACS Catal.* **3**, 2449 (2013).
- ¹⁹ J. Lahtinen, T. Anraku, and G.A. Somorjai, *Catal. Lett.* **25**, 241 (1994).
- ²⁰ G.D. Weatherbee and C.H. Bartholomew, *J. Catal.* **68**, 67 (1981).
- ²¹ R. Mutschler, E. Moiolli, W. Luo, N. Gallandat, and A. Züttel, *J. Catal.* **366**, 139 (2018).
- ²² K.O. Xavier, R. Sreekala, K.K.A. Rashid, K.K.M. Yusuff, and B. Sen, *Catal. Today* **49**, 17 (1999).
- ²³ B. Mutz, M. Belimov, W. Wang, P. Sprenger, M.-A. Serrer, D. Wang, P. Pfeifer, W. Kleist, and J.-D. Grunwaldt, *ACS Catal.* **7**, 6802 (2017).
- ²⁴ S. Zhang, L. Nguyen, J.-X. Liang, J. Shan, J. Liu, A.I. Frenkel, A. Patlolla, W. Huang, J. Li, and F. Tao, *Nat. Commun.* **6**, 1 (2015).
- ²⁵ J. He, N.J.J. Johnson, A. Huang, and C.P. Berlinguette, *ChemSusChem* **11**, 48 (2018).
- ²⁶ M. Schubert, S. Pokhrel, A. Thomé, V. Zielasek, T.M. Gesing, F. Roessner, L. Mädler, and M. Bäumer, *Catal. Sci. Technol.* **6**, 7449 (2016).
- ²⁷ S. Wohlrab, D. Ehrlich, J. Wambach, H. Kuhlenbeck, and H.-J. Freund, *Surf. Sci.* **220**, 243 (1989).
- ²⁸ C. Vogt, E. Groeneveld, G. Kamsma, M. Nachtegaal, L. Lu, C.J. Kiely, P.H. Berben, F. Meirer, and B.M. Weckhuysen, *Nat. Catal.* **1**, 127 (2018).
- ²⁹ V. Iablokov, S.K. Beaumont, S. Alayoglu, V.V. Pushkarev, C. Specht, J. Gao, A.P. Alivisatos, N. Kruse, and G.A. Somorjai, *Nano Lett.* **12**, 3091 (2012).
- ³⁰ F.C. Meunier, *Chem. Soc. Rev.* **39**, 4602 (2010).
- ³¹ T. Franken, J. Terreni, A. Borgschulte, and A. Heel, *J. Catal.* **382**, 385 (2020).
- ³² N. Boreriboon, X. Jiang, C. Song, and P. Prasassarakich, *Top Catal.* **61**, 1551 (2018).
- ³³ L. Wang, W. Zhang, X. Zheng, Y. Chen, W. Wu, J. Qiu, X. Zhao, X. Zhao, Y. Dai, and J. Zeng, *Nat. Energy* **2**, 869 (2017).
- ³⁴ G.D. Weatherbee and C.H. Bartholomew, *J. Catal.* **87**, 352 (1984).
- ³⁵ C. Liu, T.R. Cundari, and A.K. Wilson, *J. Phys. Chem. C* **116**, 5681 (2012).
- ³⁶ M. Spodaryk, N. Gasilova, and A. Züttel, *J. Alloys and Compd.* **775**, 175 (2019).
- ³⁷ A. Boffa, C. Lin, A.T. Bell, and G.A. Somorjai, *J. Catal.* **149**, 149 (1994).

-
- ³⁸ M.S. Duyar, A. Ramachandran, C. Wang, and R.J. Farrauto, *J. CO₂ Util.* **12**, 27 (2015).
- ³⁹ G.D. Weatherbee and C.H. Bartholomew, *J. Catal.* **77**, 460 (1982).
- ⁴⁰ A. Karelavic and P. Ruiz, *ACS Catal.* **3**, 2799 (2013).
- ⁴¹ G. Garbarino, D. Bellotti, E. Finocchio, L. Magistri, and G. Busca, *Catal. Today* **277**, 21 (2016).
- ⁴² U. Burghaus, *Prog. Surf. Sci.* **89**, 161 (2014).
- ⁴³ B. Bartos, H.J. Freund, H. Kuhlenbeck, M. Neumann, H. Lindner, and K. Müller, *Surf. Sci.* **179**, 59 (1987).
- ⁴⁴ C.P. Rinsland, D.C. Benner, and V.M. Devi, *Appl. Opt.*, **AO 25**, 1204 (1986).
- ⁴⁵ K. Zhao, L. Wang, M. Calizzi, E. Moiola, and A. Züttel, *J. Phys. Chem. C* **122**, 20888 (2018).
- ⁴⁶ A. Züttel, *Mater. Today* **6**, 24 (2003).
- ⁴⁷ K. Zhao, L. Wang, E. Moiola, M. Calizzi, and A. Züttel, *J. Phys. Chem. C* **123**, 8785 (2019).
- ⁴⁸ K. Zhao, M. Calizzi, E. Moiola, M. Li, A. Borsay, L. Lombardo, R. Mutschler, W. Luo, A. Züttel, Submitted.
- ⁴⁹ G. Busca, J. Lamotte, J.C. Lavalley, and V. Lorenzelli, *J. Am. Chem. Soc.* **109**, 5197 (1987).
- ⁵⁰ K. Ito and H.J. Bernstein, *Can. J. Chem.* **34**, 170 (1956).
- ⁵¹ H.R. Zelsmann, Y. Marechal, A. Chosson, and P. Faure, *J. Mol. Struct.* **29**, 357 (1975).
- ⁵² Y.T. Chang, Y. Yamaguchi, W.H. Miller, and H.F. Schaefer, *J. Am. Chem. Soc.* **109**, 7245 (1987).
- ⁵³ E.K. Plyler, *J. Res. Natl. Bur. Stand.* **48**, 281 (1952).
- ⁵⁴ J. Paul and F.M. Hoffmann, *Catal. Lett.* **1**, 445 (1988).
- ⁵⁵ B. Bartos, H.J. Freund, H. Kuhlenbeck, M. Neumann, H. Lindner, and K. Müller, *Surf. Sci.* **179**, 59 (1987).
- ⁵⁶ H.J. Freund and R.P. Messmer, *Surf. Sci.* **172**, 1 (1986).
- ⁵⁷ H.J. Freund and M.W. Roberts, *Surf. Sci. Rep.* **25**, 225 (1996).
- ⁵⁸ U. Burghaus, in *New and Future Developments in Catalysis* (Elsevier, Amsterdam, 2013), pp. 27–47.

Chapter 3 Identifying Reaction Species by Evolutionary Fitting and Kinetic Analysis: an Example of CO₂ Hydrogenation in DRIFTS

Kun Zhao^{a,b,†*}, Ligang Wang^{c,d,†}, Emanuele Moioli^{a,b}, Marco Calizzi^{a,b*}, Andreas Züttel^{a,b}

^aLaboratory of Materials for Renewable Energy, Institute of Chemical Sciences and Engineering, École Polytechnique Fédérale de Lausanne (EPFL), 1951 Sion, Switzerland

^bSwiss Federal Laboratories for Materials Science and Technology (EMPA), 8600 Dübendorf, Switzerland

^cGroup of Energy Materials, Institute of Mechanical Engineering, École Polytechnique Fédérale de Lausanne (EPFL), 1951 Sion, Switzerland

^dIndustrial Process and Energy Systems Engineering, Institute of Mechanical Engineering, École Polytechnique Fédérale de Lausanne (EPFL), 1951 Sion, Switzerland

Preprint version: preprint version of the manuscript published on the scientific journal *The Journal of Physical Chemistry C*. 2019, 123, 8785-8792. DOI: 10.1021/acs.jpcc.8b11105.

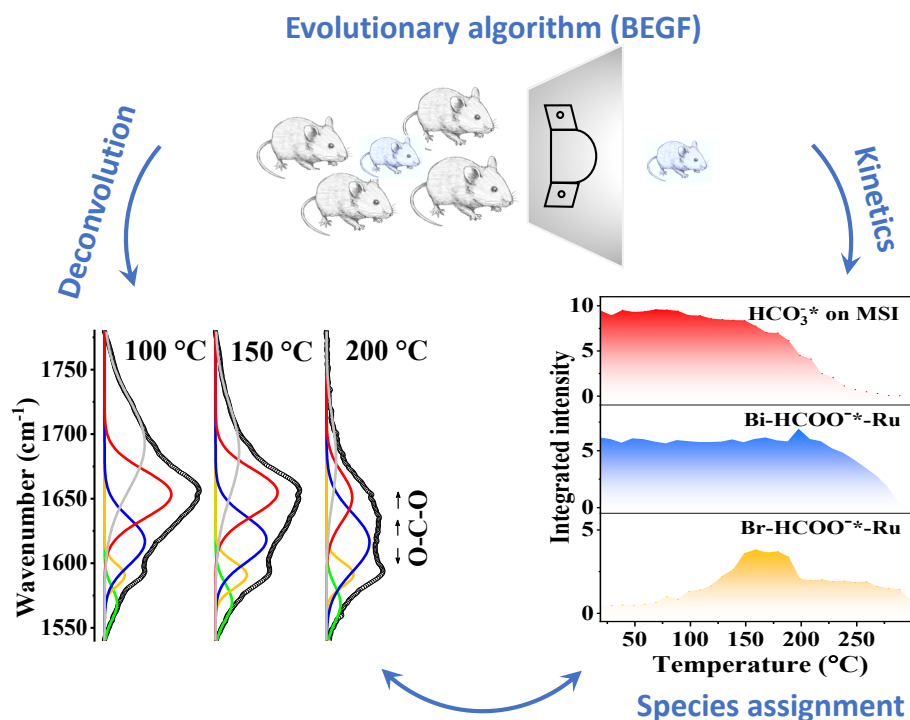
Copyright permission: adapted with permission from Zhao. K., et al *J. Phys. Chem. C*, 2019, 123, 8785. Copyright 2019 American Chemical Society.

Edit: caption numbers of figures, tables, and equations were edited to adapter the thesis chapter number.

Summary: This Chapter is methodological work focusing on analysis of the sophisticated diffuse reflectance infrared spectra. A fitting program has been developed to deconvolute the spectral sets and output the developing plots of each IR peak from the catalyzed CO₂ hydrogenation process on Ru/Al₂O₃ surface.

Abstract

Diffuse reflectance infrared Fourier transform spectroscopy (DRIFTS) investigations of molecules at the surface of catalysts exhibit strong overlap of the adsorption peaks. Therefore, the investigation of the CO₂ hydrogenation on a highly active catalyst surfaces requires a deconvolution of the adsorption spectra in order to clearly assign the signal to the chemical species. We developed an autonomous and efficient bilevel evolutionary Gaussian fitting (BEGF) procedure with a genetic algorithm at the upper level and a multi-peak Gaussian fitting algorithm at the lower level to analyze self-consistently the set of spectra of an entire experiment. We show two examples of the application of BEGF procedure by analyzing the DRIFTS spectral sets of ex-situ-HCOO⁻* and CO₂ hydrogenation on Ru/Al₂O₃. The fitting procedure deconvoluted the overlapped peaks, and identified the bond vibrations of carbon monoxide, formate, bicarbonate and carbonate through the developing trends of the peak intensities along the reaction. These revealed the progression of those species over the reaction timeline.



3.1 Introduction

Heterogeneous catalysis on surfaces, such as CO₂ hydrogenation catalysis, has been widely studied by diffuse reflectance infrared Fourier transformation spectroscopy (DRIFTS), as both the gas phase components and the surface adsorption species can be detected in situ and in operando.^{1–7} The correct assignment of the infrared (IR) peaks is not easy, because they are strongly overlapped. Especially, the O–C–O asymmetric stretching modes of HCO₃[–], HCOO[–], COOH[–] and bent CO₂^{δ–} share very close positions in the range of 1800–1300 cm^{–1}.⁸ This has led to discrepant explanations of the production of the adsorption species, thence diverse reaction pathways about either bicarbonate, formate or carbon monoxide is the key intermediate.^{7,9,10,11} Many issues affect the analysis of CO₂ hydrogenation using IR spectroscopy. First, the determination of the IR peak positions of the species present on reactive surfaces such as Ru, Rh, Pd, etc. is not simple due to the strong overlap of the peaks. As a result, the manual assignment of the peak positions among the multi-peaks and shoulders does not have an obvious unique solution. Second, some subpeaks in the overlapped region vanish or appear during the reaction, which is easily neglected in the analysis. Thus, assigning the peaks using data only at one or a few stages in the reaction can lose information. A global analysis of the spectra taken over the entire course of the reaction is necessary. This brings us to the third issue: there is no efficient procedure to fit self-consistently the peaks of all the spectra recorded during the reaction. Fitting spectra non-self-consistently, or using inconsistent parameters, can give an incorrect description of the development of the peaks along the reaction coordinate. A multi-peak Gaussian curve fitting can be performed with nonlinear gradient-based solvers,¹² but the results depend strongly on the guesses of initial values and bounds of the parameters related to each peak. Bad guesses lead the solvers be trapped at local optima, resulting in unsatisfactory or even wrong results. Moreover, most of the deconvolution methods treat one peak or one spectrum instead of treating the spectral set at once.

Here, we attack the three issues just raised by developing a novel bilevel evolutionary Gaussian fitting (BEGF) procedure to fit the peaks from a set of spectra and select the reasonably deconvoluted peaks automatically. This BEGF procedure combines gradient-free evolutionary algorithms at the upper-level and nonlinear multi-peak Gaussian fittings at the lower level to optimize the peaks. An evolutionary algorithm is an optimization algorithm that ranks the candidate solutions, recombines the parameters of the best ones to create a new generation of candidate solutions and iterates till convergence is reached.¹³ The evolutionary algorithm overcomes the problem of Gaussian fitting being trapped at local optima. The fitting results elucidate the developing trends of the resolved peaks

along the reaction. According to the similarities of the peak developments in the reaction, and combined with the peak positions from the standard samples such as formic acid (HCOOH), sodium carbonate (Na₂CO₃), calcium carbonate (CaCO₃), sodium bicarbonate (NaHCO₃) and potassium bicarbonate (KHCO₃), the peaks were clearly assigned to the bond vibrations of the specific species.

In the next section, we provide a description of the BEGF algorithm. More detailed information and the MATLAB code used for the work reported here are given in the SI. Later on, we describe the procedure with two examples: (1) formate hydrogenation where formate was from HCOOH droplet and therefore named as ex-situ-HCOO⁻* to distinguish the formate formed from CO₂ hydrogenation process; (2) CO₂ hydrogenation. These two examples show how the procedure helps the assignment of the peaks and analyze the reactive progression of the reaction species.

3.2 Fitting and Experimental Methods

3.2.1 Bilevel evolutionary Gaussian fitting (BEGF) procedure

The multi-peak Gaussian fitting is a least-square problem (Eq. 3.1), which minimizes the sum of squared errors between the fitted value and the experimental data of the spectrum to find the best fit:

$$\min_{\mathbf{a}, \mathbf{b}, \mathbf{c}} f = \sum_{i=1}^{N_s} \left(\sum_{j=W_s}^{W_e} (Y_{i,j}(\mathbf{a}_i, \mathbf{b}, \mathbf{c}_i) - Y_{i,j}^*)^2 \right), \mathbf{a}_i = \{... a_{i,k} ... \}, \mathbf{b} = \{... b_k ... \}, \mathbf{c}_i = \{... c_{i,k} ... \}, \quad \text{Eq. 3.1}$$

$$\text{with } Y_{i,j} = \sum_{k=1}^{N_{peak}} a_{i,k} e^{-\left(\frac{j-b_k}{c_{i,k}}\right)^2}, \quad \text{Eq. 3.2}$$

where i stands for the i^{th} spectrum in the total N_s spectra, and j is the wavenumber within the defined range $[W_s, W_e]$, where W_s and W_e are the starting and ending wavenumber. $Y_{i,j}$ and $Y_{i,j}^*$ are the fitted and measured values, respectively. The variables $a_{i,k}$, b_k and $c_{i,k}$ are the height, position and width, respectively, of each Gaussian peak k ($1 \leq k \leq N_{peak}$), respectively. a_i and c_i vary along the reaction, while b is generally assumed not to change as the reaction proceeds.

The optimization problem is highly-nonlinear due to the Gaussian function used in the definition of $Y_{i,j}$ (Eq. 3.1 and 3.2). The whole problem can be solved by gradient-based solvers. However, in our experience with fitting DRIFTS spectra, gradient-based solvers get trapped at local minima depending on the guesses of the initial values of Gaussian parameters, and these guesses are usually obtained manually by time-consuming trial-and-error.

To overcome this difficulty, we decomposed the mathematical optimization problem into two levels: for the upper level we used a genetic algorithm to provide initial values for a multi-peak Gaussian fitting algorithm used on the lower level.

The schema of the BEGF process is shown in Figure 3.1, with the problem decomposition described as:

Upper level:

$$\min_{\mathbf{I}, \mathbf{L}, \mathbf{U}} \sum_{i=1}^{N_s} \delta_i(\mathbf{I}, \mathbf{L}, \mathbf{U}), \mathbf{I} = \{\dots \{I_{a_k}, I_{b_k}, I_{c_k}\} \dots\}, \mathbf{L} = \{\dots \{L_{a_k}, L_{b_k}, L_{c_k}\} \dots\}, \mathbf{U} = \{\dots \{U_{a_k}, U_{b_k}, U_{c_k}\} \dots\}. \text{Eq. 3.3}$$

Lower level:

$$\min_{\mathbf{a}, \mathbf{b}, \mathbf{c}} \delta_i(\mathbf{a}_i, \mathbf{b}, \mathbf{c}_i) = \min_{\mathbf{a}, \mathbf{b}, \mathbf{c}} \sum_{j=W_s}^{W_e} (Y_{i,j} - Y_{i,j}^*)^2 = \min_{\mathbf{a}, \mathbf{b}, \mathbf{c}} \sum_{j=W_s}^{W_e} \left(\sum_{k=1}^{N_{\text{peak}}} \left(a_{i,k} e^{-\left(\frac{x-b_k}{c_{i,k}}\right)^2} \right) - Y_{i,j}^* \right)^2, \quad \text{Eq. 3.4}$$

$$\mathbf{a}_i = \{\dots a_{i,k} \dots\}, \mathbf{b} = \{\dots b_k \dots\}, \mathbf{c}_i = \{\dots c_{i,k} \dots\}$$

$$\text{subject to } L_{a_k} \leq a_{i,k} \leq U_{a_k}, L_{b_k} \leq b_k \leq U_{b_k}, L_{c_k} \leq c_{i,k} \leq U_{c_k}$$

where \mathbf{I} shows the initial values of the parameters (a height, b position and c width) of the Gaussian peaks. \mathbf{L} and \mathbf{U} are the lower and upper bounds of the parameters of the Gaussian peaks, which are used to constrain the multi-peak Gaussian fitting.

The BEGF algorithm works as follows and is sketched in Figure 3.1. The original spectra are first corrected by subtracting a baseline, which was taken as a straight line between the endpoints of the defined wavenumber range. The baseline-corrected spectra are used in each run of the low-level algorithm. The solving procedure starts from the upper-level algorithm by generating a number of global candidate solutions (individuals, represented by a set of values of \mathbf{I} , \mathbf{L} , and \mathbf{U} (Eq. 3.3), which are randomly generated within the user-specified bounds) to form an initial population. Each individual of the population is passed to the lower-level algorithm to obtain the best fit values for the parameters \mathbf{a}_i , \mathbf{b} , and \mathbf{c}_i and to assign the sum of the fitting errors as the value of the objective function (Eq. 3.4). The evaluated individual is then passed back to the upper-level algorithm. After evaluating all individuals in the initial population, the upper-level algorithm compares the individuals and discards those with large errors. Afterwards, the population starts to evolve iteratively by selecting some existing individuals as parents and generating a new individual as a child with certain crossover and mutation mechanisms. The newly generated child individual is further evaluated in the lower level, returned to the upper level with the objective value and compared with the parent

individuals. The child individual will be preserved if better than the parents; otherwise discarded. In such a way, the whole population is updated by always keeping the better individuals until convergence is reached: no better individual is found after a number of latest individual evaluations. The rate of convergence depends on the complexity of the spectra.

The BEGF algorithm starts with a user-specified number of Gaussian peaks. The redundant Gaussian peaks are removed when the L_{a_k} and U_{a_k} for peak k optimized at the upper level reach zero simultaneously.

Although good initial guesses are not needed for the genetic algorithm, using apparent information of the peaks in the spectra as initial values reduces the search time. Further details of the algorithm, including a MATLAB code implementation, are given in the SI.

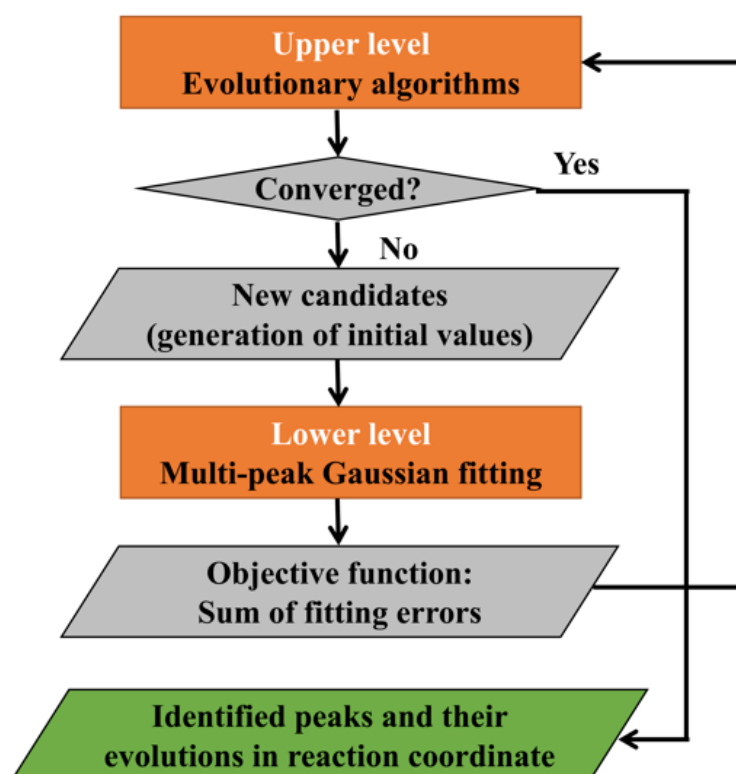


Figure 3.1. The developed bilevel evolutionary Gaussian fitting algorithm.

Our bilevel algorithm is distinguished from available fitting codes by the following features: (1) it consistently fits the peaks in a given range of wavelengths across the entire set of spectra measured during a reaction; (2) the number of Gaussian peaks used for fitting is determined automatically; (3)

the centroid of a given peak is identical for all spectra; (4) peak evolution directly gives the kinetics of the species; (5) manual intervention is not needed; (6) good initial guesses are not necessary.

3.2.2 Experimental methods

Ex-situ-HCOO^{-*} and CO₂ hydrogenation on Ru/Al₂O₃ (Sigma-Aldrich, 0.5 wt% loading on 3.2 mm pellets of Al₂O₃) pellets and Al₂O₃ (Sigma-Aldrich) pellets were carried out in the reaction chamber (HVC, Harrick Scientific) of DRIFTS (Bruker Tensor 27).

Ex-situ-HCOO^{-*} was obtained by adding one drop of formic acid to the surface of Ru/Al₂O₃ or Al₂O₃ exposed to air, followed by pumping for 24 h to reach a vacuum of 5×10^{-3} mbar at room temperature (RT) in DRIFTS. The hydrogenation of HCOOH on Ru/Al₂O₃ and Al₂O₃ was performed by heating in 1 bar H₂ from RT to 350 °C at a rate of 1 °C/min in DRIFTS.

CO₂ hydrogenation was performed by mixing 200 mbar of CO₂ and 800 mbar of H₂ at RT, and heating to 300 °C at a rate of 1 °C/min on H₂-pretreated Ru/Al₂O₃ and Al₂O₃ in DRIFTS, as in our previous work.¹⁴

3.3 Results and Discussions

Ex-situ-HCOO^{-*} and CO₂ hydrogenations were used as reaction models for showing the complex spectra and how the BEGF program resolves the peak positions and variations. Formate is one of the intermediates of CO₂ hydrogenation. For this reason, we first analyzed the spectra of HCOOH hydrogenation to understand the reactivities of ex situ formate (ex-situ-HCOO^{-*}) in H₂ thermal reduction, and then turned to the analysis of CO₂ hydrogenation.

3.3.1 BEGF analysis of spectra of ex-situ-HCOO^{-*} hydrogenation

3.3.1.1 Convergence of fitting

The error evolution approaching convergence as a function of time and iteration numbers is illustrated in Figure 3.2 (a) for the fitting in the range of 1800–1500 cm⁻¹ from 20 to 220 °C, noting that above 220 °C the peaks and the baseline in this range changed significantly. Re-confining the range of the spectra above 220 °C for the new baseline correction is not necessary, but is helpful in shortening the entire fitting time. We compared the fitting with coarse initial values from wide bounds, and with fine initial values from reading of the spectra. Around 4 h were taken for the coarse initial

values to reach convergence, with around 4000 iterations, and around 1 h for the convergence of fine initial values, with around 3000 iterations. The average time of iteration in Figure 3.2 (b) decreased during evolution because the improved guesses (i.e., I , L , and U) in the iteration reduced the time for each run of lower-level Gaussian fitting. Especially, with fine bounds of I , L and U (blue line) the average time of iteration was shorter in the beginning due to the better solutions from the good bounds, which was beneficial in generating even better initial values for the next iteration. After enough iterations, the competitiveness of the preserved solutions for both blue and red lines became similar, as shown by the similarly converging average time after around 4000 iterations in the Figure 3.2 (b).

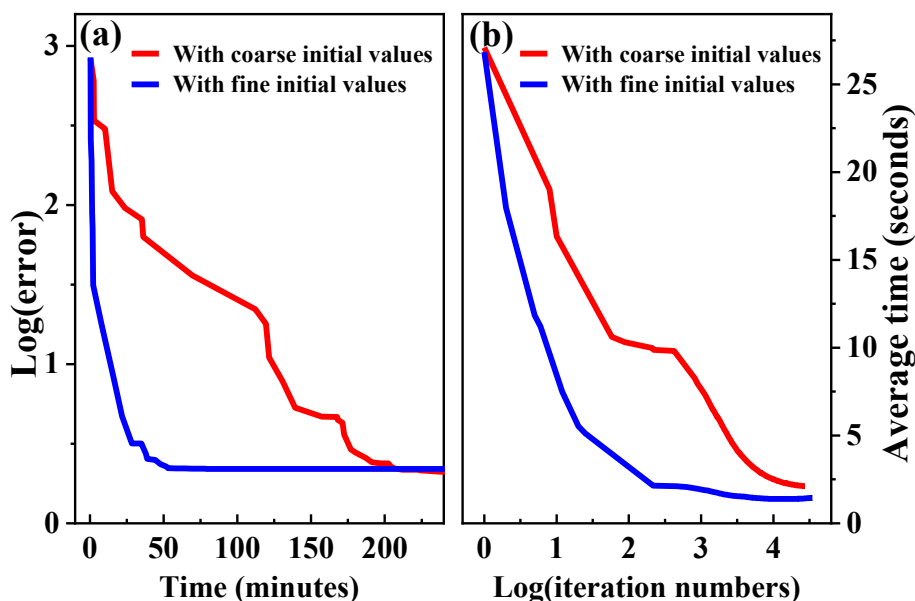


Figure 3.2. (a) The error evolution approaching convergence as a function of time and (b) the average time of iteration for the fitting in the range of 1800–1500 cm^{-1} from 20–220 $^{\circ}\text{C}$ by BEGF.

3.3.1.2 Assignment of adsorption species based on the kinetic results

The fitted spectra at 100, 150, 200, and 250 $^{\circ}\text{C}$ are shown in Figure 3.3 (a). Although the peaks are discernible, the evolution of the peak intensities along the reaction is not easily understandable by a first sight of the spectra. We then used the BEGF program to produce the integrated intensities of each peak throughout the spectral set so that we obtained the evolution profile of each peak as a function of temperature. The intensity progression both facilitated the assignments of the peaks to specific species and revealed the reactivity of each species during the catalytic reaction.

Table 3. 1. Vibrational modes and infrared peak positions (cm^{-1}) of formate, bicarbonate and carbonate from CO_2 hydrogenation.

Species	C–H as. str.	C–H b.	C=O str.	O–C–O as. str.	O–C–O s. str.	O–H b.
HCOOH	2940 (cbn), 2871, 2760 (cbn)	1415, 1405	1748, 1670	1618; 1560	1405?, 1360	1220
HCOO [–] *-MSI	--	1405	1720	1618	1405?	1220
Br-HCOO [–] *-Ru	2896	1390	--	1592	1375	1220
Bi-HCOO [–] *-Al ₂ O ₃	--	1415	1710	1560	1360	1230
HCO ₃ [–] *	--	--	1690	1650	1440	1230
CO ₃ ^{2–} *	--	--	--	1500	1450	--

as. str.: asymmetric stretching; s. str: symmetric stretching; b.: bending; (cbn): combination modes; *: adsorbed state.

As shown in Figure 3.3 (b) and (c), O–C–O asymmetric stretching (1560 and 1618 cm^{-1} , the assignments refer to Section S3.1.1 in SI) decreased from $200\text{ }^{\circ}\text{C}$ until full reduction at $250\text{ }^{\circ}\text{C}$. The unassigned peaks at 1415 cm^{-1} and 1405 cm^{-1} showed the same trend as O–C–O asymmetric stretching. By comparing that the relative intensity of peak 1415 cm^{-1} to peak 1405 cm^{-1} had a much stronger intensity on Al_2O_3 than on $\text{Ru}/\text{Al}_2\text{O}_3$ (Figure 3 (b)–(c) and Figure S3.2 (a)–(c)), peak 1415 cm^{-1} was associated to the peak 1560 cm^{-1} , and 1405 cm^{-1} was associated to 1618 cm^{-1} . Since 1560 cm^{-1} had been paired with 1360 cm^{-1} as O–C–O asymmetric and symmetric stretching on Al_2O_3 , respectively (Section S3.1.2 in SI), 1415 cm^{-1} could be assigned to C–H bending to complete the vibration modes of this species. Thence, the peak at 1405 cm^{-1} could be either C–H bending or O–C–O symmetric stretching, associated with the peak at 1618 cm^{-1} . The remaining three peaks at 1592 , 1390 and 1375 cm^{-1} varied in the same trend (Figure 3.3 (d)). In view that 1592 cm^{-1} was in the region O–C–O

asymmetric stretching, and was absent on Al_2O_3 under all experimental conditions (Figure S3.1 and S3.2), we assigned this peak to O–C–O asymmetric stretching of formate on Ru sites. The other two peaks at 1390 and 1375 cm^{-1} were assigned as C–H bending and O–C–O symmetric stretching, respectively, of this structure of formate. These assignments are consistent with the reported values.^{1,7} The combinational vibration of C–H bending and O–C–O asymmetric stretching at 2912 cm^{-1} , which gradually red-shifted to 2896 cm^{-1} during the reaction, also varied similarly as 1592 cm^{-1} (Figure S3.3). Thus, the peak at 2896 cm^{-1} could be classified as C–H stretching and a companion of the peak at 1592 cm^{-1} .

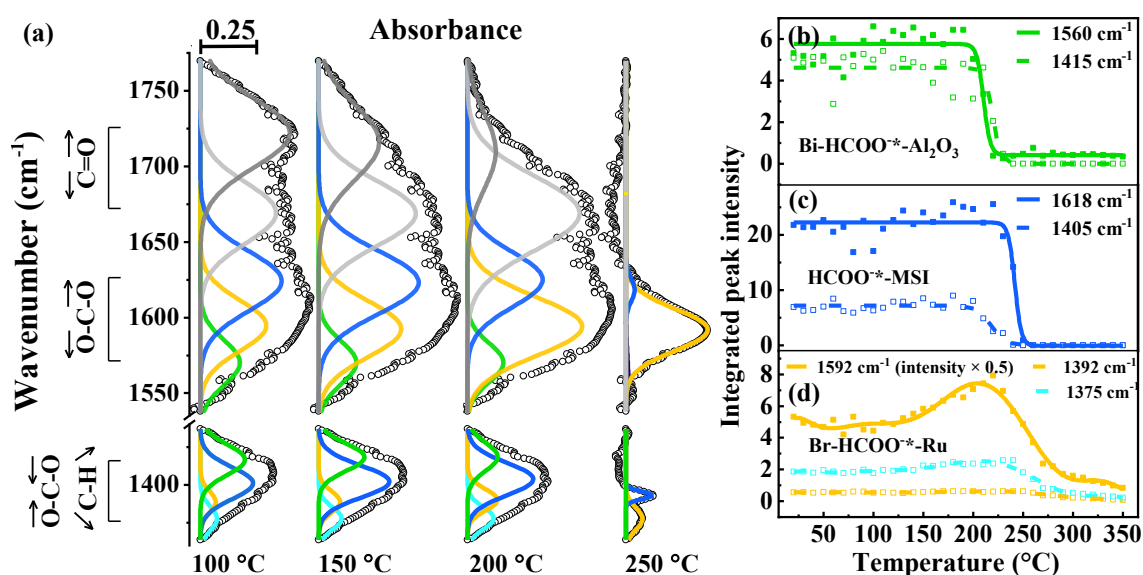


Figure 3.3 (a) The experimental spectra of ex-situ-HCOO* hydrogenation on Ru/ Al_2O_3 (black circles) with fitted peaks (colored lines) in the ranges of 1770–1538 and 1440–1360 cm^{-1} . The fitting result of the evolution of (b) Bi-HCOO*– Al_2O_3 , (c) HCOO*–MSI, (d) Br-HCOO*–Ru during the reaction of ex-situ-HCOO* hydrogenation.

The splitting value between the asymmetric and symmetric stretching ($\Delta\nu = \nu_{\text{as}} - \nu_{\text{s}}$) of O–C–O of HCOO* also indicates the orientations of the adsorption. For free and bridged formate, $\Delta\nu = 220$ –280 cm^{-1} . When $\Delta\nu$ is smaller than 220 cm^{-1} , formate is a bidentate structure; when $\Delta\nu$ is larger than 280 cm^{-1} , formate is a monodentate structure.¹⁵ Therefore, formate, with the O–C–O asymmetric stretching and symmetric stretching at 1592 and 1375 cm^{-1} , respectively, is in bridged orientation; formate with the O–C–O symmetric stretching at 1560 and 1360 cm^{-1} , respectively, is in bidentate orientation. As has been explained above, formates with main peaks at 1592 and 1560 cm^{-1} are on Ru and Al_2O_3 sites, respectively; these two formates are abbreviated as Br-HCOO*–Ru and Bi-HCOO*– Al_2O_3 , respectively. Formate with the main peak at 1618 cm^{-1} is located at the metal-support interface (MSI) because of its enhanced intensity on Ru/ Al_2O_3 compared to that on Al_2O_3 .

(Section S3.1.1 in SI), and is thus named $\text{HCOO}^{\text{-}*}$ -MSI. The related vibrational modes are listed in Table 3.1.

3.3.1.3 Reactivity of the adsorption species during ex-situ- $\text{HCOO}^{\text{-}*}$ hydrogenation

The reactive trends of each species were exposed at the same time of fitting as shown in Figure 3.3 (b)–(d)). Ex-situ- $\text{HCOO}^{\text{-}*}$ on $\text{Ru}/\text{Al}_2\text{O}_3$ was reduced by H_2 at 200 °C until being fully consumed at 250 °C. Along with the decrease of ex-situ- $\text{HCOO}^{\text{-}*}$, three species emerged (Figure S3.3 and S3.4). Those were adsorbed carbon monoxide (CO^*) on Ru, gaseous CO_2 , and CH_4 gas with peaks in the ranges 2100–1900, 2450–2250, and 3100–2900 cm^{-1} , respectively. Consequently, ex-situ- $\text{HCOO}^{\text{-}*}$ on $\text{Ru}/\text{Al}_2\text{O}_3$ was reduced by H_2 at 200 °C until being fully consumed at 250 °C. The products were adsorbed CO^* , gaseous CO_2 and gaseous CH_4 . CO^* came either from CO_2 reduction or from formate decomposition because CO^* increased at the same temperature as CO_2 formation and kept increasing until 230 °C, while both CO_2 and formate were reduced. CH_4 also came either from formate or from CO_2 hydrogenation because CH_4 increased from 220 to 250 °C, while both formate and CO_2 reduced between 200 and 250 °C. There was no evidence of conversion between CO^* and CH_4 , because the concentrations of both CO^* and CH_4 did not change above 270 °C.

In comparison, ex-situ- $\text{HCOO}^{\text{-}*}$ hydrogenation on Al_2O_3 produced noticeable gaseous CO above 200 °C which was represented by the occurrence of the rotational-vibrational peaks centered at 2142 cm^{-1} (Figure S3.2 (e)), and invariant adsorbed CO_2^* which was represented by $\text{O}=\text{C}=\text{O}$ symmetric stretching and resonance at 1387 and 1288 cm^{-1} , respectively (Figure S3.2 (f)).

3.3.2 BEGF analysis of spectra of CO_2 hydrogenation

3.3.2.1 Convergence of fitting

The information of the adsorption species during CO_2 hydrogenation on $\text{Ru}/\text{Al}_2\text{O}_3$ was mainly in the overlapped peaks below 2100 cm^{-1} , including $\text{HCO}_3^{\text{-}*}$, $\text{CO}_3^{2\text{-}*}$, $\text{HCOO}^{\text{-}*}$ and CO^* , as we presented in our previous work.¹⁴ The main contribution of this work is the methodology of decoupling the peaks and understanding their meaning via the BEGF program. The initial values of peak positions in BEGF were taken from the IR bands of the samples of carbonates and bicarbonates (Figure S3.5). Even though the initial values can also be used in regular multi-peak Gaussian fitting procedures, the pseudo-solutions from the local optima require the heavy manual work of repeatedly adjusting the initial values to reach consistent results, including the number of Gaussian peaks, peak positions and

the variations of the integrated intensity for the related experiments. With the BEGF program, the spectral set of CO₂ hydrogenation was resolved by global solution within one day (Figure S3.6), and the fitted results are consistent with the results of our previous publication, obtained by an inefficient Gaussian fitting.

3.3.2.2 Assignment of adsorption species based on the kinetic results

By comparing the trend of the integrated intensity of each peak along with the reaction coordinate (details in the following paragraphs), we found several groups of peaks in the wavenumber range of 1800–1480 cm⁻¹ (Figure 3.4) – group I: 1560 and 1360 cm⁻¹; group II: 1618 and 1405 cm⁻¹; group III: 2895, 1592, 1390 and 1375 cm⁻¹; group IV: 1650, 1440 and 1230 cm⁻¹; and group V: 1500 and 1460 cm⁻¹. Based on the assignment of formate from Section 3.3.1 (see also Table 3.1), groups I to III belonged to Br-HCOO^{-*}-Ru, HCOO^{-*}-MSI, and Bi-HCOO^{-*}-Al₂O₃, respectively. Referring to the measured peaks from the reference samples (Figure S3.5), groups IV and V belonged to adsorbed bicarbonate (HCO₃^{-*}) and adsorbed carbonate (CO₃^{2-*}), respectively. The splitting value of the O–C–O asymmetric (ν_{as}) and symmetric (ν_s) stretching bands of CO₃^{2-*} corresponds to different adsorption orientations. A splitting value ($\Delta\nu = \nu_{as} - \nu_s$) less than 100 cm⁻¹ relates to a monodentate structure, $\Delta\nu$ larger than 200 cm⁻¹ relates to a bidentate structure, and $\Delta\nu$ larger than 300 cm⁻¹ relates to a bridged structure.⁸ Since $\Delta\nu$ was far less than 100 cm⁻¹ in our case, CO₃^{2-*} must be adsorbed on the surface with a monodentate structure. Its precursor HCO₃^{-*}, which has a similar molecular structure, could also be monodentate.

In the wavenumber range of 2100–1800 cm⁻¹, five adsorption structures of CO* were deconvoluted with peaks at 2035, 2015, 1990, 1950 and 1905 cm⁻¹. The high frequency at 2035 cm⁻¹ was assigned to linear-CO* on Ru⁰; the peak at 2015 cm⁻¹ was assigned to linear-CO* on isolated Ru⁰ surrounded by partially oxidized Ru^{δ+}; the low frequencies at 1990, 1950 and 1905 cm⁻¹ corresponded to bridged-CO*.^{7,12,17}

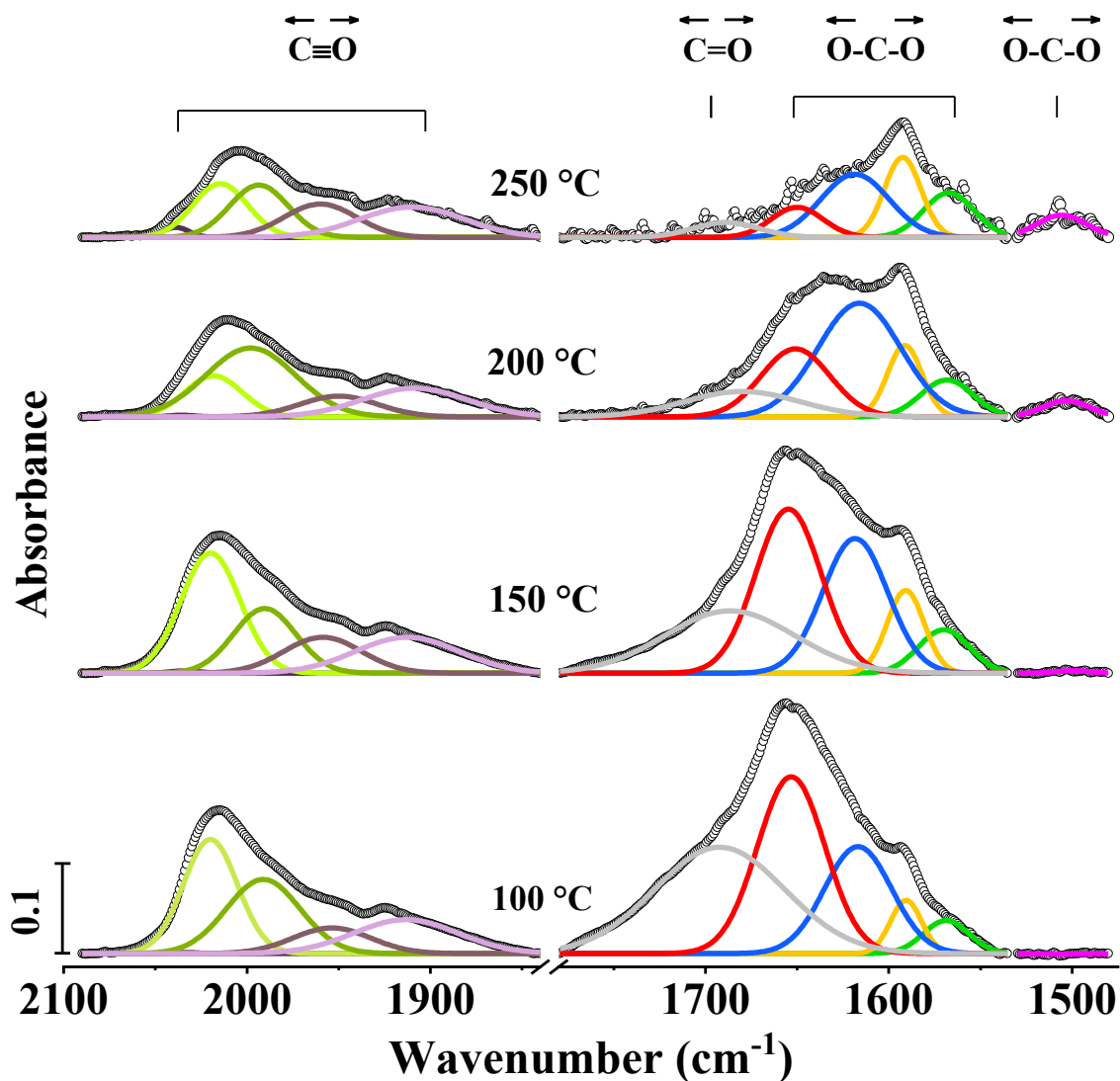


Figure 3.4. The spectra of CO₂ hydrogenation on Ru/Al₂O₃ (black circles) with fitted Gaussian peaks (colored lines) in the ranges 2100–1840, 1780–1535 and 1530–1480 cm⁻¹. The vibrations in the range of 2100–1840 cm⁻¹ are C≡O asymmetric stretching, and in 1780–1535 cm⁻¹ are O-C-O asymmetric stretching of Bi-HCOO⁻-Al₂O₃ (green peak), HCOO⁻-MSI (blue peak), Br-HCOO⁻-Ru (yellow peak), HCO₃⁻ (red peak), and CO₃²⁻ (magenta).

Isotope spectra

To assist the peak assignment, especially to separate the strongly overlapped frequencies of O-C-O symmetric stretching and C-H bending modes, we have done the isotopic experiments with ¹³CO₂ at the same conditions as CO₂ hydrogenation. As shown in Figure 3.5 (a) and (b), there are certain shifts to the low frequency of the assigned peaks comparing to the rich carbon species, including C-H stretching of CH₄ shifted from 3016 to 3007 cm⁻¹, C-H bending of CH₄ shifted from 1306 to 1297

cm^{-1} , the center of $\text{O}=\text{C}=\text{O}$ asymmetric stretching of CO_2 shifted from 2350 to 2283 cm^{-1} . The rest of the peak positions of the adsorption species were listed in Table 3.2. ^{13}C spectra facilitated to confirm the strong peaks of asymmetric stretching modes. However, it did not help the separation of O-C-O symmetric stretching and C-H bending modes. This could be understood that ^{13}C shifted the O-C-O symmetric stretching and C-H bending modes simultaneously as they both contain carbon bond. Moreover, the signal/noise ratio did not improve as the intensity of infrared absorbance decreased due to the heavier mass.

Instead of using ^{13}C , we considered that D_2 could be more helpful to separate O-C-O and C-H vibrations. Because C-H would be changed to C-D, so that the vibrational frequency could be moved away from O-C-O vibrational frequency in the infrared spectra. Therefore, we did CO_2 deuteration by mixing 200 mbar CO_2 and 800 mbar pure D_2 using the same conditions and procedures. Unfortunately, the peak intensities were weakened more significantly in the low frequency region ($<1500 \text{ cm}^{-1}$) (Figure 3.5 (c) and (d)). Except the obvious peaks from $\text{CD}_x\text{H}_{4-x}$ ($x=2,3,4$),¹⁶ only slight shifts of the strong peaks of the adsorption species were observed (Table 3.3).

Moreover, the reaction kinetics of these two isotopic experiments did not fully match the CO_2 hydrogenation results. For instance, the onset and ending temperatures of methane production are higher and lower, respectively, compared to those in CO_2 hydrogenation experiment; the peak intensities were plausibly monotonically increasing/decreasing, nevertheless in fact occurring complicated shifts at high temperature ($> 150 \text{ }^\circ\text{C}$). The similar phenomena showed in the spectra of $^{13}\text{CO}_2$ hydrogenation in DRIFTS in reference 1. An investigation of the isotopic effect and comprehensive analysis of the kinetics from these isotopic data await future work to qualify the conclusions.

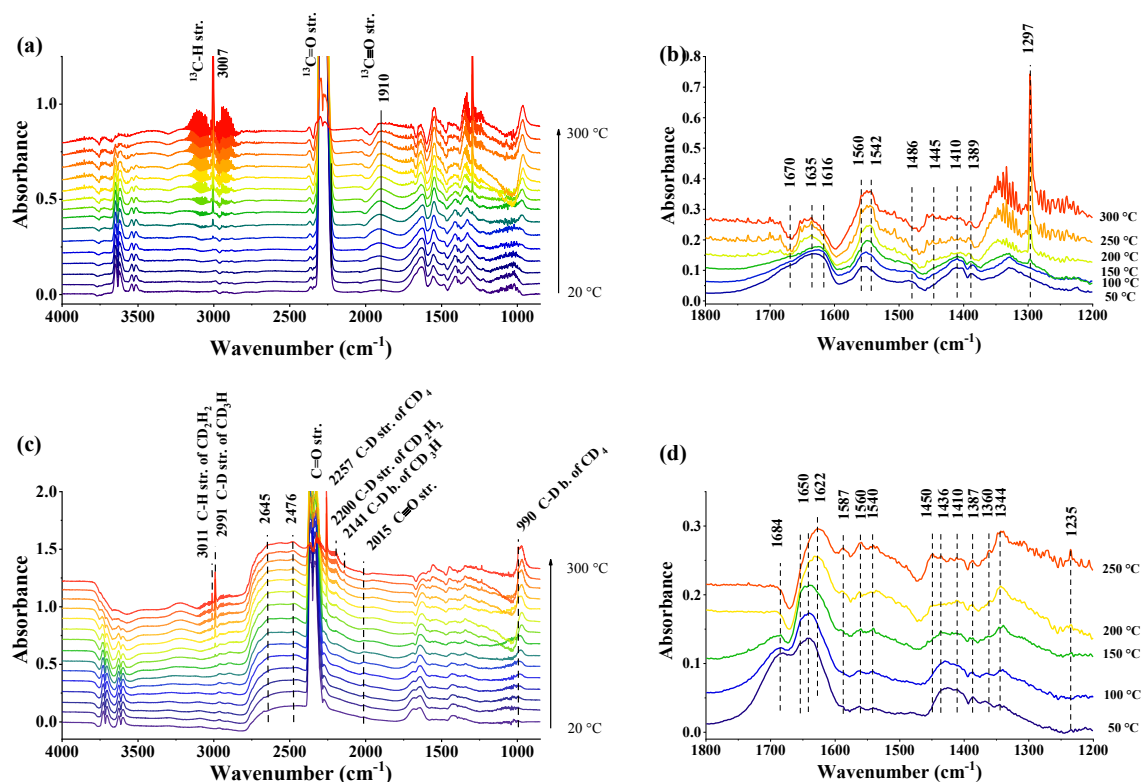


Figure 3.5. The full infrared spectra of (a) $^{13}\text{CO}_2$ hydrogenation by mixing 200 mbar $^{13}\text{CO}_2$ and 800 mbar H_2 , after which heated from 20 to 300 $^\circ\text{C}$ by 1 $^\circ\text{C}/\text{min}$, (c) $^{12}\text{CO}_2$ deuteration in pure D_2 by mixing 200 mbar $^{12}\text{CO}_2$ and 800 mbar D_2 , after which heated from 20 to 300 $^\circ\text{C}$ by 1 $^\circ\text{C}/\text{min}$. The extracted spectra in the wavenumber range between 1800 to 1200 cm^{-1} from (b) $^{13}\text{CO}_2$ hydrogenation and (d) $^{12}\text{CO}_2$ deuteration.

Table 3.2. Vibrational modes and infrared peak positions (cm^{-1}) of ^{13}C -formate, -bicarbonate and -carbonate from $^{13}\text{CO}_2$ hydrogenation.

Species	$^{13}\text{C}=\text{O}$ str.	$\text{O}-^{13}\text{C}-\text{O}$ as. str.	$\text{O}-^{13}\text{C}-\text{O}$ s. str.	$\text{O}-\text{H}$ b.
$\text{H}^{13}\text{COO}^*-\text{MSI}$	1700	1616	--	1220
$\text{Br}-\text{H}^{13}\text{COO}^*-\text{Ru}$		1575	--	--
$\text{Bi}-\text{H}^{13}\text{COO}^*-\text{Al}_2\text{O}_3$	--	--	--	--
$\text{H}^{13}\text{CO}_3^*-\text{}$	1670	1635	--	1230

Table 3.3. Vibrational modes and infrared peak positions (cm^{-1}) of D-formate, -bicarbonate and -carbonate from CO_2 hydrogenation in pure D_2 .

Species	C=O str.	O–C–O as. str.	O–C–O s. str.	O–D b.
$\text{DCOO}^{\text{-}*}\text{-MSI}$	1705	1622	1410	--
$\text{Br-DCOO}^{\text{-}*}\text{-Ru}$	--	1587	--	--
$\text{Bi-DCOO}^{\text{-}*}\text{-Al}_2\text{O}_3$	--	1560	--	--
$\text{DCO}_3^{\text{-}*}$	1684	1659	1436	1230
$\text{CO}_3^{2\text{-}*}$	--	1500	1450	--

Note: not labeled carbon is regular ^{12}C .

3.3.2.3 Reactivities of adsorption species during CO_2 hydrogenation

In-situ- $\text{HCOO}^{\text{-}*}$

To distinguish the formate from the ex-situ- $\text{HCOO}^{\text{-}*}$ in Section 3.3.1, we named the formate formed from CO_2 hydrogenation process as in-situ- $\text{HCOO}^{\text{-}*}$. $\text{Bi-HCOO}^{\text{-}*}\text{-Al}_2\text{O}_3$ increased very slightly during the whole reaction (Figure 3.6 (a)), indicating an inactive property. $\text{HCOO}^{\text{-}*}\text{-MSI}$ was abundant and stable up to 220 $^{\circ}\text{C}$, after which it was consumed until its disappearance at 300 $^{\circ}\text{C}$ (Figure 3.6 (b)), consistent with the result of the conversion equilibrium between $\text{HCOO}^{\text{-}*}\text{-MSI}$ and $\text{CO}_2^{\text{-}*}$ (Section S3.2.1 in SI). Conversely, $\text{Br-HCOO}^{\text{-}*}\text{-Ru}$ increased from 70 to 150 $^{\circ}\text{C}$, followed by a slow decrease (Figure 3.6 (c)), implying multiple kinetic steps.

These in-situ- $\text{HCOO}^{\text{-}*}$ species exhibited different reactivities from ex-situ- $\text{HCOO}^{\text{-}*}$ species in the hydrogenation reaction. For in-situ- $\text{HCOO}^{\text{-}*}$, $\text{Bi-HCOO}^{\text{-}*}\text{-Al}_2\text{O}_3$ was inert; $\text{HCOO}^{\text{-}*}\text{-MSI}$ was the most reactive towards reduction; and $\text{Br-HCOO}^{\text{-}*}\text{-Ru}$ formed during the reaction until 150 $^{\circ}\text{C}$ and was then consumed. For ex-situ- $\text{HCOO}^{\text{-}*}$, $\text{Bi-HCOO}^{\text{-}*}\text{-Al}_2\text{O}_3$ and $\text{HCOO}^{\text{-}*}\text{-MSI}$ were the most reactive towards reduction; $\text{Br-HCOO}^{\text{-}*}\text{-Ru}$ increased between 100 and 220 $^{\circ}\text{C}$, followed by a decrease.

Therefore, the ex-situ-HCOO⁻* assists in the peak assignments for in-situ-HCOO⁻* but not in the prediction of the reactivities of the species.

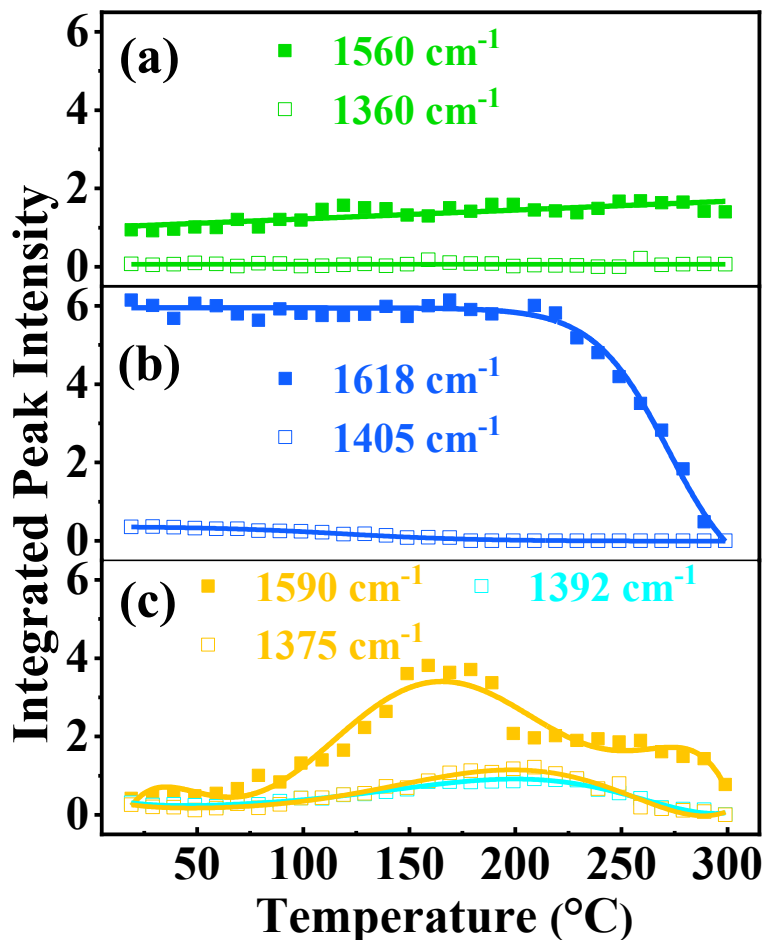


Figure 3.6. The fitting result of the evolution of (a) Bi-HCOO⁻*-Al₂O₃, (b) HCOO⁻*-MSI, (c) Br-HCOO⁻*-Ru during the CO₂ hydrogenation.

HCO₃⁻* and CO₃²⁻*

HCO₃⁻* on Ru/Al₂O₃ decreased slowly below 130 °C, then accelerated until complete consumption at 300 °C (Figure 3.7 (a)). In comparison, HCO₃⁻* on Al₂O₃ was reduced at 100 °C and fully converted at 160 °C (Figure S7 (a) and (b)). This illustrated that HCO₃⁻* was formed continuously on Ru/Al₂O₃ from CO₂ until the CO₂ concentration dropped, but could not be continuously formed on Al₂O₃. In addition, the peak intensity of HCO₃⁻* was much stronger on Ru/Al₂O₃ than on Al₂O₃. These implied that HCO₃⁻* on Ru/Al₂O₃ was formed at the MSI. HCO₃⁻* reduction showed a relation with CO₃²⁻* formation above 200 °C (Figure 3.7 (b)), indicating a deprotonation process.

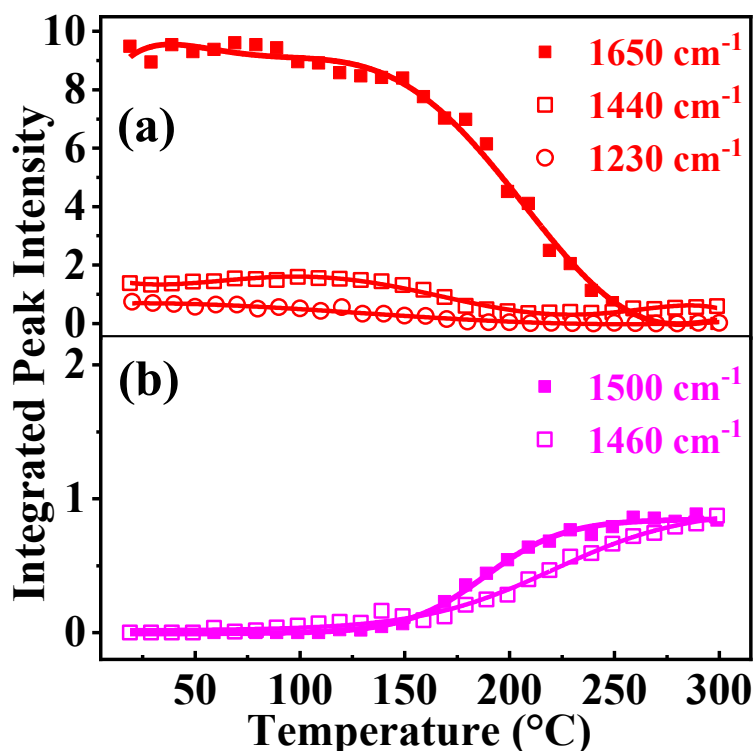


Figure 3.7. The fitting result of the evolution of (a) HCO₃* and (b) CO₃²⁻ during CO₂ hydrogenation.

CO*

Five CO* on Ru/Al₂O₃ showed distinct reactivities. The linear-CO* on Ru⁰ was of negligible intensity and invariable, while the linear-CO* on isolated Ru⁰ showed an accumulation till 150 °C and a consumption afterwards (Figure 3.8 (a)). The bridged-CO* exhibited an increase until 100 °C, followed by a decrease up to the reach of an equilibrium level at 200 °C (Figure 3.8 (b)). These plots suggested that linear-CO* on Ru⁰ was inactive in CO₂ hydrogenation reaction. The other four forms of CO* participate in the reaction, yet carrying distinct reactivities. It has been reported that the different peak position of CO* is the result of changed coverage of CO*.^{9,17} The peak red-shifted when CO* coverage increased. This happened by supplying low-pressure CO gas to single crystalline metal surfaces at a certain low temperature.¹⁸ However, in our reaction conditions, the broad CO* peak showed the evolution of subpeaks related to the kinetics of each adsorption structure of CO* during the reaction. Among those structures of CO*, linear-CO* on isolated Ru⁰, surrounded by partially oxidized Ru^{δ+}, showed a longer accumulation and a faster reduction, indicating a higher reactivity than the other structures of CO*.

On the other hand, CO* on Al₂O₃ generated one broad and weak peak between 2200 and 2100 cm⁻¹. This peak disappeared after pumping to a vacuum (Figure S3.10), in accordance with results reported for adsorbed CO* on metal oxides from CO gas.¹⁹ The weak adsorption and high frequency (> 2100 cm⁻¹) of CO* on Al₂O₃ confirmed that the strong adsorption and low frequency (< 2100 cm⁻¹) of CO* on Ru/Al₂O₃ were adsorbed on Ru sites.

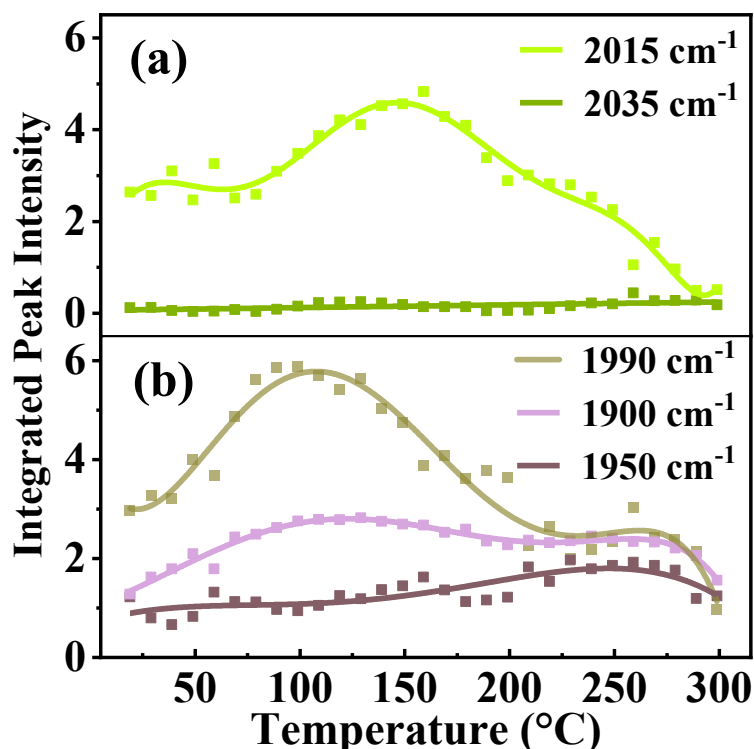


Figure 3.8. The fitting result of the evolution of (a) linear-CO* and (b) bridged-CO* during the reaction.

3.4 Conclusions

We resolved comprehensively the strongly overlapped and controversial IR peaks of CO₂ hydrogenation reaction in DRIFTS by a bilevel evolutionary Gaussian fitting procedure. This procedure allowed the robust and automatic identification of the peaks and their evolution along the reaction coordinate with no need for manual intervention. This method helped to attribute the peaks to the right species, and gave the kinetic curves of those species directly. The isotopes ¹³C and D were used to assist the assignment of the infrared peaks. From the analysis of ex-situ-HCOO* and CO₂ hydrogenation on Ru/Al₂O₃ and on Al₂O₃ surfaces, those kinetic curves of the resolved species revealed straightforwardly their reactivities during the reactions. In-situ-HCOO* formed from CO₂ hydrogenation was assigned thanks to the peak analysis of ex-situ-HCOO*, even though the reactivities

of each adsorption structure being distinct from those of ex-situ-HCOO⁻*. During CO₂ hydrogenation, in-situ-HCOO⁻* adsorbed on the metal–support interface exhibited a high reactivity, similar to CO₂ conversion; in-situ-HCOO⁻* adsorbed on Ru showed less reactivity, and in-situ-HCOO⁻* adsorbed on Al₂O₃ was inactive. Bicarbonate also showed high reactivity, similar to CO₂ conversion. CO* showed distinctive properties during CO₂ hydrogenation, in that it was formed until the middle of the reaction and reduced afterwards. These results from BEGF analysis are identical to our previous work by manual iteration of Gaussian fitting. This BEGF method is not only suitable for IR spectra, but is universal for the deconvolution of overlapping spectra.

AUTHOR INFORMATION

† The authors contributed equally to this work

Corresponding Author

*marco.calizzi@epfl.ch

*kun.zhao@epfl.ch

ORCID

Kun Zhao: 0000-0002-7182-8089

Marco Calizzi: 0000-0001-5319-2657

Notes

The authors declare no competing financial interests.

ACKNOWLEDGMENTS

SCCER HeE, which is financially supported by Innosuisse, the Swiss Innovation Agency, is gratefully acknowledged. K.Z also gratefully thanks Daniel Auerbach for the full discussions and revisions of this work.

ASSOCIATED CONTENT

The Supporting Information contains:

- All the figures mentioned in the main text, including HCOOH adsorption and hydrogenation on Al₂O₃, FT-IR transmittance of Na₂CO₃, CaCO₃, KHCO₃ and NaHCO₃, CO₂ adsorption and hydrogenation on Al₂O₃.
- The BEGF program.

This material is available free of charge via the Internet at <http://pubs.acs.org>.

References

- (1) Wang, F.; He, S.; Chen, H.; Wang, B.; Zheng, L.; Wei, M.; Evans, D. G.; Duan, X. Active Site Dependent Reaction Mechanism over Ru/CeO₂ Catalyst toward CO₂ Methanation. *J. Am. Chem. Soc.* **2016**, *138*, 6298–6305.
- (2) Sapi, A.; Halasi, G.; Kiss, J.; Dobo, D. G.; Juhasz, K. L.; Kolcsar, V. J.; Ferencz, Z.; Vari, G.; Matolin, V.; Erdohelyi, A.; et al. In Situ DRIFTS and NAP-XPS Exploration of the Complexity of CO₂ Hydrogenation over Size-Controlled Pt Nanoparticles Supported on Mesoporous NiO. *J. Phys. Chem. C* **2018**, *122*, 5553–5565.
- (3) Martin, N. M.; Hemmingsson, F.; Wang, X.; Merte, L. R.; Hejral, U.; Gustafson, J.; Skoglundh, M.; Meira, D. M.; Dippel, A.-C.; Gutowski, O.; et al. Structure–Function Relationship during CO₂ Methanation over Rh/Al₂O₃ and Rh/SiO₂ Catalysts under Atmospheric Pressure Conditions. *Catal. Sci. Technol.* **2018**, *8*, 2686–2696.
- (4) Xu, M.; Yao, S.; Rao, D.; Niu, Y.; Liu, N.; Peng, M.; Zhai, P.; Man, Y.; Zheng, L.; Wang, B.; et al. Insights into Interfacial Synergistic Catalysis over Ni@TiO₂-x Catalyst toward Water–Gas Shift Reaction. *J. Am. Chem. Soc.* **2018**, *140*, 11241–11251.
- (5) Zhang, S. R.; Tang, Y.; Nguyen, L.; Zhao, Y. F.; Wu, Z.; Goh, T. W.; Liu, J. J. Y.; Li, Y. Y.; Zhu, T.; Huang, W. Y.; et al. Catalysis on Singly Dispersed Rh Atoms Anchored on An Inert Support. *ACS Catal.*, **2018**, *8*, 110–121.
- (6) Newton, M. A.; Ferri, D.; Smolentsev, G.; Marchionni, V.; Nachttegaal, M. Kinetic Studies of the Pt Carbonate-Mediated, Room-Temperature Oxidation of Carbon Monoxide by Oxygen over Pt/Al₂O₃ Using Combined, Time-Resolved XAFS, DRIFTS, and Mass Spectrometry. *J. Am. Chem. Soc.* **2016**, *138*, 13930–13940.
- (7) Szanyi, J.; Kwak, J. H. Dissecting the Steps of CO₂ Reduction: 2. The Interaction of CO and CO₂ with Pd/γ-Al₂O₃: an In Situ FTIR Study. *Phys. Chem. Chem. Phys.* **2014**, *16*, 15126–15138.
- (8) Taifan, W.; Boily, J.-F.; Baltrusaitis, J. Surface Chemistry of Carbon Dioxide Revisited. *Surf. Sci. Rep.* **2016**, *71*, 595–671.
- (9) Marwood, M.; Doepper, R.; Renken, A. In-situ Surface and Gas Phase Analysis for Kinetic Studies under Transient Conditions the Catalytic Hydrogenation of CO₂. *Appl. Catal. A Gen.* **1997**, *151*, 223–246.
- (10) Zheng, J.; Wang, C.; Chu, W.; Zhou, Y.; Kohler, K. CO₂ Methanation over Supported Ru/Al₂O₃ Catalysts: Mechanistic Studies by In Situ Infrared Spectroscopy. *ChemistrySelect* **2016**, *1*, 3197–3203.
- (11) Miao, B.; Ma, S. S. K.; Wang, X.; Su, H.; Chan, S. H. Catalysis Mechanisms of CO₂ and CO Methanation. *Catal. Sci. Technol.* **2016**, *6*, 4048–4058.
- (12) Chin, S. Y.; Williams, C. T.; Amiridis, M. D. FTIR Studies of CO Adsorption on Al₂O₃- and SiO₂-Supported Ru Catalysts. *J. Phys. Chem. B* **2006**, *110*, 871–882.
- (13) Deb, K. An Introduction to Genetic Algorithms. *Sadhana* **1999**, *24*, 293–315.
- (14) Zhao, K.; Wang, L.; Calizzi, M.; Moiola, E.; Zuttel, A. In Situ Control of the Adsorption Species in CO₂ Hydrogenation: Determination of Intermediates and Byproducts. *J. Phys. Chem. C* **2018**, *112*, 20888–20893.

-
- (15) Shido, T.; Asakura, K.; Iwasawa, Y. Reactant-Promoted Reaction Mechanism for Catalytic Water-Gas Shift Reaction on MgO. *J. Catal.* **1990**, *122*, 55–67.
- (16) Wilmshurst, J. K.; Bernstein, H. J. The Infrared Spectra of CH₄, CH₃D, CH₂D₂, CD₃H, and CD₄. *Can. J. Chem.* **1957**, *35*, 226–235.
- (17) Garbarino, G.; Bellotti, D.; Finocchio, E.; Magistri, L.; Busca, G. Methanation of Carbon Dioxide on Ru/Al₂O₃: Catalytic Activity and Infrared Study. *Catal. Today* **2016**, *277*, 21–28.
- (18) Hoffmann, F. M. Infrared Reflection-Absorption Spectroscopy of Adsorbed Molecules. *Surf. Sci. Rep.* **1983**, *3*, 107–192.
- (19) Hadjiivanov, K. I.; Vayssilov, G. N. Characterization of Oxide Surfaces and Zeolites by Carbon Monoxide as an IR Probe Molecule. *Adv. Catal.* **2002**, *47*, 307–511.

Supporting Information

Identifying Reaction Species by Evolutionary Fitting and Kinetic Analysis: an Example of CO₂ Hydrogenation in DRIFTS

Kun Zhao^{a,b,†*}, Ligang Wang^{c,d,†}, Emanuele Moioli^{a,b}, Marco Calizzi^{a,b*}, Andreas Züttel^{a,b}

^aLaboratory of Materials for Renewable Energy, Institute of Chemical Sciences and Engineering, École Polytechnique Fédérale de Lausanne (EPFL), 1951 Sion, Switzerland

^bSwiss Federal Laboratories for Materials Science and Technology (EMPA), 8600 Dübendorf, Switzerland

^cGroup of Energy Materials, Institute of Mechanical Engineering, École Polytechnique Fédérale de Lausanne (EPFL), 1951 Sion, Switzerland

^dIndustrial Process and Energy Systems Engineering, Institute of Mechanical Engineering, École Polytechnique Fédérale de Lausanne (EPFL), 1951 Sion, Switzerland

Table of Contents:

Sections:

S3.1 HCOOH on Al₂O₃ and on Ru/Al₂O₃

S3.1.1 HCOOH adsorption on Al₂O₃ and on Ru/Al₂O₃

S3.1.2 Evolution of adsorption state during ex-situ-HCOO^{-*} hydrogenation on Al₂O₃

S3.1.3 Evolution of adsorption state during ex-situ-HCOO^{-*} hydrogenation on Ru/Al₂O₃

S3.2 Other supplementary figures

S3.3 Global optimization by evolutionary algorithms

Figures:

Figure S3.1 HCOOH adsorption on Ru/Al₂O₃ and on Al₂O₃

Figure S3.2 Ex-situ-HCOO^{-*} hydrogenation on Al₂O₃

Figure S3.3 Ex-situ-HCOO^{-*} hydrogenation on Ru/Al₂O₃

Figure S3.4 Evolution of the productions from ex-situ-HCOO^{-*} hydrogenation on Ru/Al₂O₃

Figure S3.5 FT-IR transmittance of Na_2CO_3 , CaCO_3 , KHCO_3 and NaHCO_3

Figure S3.6 Fitting time of CO_2 hydrogenation on Al_2O_3

Figure S3.7 Evolution of adsorption species from CO_2 hydrogenation on Al_2O_3

Figure S3.8 CO_2 adsorption and its co-adsorption with H_2 on Al_2O_3

Figure S3.9 Flowchart of an evolutionary algorithm

S3.1 HCOOH on Ru/Al₂O₃ and Al₂O₃ surfaces

S3.1.1 HCOOH adsorption on Ru/Al₂O₃ and Al₂O₃ surfaces

HCOOH on Ru/Al₂O₃ and Al₂O₃ surfaces at room temperature (RT) shows the strongest absorbance at 1748 cm⁻¹, assigned to C=O asymmetric stretching (Figure S3.1). The relatively weak peak observed at 1670 cm⁻¹ is assigned to C=O symmetric stretching.¹⁻²³ The peaks between 1670 and 1450 cm⁻¹ are not obvious. The peaks at 1420–1380 cm⁻¹ are a mixture of O–C–O symmetric stretching and C–H bending, needing to be identified by the variation trend of integrated intensity in the main text in Section 3.3.1.2. The peaks at 1360 and 1220 cm⁻¹ are assigned to O–C–O symmetric stretching and O–H bending of adsorbed formate (HCOO^{-*}), respectively.^{4,5} The peak at 2940 cm⁻¹ is a combination of O–C–O asymmetric stretching and C–H bending, and the peak at 2870 cm⁻¹ is C–H asymmetric stretching.^{5,6}

After evacuating the superfluous HCOOH, we called the adsorbed formate ex-situ-HCOO^{-*}, to distinguish it from the in-situ-HCOO^{-*} produced during CO₂ hydrogenation described in the main text, Section 3.3.2. The peak of C=O asymmetric stretching red-shifted from 1748 cm⁻¹ to 1720 and 1710 cm⁻¹ on Ru/Al₂O₃ and Al₂O₃ surfaces, respectively. The combinational vibration of O–C–O

¹ Chang, Y. T.; Yamaguchi, Y.; Miller, W. H.; Schaefer, H. F. An Analysis of the Infrared and Raman Spectra of the Formic Acid Dimer (HCOOH)₂. *J. Am. Chem. Soc.* **1987**, *109*, 7245–7253.

² Pettersson, M.; Lundell, J.; Khriachtchev, L.; Räsänen M. IR Spectrum of the Other Rotamer of Formic Acid, cis-HCOOH. *J. Am. Chem. Soc.* **1997**, *119*, 11715–11716.

³ Reva, I. D.; Plokhotnichenko, A. M.; Radchenko, E. D.; Sheina, G. G.; Blagoi, Y. P. The IR Spectrum of Formic Acid in an Argon Matrix. *Spectrochim. Acta Part A: Mol. Spectrosc.* **1994**, *50*, 1107–1111.

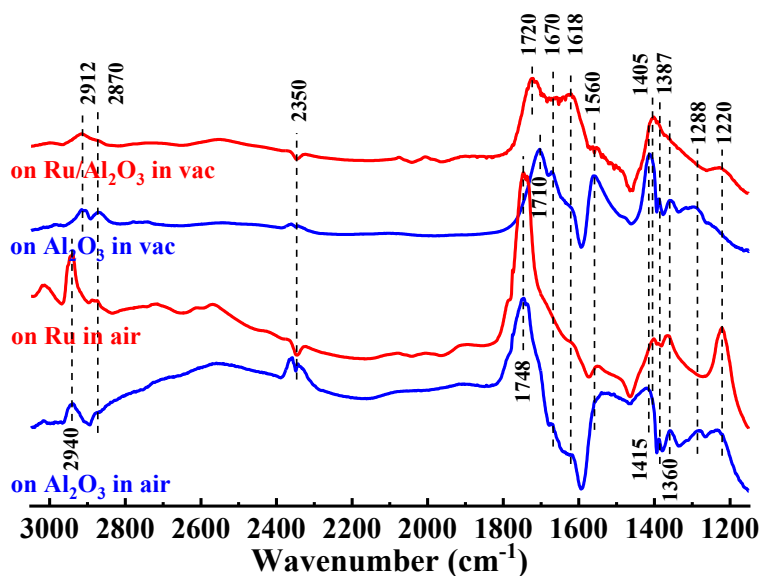
⁴ Taifan, W.; Boily, J.-F.; Baltrusaitis, J. Surface Chemistry of Carbon Dioxide Revisited. *Surf. Sci. Rep.* **2016**, *71*, 595–671.

⁵ Busca, G.; Lamotte, J.; Lavalley, J. C.; Lorenzelli, V. FT-IR Study of the Adsorption and Transformation of Formaldehyde on Oxide Surfaces. *J. Am. Chem. Soc.* **1987**, *109*, 5197–5202.

⁶ Roiaz, M.; Monachino, E.; Dri, C.; Greiner, M.; Knop-Gericke, A.; Schlögl, R.; Comelli, G.; Vesselli, E. Reverse Water–Gas Shift or Sabatier Methanation on Ni(110)? Stable Surface Species at Near-Ambient Pressure. *J. Am. Chem. Soc.* **2016**, *138*, 4146–4154.

asymmetric stretching and C–H bending also red-shifted from 2940 to 2912 cm^{-1} on both surfaces. The O–H bending peak weakened on both surfaces.

One of the most interesting observations following evacuation is the protrusion of peaks at 1618 and 1560 cm^{-1} , assigned to O–C–O asymmetric stretching of formate.^{5–7} The ratio of peak intensity of the 1618 and 1560 cm^{-1} peaks on Ru/ Al_2O_3 was apparently much larger than that on Al_2O_3 . Therefore, the peak at 1560 cm^{-1} is ascribed to formate on the support Al_2O_3 , and the peak at 1618 cm^{-1} is ascribed to formate on Ru or the metal-support interface (MSI) of Ru/ Al_2O_3 . Another distinctive difference between the HCOOH adsorption on Ru/ Al_2O_3 and Al_2O_3 surfaces is the feature of CO_2 : on Al_2O_3 , the peak centered at 2350 cm^{-1} is typically CO_2 asymmetric stretching, accompanied by the weak symmetric stretching and fermi resonance at 1387 and 1288 cm^{-1} , respectively; whereas on Ru/ Al_2O_3 , CO_2 peaks are absent. This indicates that some formate on Al_2O_3 decomposed to CO_2 at RT. Combined with the phenomenon of weakened intensity of O–C–O asymmetric stretching at 1618 cm^{-1} from Ru/ Al_2O_3 to Al_2O_3 , we conjecture that this O–C–O asymmetric stretching is in equilibrium between formate and CO_2 at MSI ($\text{HCOO}^{-*} \rightleftharpoons \text{CO}_2^{-*} + \text{H}^* \rightleftharpoons \text{CO}_2 + \text{H}^*$). When attached to Al_2O_3 sites, this formate decomposes to CO_2 ; when attached to Ru sites, it retains its integrity.



⁷ Marwood, M.; Doepper, R.; Renken, A. In-Situ Surface and Gas Phase Analysis for Kinetic Studies under Transient Conditions the Catalytic Hydrogenation of CO_2 . *Appl. Catal. A Gen.* **1997**, *151*, 223-246.

Figure S3.1. Infrared spectra of HCOOH adsorption on Ru/Al₂O₃ (red lines) and on Al₂O₃ (blue lines) in air and in vacuum by pumping to low vacuum of 5×10^{-3} mbar.

S3.1.2 Evolution of adsorption state during ex-situ-HCOO^{-*} hydrogenation on Al₂O₃

On Al₂O₃, the peak intensities of Br-HCOO^{-*}-Al₂O₃, with the main peak at 1560 cm⁻¹, decreased slowly with temperature (Figure S3.2 (b)). The peak intensities of Br-HCOO^{-*}-Al₂O₃, with the main peak at 1618 cm⁻¹, are weak, and do not vary obviously (Figure S3.2 (c)). The C=O asymmetric stretching at 1710 cm⁻¹ decreased the most obviously (Figure S3.2 (d)). The intensity of C–H stretching at 2870 cm⁻¹ increased below 250 °C followed by a decrease; the combinational vibration at 2912 cm⁻¹ red-shifted to 2895 cm⁻¹, with the intensity varying the same as the C–H stretching mode; the combination of O–C–O symmetric stretching and C–H bending showed up at 2760 cm⁻¹, also with the same intensity trend as the C–H stretching (Figure S3.2 (d)).

Gaseous CO formed at 200 °C (Figure S3.2 (e)), represented by the occurrence of the rotational-vibrational peaks centered at 2142 cm⁻¹. Adsorbed CO₂ maintained equilibrium in the whole process (Figure S3.2 (f)), represented by the unchanged peak intensity of O=C=O symmetric stretching and resonance at 1387 and 1288 cm⁻¹. The bond vibration of the CO₂ produced could be the reason for the increase in intensity of the combinational vibrations.

Therefore, HCOO^{-*} hydrogenation on Al₂O₃ produced only gaseous CO. No CH₄ was observed.

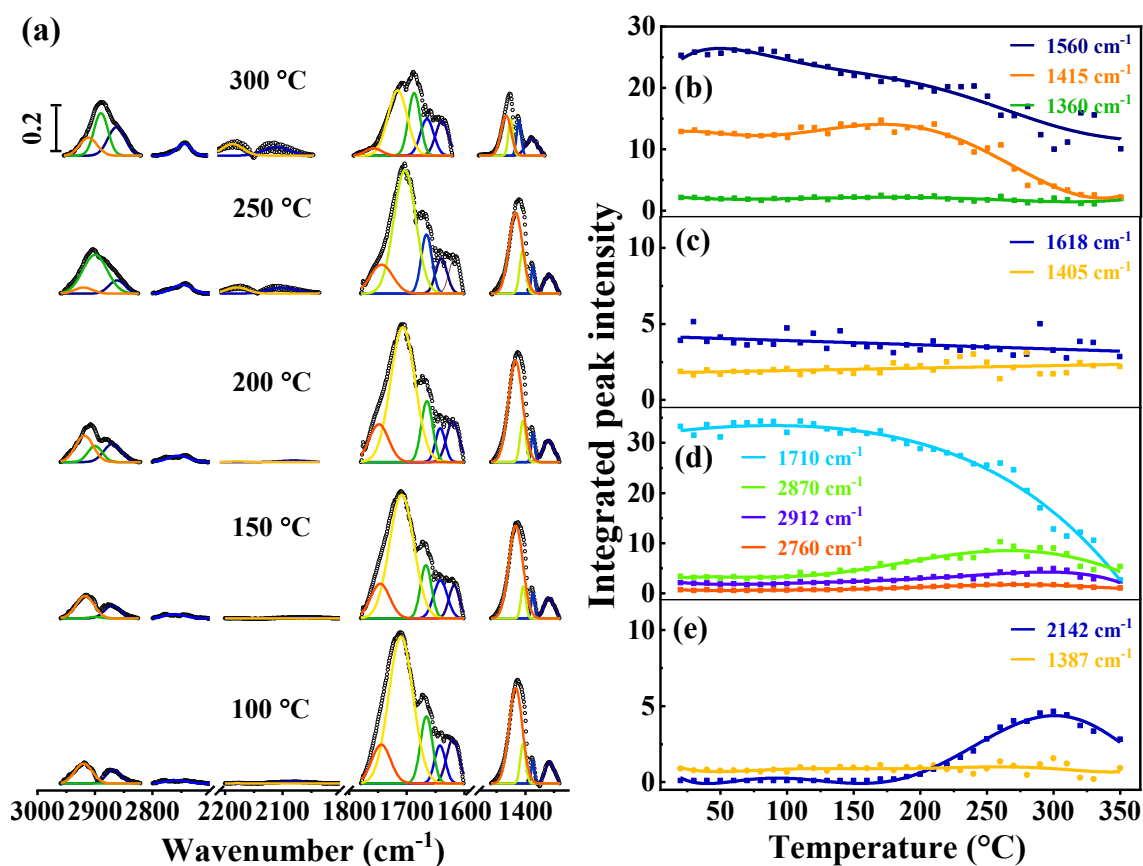


Figure S3.2. The fitting result of ex-situ-HCOO* hydrogenation on Al₂O₃. (a) The fitted spectra at separated ranges from 100 to 300 °C. The evolution of (b) Bi-HCOO*-Al₂O₃ (c) HCOO*-MSI at Al₂O₃ sites, (d) C=O asymmetric stretching and C-H stretching and C-H combination, (e) gaseous CO at 2142 cm⁻¹ and adsorbed CO₂* at 1387 cm⁻¹ during the reaction.

S3.1.3 Evolution of adsorption state during ex-situ-HCOO⁻* hydrogenation on Ru/Al₂O₃

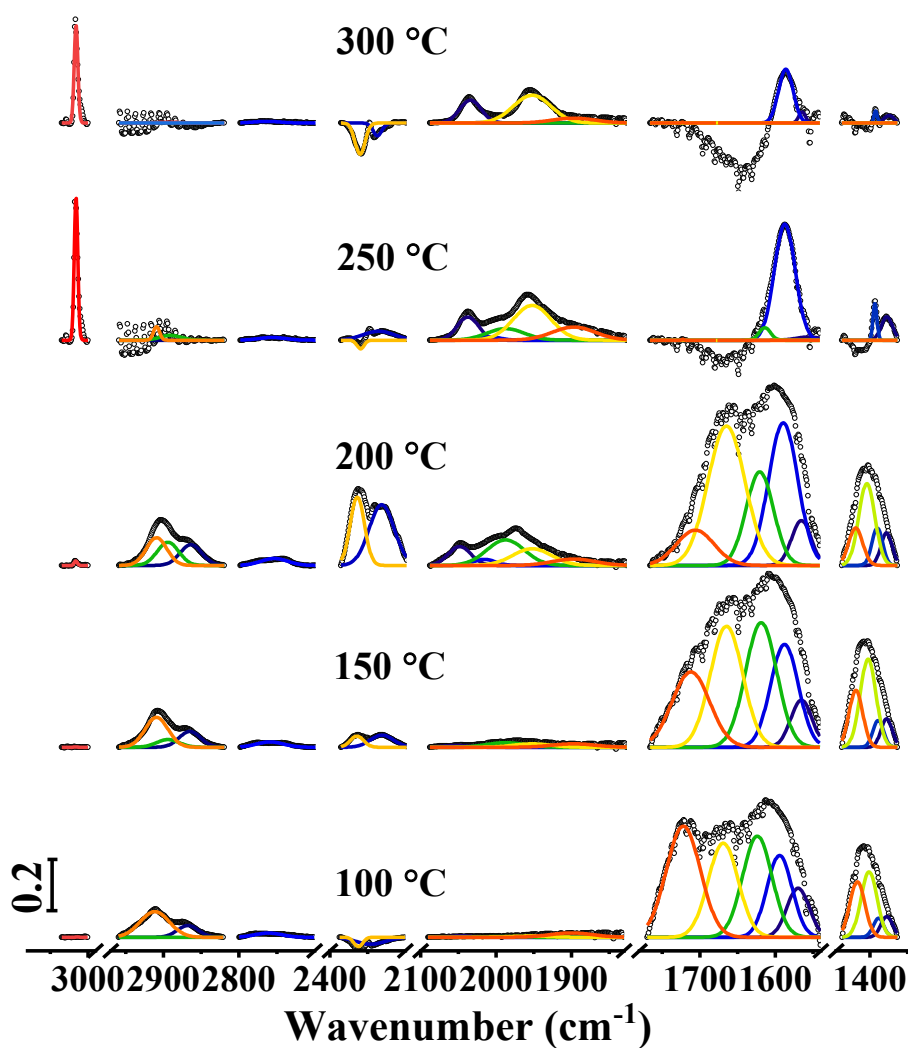


Figure S3.3. The experimental spectra of ex-situ-HCOO⁻* hydrogenation on Ru/Al₂O₃ (black circles) with fitted peaks (colored lines) in the ranges 3035–3000, 2960–2820, 2800–2700, 2390–2300, 2090–1830, 1770–1538, and 1440–1360 cm⁻¹.

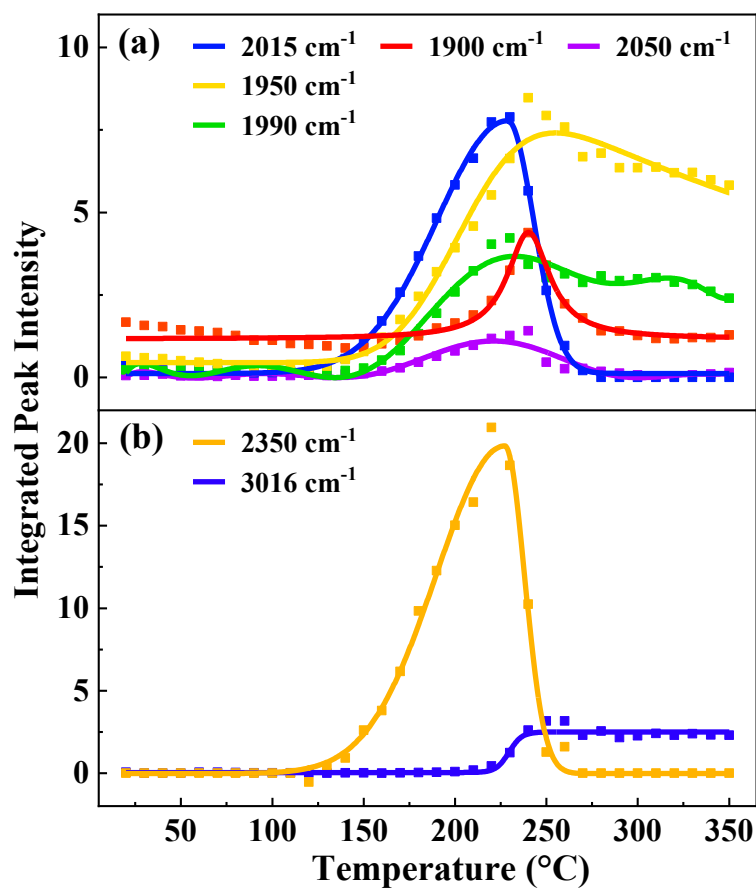


Figure S3.4. The evolution of the generations during the reaction of ex-situ-HCOO* hydrogenation on Ru/Al₂O₃. (a) linear-CO* at 2015 and 2050 cm⁻¹, bridged-CO* at 1990, 1950 and 1900 cm⁻¹, and (b) gaseous CO₂ centered at 2350 cm⁻¹ and gaseous CH₄ centered at 3016 cm⁻¹.

S3.2. Other supplementary figures

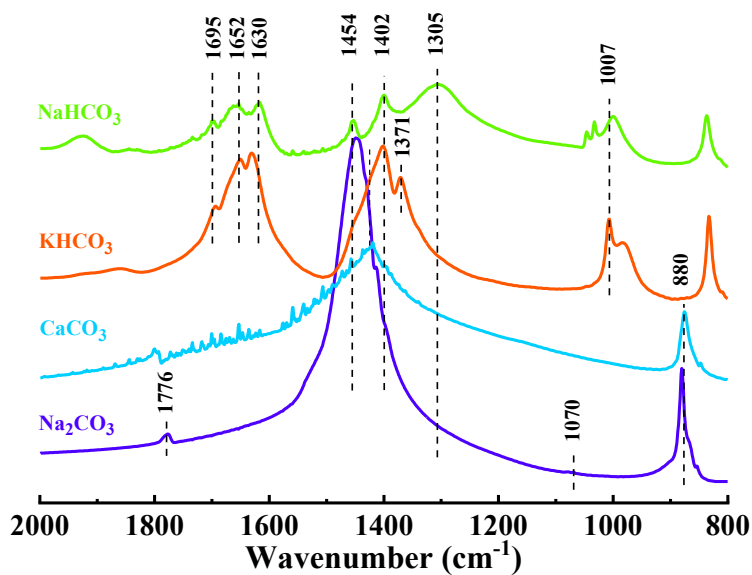


Figure S3.5. FT-IR transmittance of Na_2CO_3 , CaCO_3 , KHCO_3 and NaHCO_3 .

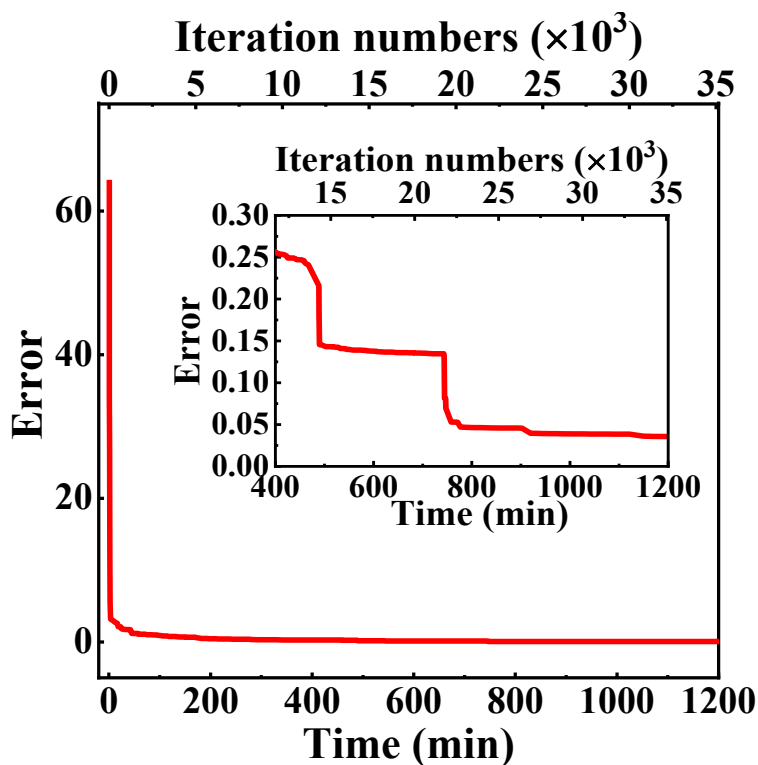


Figure S3.6. The error evolution approaching convergence as a function of time for fitting the spectra set of CO_2 hydrogenation on $\text{Ru}/\text{Al}_2\text{O}_3$ in the range of $1780\text{--}1535\text{ cm}^{-1}$ from $20\text{--}300\text{ }^\circ\text{C}$ by BEGF.

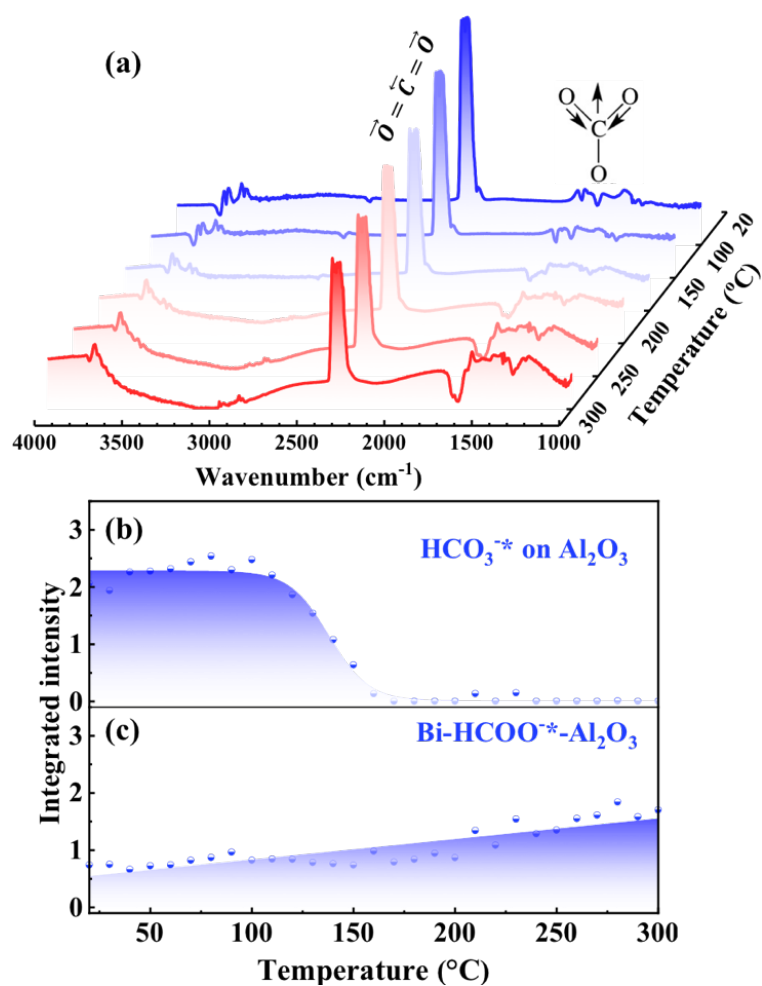


Figure S3.7. (a) DRIFT spectra of CO₂ hydrogenation on Al₂O₃. Evolution of (b) HCO₃⁻*, (c) Bi-HCOO⁻*-Al₂O₃ during the reaction.

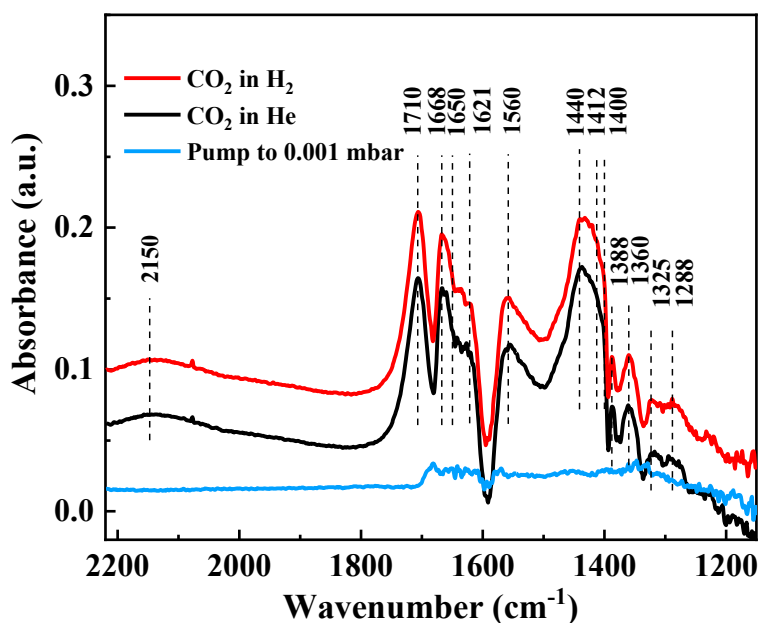


Figure S3.8. The infrared spectra of CO₂ adsorption (200 mbar CO₂ and 800 mbar He) and its co-adsorption with H₂ (200 mbar CO₂ and 800 mbar H₂) on Al₂O₃ at RT under 1 bar.

S3.3 Global optimization by evolutionary algorithms⁸

Evolutionary algorithms, inspired by biological evolution, are generic, stochastic, derivative-free, population-based, direct search techniques. They often perform better than derivative-based deterministic algorithms for solving complex non-linear optimization problems, even with multi-modal, noncontinuous objective functions, incoherent solution space and discrete decision variables; moreover, global optimality, although not guaranteed, can be closely approached within a limited number of function evaluations. Genetic algorithms are one type of evolutionary algorithm.

As given in Figure S3.9, the basic run of an evolution algorithm starts from an initialization, in which a set (population) of candidate solutions (individuals) with randomly generated decision variables are proposed and evaluated for assigning the fitnesses (the objective function value, if feasible; otherwise, a penalty value). Afterwards, for evolving the current parent population to an offspring population, the algorithm starts an iteration loop of parent selection, recombination (crossover), mutation, evaluation and offspring selection. To produce each new individual, based on the fitness values, one

⁸ Doctoral thesis: Ligang Wang, *et al.* Thermo-economic Evaluation, Optimization and Synthesis of Large-scale Coal-fired Power Plants, Doctoral thesis, Technical University of Berlin, 2016, <https://depositonce.tu-berlin.de/handle/11303/5852>.

or more parents are selected to have crossover and mutation. A crossover operation takes place randomly and reassembles parts of the selected parents, whereas a mutation operation performs a small random perturbation of one individual. The newly-born offspring are then evaluated; finally, a ranking of offspring (and parent) individuals is performed, so that those individuals with larger possibility of leading to the optimality survive and are selected as the offspring population. The iteration continues until a termination criterion, e.g., a limit of computation time or total fitness-evaluation number, is reached.

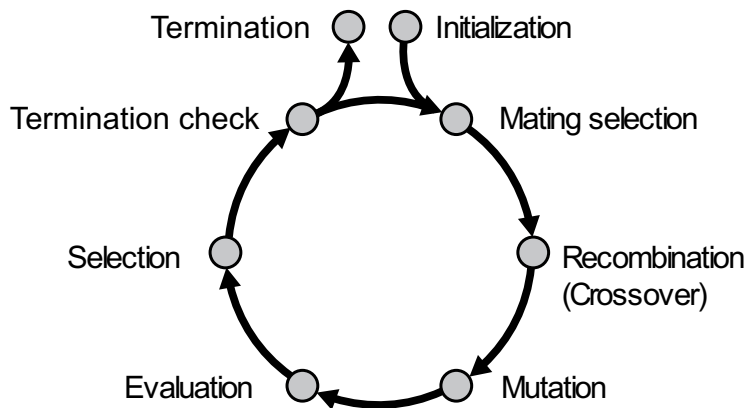


Figure S3.9. Flowchart of an evolutionary algorithm¹

Selection, crossover and mutation are three genetic operators of evolutionary algorithms for maintaining local intensification and diversification of the search. Different strategies on these three aspects lead to a variety of evolutionary algorithms. Selection strategy exerts influence mainly on population diversity. One commonly used strategy of selection is the $(\mu + \lambda)$ -selection proposed in evolution strategies, where μ and λ , satisfying $1 \leq \mu \leq \lambda$, denote the sizes of parent and offspring populations, respectively. Selection ranks the fitness of all $\mu + \lambda$ individuals and takes the μ best individuals.

Depending on the search space and objective function, the crossover and/or the mutation may or may not occur in specific instantiations of the algorithm. Crossover intensifies the local search but is not essential, as self-adaption of individuals is available due to mutation, which, in contrast, is usually dispensable to avoid premature convergence toward sub-optimal solutions. There are different mechanisms of crossover and mutation. For example, a genetic algorithm usually employs bit strings to represent variables.

Chapter 4 In Situ Control of the Adsorption Species in CO₂ Hydrogenation: Determination of Intermediates and By-products

Kun Zhao^{a,b*}, Ligang Wang^c, Marco Calizzi^{a,b}, Emanuele Moioli^{a,b}, Andreas Züttel^{a,b*}

^aLaboratory of Materials for Renewable Energy, Institute of Chemical Sciences and Engineering, Basic Science Faculty (SB), École Polytechnique Fédérale de Lausanne (EPFL), 1951 Sion, Switzerland

^bSwiss Federal Laboratories for Materials Science and Technology (EMPA), 8600 Dübendorf, Switzerland

^cGroup of Energy Materials (GEM), Institute of Mechanical Engineering (IGM), School of Engineering (STI), École Polytechnique Fédérale de Lausanne (EPFL), 1951 Sion, Switzerland

Preprint version: preprint version of the manuscript published on the scientific journal *The Journal of Physical Chemistry C*. 2018, 122, 20888-20893. DOI: 10.1021/acs.jpcc.8b06508

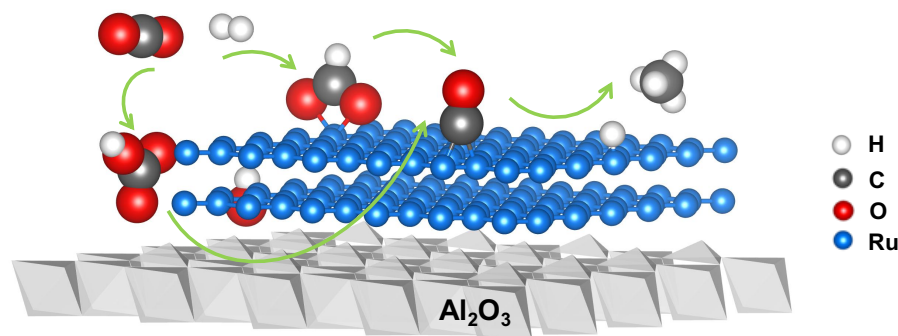
Copyright permission: adapted with permission from Zhao. K., et al *J. Phys. Chem. C*, 2018, 122, 20888. Copyright 2019 American Chemical Society.

Edit: caption numbers of figures, tables, and equations were edited to adapter the thesis chapter number.

Summary: this Chapter is continuous work after the previous methodological work on resolving the IR spectra. The surface reaction steps of CO₂ hydrogenation on Ru/Al₂O₃ were identified through in situ control of the development of each adsorbed species.

Abstract

CO₂ hydrogenation over catalysts is a potentially exciting method to produce fuels while closing the CO₂ cycle and mitigating global warming. The mechanism of this process has been controversial due to the difficulty in clearly identifying the species present and distinguishing which are reaction intermediates and which are byproducts. We in situ manipulated the independent formation and hydrogenation of each adsorption species produced in CO₂ hydrogenation reaction over Ru/Al₂O₃ using operando diffuse reflectance infrared Fourier transformation spectroscopy (DRIFTS) and executed a novel iterative Gaussian fitting procedure. The adsorption species and their role in CO₂ hydrogenation reaction have been clearly identified. The adsorbed carbon monoxide (CO*) of four reactive structures was the key intermediate of methane (CH₄) production. Bicarbonate (HCO₃^{-*}), formed on the metal-support interface, appeared to be not only the primary product of CO₂ chemisorption, but also a reservoir of CO*, and consisted the dominate reaction steps of CO₂ methanation from the interface to the metal surface. Bidentate formate (Bi-HCOO*) formed on Ru under a certain condition, consecutively converting to CO* to merge into the subsequent methanation process. Nonreactive byproducts of the reaction were also identified. The evolution of the surface species revealed the essential steps of the CO₂ activation and hydrogenation reactions which inevitably initiated from HCO₃^{-*} to CO* and finally from CO* to CH₄.



4.1 Introduction

CO₂ reduction by H₂ is a promising way to store hydrogen energy in hydrocarbons, producing synthetic fuels that exhibit the same energy density as fossil fuels to meet the increasing energy demands.^{1,2} Moreover, the use of CO₂ as feedstock allows closure of the CO₂ cycle, reducing CO₂ emission and alleviating global warming. The mechanisms of CO₂ hydrogenation have been widely investigated on supported group VIII metals such as Ni, Ru and Rh.³⁻⁸ One of the principal analytical methods used is infrared spectroscopy, particularly diffuse reflectance infrared Fourier transformation spectroscopy (DRIFTS) for studying both the gaseous phase and the adsorption species on the catalyst surface. The main product is commonly found to be gaseous CH₄. However, various reaction mechanisms have been proposed referring to different intermediates. Gaseous CO and adsorbed CO* were considered as important intermediates of CO₂ methanation because the well-known reversed water gas shift (RWGS) reaction could take place in the path of CH₄ production.⁹⁻¹² Some research has found that gaseous CO is not an intermediate as CO₂ produced without visible occurrence of gaseous CO.^{13,14} Instead, the adsorbed CO*, which is formed via surface RWGS reaction, is more favorable to be the intermediate as the adsorbed CO* exhibits relation with CH₄ formation.¹⁵⁻¹⁹ However, other research also support that the adsorbed formate (HCOO*) is the intermediate rather than CO*.²⁰ The mechanism of CO₂ hydrogenation is still controversial.

There are two key problems with the previous work: difficulties in the definitive determination of the species appeared during the reaction, and difficulty with knowing whether a given species is an intermediate or a byproduct of CO₂ methanation.

To address the first problem, we resolved the peaks of the adsorbates using Gaussian fittings which were iteratively improved to produce a consistent view of the trends in observed species. To address the second problem, we controlled the formation of each adsorption species in situ, following by reducing the obtained adsorption species individually in H₂ to monitor their role in hydrogenation process. This allowed us to trace the origin and reaction path of each adsorption species, and to determine the key intermediate of CO₂ methanation. We found that the essential pathway of CO₂ activation was CO₂ → HCO₃* → CO* whether H₂ was present or not. The surface RWGS reaction and HCOO* contributed to CO* formation only when the system had abundant CO₂ and H₂. CO* was the key intermediates of CO₂ methanation. Besides, the reactivities of the adsorption species were adsorption structure-dependent.

4.2 Experimental Section

Chemicals and Apparatus. The experiments were performed on ground Ru/Al₂O₃ (Sigma-Aldrich, 0.5 wt.% loading on 3.2 mm pellets) or Al₂O₃ (Sigma-Aldrich). The infrared spectra were recorded using a Bruker Tensor 27 spectrophotometer with a resolution of 2 cm⁻¹, equipped with the Praying Mantis accessory and high-temperature reaction chamber (HVC) from Harrick Scientific for the diffuse reflectance infrared Fourier transformation spectroscopy (DRIFTS). The chamber was connected to He (purity 99.999%), H₂ (purity 99.999%) and CO₂ (purity 99.998%) gas lines and a turbomolecular pump. The tubing and the chamber were heated at 100 °C under vacuum overnight after loading the sample. The background pressure was 1×10⁻⁵ mbar. The spectrophotometer was continuously flushed with clean dry compressed air.

Sample Preparation. Ru/Al₂O₃ and Al₂O₃ was pre-reduced in the DRIFTS cell in H₂ flow with heating from room temperature (RT) to 350 °C at a heating rate of 2 °C/min and maintained at 350 °C for 4 h to remove the surface oxides on the Ru metal. The sample was then allowed to cool to RT in H₂ flow. A high vacuum of 1×10⁻⁵ mbar was recovered after pumping.

Experiments Performed. Following the pretreatment, seven sets of experiments were done: **Exp. I** CO₂ hydrogenation reaction. This was initiated by mixing 200 mbar of CO₂ and 800 mbar of H₂ at RT, and heated to 300 °C with a rate of 1 °C/min on both Ru/Al₂O₃ and Al₂O₃. **Exp. II** CO₂ adsorption reaction. This was initiated by mixing 200 mbar of CO₂ and 800 mbar of He at RT, followed by heating to 300 °C with a rate of 1 °C/min on both Ru/Al₂O₃ and Al₂O₃. **Exp. III** HCO₃⁻* decomposition reaction. This was initiated by mixing 200 mbar of CO₂ and 800 mbar of He at RT, followed by pumping to high vacuum of 5×10⁻⁵ mbar, then heating to 300 °C with a rate of 1 °C/min on Ru/Al₂O₃. **Exp. IV** CO* hydrogenation. This was obtained directly from HCO₃⁻* decomposition experiment at 300 °C, followed by cooling down to RT, then filling with 1 bar of H₂ and heating to 300 °C with a rate of 1 °C/min on Ru/Al₂O₃. **Exp. V** HCO₃⁻* hydrogenation reaction. This was initiated by mixing 200 mbar of CO₂ and 800 mbar of He at RT, followed by pumping to high vacuum of 5×10⁻⁵ mbar, then filling the cell with 1 bar of H₂ and heating to 300 °C with a rate of 1 °C/min on Ru/Al₂O₃. There are also two experiments which were done without reducing the surface: **Exp. VI** HCOOH adsorption. HCOOH was obtained from external HCOOH droplet. The HCOOH droplet was added on the sample of Ru/Al₂O₃ and Al₂O₃ in air. Afterwards, the sample was pumped to low vacuum of 5×10⁻³ mbar over 24h at RT. **Exp. VII** HCOOH hydrogenation. To determine the

hydrogenation properties of HCOOH on Ru/Al₂O₃ and Al₂O₃, the samples were exposed to 1 bar of H₂ after Exp VI, and then heated to 300 °C with a rate of 1 °C/min.

In addition, solid reference samples of Na₂CO₃, CaCO₃, NaHCO₃ and KHCO₃ were analyzed by transmission FT-IR to obtain the infrared bands of CO₃²⁻ and HCO₃⁻.

Gaussian fittings. Four regions were separately fitted: 2100 ~ 1800 cm⁻¹, 1800 ~ 1530 cm⁻¹, 1530 ~ 1420 cm⁻¹, 1420 ~ 1350 cm⁻¹. The baseline of each region was taken as a linear function. The position, width and height of each Gaussian contribution were all constrained. The initial values of these constraints were taken from a combination of an estimation of the peak ranges observed in the spectra and the measured peaks of the reference samples. These initial parameters were used to simulate all the peaks in these ranges from all the experiments. The results of a fitting run were used to give the new values of parameters and constraint ranges for the next fitting run. This process was iterated manually hundreds of times until two criteria were met: (1) all the peaks followed regular and physically meaningful trends as the reaction proceeded; and (2) subsequently fits did not change the parameters of the peak position, height, and width.

The combination of the measurement of the reference samples and the Gaussian fittings through the reaction coordination helped to identify and assign the observed peaks.

4.3 Results and Discussions

4.3.1 Correlations of coexisting adsorption species in the CO₂ hydrogenation reaction

In order to learn what species comes out during CO₂ hydrogenation, we triggered CO₂ hydrogenation reaction on Ru/Al₂O₃ by mixing CO₂ and H₂ followed by program heating (Exp. I). Figure 4.1(a) shows the main reaction of CO₂ converting to CH₄ from 100 °C. The variations in the complex peaks below 2200 cm⁻¹ suggest the development of adsorption species from CO₂ and H₂ co-adsorption during the hydrogenation reaction. The peaks were distinguished in three regions: C-O stretching of adsorbed carbon monoxide (CO*) between 2100 and 1800 cm⁻¹; O-C-O stretching of adsorbed bicarbonates (HCO₃⁻*), carbonates (CO₃²⁻*) and formate (HCOO⁻*) between 1700 and 1400 cm⁻¹; and C-H and O-H bending between 1400 and 1200 cm⁻¹ (Fig 1(a)). To identify the infrared peaks, we measured reference samples of carbonates, bicarbonates, and surface formic acid on Ru/Al₂O₃ and Al₂O₃ (Figure S4.1 and S4.2). More importantly, we resolved the peaks of the adsorbates of each

reaction using Gaussian fittings (Figure S4.3). The peak assignments are summarized in Table 4.1 based on the combination of reference peaks and gaussian fittings.

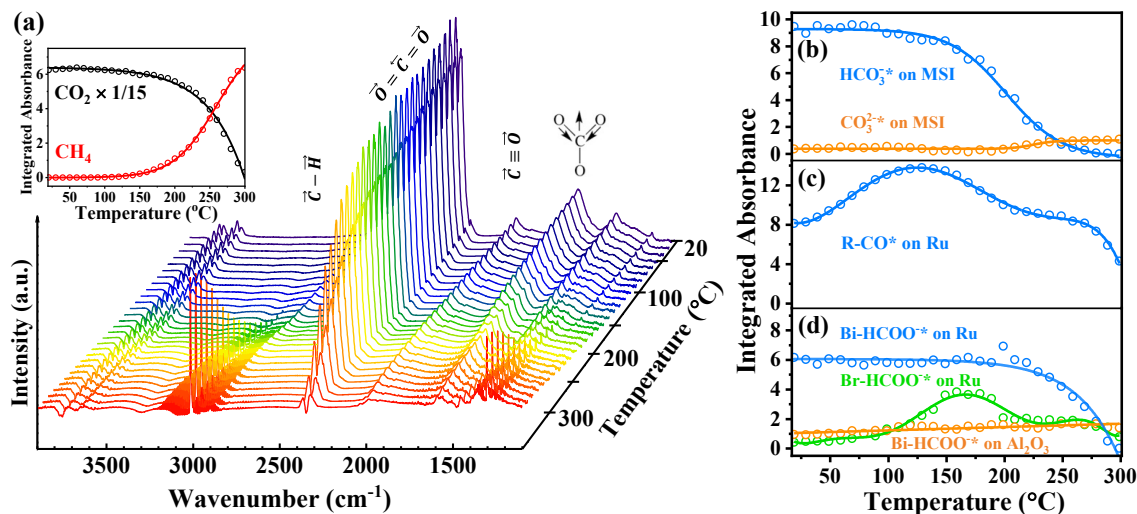


Figure 4.1. (a) Infrared absorbance spectra with the insertion of CO₂ to CH₄ conversion during CO₂ hydrogenation (Exp. I). And evolution of adsorption species of (b) HCO₃⁻* with peak at 1650 cm⁻¹ and CO₃²⁻* with peak at 1450 cm⁻¹ located at MSI, (c) R-CO* on Ru, (d) Bi-HCOO* on Ru, Br- and Br-HCOO* on Ru, and Bi-HCOO* on Al₂O₃. In (b)-(d), circles are the original data of integrated peak intensity from Gaussian fittings, and the lines are the non-linear fittings of those original data.

At RT, four types of adsorption species were formed during the CO₂ hydrogenation reaction on Ru/Al₂O₃: HCO₃⁻*, CO₃²⁻*, CO*, and HCOO*. HCO₃⁻* were formed by reaction of CO₂ with the surface hydroxyl groups on the Al₂O₃ support following the H₂ pretreatment. The intensity of HCO₃⁻* was larger on Ru/Al₂O₃ than on bare Al₂O₃, and HCO₃⁻* on Al₂O₃ could not be continuously formed from CO₂ on Al₂O₃ (Figure S4.4 and S4.5), indicating the adsorption of HCO₃⁻* is increased by the metal-support interface (MSI). As shown in Figure 4.1(b), during the temperature ramp the concentration of HCO₃⁻* was initially constant and started to decrease above about 150 °C. CO₃²⁻* increased gradually with increasing temperature above 200 °C, the increase most likely came from HCO₃⁻* deprotonation. Assuming that the peak intensities for O-C-O stretching are similar in HCO₃⁻* and CO₃²⁻* at the same site and coverage, the much lower intensity of CO₃²⁻* indicates that only some of the HCO₃⁻* decomposed to CO₃²⁻*, and the remaining HCO₃⁻* molecules were consumed in other processes, for instance desorption or decomposition.

Reactive CO* (R-CO*) with the peaks at 2015, 1990, 1950, and 1905 cm⁻¹ (Table 4.1 and Figure S4.6) increased from RT up to 150 °C (Figure 4.1(c)) and then decreased, indicating that its

production was slower than its consumption above 150 °C. At 220 °C, R-CO* concentration leveled off, possibly because a new route of R-CO* production became active. Nevertheless, linear-CO* on Ru⁰ at 2035 cm⁻¹ (Table 4.1) remained constant throughout the entire experiment, indicating the inert character of this species (Figure S4.6). It has been reported that hydrogen-perturbed CO could locate in the range between 1840 – 1700 cm⁻¹, and could be H₂CO species or carbonyl hydrides and formyl/formaldehyde.^{21,22} In our case, we did not have peaks between that region as shown in Figure S4.6. The discrepancy between the reference and our work could be originated by the different effects of different catalyst surfaces which are sensitive/selective to the different adsorption species.

HCOO* is present in three forms (bidentate on Ru with a high frequency of 1620 cm⁻¹, bridged on Ru with a frequency of 1590 cm⁻¹ and bidentate on Al₂O₃ with a frequency of 1560 cm⁻¹ (Table 4.1). Bidentate-HCOO* (Bi-HCOO*) on Ru was abundant and stable up to 220 °C, after which it was consumed and completely disappeared at 300 °C. Conversely, bridged-HCOO* (Br-HCOO*) on Ru, increased from 70 to 160 °C, followed by a slow decrease (Figure 4.1 (d)). Bidentate-HCOO* (Bi-HCOO*) on Al₂O₃ showed only one weak peak at 1560 cm⁻¹ (Figure 4.1 (d)). The slight increase in production of this species, instead of consumption, indicates it is not reactive during CO₂ hydrogenation.

4.3.2 Unraveling the roles of individual species using in situ control

The temperature-dependent evolution of the abovementioned species shows correlations with the CO₂ methanation reaction. However, their simultaneous existence makes the determination of their origins and roles in the reaction equivocal. To unravel these mysteries, we isolate the adsorption species step by step in the following sections.

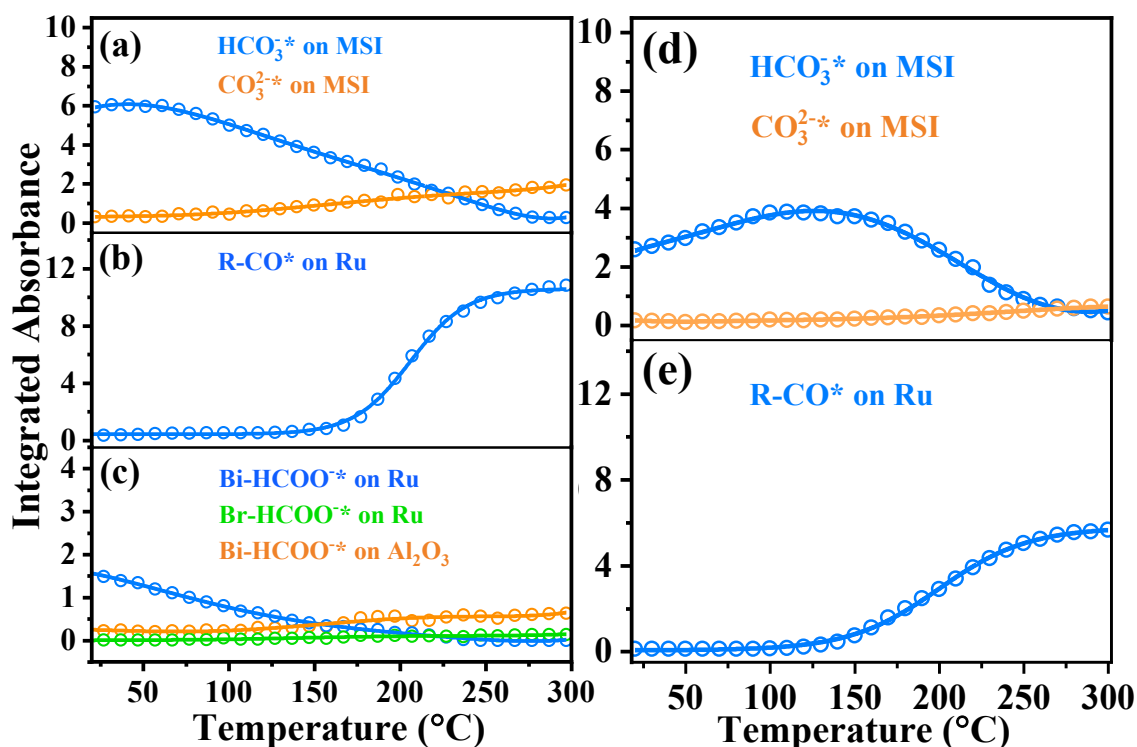


Figure 4.2. (a) HCO_3^* and CO_3^{2-*} , (b) R-CO^* , (c) three structural HCOO^* during CO_2 adsorption reaction (Exp. II); (d) HCO_3^* and CO_3^{2-*} , (e) R-CO^* during HCO_3^* decomposition (Exp. III). The peak positions were the same as in Figure 4.1. The circles are the original data of integrated peak intensity from Gaussian fittings, and the lines are the non-linear fittings of those original data.

4.3.2.1 Interactions of CO_2 and the surface

We first investigated the interactions between CO_2 and the surface by replacing H_2 with He, keeping all other conditions the same (Exp. II). The results are shown in Figure 4.2(a)-(c). At RT, HCO_3^* was the main species formed when the surface was exposed in CO_2 , indicating that it is the primary product of CO_2 adsorption (Figure 4.2(a)). HCO_3^* decreased almost linearly with increasing temperature after 50 °C. Simultaneously, CO_3^{2-*} increased almost linearly with increasing temperature. These trends are similar as those in the CO_2 hydrogenation reaction Figure 4.1(b). The higher ratio of $\text{CO}_3^{2-*}/\text{HCO}_3^*$ for CO_2 adsorption than that for CO_2 hydrogenation reflects the more favorable deprotonation of HCO_3^* in H_2 -deficient condition.

All the CO^* showed the same peaks as those in CO_2 hydrogenation except for a 25 cm^{-1} redshift of the peak of linear- CO^* at 2035 cm^{-1} (Figure S4.7). This redshift was probably due to the adsorption of linear- CO^* onto the oxidized metal surface ($\text{Ru}^{\delta+}$) in a hydrogen-deficient environment. This linear- CO^* at 2035 cm^{-1} showed no change in the whole process, as same insensitiveness as in CO_2

hydrogenation reaction (Figure S4.7). Notably, R-CO* increased above 150 °C (Figure 4.2(b)). This increase in R-CO* production explains the plateau in R-CO* concentration starting at 220 °C in CO₂ hydrogenation (Figure 4.1(c)). However, whether these CO* was produced from the decomposition of CO₂ or HCO₃⁻* is not clear yet and needed further controlling experiments.

Bi-HCOO* on Ru at RT had much weaker intensity (Figure 4.2(c)) than the corresponding intensity when H₂ was present (Figure 4.1(d)). The intensity decreased with increasing temperature until complete disappearance at 220 °C. We speculate that Bi-HCOO* is not formed from HCO₃⁻* since HCOO* does not increase when HCO₃⁻* decreases. Rather, Bi-HCOO* must be formed by CO₂ reacting with adsorbed H atoms on the surface. Thus, we conclude that there must be a small amount of residual H atoms present in this experiment, and that the small concentration of H explains the small concentration of Bi-HCOO*. Br-HCOO* on Ru was almost invisible, indicating that CO₂, HCO₃⁻* and CO* do not form Br-HCOO* in a hydrogen-deficient environment. Bi-HCOO* on Al₂O₃ slightly increased above 150 °C when Bi-HCOO* on Ru disappeared possibly due to migration of Bi-HCOO* on Ru to Al₂O₃ support.¹⁵

4.3.2.2 In situ isolation and decomposition of HCO₃⁻*

To determine whether CO* was formed from the decomposition of CO₂ or HCO₃⁻*, we pumped out the gases after CO₂ adsorption at RT (Exp. III). In this way, we produced a surface exclusively covered by HCO₃⁻* at RT. The catalyst was then heated. Broadly speaking, during heating HCO₃⁻* decreased (Figure 4.2(d)) starting from 130 °C and there was a corresponding increase in R-CO* concentration (Figure 4.2(e)), excluding the inert linear-CO* at 2065 cm⁻¹ (Figure S4.8). Thus, we conclude that the R-CO* originates from HCO₃⁻* and not from CO₂. The 20 °C-lower temperature than the onset temperature of R-CO* formation in CO₂ adsorption reaction (Figure 4.2(b)) is probably the reason of released active sites in high vacuum. We currently do not have an explanation for the increase in HCO₃⁻* at the beginning of the temperature ramp, but the broad conclusion stands.

4.3.2.3 In situ isolation and hydrogenation of CO*

To find out which adsorption species can react to form CH₄, we hydrogenated them separately by preparing them individually with in situ control.

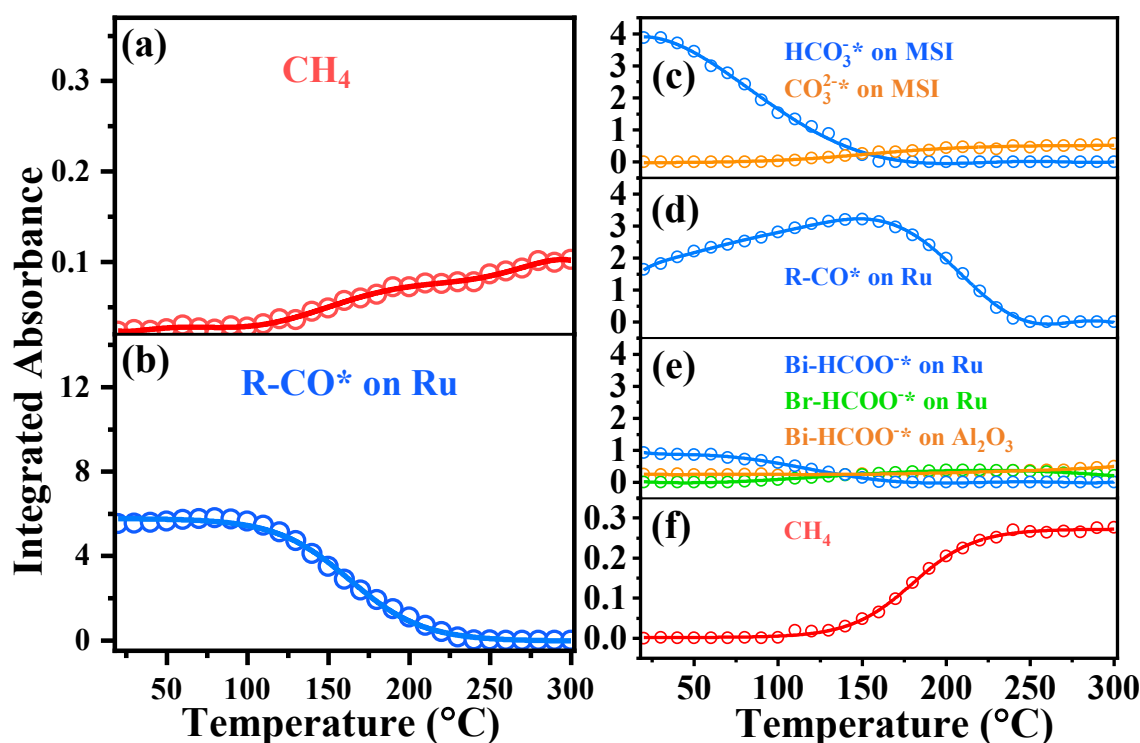


Figure 4.3. (a) Production of CH₄ and (b) reduction of CO* during R-CO* hydrogenation (Exp. IV). Evolution of (c) HCO₃^{-*} and CO₃^{2-*}, (d) R-CO*, (e) three structural HCOO*, (f) CH₄ during HCO₃^{-*} hydrogenation (Exp. V). The peak positions were the same as in Figure 1. The circles are the original data of integrated peak intensity from Gaussian fittings, and the lines are the non-linear fittings of those original data.

We first isolated all the CO* in situ from HCO₃^{-*} decomposition following the process shown in Figure 4.2(d) and (e) and cooling to RT. 1 bar of H₂ was then filled followed by program heating (Exp. IV). As shown in Figure 4.3(a) and (b), R-CO* decreased and CH₄ increased starting at 120 °C. Note that this onset temperature is 20 °C higher than that observed in the CO₂ hydrogenation reaction (Figure 4.1(a)) probably because of the lower R-CO* concentration in this case. Linear-CO* at 2040 cm⁻¹ was still inert in this hydrogenation process (Figure S4.9). Thus, we conclude R-CO* is clearly an intermediate in the CH₄ formation reaction while the linear-CO* above 2035 cm⁻¹ is a byproduct.

4.3.2.4 In situ isolation and hydrogenation of HCO₃^{-*}

Next, we investigate whether HCO₃^{-*} is an intermediate. HCO₃^{-*} was obtained in situ from CO₂ adsorption followed by pumping to high vacuum at RT (Exp. V). As shown in Figure 4.3(c)-(e), when the sample was heated in H₂, HCO₃^{-*} concentration decreased immediately till completely consumed by 150 °C. Meanwhile, R-CO* and Bi-HCOO* on Ru immediately produced at RT. There is a corresponding increase in the concentration of R-CO* which is the result of surface RWGS

reaction triggered by HCO_3^-* hydrogenation at MSI. Thus, we conclude that HCO_3^-* is an intermediate in the overall reaction, producing CO^* which is subsequently converted to CH_4 (Figure 4.3(f)).

4.3.2.5 The role of HCOO^-*

Finally, we consider whether HCOO^-* is an intermediate. Unfortunately, we were unable to produce isolated HCOO^-* by in situ control because HCO_3^-* was always present when HCOO^-* was produced. Nonetheless, we have evidence that Bi- HCOO^-* on Ru formed in our in situ control is a reaction intermediate. Figure 4.1(d) shows that in CO_2 hydrogenation reaction Bi- HCOO^-* on Ru formed from CO_2 hydrogenation, and was consumed in the same shape of the reactive species of CO_2 , HCO_3^-* and R-CO^* above 220 °C. This consumption could involve the formation reaction of CO^* or CH_4 . In Figure 4.3(e) when there was no CO_2 , Bi- HCOO^-* on Ru formed by the previous step of CO_2 adsorption reacting with residual hydrogen on the surface. Bi- HCOO^-* on Ru started to decrease at a 40 °C-lower temperature than the onset temperature of CH_4 formation. Therefore, we conclude Bi- HCOO^-* on Ru is reduced by hydrogen to form CO^* instead of directly to CH_4 . Additionally, Bi- HCOO^-* on Ru could convert to bridged form on Ru from 70 to 160 °C as illustrated in Figure 4.1(d) and Figure 4.3(e). This Br- HCOO^-* on Ru could be reduced above 160 °C but not completely when it was abundant (Figure 4.1(d)). However, it kept constant above 160 °C when it had low concentration. These imply Br- HCOO^-* on Ru has a high activation energy of hydrogenation. Bi- HCOO^-* on Al_2O_3 was a byproduct as it always slowly increased by the migration of those HCOO^-* on Ru in all the experiments.

The distinct reactivities between the HCOO^-* of different adsorption structures on Ru can be understood by atomic structure of the surface. The distance between neighboring Ru atoms in a hexagonal structure is 2.71 Å, while the distance between the two oxygen atoms of formate is 2.20 Å. These two comparable distances facilitate adsorption of the bridged structure of formate to the surface of the bulk Ru, where the two oxygen atoms bind to two adjacent Ru atoms. A larger distance between Ru atoms, e.g. at the edge or defect where some Ru atoms are isolated, is required to accept Bi- HCOO^-* on Ru so that two oxygen atoms bind to one Ru atom. Therefore, the bulk sites of the surface result in the stable Br- HCOO^-* on Ru, and the edge or defect centers promote the high reactivity of Bi- HCOO^-* on Ru.

We also prepared isolated HCOO^-* by ex situ application of a drop of HCOOH to the sample in air followed by pumping to vacuum. All the forms of HCOO^-* on Ru/ Al_2O_3 were reactive and started to form CO^* above 150 °C (Figure S4.2). Above 220 °C, Bi- HCOO^-* on Ru and on Al_2O_3 were

substantially reduced, leading to CO* formation slowing down and CH₄ formation. Br-HCOO* on Ru was not reduced completely. The ex situ experiment supports the conclusion that Bi-HCOO* on Ru is a reaction intermediate and Br-HCOO* on Ru possesses high activation energy of reduction; but, on the other hand, it showed a discrepancy with the in situ experiment where Bi-HCOO* on Al₂O₃ was also reactive. The discrepancy is not surprising given that the ex situ experiment involved exposure to air and the high acidity of the sample. The discrepancy points out the danger of obtaining misleading results by ex situ preparation.

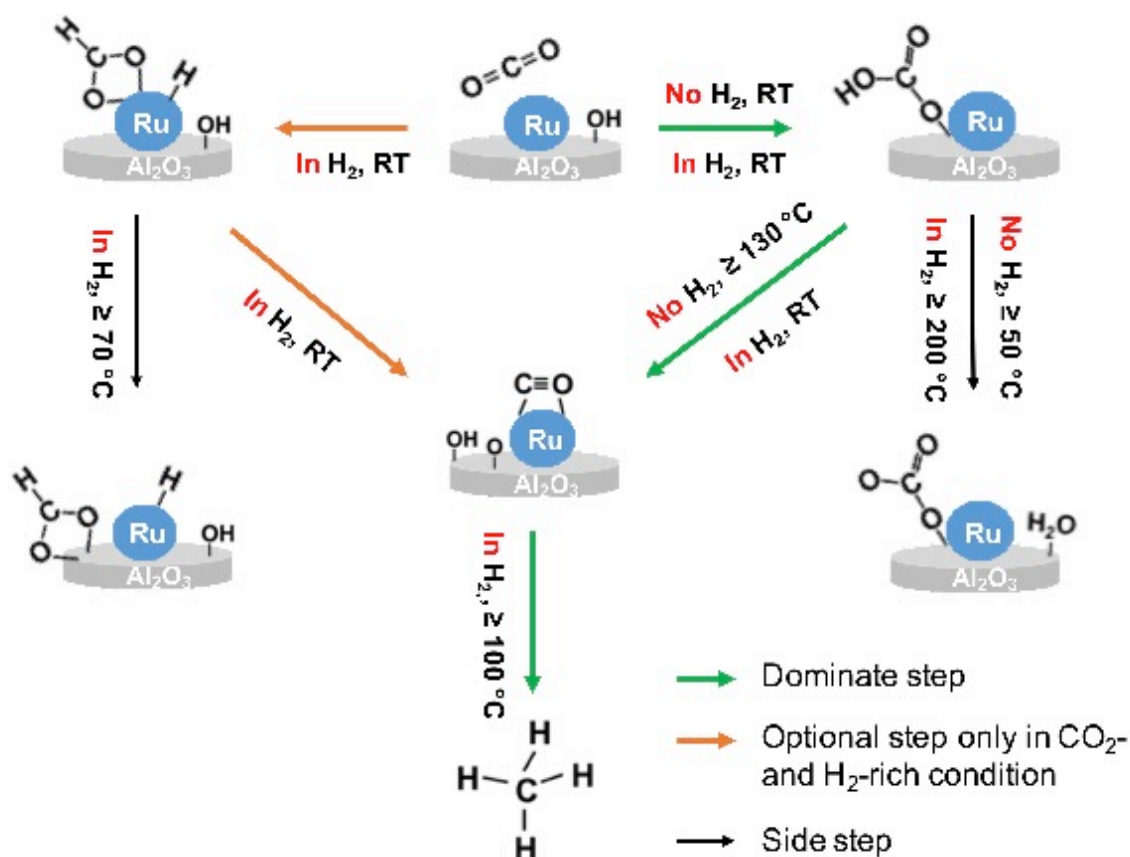


Figure 4.4 Schema of the hydrogenation steps of CO₂ on Ru/Al₂O₃.

Table 4.1. Vibrational modes and infrared peak positions (cm⁻¹) of the reference samples and the reaction species from this work.

Species	C-H as. str.	C-H b.	C=O str.	O-C-O as. str.	O-C-O s. str.	O-C-O b.	O-H b.	C-OH str.
CO ₃ ²⁻	--	--	1776	1454	1454	880	--	--
CO ₃ ^{2-*} †23	--	--	--	1500	1450	--	--	--
HCO ₃ ⁻	--	--	1695	1650, 1630	1402, 1371	--	1305	1007
HCO ₃ ^{-*} †20, 23-27	--	--	1690	1650	1440	--	1230	--
HCOOH ^{†28-30}	2940, 2871	1415	1748, 1670	1620; 1560 (on Al ₂ O ₃)	1405, 1360	--	1220	970
Bi-HCOO ^{-*} on Ru	2913, 2895, 2870	1390	1720	1620	1405	--	1220	970
Br-HCOO ^{-*} on Ru	2913, 2895, 2870	1390	1720	1590	1375	--	1220	970
Bi-HCOO ^{-*} on Al ₂ O ₃ ^{†31}	2918, 2895, 2870	1387	1710	1560	1360	--	1230	970

Table 4.2 Vibrational modes and infrared peak positions (cm⁻¹) of CO* from this work.

Species	C≡O as. str.
Linear-CO* on Ru ^{δ+26,30,32-35}	2060
Linear-CO* on Ru ^{0+26,30,32-35}	2035
Linear-CO* on Ru ⁰ /Ru ^{δ+26,30,32-35}	2015
Bridged-CO* on Ru ^{†26,30,32-35}	1990, 1950, 1905
Gaseous CO	2150

str.: stretching. as.: asymmetric. s.: symmetric. b.: bending. (w): weak. *: adsorbed state. †the corresponding bond vibrations and infrared peak positions are comparable to the given references.

The way of distinguish bidentate and bridged structures of formate: bidentate-HCOO* has the splitting value of O-C-O asymmetric (ν_{as}) and symmetric (ν_s) stretching $\Delta\nu = \nu_{as} - \nu_s$ less than 220 cm⁻¹; bridged-HCOO* has $\Delta\nu$ in the range of 220 – 280 cm⁻¹.³⁶

4.4 Conclusions

The results we have just described, can be understood in terms of the reaction mechanisms summarized in Figure 4.4. There are two pathways to CO₂ methanation. One is initiated by HCO₃⁻* formation, illustrated by the green arrow. The other is initiated by the formation Bi-HCOO* on Ru, illustrated by the orange arrow. In the HCO₃⁻* pathway, first, HCO₃⁻* is formed at RT when CO₂ adsorbs and reacts with the surface hydroxyl groups on the metal-support interface which originated from the H₂ pre-reduction of the surface. Next, the HCO₃⁻* is reduced to CO* by hydrogen at RT. HCO₃⁻* also produces CO* via thermal decomposition above 130 °C in high vacuum and above to 170 °C in a CO₂ and H₂ rich environment. The temperature shift is due to competition for adsorption sites. In the Bi-HCOO* pathway, the first step is the reaction of CO₂ and hydrogen to produce Bi-HCOO* on Ru at RT. This species then reacts with hydrogen to produce CO* on Ru at RT. Alternatively, Bi-HCOO* on Ru converts to more stable Br-HCOO* on Ru which has a higher activation

energy to reaction and does not fully convert under our conditions (not shown in the figure). In both pathways, the final process is the hydrogenation of R-CO* to CH₄ above 100 °C. R-CO* is consequently a key intermediate in CO₂ methanation.

In addition to the pathways leading to CH₄ formation, there are also notable side reactions that lead to non-reactive byproducts. As shown by the black arrow on the right side of Figure 4.4, HCO₃^{-*} decomposes to CO₃^{2-*} at 50 °C in a hydrogen-deficient environment, and 200 °C in hydrogen-rich environment. The black arrow on the left side of Figure 4.4 shows Bi-HCOO^{-*} on Ru converts to Bi-HCOO^{-*} on Al₂O₃. Besides, linear-CO* on Ru⁰ forms along with R-CO*, but also insensitive to the hydrogenation reaction (not shown in the figure).

In summary, we unraveled surface reaction mechanism of CO₂ hydrogenation via in situ control of the individual formation and hydrogenation of each adsorption species in operando DRIFTS combined with iterative Gaussian fitting. CO₂ → HCO₃^{-*} → CO* → CH₄ is the dominate reaction step which takes place from the metal-support interface to the metal surface. This enlightens us the effective pathway and surface sites for CO₂ methanation.

AUTHOR INFORMATION

Corresponding Author

*andreas.zuettel@epfl.ch *kun.zhao@epfl.ch

ORCID

Andreas Züttel: 0000-0002-5708-1855

Kun Zhao: 0000-0002-7182-8089

Notes

The authors declare no competing financial interests.

ACKNOWLEDGMENT

SCCER HeE which is financially supported by Innosuisse - Swiss Innovation Agency is greatly acknowledged. K.Z also gratefully thanks Daniel Auerbach for the full discussions and revisions of this work.

ASSOCIATED CONTENT

Supporting Information

The infrared spectra of all the experiments, the evolution of each vibrational modes of each species, and the explanation of bicarbonate adsorption at MSI are illustrated. This material is available free of charge via the Internet at <http://pubs.acs.org>.

References

- (1) Züttel, A.; Maun, P.; Kato, S.; Callini, E.; Holzer, M.; Huang, J. Storage of Renewable Energy by Reduction of CO₂ with Hydrogen. *Chimia* **2015**, *69*, 264-268.
- (2) Kato, S.; Matam, S. K.; Kerger, P.; Bernard, L.; Battaglia, C.; Vogel, D.; Rohwerder, M.; Züttel, A. The Origin of the Catalytic Activity of a Metal Hydride in CO₂ Reduction *Angew. Chem. Int. Ed.* **2016**, *55*, 1-6.
- (3) Weatherbee, G. D.; Bartholomew, C. H. Hydrogenation of CO₂ on Group VIII metals IV. Specific Activities and Selectivities of Silica-Supported Co, Fe, and Ru. *J. Catal.* **1984**, *87*, 352-362.
- (4) Jalama, K. Storage of Renewable Energy by Reduction of CO₂ with Hydrogen Carbon dioxide hydrogenation over nickel-, ruthenium-, and copper-based catalysts: Review of kinetics and mechanism. *Catal. Rev.* **2017**, *59*, 95-164.
- (5) Frontera, P.; Macario, A.; Ferraro, M.; Antonucci, P. L. Supported Catalysts for CO₂ Methanation: A Review. *Catalysts* **2017**, *7*, 59.
- (6) Homs, N.; Toyir, J.; Piscina, P. R. Catalytic Processes for Activation of CO₂. *New and Future Developments in Catalysis: Activation of Carbon Dioxide, chapter 1*; Suib, S. L., Ed.; Elsevier, **2013**, 1-26.
- (7) Ge, Q. F. Mechanistic Understanding of Catalytic CO₂ Activation from First Principles Theory. *New and Future Developments in Catalysis: Activation of Carbon Dioxide, Chapter 3*; Suib, S. L., Ed.; Elsevier, **2013**, 49-79.
- (8) Wang, W.; Wang, S. P.; Ma, X. B.; Gong, J. L. Recent Advances in Catalytic Hydrogenation of Carbon Dioxide. *Chem. Soc. Rev.* **2011**, *40*, 3703-3727.
- (9) Maitlis, P. M.; Quyoum, R.; Long, H. C.; Turner, M. L. Towards a Chemical Understanding of the Fischer–Tropsch Reaction: Alkene Formation. *Appl. Catal. A Gen.* **1999**, *186*, 363-374.
- (10) Santen, R. A. van.; Markvoort, A. J.; Filot, I. A. W.; Ghouriab, M. M.; Hensen, E. J. M. Mechanism and Microkinetics of the Fischer–Tropsch Reaction. *Phys. Chem. Chem. Phys.* **2013**, *15*, 17038-17063.
- (11) Filot, I. A. W.; Santen, R. A. van; Hensen, E.; J. M. The Optimally Performing Fischer–Tropsch Catalyst. *Angew. Chem. Int. Ed.* **2014**, *126*, 12960-12964.
- (12) Munnik, P.; Jongh, P. E.; Jong, K. P. Recent Developments in the Synthesis of Supported Catalysts. *Chem. Rev.* **2015**, *115*, 6687-6718.
- (13) Vlasenko, V. M.; Yuzefovich, G. E. Mechanism of the Catalytic Hydrogenation of Oxides of Carbon to Methane. *Russ. Chem. Rev.* **1969**, *38*, 728-739.
- (14) Garbarino, G.; Bellotti, D.; Finocchio, E.; Magistri, L.; Busca, G. Methanation of Carbon Dioxide on Ru/Al₂O₃: Catalytic Activity and Infrared Study. *Catal. Today* **2016**, *277*, 21-28.

-
- (15) Marwood, M.; Doepper, R.; Renken, A. In-situ Surface and Gas Phase Analysis for Kinetic Studies under Transient Conditions The catalytic hydrogenation of CO₂. *Appl. Catal. A Gen.* **1997**, *151*, 223-246.
- (16) Marwood, M.; Vyve, F. V.; Doepper, R.; Renken, A. Periodic Operation Applied to the Kinetic Study of CO₂ Methanation. *Catal. Today* **1994**, *20*, 437-448.
- (17) Prairie, M. R.; Renken, A.; Highfield, J. G.; Thaimpi, K. R.; Grätzel, M. A Fourier Transform Infrared Spectroscopic Study of CO₂ Methanation on Supported Ruthenium. *J. Catal.* **1991**, *129*, 130-144.
- (18) Eckle, S.; Anfang, H. G.; Behm, J. Reaction Intermediates and Side Products in the Methanation of CO and CO₂ over Supported Ru Catalysts in H₂-Rich Reformate Gases. *J. Phys. Chem. C* **2011**, *115*, 1361-1367.
- (19) Miao, B.; Ma, S. S. K.; Wang, X.; Su, H. B.; Chan, S. H. Catalysis Mechanisms of CO₂ and CO Methanation. *Catal. Sci. Technol.* **2016**, *6*, 4048-4058.
- (20) Wang, F.; He, S.; Chen, H.; Wang, B.; Zheng, L. R.; Wei, M.; Evans, D. G.; Duan, X. Active Site Dependent Reaction Mechanism over Ru/CeO₂ Catalyst toward CO₂ Methanation. *J. Am. Chem. Soc.* **2016**, *138*, 6298-6305.
- (21) Sápi, A.; Halasi, G.; Kiss, J.; Dobó, D. G.; Juhász, K. L.; Kolcsár, V. J.; Ferencz, Z.; Vári, G.; Matolin, V.; Erdőhelyi, A.; Kukovecz, Á; Kónya, Z. In Situ DRIFTS and NAP-XPS Exploration of the Complexity of CO₂ Hydrogenation over Size-Controlled Pt Nanoparticles Supported on Mesoporous NiO. *J. Phys. Chem. C* **2018**, *122*, 5553-5565.
- (22) Fisher, I. A.; Bell, A. T. A Comparative Study of CO and CO₂ Hydrogenation over Rh/SiO₂. *J. Catal.* **1996**, *162*, 54-65.
- (23) Taifan, W.; Boily, J. F.; Baltrusaitis, J. Surface Chemistry of Carbon Dioxide Revisited. *Surf. Sci. Rep.* **2016**, *71*, 595-671.
- (24) Rudolph, W. W.; Fischer, D.; Irmer, G. Vibrational Spectroscopic Studies and Density Functional Theory Calculations of Speciation in the CO₂-Water System. *Appl. Spectrosc.* **2006**, *60*, 130-144.
- (25) Rudolph, W. W.; Irmer, G.; Königsberger, E. Speciation Studies in Aqueous HCO₃⁻—CO₃²⁻ Solutions. A combined Raman spectroscopic and thermodynamic study. *Dalton Trans.* **2008**, 900-908.
- (26) Garbarino, G.; Bellotti, D.; Finocchio, E.; Magistri, L.; Busca, G. Methanation of Carbon Dioxide on Ru/Al₂O₃: Catalytic Activity and Infrared Study. *Catal. Today* **2016**, *277*, 21-28.
- (27) Miao, B.; Ma, S. S. K.; Wang, X.; Su, H. B.; Chan, S. H. Catalysis Mechanisms of CO₂ and CO Methanation. *Catal. Sci. Technol.* **2016**, *6*, 4048-4058.
- (28) Chang, Y. T.; Yamaguchi, Y.; Miller, W. H.; Schaefer III, H. F. An Analysis of the Infrared and Raman Spectra of the Formic Acid Dimer (HCOOH)₂. *J. Am. Chem. Soc.* **1987**, *109*, 7245-7253.
- (29) Zelsmann, H. R.; Marechal, Y. The Raman and IR Spectra of HCOOH and DCOOD Crystals at Low Temperature. *J. Mol. Struct.* **1976**, *29*, 367-368.
- (30) Chin, S. Y.; Williams, C. T.; Amiridis, M. D. J. FTIR Studies of CO Adsorption on Al₂O₃- and SiO₂-Supported Ru Catalysts. *J. Phys. Chem. B* **2006**, *110*, 871-882.
- (31) Busca, G.; Lamotte, J.; Lavalley, J. C.; Lorenzelli, V. FT-IR Study of the Adsorption and Transformation of Formaldehyde on Oxide Surfaces. *J. Am. Chem. Soc.* **1987**, *109*, 5197-5202.

-
- (32) Szanyi, J.; Kwak, J. H. Dissecting the steps of CO₂ reduction: 2. The Interaction of CO and CO₂ with Pd/ γ -Al₂O₃: an In Situ FTIR Study. *Phys. Chem. Chem. Phys.* **2014**, *16*, 15126-15138.
- (33) Vogt, C.; Groeneveld, E.; Kamsma, G.; Nachtegaal, M.; Lu, L.; Kiely, C. J.; Berben, P. H.; Meirer, F.; Weckhuysen, B. M. Unravelling Structure Sensitivity in CO₂ Hydrogenation over Nickel. *Nat. Catal.* **2018**, 127-134.
- (34) Hadjiivanov, K. I.; Vayssilov, G. N. Characterization of Oxide Surfaces and Zeolites by Carbon Monoxide as an IR Probe Molecule. *Adv. Catal.* **2002**, *47*, 307-511.
- (35) Hoffmann, F. M. Infrared Reflection-Absorption Spectroscopy of Adsorbed Molecules. *Surf. Sci. Rep.* **1983**, *3*, 107-192.
- (36) Shido, T.; Asakura, K.; Iwasawa, Y. Reactant-Promoted Reaction Mechanism for Catalytic Water-Gas Shift Reaction on MgO. *J. Catal.* **1990**, *122*, 55-67.

Supporting Information

In Situ Control of the Adsorption Species in CO₂ Reduction: Determination of Intermediates and Byproducts

Kun Zhao^{a,b*}, Ligang Wang^c, Marco Calizzi^{a,b}, Emanuele Moioli^{a,b}, Andreas Züttel^{a,b*}

^aLaboratory of Materials for Renewable Energy, Institute of Chemical Sciences and Engineering, École Polytechnique Fédérale de Lausanne (EPFL), 1951 Sion, Switzerland

^bSwiss Federal Laboratories for Materials Science and Technology (EMPA), 8600 Dübendorf, Switzerland

^cGroup of Energy Materials, Institute of Mechanical Engineering, École Polytechnique Fédérale de Lausanne (EPFL), 1951 Sion, Switzerland

Table of Contents:

Figure S4.1 Infrared spectra of reference samples

Figure S4.2 HCOO^{-*} hydrogenation on Ru/Al₂O₃ and on Al₂O₃

Figure S4.3 Gaussian fitting examples

Figure S4.4 CO₂ adsorption and co-adsorption with H₂ on Al₂O₃

Figure S4.5 Evolution of HCO₃^{-*} during CO₂ hydrogenation on reduced Ru/Al₂O₃ and Al₂O₃

Figure S4.6 Evolution of adsorption species during CO₂ hydrogenation in detail

Figure S4.7 Evolution of adsorption species during CO₂ adsorption in detail

Figure S4.8 Evolution of adsorption species during HCO₃^{-*} decomposition in detail

Figure S4.9 Evolution of adsorption species during CO^{*} hydrogenation in detail

Figure S4.10 Evolution of adsorption species during HCO₃^{-*} hydrogenation in detail

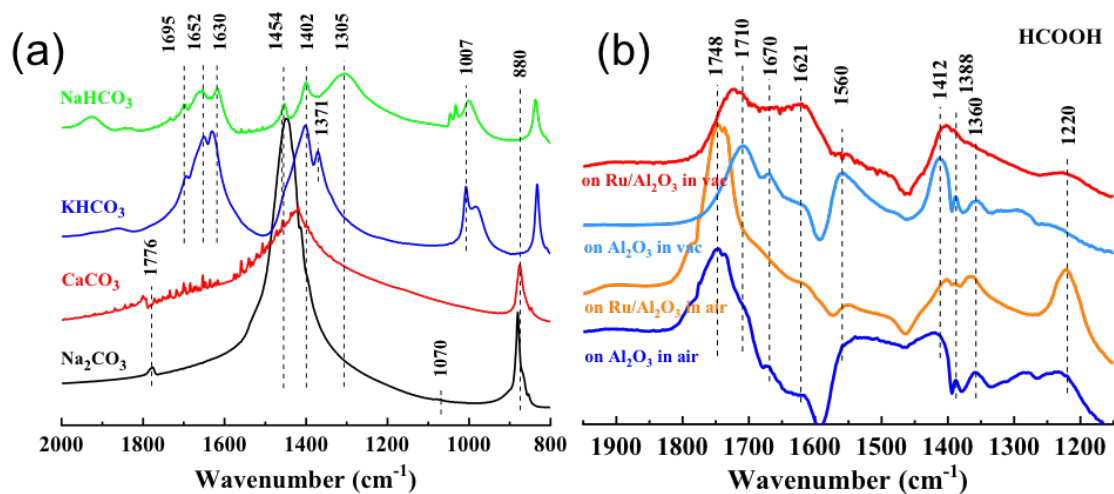


Figure S4.1. (a) FT-IR transmittance of Na_2CO_3 , CaCO_3 , KHCO_3 and NaHCO_3 . (b) Infrared spectra of Exp. VI adsorption of HCOOH on $\text{Ru}/\text{Al}_2\text{O}_3$ and Al_2O_3 in air followed by pumping to low vacuum.

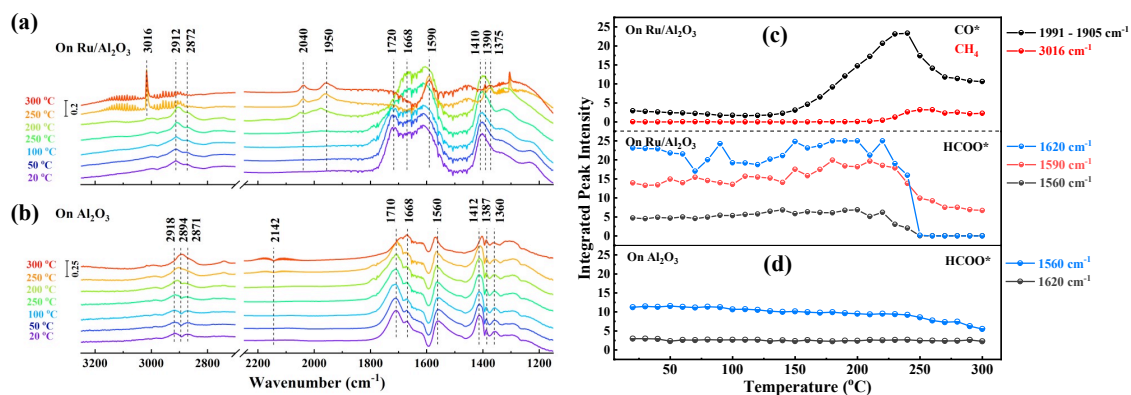


Figure S4.2. Infrared spectra of Exp. VII HCOOH hydrogenation on (a) $\text{Ru}/\text{Al}_2\text{O}_3$ and (b) Al_2O_3 . Variations of the peak positions with temperature on (c) $\text{Ru}/\text{Al}_2\text{O}_3$ and (d) Al_2O_3 . The infrared peaks at 1991-1905 cm^{-1} represent the bridged- CO^* on Ru , the peak of 3016 cm^{-1} represents CH_4 , the peaks at 1620, 1590, 1560 cm^{-1} represent bidentate- HCOO^* on Ru , bridged- HCOO^* on Ru , and bidentate- HCOO^* on Al_2O_3 respectively.

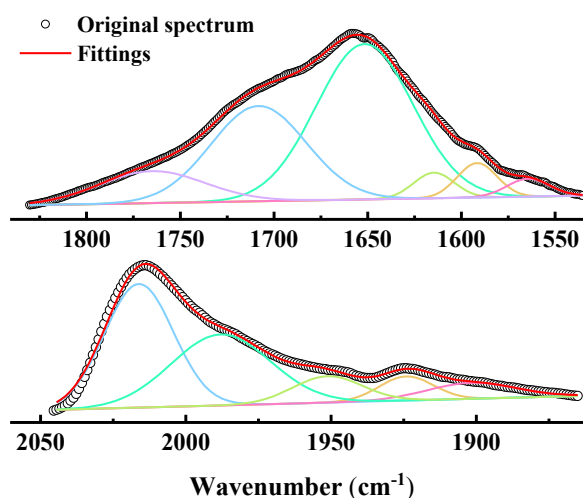


Figure S4.3. Gaussian fitting examples in the range of 1780~1600 cm^{-1} (upper panel) and 2070~1845 cm^{-1} (bottom panel) under 200 mbar CO_2 and 800 mbar H_2 at 20 °C in Exp. I on $\text{Ru}/\text{Al}_2\text{O}_3$.

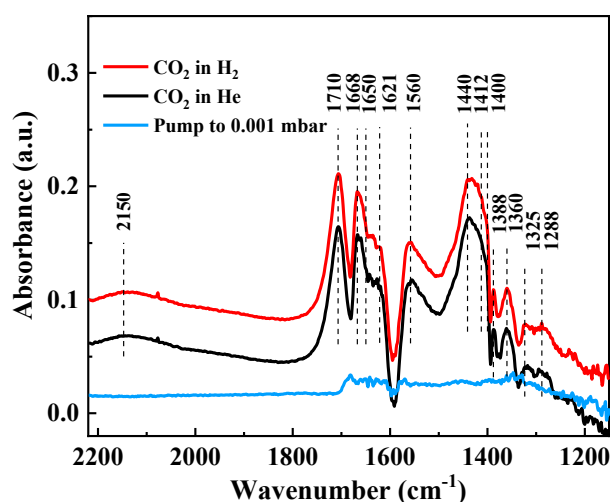


Figure S4.4. The infrared spectra of CO_2 adsorption (200 mbar CO_2 and 800 mbar He) and its co-adsorption with H_2 (200 mbar CO_2 and 800 mbar H_2) on Al_2O_3 at room temperature under 1 bar. The assignment of the peak positions were listed in Table S4.1.

Concerning the adsorption site of HCO_3^* , we do not have direct proof of HCO_3^* adsorption on the metal-support interface (MSI), but we judged this by three sufficient points: (1) the surface hydroxyl group (OH^*) is generally on Lewis acid site of Al_2O_3 . Since HCO_3^* formed by CO_2 reacting with OH^* , HCO_3^* has to locate on Al_2O_3 initially. (2) HCO_3^* formed on $\text{Ru}/\text{Al}_2\text{O}_3$ was much stronger than on Al_2O_3 (Figure S4.10). Thus this enhancement is because of the effect of MSI. (3) During CO_2 hydrogenation, HCO_3^* on $\text{Ru}/\text{Al}_2\text{O}_3$ was continuously formed from CO_2 until CO_2

concentration dropped. However, $\text{HCO}_3^-\ast$ on Al_2O_3 consumed fast and depleted at 160 °C, illustrating that $\text{HCO}_3^-\ast$ could not be continuously formed from CO_2 on Al_2O_3 . This proved that $\text{HCO}_3^-\ast$ from CO_2 hydrogenation on $\text{Ru}/\text{Al}_2\text{O}_3$ was located on MSI instead of on Al_2O_3 .

The intermediates located at the interface were $\text{HCO}_3^-\ast$ and bidentate $\text{HCOO}^-\ast$ on Ru. These two species were formed at the interface and active in the hydrogenation reaction. This means before the CO^\ast hydrogenation step, the CO_2 activation steps favourably took place at MSI. We added this explanation in the supporting information.

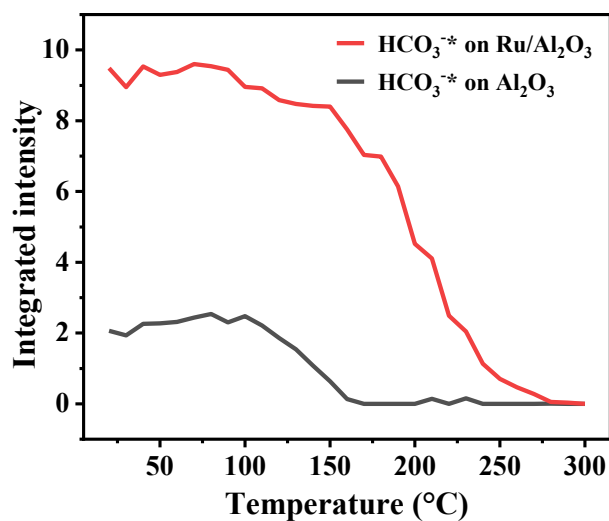


Figure S4.5 $\text{HCO}_3^-\ast$ evolution during CO_2 hydrogenation on reduced $\text{Ru}/\text{Al}_2\text{O}_3$ and Al_2O_3 .

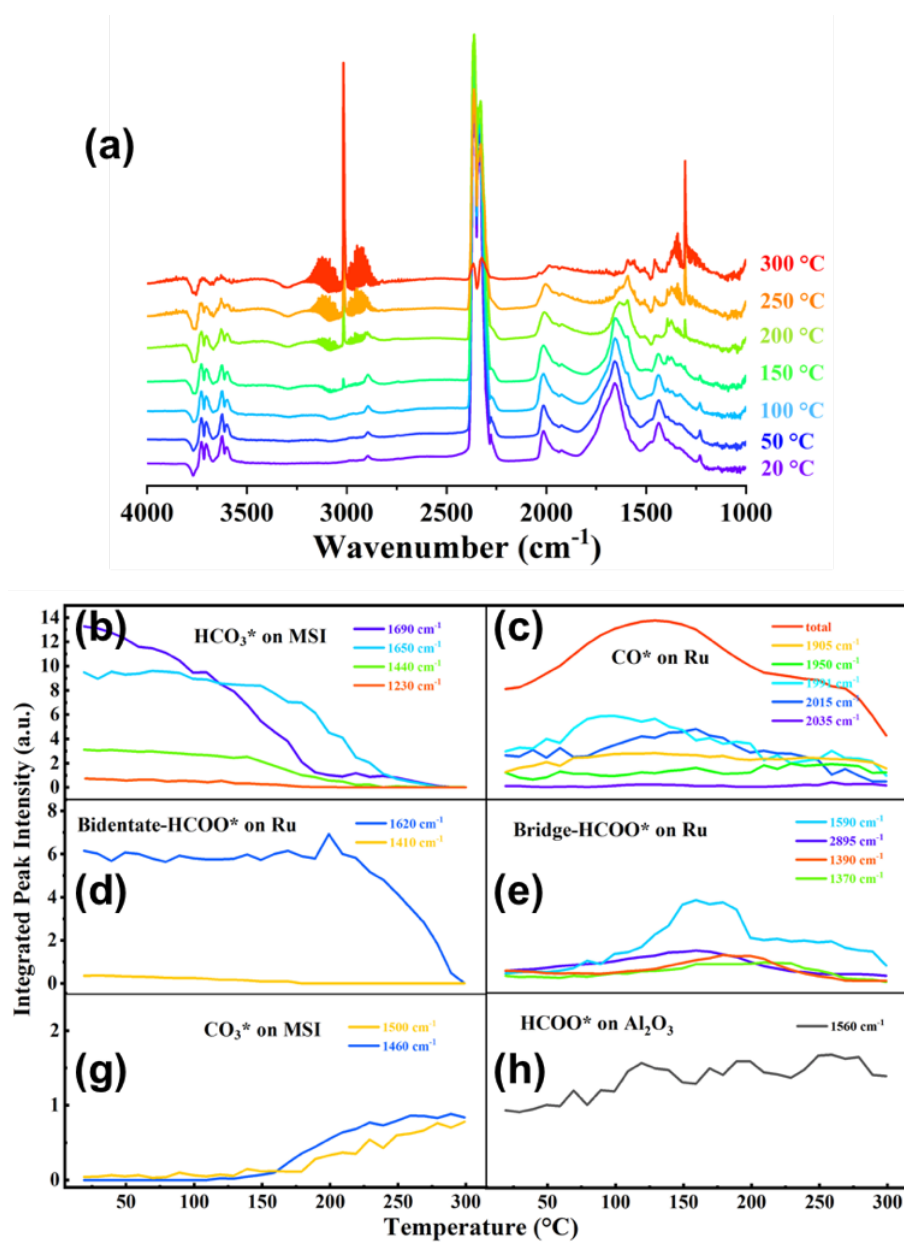


Figure S4.6. (a) The infrared spectra of Exp. I CO_2 hydrogenation on $\text{Ru}/\text{Al}_2\text{O}_3$. The temperature-dependent evolutions of bond vibrations of the adsorption species (b) HCO_3^* on metal-support interface (MSI), (c) all the structures of CO^* on Ru, (d) bidentate- HCOO^* on Ru, (e) bridged- HCOO^* on Ru, (g) CO_3^{2-} on MSI, and (h) bidentate- HCOO^* on Al_2O_3 . The assignment of infrared peak positions are listed in Table S4.1.

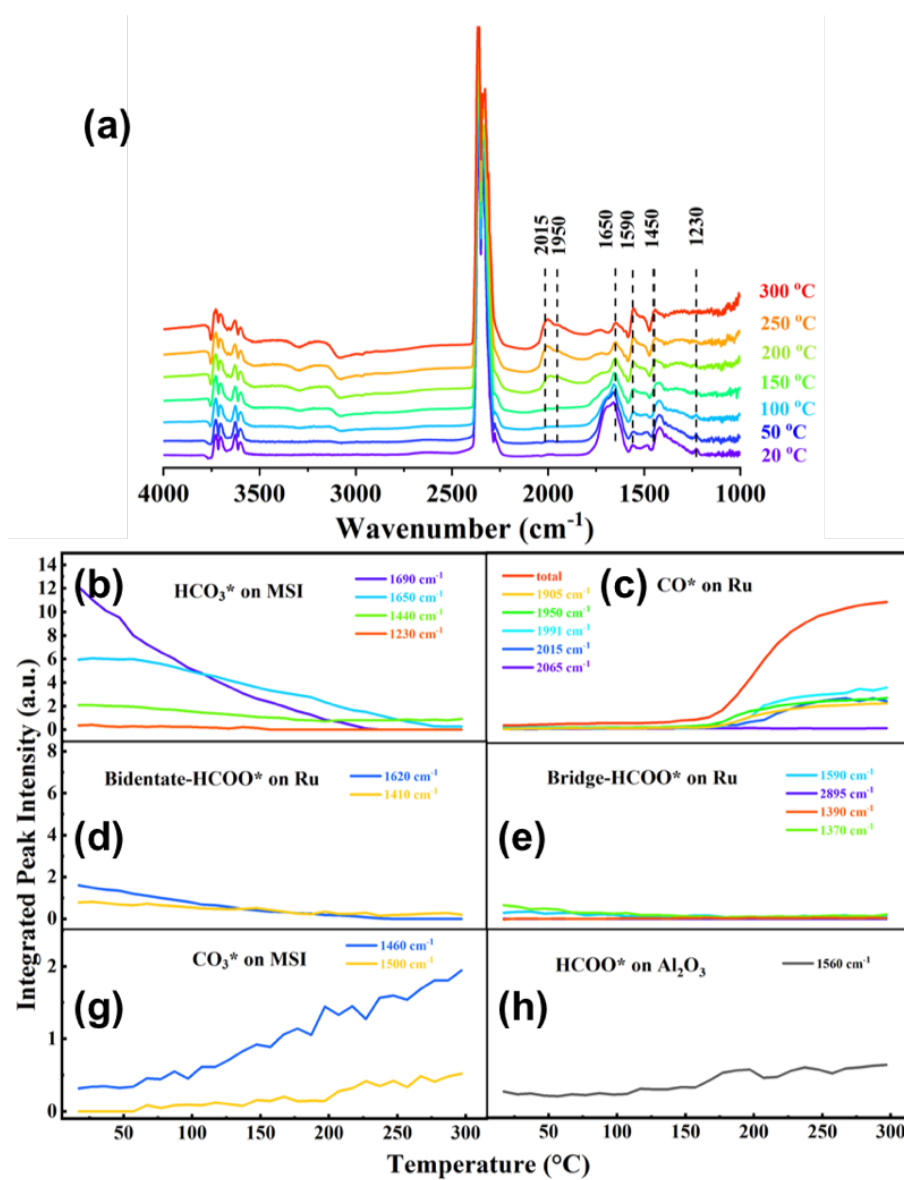


Figure S4.7 (a) The infrared spectra of Exp. II CO₂ adsorption on Ru/Al₂O₃. The temperature-dependent evolutions of bond vibrations of the adsorption species (b) HCO₃* on MSI, (c) all the structures of CO* on Ru, (d) bidentate-HCOO* on Ru, (e) bridged-HCOO* on Ru, (g) CO₃²⁻* on MSI and (h) bidentate-HCOO* on Al₂O₃. The assignment of infrared peak positions are listed in Table S4.1.

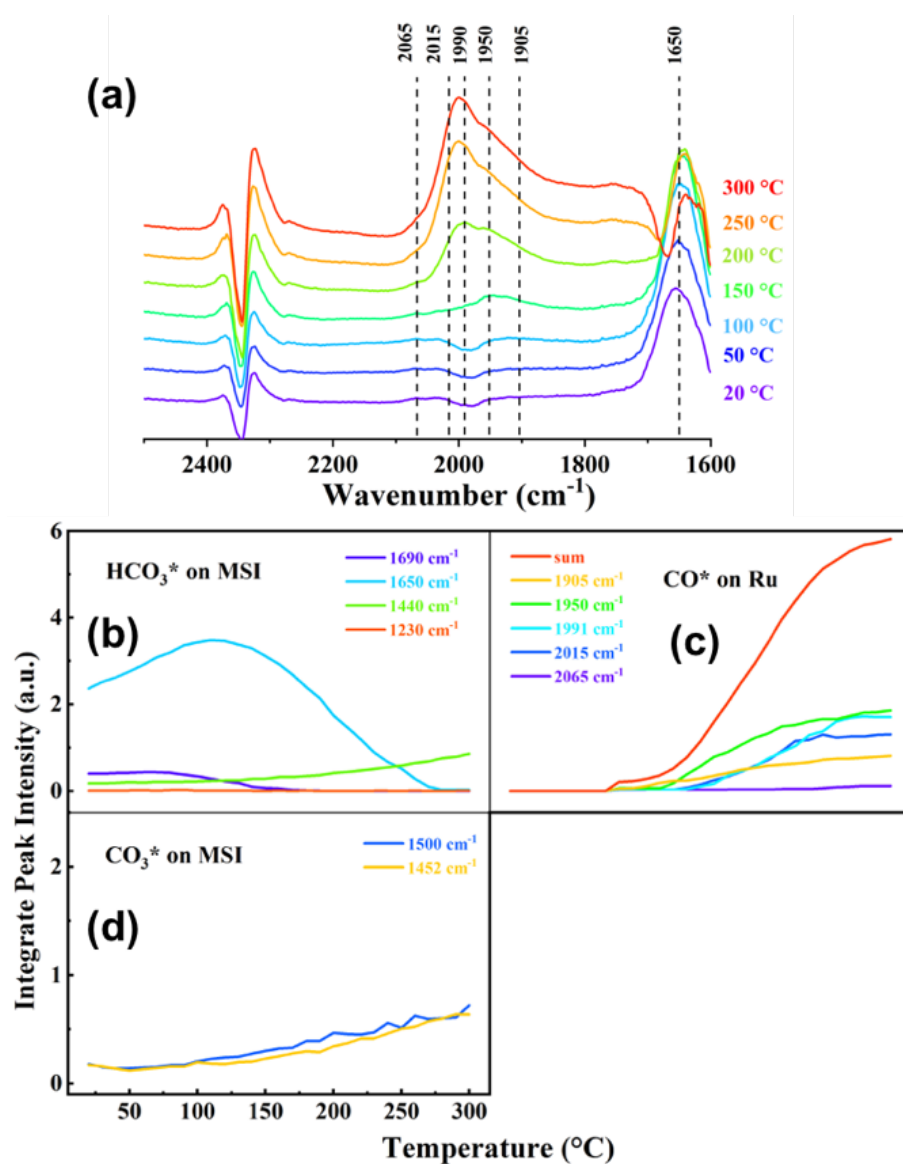


Figure S4.8 (a) The infrared spectra of Exp. III HCO_3^* decomposition on $\text{Ru}/\text{Al}_2\text{O}_3$. The temperature-dependent evolutions of bond vibrations of the adsorption species (b) HCO_3^* on MSI, (c) all the structures of CO^* on Ru and (d) CO_3^{2-*} on MSI. The assignment of infrared peak positions are listed in Table S4.1.

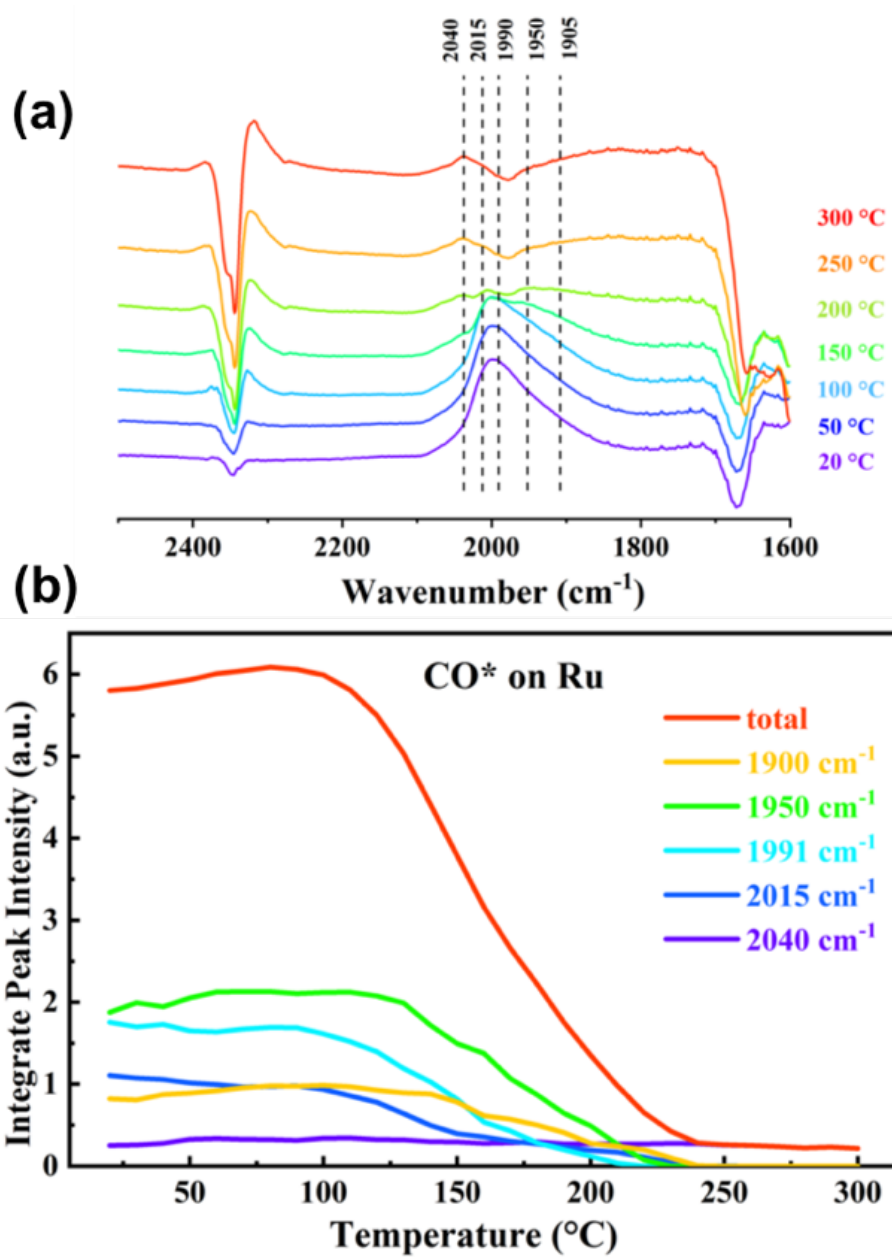


Figure S4.9 (a) The infrared spectra of Exp. IV CO* hydrogenation on Ru/Al₂O₃. (b) Variations of the bond vibrations for all CO* species with temperature. The assignment of infrared peak positions are listed in Table S4.1.

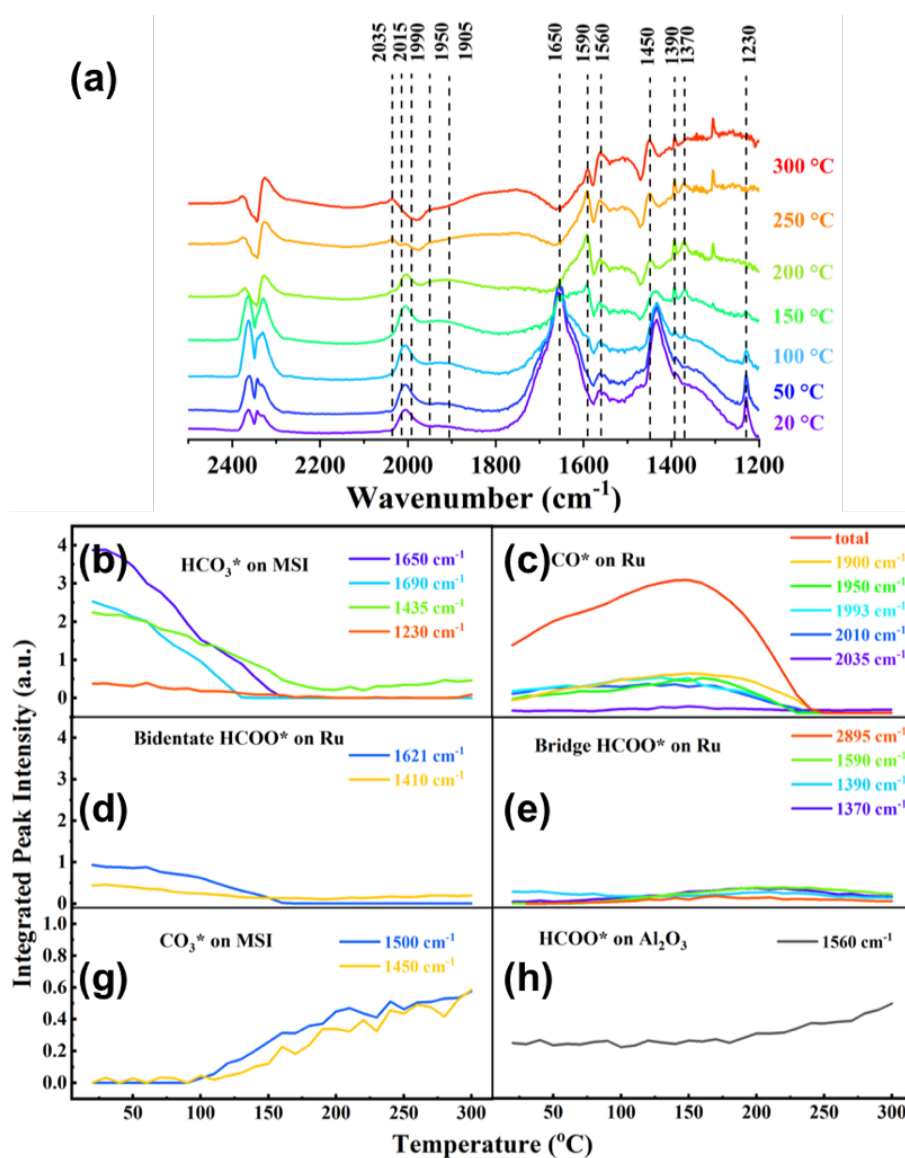


Figure S4.10 (a) The infrared spectra of Exp. V HCO_3^- hydrogenation on $\text{Ru}/\text{Al}_2\text{O}_3$. The temperature-dependent evolutions of bond vibrations of the adsorption species (b) HCO_3^- on MSI, (c) all structures of CO^* on Ru, (d) bidentate- HCOO^* on Ru, (e) bridged- HCOO^* on Ru, (g) CO_3^{2-} on MSI and (h) bidentate- HCOO^* on Al_2O_3 . The assignments of infrared peak positions are listed in Table S4.1.

Chapter 5 Unraveling and Optimizing the Metal-Metal Oxide Synergistic Effect in a Highly Active $\text{Co}_x(\text{CoO})_{1-x}$ Catalyst for CO_2 Hydrogenation

Kun Zhao^{a,b,*}, Marco Calizzi^{a,b}, Emanuele Moioli^{a,b}, Mo Li^{a,b}, Alexandre Borsay^{a,b}, Loris Lombardo^{a,b}, Robin Mutschler^{a,b}, Wen Luo^{a,b,*}, Andreas Züttel^{a,b}

^a Laboratory of Materials for Renewable Energy, Institute of Chemical Sciences and Engineering, École Polytechnique Fédérale de Lausanne (EPFL), 1951 Sion, Switzerland

^b Swiss Federal Laboratories for Materials Science and Technology (EMPA), 8600 Dübendorf, Switzerland

Preprint version: preprint version of the manuscript submitted on the scientific journal Journal of Catalysis.

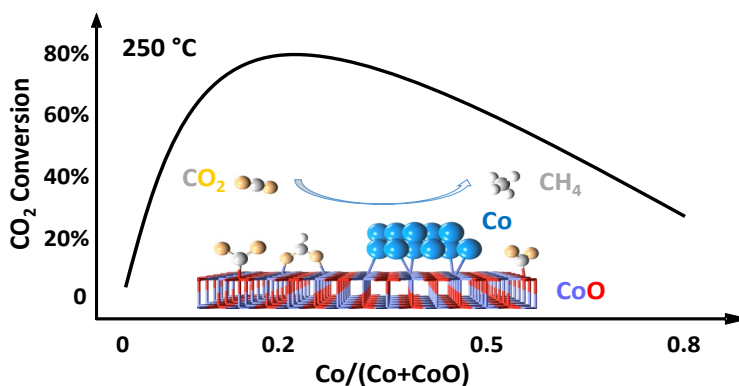
Edit: caption numbers of figures, tables, and equations were edited to adapter the thesis chapter number.

Summary: this Chapter is further work of developing new catalyst based on the previous discoveries of the relation between catalyst compositions and their reactivities in the CO_2 hydrogenation. The catalyst with high concentration of metal oxide boosts CO_2 conversion due to the enhanced CO_2 adsorption on the metal oxide.

Abstract

The relation between catalytic reactivities and metal/metal oxide ratios, as well as the functions of the metal and the metal oxides were investigated in the CO₂ hydrogenation reaction over highly active Co_x(CoO)_{1-x} catalysts in operando. The catalytic reactivity of the samples in the CO₂ methanation improves with the increased CoO concentration. Strikingly, the sample with the highest concentration of CoO, i.e., Co_{0.2}(CoO)_{0.8}, shows activity at temperatures lower than 200 °C where the other samples with less CoO are inactive. The origins of this improvement are the increased amount and moderate binding of adsorbed CO₂ on CoO sites. The derivative adsorption species are found to be intermediates of the CH₄ formation. The metallic Co functions as the electronically catalytic site which provides electrons for the hydrogenation steps. As a result, an abundant amount of CoO combined with Co is the optimal composition of the catalyst for achieving the highest reactivity for CO₂ hydrogenation.

Keywords: Cobalt and cobalt oxide; Reactivity; CO₂ hydrogenation; Active site; Adsorption; Activation energy



5.1 Introduction

CO₂ conversion to hydrocarbons has received enormous attention in the past decade for the possibilities of exploiting CO₂ as feedstock in the storage of sustainable energy and of closing the carbon cycle. Metal oxides-supported transition metals such as Fe, Co, Ni, Cu and Ru have been studied as effective catalysts in the CO₂ hydrogenation reaction. The main products of the reaction over the above-mentioned catalysts at atmospheric pressure are CH₄ and CO [1–5].

In general, CO₂ hydrogenation catalysts are prepared in the form of supported metal particles. The metal site is considered as the reactive center while the support is used for dispersing and stabilizing the metal nanoparticles [6,7]. However, recent studies showed that the support could also have an important role in the heterogeneous catalysis of carbon-related reactions. In methanol synthesis from CO₂ and H₂ on Cu-based supported catalysts, the ZrO₂ support facilitates the moderate bindings of the key reaction intermediates at the interface of Cu and ZrO₂ [8,9]. Moreover, different supports lead to different key intermediates of methanol production, e.g., TiO₂ and ZnO₂ support surfaces produce formate intermediate, while ZrO₂ support surface forms CO*, HCO*, and H₂CO* intermediates. The formate intermediate is less active for methanol formation compared to the other intermediates, resulting in a less active catalyst with TiO₂ support [10–12]. In higher alcohol synthesis from syngas over Co/CeO₂ catalyst, the CeO₂ support functions for dispersing the Co nanoparticles. However, the Co is partially oxidized into CoO_x due to the strong metal-support interactions. This results in an active Co-CoO_x pair for the higher alcohol synthesis where the Co site accounts for CO dissociation to form CH_x species and the CoO_x site accounts for CO undissociated activation to form CH_xO* species. These CH_x and CH_xO* species combine to form higher alcohol at the interface of Co and CoO_x [13]. In CO₂ and CO hydrogenation reaction, the partially cobalt nanoparticles on TiO₂ supports, Co/CoO/TiO₂, exhibit higher CO₂ and CO conversion rate than the metallic Co/TiO₂, indicating CoO improves reactivity of the catalyst either by the component itself or by forming active interface with the metal or with the support. However, changing the TiO₂ support to SiO₂ support reversed the activity, implying that different support varies the activity of the catalyst [14]. An early work from Somorjai and co-workers claimed a promotion effect of oxide on Rh metal surface for the CO and CO₂ hydrogenation [15]. The promotion effect was attributed to the high Lewis acidity of the metal cations of the oxide by the possible function of cleavage of the C–O bond at the interface of Rh/oxide for CH₄ formation. Therefore, they suggested the support participated in the catalytic reaction via cleaving chemical bonds, but this was still disputable. Recent work using supports from Lewis acidic to basic properties to study the support effects in Fischer-Tropsch reaction

demonstrated a volcano relation between the reaction rate and Lewis acid-base nature of the support, where the supports was not considered to be catalytic active [16].

The above-mentioned arguments on the role of the support motivate us to clarify the role of the support in the CO₂ hydrogenation reaction, and the relation between the combinations of metal and support and their catalytic reactivity, as these are important for the design of efficient catalysts for CO₂ conversion. In our previous study on a Ru/Al₂O₃ catalyst, we found that CO₂ adsorbed initially on the Al₂O₃ surface and on the interface of Al₂O₃ and Ru. Then the adsorbed CO₂ and its derivative species migrate to the Ru atoms for the subsequent hydrogenation steps. The support itself did not provide a site for the CO₂ hydrogenation steps [17,18]. Herein, we hypothesized that there might be an optimized metal to metal oxide ratio for the highest reactivity toward CO₂ hydrogenation.

To explore this hypothesis, we would like to synthesize catalysts with varying fractions of metal and support for CO₂ hydrogenation. However, a “foreign” support could create multiple interfaces, i.e. metal/metal oxide interface, metal/support interface, metal oxide/support interface due to strong metal-support interaction, and this would make it difficult to explore cleanly the effect of the metal/metal oxide ratio [19–22]. To avoid this complexity and to vary only the metal/oxide ratio, we designed a “self-supported” cobalt catalyst with different ratios of the metallic Co and the CoO, i.e., Co_x(CoO)_{1-x} with 0 < *x* < 1.

Herein, we developed an in operando reduction method to synthesize the Co_x(CoO)_{1-x} samples and to analyze the CO₂ hydrogenation reaction in continuous experiments on one platform: a diffuse reflectance infrared Fourier transform spectroscopy-mass spectroscopy-gas chromatograph (DRIFTS-MS-GC) instrument, previously described [23]. The molar concentrations of Co were quantified using the H₂ consumption from the MS data. To verify this in situ quantification, X-ray photoelectron spectroscopy (XPS) was applied to analyze the compositions and the ratios of Co content in the catalysts. Subsequently, the reactivity of these Co_x(CoO)_{1-x} samples in the CO₂ hydrogenation reaction was investigated in the DRIFTS-MS-GC instrument. The gas phase and catalyst surface were observed simultaneously to unravel the reaction mechanisms. To understand the origins of the different reactivities, we analyzed the gas–surface interaction using temperature-programmed desorption–mass spectroscopy (TPD-MS). Additionally, surface electronic structures of these samples were measured using near ambient-pressure X-ray photoelectron spectroscopy (NAP-XPS) to check whether the oxide creates special electronic states for the catalysis.

The specific purpose of this work is to answer three key scientific questions: (1) What is the optimal ratio of metal/metal oxide to achieve the highest reactivity in CO₂ hydrogenation? (2) Is the role of the support simply to disperse the metal nanoparticles or does it have a direct role in the reaction? (3) If there is a direct role, is it only to provide adsorption sites for CO₂ and the associated adsorbed species, or also to provide electronically active sites that reduce those adsorbed species to hydrocarbons?

We found that the reactivity of the samples depended strongly on the Co/(Co+CoO) molar ratio. Importantly, we produced a catalyst that is highly active at low reaction temperature. The catalyst with a higher concentration of CoO has a lower onset reaction temperature, a lower activation energy of CH₄ formation, and a higher CO₂ conversion. We demonstrate that the improved activity of the catalyst stems solely from the role of CoO in providing sites for CO₂ adsorption and lowering the CO₂ binding energy, but not in providing active sites for the hydrogenation reaction.

5.2 Experimental Methods

5.2.1 Sample preparations

The samples were prepared by starting with Co₃O₄ and then reducing this material in H₂ at various temperature/time profiles to produce several self-supported catalysts with controlled ratios of Co and CoO, Co_x(CoO)_{1-x} (0 < x < 1). Co₃O₄ was obtained by calcination of Co(NO₃)₂·6H₂O (Sigma-Aldrich, 98%) at 300 °C for 12 h followed by a temperature ramp of 2 °C min⁻¹ to 400 °C and then continued calcination for 2 h at 400 °C.

To determine the temperature required for reducing Co₃O₄, the reduction process was tracked with a microbalance (Rubotherm, Germany). Typically, 160 mg of Co₃O₄ was loaded in the microbalance and a gas flow mixture of 30 mL min⁻¹ H₂ and 45 mL min⁻¹ He at 1 bar was supplied 3 h before the reduction to remove the air. A heating ramp of 2 °C min⁻¹ from 25 °C to 400 °C was then applied and the mass loss due to reduction was monitored with an accuracy of 1 µg.

Co_x(CoO)_{1-x} (0 < x < 1) catalyst synthesis. The actual catalyst samples used in this study were prepared by reduction of Co₃O₄ in the reaction chamber (HVC, Harrick Scientific) of a DRIFTS instrument (Bruker Tensor 27) in a mixture of H₂/He (flow rate 6 mL min⁻¹/4 mL min⁻¹). Control of the reduction temperature and time allowed us to obtain samples with different Co ratios in a reproducible manner. During reduction, the pressure in the chamber was kept constant at 1 bar by a back

pressure valve installed at the exhaust side of the reaction chamber. A quadrupole mass spectrometer (MS, Pfeiffer OmniStar 320) was connected with the DRIFTS reaction chamber to analyze the composition of reactant and product gases using a Faraday detector.

5.2.2 Characterization

MS measurements. The amount of H_2 consumed during the reduction was determined by MS analysis. This allowed us to quantify the removal of O atoms from Co_3O_4 during the reduction process and thus obtain the bulk composition of the catalyst.

XPS core level measurements. To quantify the fraction of metallic cobalt on the surface of the $Co_x(CoO)_{1-x}$ catalysts, samples were transferred to the XPS through a glovebox to avoid surface oxidation by the air. The XPS is equipped with a dual anode X-ray source and a Phoibos 100 (SPECS GmbH) hemispherical energy analyzer. The Mg K_α (1253.6 eV) source was used for this study. The survey scan and narrow scan were collected at 90 eV and 20 eV pass energy, respectively. The oxidation states of partially oxidized Co samples were deconvoluted using CasaXPS software. Separate measurements of Co, CoO and Co_3O_4 were used to provide the standard peaks used for the deconvolution.

NAP-XPS valence band measurements. In addition to the core level XPS spectra, we performed measurements of the valence band to probe which components of our samples are catalytically active. The above XPS instrument did not have sufficient resolution for this purpose. Instead, we used a NAP-XPS (SPECS GmbH) instrument. An Al K_α (1486.6 eV) monochromatic X-ray source and a Phoibos 150 NAP hemispherical energy analyzer were used. Survey scans were taken with 50 eV pass energy and narrow scans with 10 eV pass energy. Unfortunately, we could not transfer the samples to this system without exposure to air. To overcome this difficulty we reduced air exposed sample in-situ in the NAP-XPS using H_2 . This allowed us to study partially reduced samples and measure the valence band of the Co and CoO components. The details of this procedure are given in section 3.6.

N_2 adsorption-desorption isotherm. The specific surface areas were evaluated using a BELSORP mini system (MicrotracBEL Corp., Japan) by nitrogen adsorption-desorption isotherms at 77 K, and was calculated by the Brunauer-Emmet-Teller (BET) method from the built-in software. The empty tube was measured at the same time of the measurements of the samples in order to eliminate the dead volume. The results were listed in Table 1. As we obtained small values of BET surface areas,

we measured the nitrogen adsorption-desorption isotherm again in another instrument, Micromeritics Tristar 3000, to be sure of the obtained values. The CO₂ adsorption-desorption isotherm was measured as well at room temperature using Micromeritics Tristar 3000 instrument for evaluating the CO₂ adsorption amount. The BET surface areas and CO₂ adsorption amounts from the Micromeritics Tristar 3000 instrument were listed in Table S1. As the samples were transferred through a glovebox, no activation was applied before the measurements. The accuracies of the measurements were 0.01 cm² mg⁻¹.

TEM. The morphology of the samples was visualized in TEM (FEI Tecnai Spirit microscope) operating at 120 kV. The ultrasonic dispersion in ethanol was applied for the sample preparation. The dispersed samples with ethanol were dropped onto the TEM carbon/copper grids and dried in air.

5.2.3 CO₂ hydrogenation

CO₂ hydrogenation reaction on Co_x(CoO)_{1-x} samples was carried out in an operando surface-gas analysis system. The reactor is a DRIFTS reaction chamber, which at the inlet is connected to a mass flow controller system, and at the outlet is connected to an MS and GC (SRI 8610C). The GC was equipped with a flame ionization detector (FID) and a thermal conductivity detector (TCD). This setup allows gathering surface information by DRIFTS while quantifying the gases by MS and GC. For CO₂ hydrogenation reaction, typically, a Co_x(CoO)_{1-x} sample (160 mg) was compressed into a pellet with 4 mm high and 6 mm diameter. In general, the inlet gas was a mixture of CO₂/H₂/He with flow rates of 1.5 mL min⁻¹/6 mL min⁻¹/4 mL min⁻¹, respectively, at 1 bar. The reaction temperature was programmed from 20 to 350 °C at a heating rate of 2 °C/min. The background of the infrared spectra was taken on the as-reduced sample surface (or 3 h of H₂/He flushed surface for Co₃O₄) in H₂/He flow at room temperature. The infrared spectra were collected every 10 min with spectroscopic resolution of 2 cm⁻¹. The MS determined the mass range of 0–50 amu with a rate of 0.5 s per mass unit. The GC took 9 min for each spectrum, with a cooling interval of 4 min between each scan.

5.2.4 CO₂ + H₂ adsorption

CO₂ + H₂ co-adsorption on the samples at room temperature was measured with TPD-MS in a flow gas condition where He was used as the carrier gas. The experimental steps include: (1) Co₃O₄ sample was loaded in a quartz tube in air and reduced in H₂/He flow (6 mL min⁻¹/4 mL min⁻¹) in TPD-MS to obtain the fresh Co_x(CoO)_{1-x} sample; (2) the as-prepared Co_x(CoO)_{1-x} sample was flushed by He for one hour; (3) 10 mL min⁻¹ CO₂ and 10 mL min⁻¹ H₂ gases were applied for 20 min; (4) He

flush for at least 40 min to remove the gas phase CO_2 and H_2 ; (5) heating started to trigger the desorption. The working pressure on the sample was 1 bar. The spectra were taken using a Faraday detector at heating rates of 5, 10, 15, 25, and $40\text{ }^\circ\text{C min}^{-1}$.

5.3 Results and Discussion

5.3.1 Sample synthesis and characterization

It is generally accepted that the reduction of Co_3O_4 proceeds in a two-step process: Co_3O_4 to CoO , and CoO to Co . However, the reduction temperature of each step is strongly influenced by the properties of Co_3O_4 [13,24–27]. To determine the reduction process of our Co_3O_4 sample, a microbalance was used to monitor the weight loss during the reduction. As shown in Figure 5.1, the mass loss shows that Co_3O_4 starts to be reduced at around $200\text{ }^\circ\text{C}$. Until $300\text{ }^\circ\text{C}$, approximately 7% mass loss can be observed, indicating the removal of one oxygen atom per Co_3O_4 molecule to form CoO . Above $300\text{ }^\circ\text{C}$, the slope of the mass loss curve increases and finally the mass loss reaches a plateau of 27% at $370\text{ }^\circ\text{C}$, which can be ascribed to the complete reduction of Co_3O_4 to metallic cobalt. This analysis demonstrates that through controlling the reduction temperature and the reduction time, we can obtain samples with different extents of partially reduced Co.

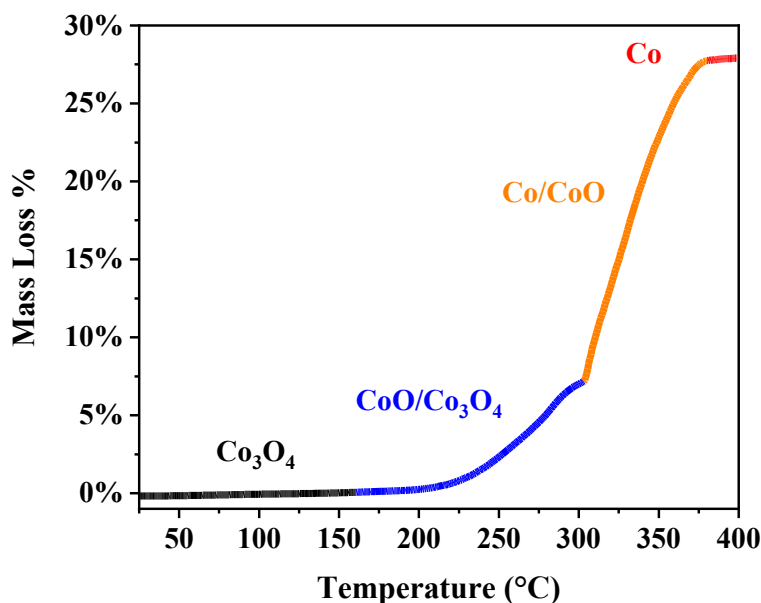


Figure 5.1. Mass loss of Co_3O_4 sample when reduced in H_2/He flow with a heating rate of $2\text{ }^\circ\text{C min}^{-1}$ in a microbalance.

Using the microbalance results as a guidance to find the temperature to use for reduction, we prepared the catalyst samples in situ in the DRIFTS reaction chamber. This avoided exposing the samples to

air before running reactions. We produced three $\text{Co}_x(\text{CoO})_{1-x}$ samples at different conditions. The amount of reduced Co in each sample was determined by quantifying the H_2 consumed during the reduction. Details on the experimental procedures are given in Section S5.1 and Figure S5.1. The method of preparation was very reproducible as shown in Figure S5.2. Table 5.1 summarizes the results of the sample preparation for three sets of temperature-time processing conditions. The table gives the $\text{Co}/(\text{Co}+\text{CoO})$ ratios as determined by hydrogen consumption from the MS analysis as well as data on this ratio obtained by XPS and surface area determined by BET. It is clear that higher reduction temperatures lead to a higher fraction of reduced Co. The reduction time at a given temperature was chosen to obtain a stable ratio of $\text{Co}/(\text{Co}+\text{CoO})$. XRD patterns of $\text{Co}_x(\text{CoO})_{1-x}$ also confirm the reduction of Co_3O_4 to metallic cobalt and CoO (Figure S5.3).

Table 5.1. H_2 reduction conditions, metal ratio and specific surface area of $\text{Co}_x(\text{CoO})_{(1-x)}$ samples.

Sample	H_2 reduction conditions	$\text{Co}/(\text{Co} + \text{CoO})$ ratio from MS	$\text{Co}/(\text{Co} + \text{CoO})$ ratio from XPS	BET surface area ($\text{m}^2 \text{g}^{-1}$)
Co_3O_4	N/A	0	0	18.59
$\text{Co}_{0.2}$	200 °C 10 h	0.16 ± 0.01	0.19	13.92
$\text{Co}_{0.5}$	300 °C 5 h	0.57 ± 0.05	0.51	5.62
$\text{Co}_{0.8}$	400 °C 4 h	0.79 ± 0.04	0.75	2.09

Further verification of the oxidation states of $\text{Co}_x(\text{CoO})_{1-x}$ was given by XPS measurements via air-free transfer of the samples from the DRIFTS chamber to a glovebox attached to the XPS. As shown in Figure 5.2, the as-prepared Co_3O_4 sample shows typical nonsymmetric $2p_{3/2}$ and $2p_{1/2}$ peaks at 780.0 and 795.1 eV, respectively, with additional weak satellite peaks, confirming that the surface composition is Co_3O_4 . The $\text{Co}_x(\text{CoO})_{1-x}$ samples were deconvoluted with standard Co and CoO spectra, where the $2p_{3/2}$ and $2p_{1/2}$ peaks of metallic cobalt located at 778.7 and 793.7 eV, respectively, and those of CoO located at 781.1 and 796.8 eV. The ratios of the peak areas showed that the fractions of Co were 19%, 51%, and 75% for the three $\text{Co}_x(\text{CoO})_{1-x}$ samples. The slight difference in the value of Co fraction compared to the results calculated from H_2 consumption is likely due to that XPS is surface sensitive while H_2 consumption is bulk sensitive. Referring to the quantifications from both XPS and H_2 consumption, we name the samples as $\text{Co}_{0.2}$, $\text{Co}_{0.5}$, and $\text{Co}_{0.8}$.

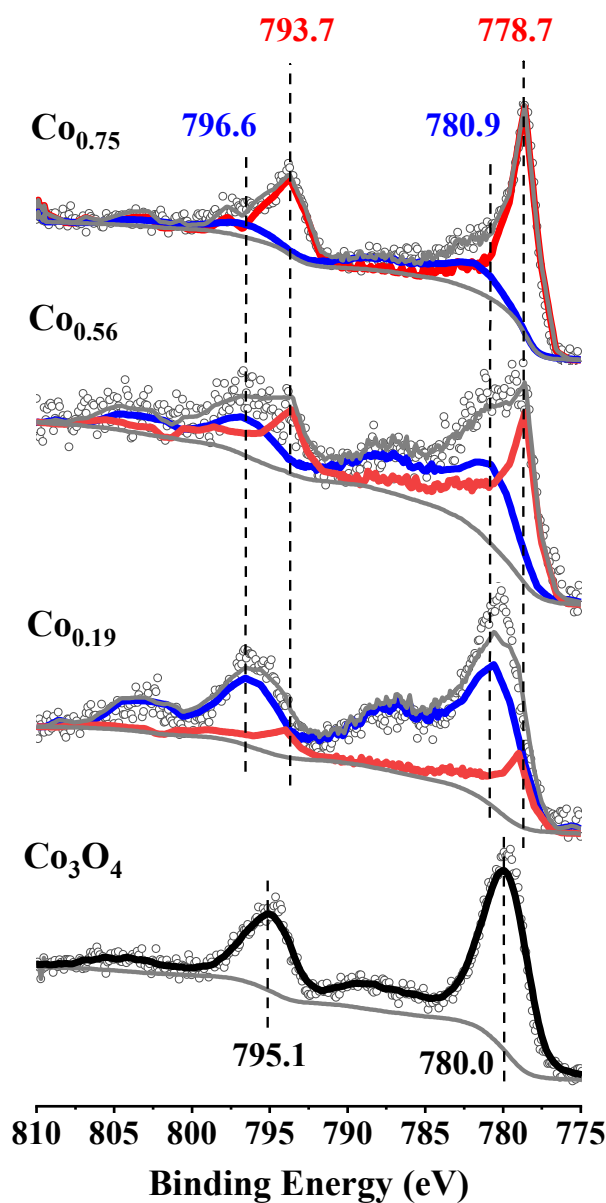


Figure 5.2. XPS of Co 2p_{3/2} and 2p_{1/2} peaks of synthesized samples. Black, blue and red lines represent the deconvoluted signals of Co₃O₄, CoO and Co states, respectively. Gray and gray dash lines are the total fitted spectra and baseline, respectively. The peaks were fitted by using the standard spectra of Co₃O₄, CoO and Co.

The morphology of the samples was visualized using TEM. As shown in Figure 5.3, all four samples show elongated particle shape and the particle width increases from 20 to 100 nm along with increasing metallic cobalt concentration. The increased particle size originates from the sintering of metallic cobalt through high temperature reduction treatment. BET measurements were used for evaluating the specific surface area (Table 5.1). In agreement with the TEM image, the specific surface area decreases with the increased ratio of metallic cobalt.

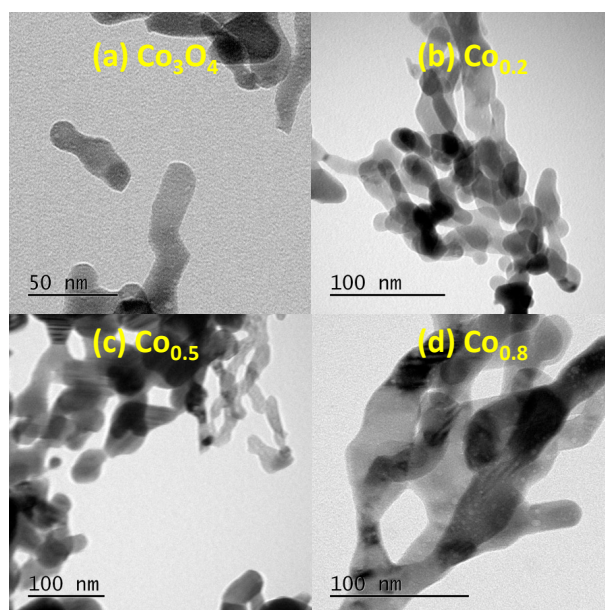


Figure 5.3. TEM of prepared samples. (a) Co_3O_4 , (b) $\text{Co}_{0.2}$, (c) $\text{Co}_{0.5}$, (d) $\text{Co}_{0.8}$.

5.3.2 Activity in the CO_2 conversion

The activities of the $\text{Co}_x(\text{CoO})_{1-x}$ samples for the CO_2 hydrogenation reaction were evaluated in the DRIFTS chamber under a $\text{CO}_2/\text{H}_2/\text{He}$ gas flow with a programmed temperature ramp. To check the reactivity of the samples in a wide temperature range, we heated the reaction chamber from room temperature up to a high temperature of 350 °C. Figure 5.4(a) shows the CO_2 conversion, as measured by the consumption of CO_2 , as a function of reaction temperature. The trend of CO_2 conversion over the different samples is in the order $\text{Co}_{0.2} > \text{Co}_{0.5} > \text{Co}_{0.8} > \text{Co}_3\text{O}_4$ at any given temperature below 280 °C. For instance, 63%, 53%, and 23% CO_2 are converted at 250 °C on $\text{Co}_{0.2}$, $\text{Co}_{0.5}$, and $\text{Co}_{0.8}$ samples, respectively. The CO_2 conversion reaches highest value with 98%, 99%, and 93% at 350 °C on $\text{Co}_{0.2}$, $\text{Co}_{0.5}$, and $\text{Co}_{0.8}$ samples, respectively. The reason of the similar high conversion at this high temperature could be that the reaction approaches the thermodynamic limit. The same trend was found in the yield of the main product CH_4 (Figure S5.4). The yields are commensurate as the CO_2 conversion. For comparison, the conversions obtained here are higher than the conversions on the commercial 0.5 wt% $\text{Ru}/\text{Al}_2\text{O}_3$ catalyst at the same applied pressure at 1 bar and space velocity at 5300 h^{-1} as in this work [3]. The maximum conversion of CO_2 on that $\text{Ru}/\text{Al}_2\text{O}_3$ is reported to be 75% and at 380 °C, where 75% conversion is found at 260 °C on our $\text{Co}_{0.2}$ sample. These conversions are also much higher than the reported <60% CO_2 conversion on the 3% $\text{Ru}/\text{Al}_2\text{O}_3$ and 20% $\text{Ni}/\text{Al}_2\text{O}_3$ samples at the temperature of 350 °C and space velocity of 55000 h^{-1} [28]. The details of CO_2 conversion, CH_4 yield, CH_4 selectivity, and CH_4 production rate per surface area via normalizing with

BET surface area at 200, 225, 250, 275, 300, 325, and 350 °C are showed in Section S5.3 Figure S5.5. The CO₂ conversion and CH₄ yield and selectivity have similar trends as the CO₂ conversion profile shown in Figure 5.4(a). The CH₄ production rate per surface area inverts this trend, plausibly indicating that the Co is the location where the hydrogenation step takes place.

In addition, we tested the reactivity of the Co_{0.2} sample for long-time CO₂ hydrogenation reaction (Figure S5.6). We found that the CO₂ conversion to CH₄ remains stable above 80% after 3 days in stream, demonstrating the sample is long-time active. Therefore, the Co_x(CoO)_{1-x} samples are highly active and efficient for the Sabatier reaction. The differences in the reactivity of these partially reduced samples imply a dependence on the initial state of the catalysts, although the samples could have been further reduced at the high reaction temperature. We believe the reactivity of the Co₃O₄ sample at high temperature is due to some limited partial reduction of this sample in the CO₂/H₂/He gas flow.

Strikingly, these partially reduced samples are quite active at low temperatures. The onset temperatures of CO₂ conversion (2% conversion) increase in the order Co_{0.2} < Co_{0.5} < Co_{0.8} < Co₃O₄, at temperatures of 160, 178, 202, and 275 °C, respectively (Figure 5.4(b)). We compared the CO₂ conversion extent at temperatures of 180, 200, and 220 °C on these samples. As shown in Figure 5.4(c), Co_{0.2} sample shows activity at 180 °C while the other samples are not active at this low temperature. Co_{0.2} sample converts 16% and 31% CO₂ at 200 and 220 °C, respectively at the applied space velocity of 5300 h⁻¹. Note that decreasing the space velocity will increase the conversion. These conversions are higher than those on all the rest of the samples at the same temperatures. These results verify our hypothesis that there is an optimal ratio of metal/metal oxide to obtain the highest reactivity toward CO₂ hydrogenation.

The rate constants of CH₄ production were calculated with the assumption of an overall first-order reaction of CO₂ to CH₄ [28–32]. As shown in Figure 5.4(d), the highest rate constant occurs on Co_{0.2} sample at the given temperatures, and decreases gradually when the metallic cobalt concentration increases (excluding the Co₃O₄ sample).

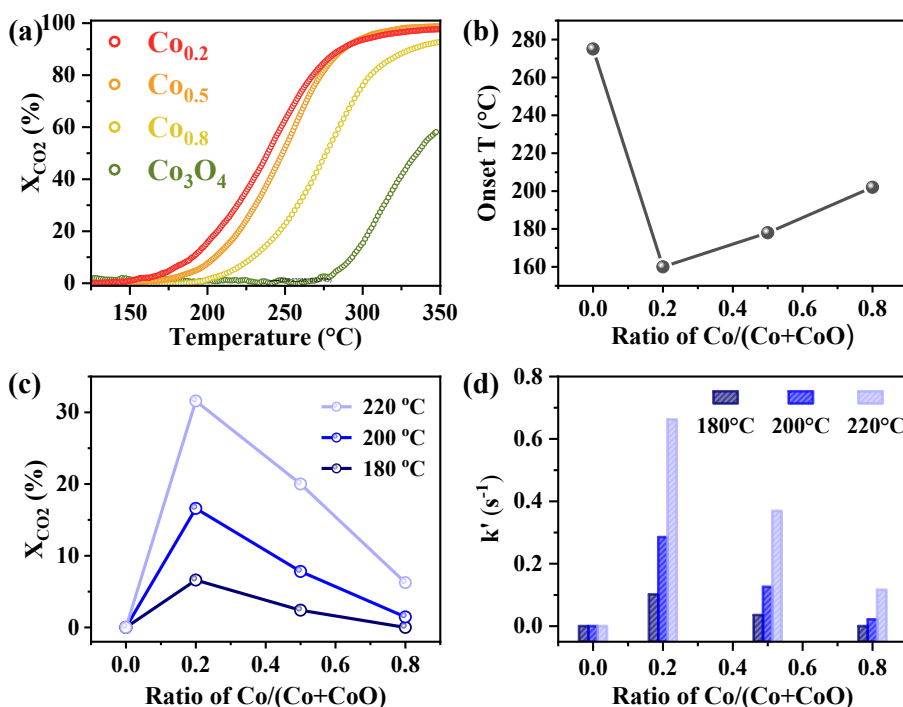


Figure 5.4. (a) CO₂ conversion as a function of temperature, (b) onset temperature of 2% CO₂ conversion, (c) CO₂ conversion at 180, 200, and 220 °C, and (d) CH₄ production rate at 180, 200, and 220 °C over the Co₃O₄, Co_{0.2}, Co_{0.5} and Co_{0.8} samples.

Small amounts of CO and C₂H₆ were also detected by MS and GC, and GC data were used to quantify the yield (Figure S5.7). The maximum yield of C₂H₆ increases for samples with increasing Co/(Co+CoO) ratio, opposite to CH₄ yield (Figure S5.8). C₂H₆ yield is around five-fold larger than CO yield on Co_x(CoO)_{1-x} samples, but threefold lower than CO yield on Co₃O₄ (Figure S5.7). These results suggest that C₂H₆, generated through carbon chain growth, is preferably produced on the samples with high Co concentration. Hence, the metallic site, instead of the oxide site, is responsible for the carbon-carbon coupling. This is in agreement with results for the Fischer–Tropsch reaction where metallic cobalt is the active site for carbon chain growth [33]. On the other hand, pure Co₃O₄ surface produces more CO than C₂H₆, suggesting that a reversed-water-gas-shift reaction is more favorable than the carbon-carbon coupling on the pure oxide surface.

The activation energy of CH₄ production, $E_a^f(\text{CH}_4)$, was determined using the Arrhenius equation. Details of the calculations based on the measured MS data are given elsewhere [23]. Figure 5.5 shows the Arrhenius plot and the values of $E_a^f(\text{CH}_4)$. The $E_a^f(\text{CH}_4)$ over the samples increases in the order of Co_{0.2} < Co_{0.5} < Co_{0.8} < Co₃O₄. Thus, we see that samples with lower activation energies have lower

onset reaction temperatures and higher CO₂ conversions before approaching to the thermodynamic limit.

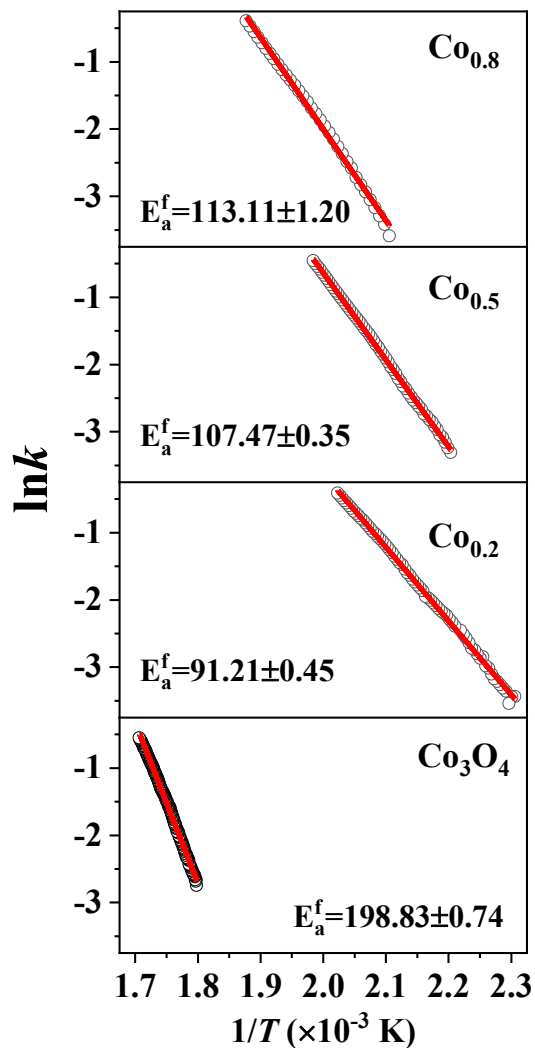


Figure 5.5. Arrhenius plot of CH₄ formation in the CO₂ conversion range of 2%–30% for Co_{0.2}, Co_{0.5}, Co_{0.8}, and Co₃O₄ samples. The corresponding temperature ranges are 160–220 °C for Co_{0.2} sample, 180–231 °C for Co_{0.5} sample, 202–260 °C for Co_{0.8} sample, and 283–313 °C for Co₃O₄ sample.

5.3.3 Sample stability during hydrogenation

As the CO₂ hydrogenation environment is highly reductive, there is an issue of the stability of the samples during the hydrogenation reaction. For temperatures well below those used to prepare the samples, we are confident that the composition is stable, since the preparation reaction was run long time enough for the composition to reach a constant value as confirmed by the ceasing in hydrogen

consumption (Figure S5.1). Hence, the measurements of onset temperatures for the reaction (Figure 5.4(a, b)) and reaction rate at low temperatures (Figure 5.4(c, d)) should correspond to the initial compositions of the samples.

To check the sample stability after high temperature reaction, the oxidation states of the samples after CO₂ hydrogenation were further investigated using XPS. We found that the Co fraction in the Co_{0.2}, Co_{0.5}, and Co_{0.8} samples increased to 25%, 74%, and 86%, respectively (Figure S5.9). Thus, the samples maintained the partial oxidation states and the Co fraction followed the same order as that of the fresh samples.

Table 5. 2. Activation energies of CH₄ formation ($E_a^f(\text{CH}_4)$), CO₂ desorption from CO₂ + H₂ co-adsorption ($E_a^{d1}(\text{CO}_2)$ and $E_a^{d2}(\text{CO}_2)$), the main adsorption products on the sample surfaces and the corresponding main infrared peaks, i.e., O–C–O asymmetric stretching ($\nu_{\text{as}}(\text{O–C–O})$). $E_a^{d1}(\text{CO}_2)$ and $E_a^{d2}(\text{CO}_2)$ refer to the first and second peak in the TPD spectrum, respectively.

Sample	$E_a^f(\text{CH}_4)$ (kJ mol ⁻¹)	$E_a^{d1}(\text{CO}_2)$ (kJ mol ⁻¹)	$E_a^{d2}(\text{CO}_2)$ (kJ mol ⁻¹)	Main adsorption species	$\nu_{\text{as}}(\text{O–C–O})$ (cm ⁻¹)
Co ₃ O ₄	198.83 ± 0.74	N/A	N/A	HCOO ⁻ *–Co ₃ O ₄	1570
Co _{0.2}	91.21 ± 0.45	38.04 ± 3.08	76.09 ± 12.45	HCOO ⁻ *–MOI; CO ₃ ²⁻ *–CoO	1620; 1520
Co _{0.5}	107.47 ± 0.35	44.47 ± 4.02	129.17 ± 9.32	HCOO ⁻ *–MOI	1620
Co _{0.8}	113.11 ± 157	--	–	–	–

5.3.4 Surface reaction mechanisms

To understand the reason why the samples with higher CoO concentration have lower activation energy of CO₂ to CH₄ conversion, we analyzed the surface species recorded by DRIFTS in the operando experiment. The adsorbed species were identified according to our previous work on IR peak assignments and intermediates identification [17,18]. The assigned vibrations of the main IR peaks are listed in Table 2. As shown in Figure 5.6(a), after CO₂ + H₂ co-adsorption, on the Co_{0.2} surface we found formate located at the metal–oxide interface (HCOO⁻*–MOI) and carbonate located on the oxide surface (CO₃²⁻*–CoO); on the Co_{0.5} surface, HCOO⁻*–MOI was the main adsorption product; on the Co_{0.8} surface, no visible adsorbed species was found; on Co₃O₄ surface, oxide-bound formate (HCOO⁻*–Co₃O₄) was observed. The peaks with wavenumbers below 1500 cm⁻¹ were not listed specifically, but they are the corresponding O–C–O symmetric and C–H bending modes according to our previous assignment [18]. The peak positions are very similar as those observed on Ru/Al₂O₃

in our previous work [18]. The formation of formate could originate from CO₂ interaction with the adsorbed H₂ on the under-coordinated cobalt atom on the interfacial CoO and/or on the metallic site of Co [34,35]; and the carbonate could be formed from CO₂ adsorption on the metal oxide surfaces [36,37]. The peak intensities of the adsorption species are the strongest on Co_{0.2} sample, implying an enhanced amount of the adsorbed species on this sample. Moreover, while the formate species formed on all the sample surfaces, CO₃^{2-*}-CoO formed exclusively on the Co_{0.2} surface. This suggests that Co_{0.2} sample might promote additional CO₂ adsorption via forming an additional chemisorption product on the CoO site.

To confirm the observations in IR, CO₂-TPD was performed. Figure 5.6(b) shows the CO₂ desorption spectra ($m/z = 44$) of the three Co_x(CoO)_{1-x} samples. The Co_{0.2} TPD shows two peaks ~110 °C and 200 °C and a weak peak at ~320 °C; Co_{0.5} shows three clear peaks at ~100 °C, 180 °C, and 260 °C respectively; Co_{0.8} is different showing only two desorption peaks at ~160 °C, and 270 °C respectively. It is common that CO₂ desorbs at room temperature on metal oxide surfaces [38–42], while below 0 °C zero on metal surfaces [43–46]. Thus, these desorption peaks are ascribed to the CO₂ adsorbed on the CoO. With the increase of metallic cobalt fraction, the peak intensity of CO₂ desorption becomes weaker, indicating a decreasing amount of adsorbed CO₂.

Note that the desorption peak intensity on the Co_{0.2} sample is more than ten-fold higher than that for the other samples. The intensity trend of the TPD measurements is consistent with the DRIFTS result of the CO₂ adsorption. However, the differences in the amount of CO₂ adsorbed on the three samples are much larger than the differences of their BET surface areas. While BET was measured using N₂ isotherm and reflects physisorption properties, CO₂ adsorption embodies chemisorption properties of the reactive surface, as CO₂ adsorption is used as an indicator of Lewis basicity of the surface [42,47,48]. Higher CO₂ adsorption capacity implies more adsorption sites, and stronger CO₂ binding implies more basic property of the surface. Therefore, the sample with more CoO component adsorbing more CO₂ further confirms that CoO acts as active sites for CO₂ adsorption. This also explains the exclusive existence of CO₃^{2-*}-CoO on the Co_{0.2} sample observed in DRIFTS: more chemisorbed CO₂ increased the concentration of CO₃^{2-*} species on CoO sites via a CO₂-surface O combination.

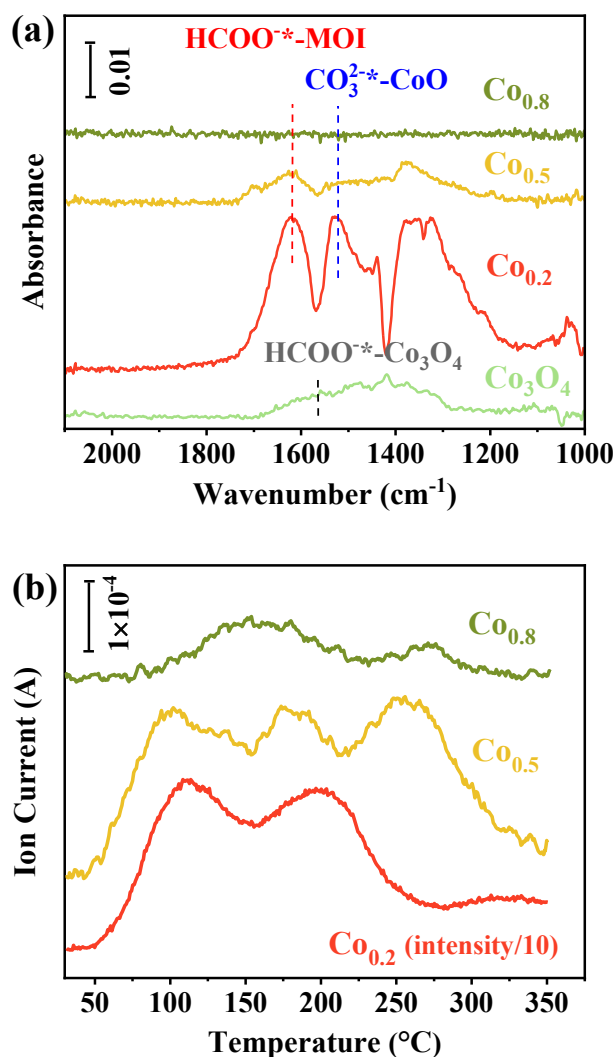


Figure 5.6. (a) DRIFTS spectra during $\text{CO}_2 + \text{H}_2$ co-adsorption at 100 $^{\circ}\text{C}$, revealing the presence of formate and carbonate species. (b) CO_2 desorption measured using TPD-MS ($m/z = 44$) from $\text{CO}_2 + \text{H}_2$ co-adsorption with a heating rate of 15 $^{\circ}\text{C min}^{-1}$, and the intensities are normalized with He intensity.

We also checked the signals of H_2 and CH_4 from the TPD-MS measurement. As shown in Figure S5.10, only very weak signals of H_2 were found and no observable CH_4 was produced. These phenomena hint that very limited amount of H_2 adsorbed on all these sample surfaces, and the hydrogenation of CO_2 either could not take place at this very low concentration of reactant gases or produced scanty products that below the detection limit.

The CO_2 binding energies were evaluated using the activation energies of CO_2 desorption, $E_a^d(\text{CO}_2)$ determined from TPD data at various heating rates (Table 5.2, Figure S5.11) [49,50],

$$\ln \frac{T_p^2}{\kappa} = \ln \frac{E_a^d}{R} - \ln k_0 + \frac{E_a^d}{R \cdot T_p},$$

in which E_a^d is the activation energy of desorption, T_p is the maximal temperature of desorption, κ is the heating rate, R is the gas constant, and k_0 is a constant.

From the first desorption peak, we find $E_a^{d1}(\text{CO}_2) = 38$ and 44 kJ mol^{-1} on $\text{Co}_{0.2}$ and $\text{Co}_{0.51}$ surfaces, respectively. $E_a^{d2}(\text{CO}_2)$, from the second desorption peak, = 76 and 129 kJ mol^{-1} on $\text{Co}_{0.2}$ and $\text{Co}_{0.5}$ surfaces, respectively. $E_a^d(\text{CO}_2)$ is not reported for the $\text{Co}_{0.8}$ sample due to the very weak desorption peaks and associated large uncertainty. The values of $E_a^{d1}(\text{CO}_2)$ and $E_a^{d2}(\text{CO}_2)$ are comparable to the reported CO_2 binding energies on pristine and defective metal oxide surfaces, respectively [51,52]. Therefore, we ascribe the low temperature desorption as originated from CO_2 adsorbed on the pristine CoO surface, which leads to similarly low activation energy of desorption on both $\text{Co}_{0.2}$ and $\text{Co}_{0.5}$ surfaces; the high temperature desorption as from CO_2 adsorbed on defective CoO surface, which leads to much stronger activation energy of desorption. The $E_a^{d2}(\text{CO}_2)$ on $\text{Co}_{0.2}$ sample is nearly twofold lower than that on $\text{Co}_{0.5}$ sample, suggesting a moderate adsorption of CO_2 on $\text{Co}_{0.2}$ surface compared to strong adsorption of CO_2 on $\text{Co}_{0.5}$ surface. As explained above, the stronger CO_2 binding indicates a stronger Lewis basic surface. Hence, the $\text{Co}_{0.5}$ surface is more basic than the $\text{Co}_{0.2}$ surface, probably due to a higher concentration of metallic cobalt of the $\text{Co}_{0.5}$ sample.

It is interesting that more CO_2 adsorbs on the $\text{Co}_{0.2}$ surface than on the $\text{Co}_{0.5}$ surface although the binding energy is actually larger for the $\text{Co}_{0.5}$ surface. We can understand this by noting that if we are below the desorption temperature, the capacity of the surface to adsorb CO_2 is related to the number of binding sites. Since $\text{Co}_{0.2}$ has more CoO sites, it can bind more CO_2 .

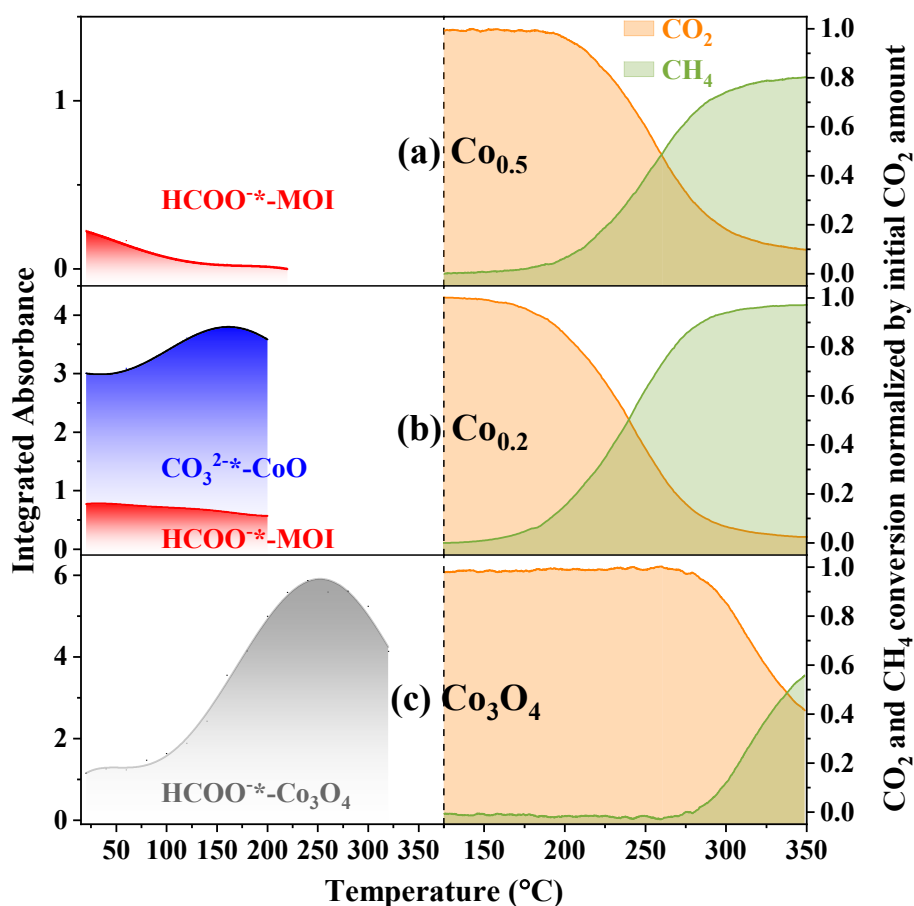


Figure 5.7. The evolution of adsorbed species and CO₂ to CH₄ conversions during CO₂ hydrogenation on (a) Co_{0.5}, (b) Co_{0.2}, (c) Co₃O₄. Left panels were data from DRIFTS, and right panels were data from MS.

The observation of enhanced adsorption of CO₂ on the Co_{0.2} sample is sufficient to explain the improved catalytic performance of Co_{0.2} because the adsorbed species might be byproducts rather than reaction intermediates. To check the reactivity of the adsorbed species, we analyzed the evolution of these adsorbed species using our previously developed method [18]. As shown in Figure 5.7(a, b), HCOO⁻*-MOI was reduced almost linearly upon heating on both Co_{0.2} and Co_{0.5} samples, indicating this species is a reaction intermediate. CO₃²⁻*-CoO on Co_{0.2} surface (Figure 5.7(b)) and HCOO⁻*-Co₃O₄ on Co₃O₄ surface (Figure 5.7(c)) increased while heating, but started to decrease when CH₄ started to be formed. Thus, these two species were also reaction intermediates. Unfortunately, water produced in the reaction condensed on the windows and gave strong IR interference. We were only able to track the surface species up to 200 °C for Co_{0.2} and Co_{0.5} samples, and 320 °C for Co₃O₄ sample. However, Liu and the co-authors have proved using theoretical calculations that the wet surfaces favored the protonation of carbonate through interacting with the neighboring hydroxyl

groups to form bicarbonate [36,37]. The bicarbonate is an intermediate of CH₄ formation from CO₂ hydrogenation reaction according to our previous work and the other report [17,53].

These results affirm that the adsorption of CO₂ has a positive effect on the CO₂ methanation reaction because all the adsorbed species are consumed. Better adsorption of CO₂ is related to an improved catalytic performance of the sample. This could also be the reason for the differences in the activation energies of CH₄ formation, where $E_a^f(\text{CH}_4)$ is the lowest on Co_{0.2} sample. This further indicates that CO₂ adsorption step is the rate determining step of the overall hydrogenation reaction.

It is interesting to compare these results with our previous results for CO₂ methanation on Ru/Al₂O₃ [17,18]. There, CO₃²⁻* and HCOO* on the oxide site are byproducts, not reaction intermediates as they are here. This confirms our previous supposition of surface-structure sensitive reactivity of the adsorbed species.

5.3.5 Surface electronic structure

A further mechanistic investigation should reveal whether the CoO component of our catalysts participated the catalytic reaction. Considering that heterogeneous catalysis proceeds by electron transfer between the adsorbates and the surface atoms, we can get this information on the activity of CoO by measuring the valence band maximum (VBM) of the surface electronic states. For this measurement, we used a higher resolution XPS which did not allow us to transfer samples without air exposure. Thus, we transferred a Co_{0.8} sample to the NAP-XPS system through air. This sample was then reduced at 350 °C with 0.4 mbar H₂ flow in the NAP-XPS sample preparation chamber. We used XPS core level spectra to determine the composition of the sample after transfer and after 1 h and 2 h of H₂ reduction (Figure S12). After 2h, the sample was fully reduced and we used this to provide standard core level and valence band spectra for Co for deconvolution with the CasaXPS software [26,54]. After 1 h, the sample was partially reduced with composition of 58% Co and 42% CoO. The core level spectrum of this partially reduced sample is shown in Figure 8(a). A deconvoluted valence band spectrum is shown in Figure 8(b). The fraction of Co from the valence band deconvolution is 47%, as compared to 58% from the core level deconvolution. The difference is not completely understood and may be related to differing surface sensitivity and/or to deconvolution error. The onset of the edge of the valence band for CoO is 1.15 eV below the Fermi level, as indicated by the line in Figure 8(b). This value is so large that at the temperatures used in this work, it is not possible to thermally excite a sufficient number of electron hole pairs to produce catalytic activity. Although

there is a “tail” extended to Fermi level, the population is very small compared to the abundantly electronic states of Co.

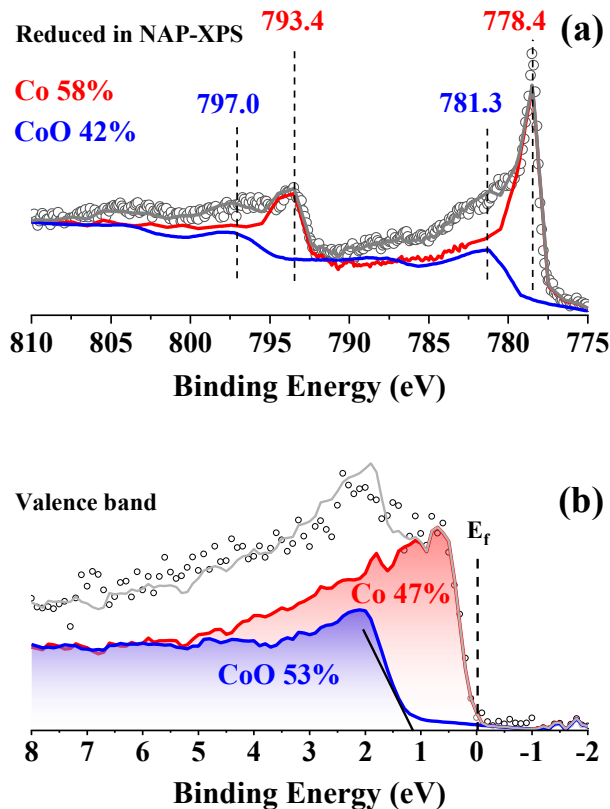


Figure 5.8. (a) Core-level XPS and (b) valence band of the partially reduced sample (58% Co and 42% CoO) prepared and measured in NAP-XPS. The black line which is crossed at 1.15 eV of x-axis shows the onset of the edge of the valence band of CoO. Fermi level (E_f) is at 0 eV.

Therefore, we conclude that the CoO component does not contribute to the hydrogenation process. In contrast, the Co component has high electron density near the Fermi level, suggesting that the excited electrons for the hydrogenation steps are offered by Co. This is in line with the indication from CH_4 production rate per surface area discussed in Section 5.3.2 that the rate per surface area increased with the increasing concentration of Co. Species which are adsorbed on the CoO sites contribute to the catalysis through migration from CoO to the interfacial Co atoms. This is the same as that found on the on $\text{Ru}/\text{Al}_2\text{O}_3$ [17].

Here we envision that, when Co concentration decreased to a critical point, the hydrogenation will be suppressed because of the lack of electronically active center. We speculate this critical point is below 5 wt% ($\sim 6\%$ molar concentration) referring to the research on $\text{Ru}/\text{Al}_2\text{O}_3$ catalysts where

increasing Ru loading from 0.1 wt% to 5 wt% on Al_2O_3 facilitates the CH_4 yield and selectivity in CO_2 hydrogenation reaction [55]. However, the in situ phase change method here used would be improper to synthesize such low concentration of Co. Different synthetic method, such as chemical or physical deposition, could be applied for extending this investigation.

In addition, we noticed that the differences in the overall kinetics of CO_2 conversion (Figure 5.4(d)) are smaller than those in the intensities of CO_2 adsorption/desorption (Figure 5.6) on these samples. This could be understood that the samples with higher Co concentration could reduce the migration distance of the adsorbed species, and reserve more available electrons for the hydrogenation steps. These effects compensated partially the drawbacks of less CO_2 adsorption and reduced the differences in the overall kinetics of CO_2 conversion.

5.4 Conclusions

We have shown a facile method to synthesize “self-supported” cobalt nanoparticles composed of $\text{Co}_x(\text{CoO})_{1-x}$ with different ratios of $x = \text{Co}/(\text{Co} + \text{CoO})$ via reduction of precursor Co_3O_4 nanoparticles in H_2 gas flow to investigate the relation between the metal/metal oxide fractions and their catalytic properties. Samples with the metal ratios of $x = 0.2, 0.5$ and 0.8 were obtained. The samples show very high activity in the Sabatier reaction. Super high conversions of CO_2 reach 98%, 99%, and 93% on $\text{Co}_{0.2}$, $\text{Co}_{0.5}$, and $\text{Co}_{0.8}$ samples, respectively at 350 °C, where the reaction meets the reaction thermodynamic limit. Below 280 °C, the activity varies with the sample in the order $\text{Co}_{0.2} > \text{Co}_{0.5} > \text{Co}_{0.8} > \text{Co}_3\text{O}_4$ at all temperatures. For instance, 63%, 53%, and 23% CO_2 are converted at 250 °C on $\text{Co}_{0.2}$, $\text{Co}_{0.5}$, and $\text{Co}_{0.8}$ samples, respectively. The $\text{Co}_{0.2}$ sample even shows low-temperature activities from 160 to 180 °C, at which temperatures the rest samples do not have activities. The overall activation energy of CH_4 formation increases with the sample in the sequence of $\text{Co}_{0.2} < \text{Co}_{0.5} < \text{Co}_{0.8} < \text{Co}_3\text{O}_4$. Therefore, there is an optimal composition of metal and metal oxide in the catalyst to achieve the highest reactivity.

The differences in reactivity among the samples originate from the different functions of the metal and the metal oxide. CoO provides active sites of CO_2 adsorption but not electron-transfer sites for the hydrogenation reaction. Co acts as an electronically active center for the hydrogenation reaction. The derivative adsorbed products are observed as formate and carbonate, and these are found to be intermediates of CH_4 formation. Of the partially reduced samples, the $\text{Co}_{0.2}$ sample has highest CoO concentration; consequently it adsorbs the largest amount of CO_2 . Moreover, the low fraction of $\text{Co}/(\text{Co} + \text{CoO})$ facilitates moderate binding of CO_2 . The CO_2 adsorption step could be the rate-

determining step of the overall methanation reaction. Therefore, the Co_{0.2} sample shows the highest reactivity: the lowest onset temperature and activation energy of CH₄ formation, and the highest conversion of CO₂ below thermodynamic limit. In comparison, the Co_{0.5} sample with its higher fraction of Co/(Co+CoO) has a higher binding energy for CO₂ due to its stronger Lewis basicity; but it adsorbs less CO₂ because there are less CoO sites. As a result, the Co_{0.5} sample converts less CO₂ than the Co_{0.2} sample. Co_{0.8} sample does not have the advantage of abundant CoO concentration, therefore not show significant CO₂ adsorption amount. This leads to the lowest reactivity of Co_{0.8} compared to Co_{0.2} and Co_{0.5} samples.

These results of this work elucidate the optimal composition of metal and metal oxide for achieving the highest catalytic reactivity in the Sabatier reaction. Furthermore, they clarified the different active functions of the metal and metal oxide in the whole CO₂ hydrogenation reaction. These two main attainments open the way for the design of efficient catalysts with the optimal ratio of metal over metal oxide.

Corresponding Author

*wen.luo@epfl.ch, *kun.zhao@epfl.ch

ACKNOWLEDGMENTS

SCCER HeE, which is financially supported by Innosuisse, the Swiss Innovation Agency, is gratefully acknowledged. The NAP-XPS system is funded by the SNSF R'EQUIP project (No. 170736). W.L acknowledges the financial support from SNSF (Ambizione Project PZ00P2_179989). M.L would like to thank the China Scholarship Council for the PhD grant (Grant No. 201506060156). We also thank Bardiya Valizadeh and Arunraj Chidambaram from Laboratory of Molecular Simulation (LSMO), EPFL for the help in BET measurement.

Supporting Information

The H₂ consumption plots and calculations, XRD, BET, normalized MS signals of CO₂ and CH₄, CH₄ yield, Arrhenius plot of CH₄ formation, yield of C₂H₆ and CO, XPS of samples after CO₂ hydrogenation reaction, Co 2p_{3/2} and 2p_{1/2} peaks measured by NAP-XPS, activation energy plots of CO₂ desorption, the evolution of the adsorption species.

References

- [1] J. Artz, T.E. Müller, K. Thenert, J. Kleinekorte, R. Meys, A. Sternberg, A. Bardow, W. Leitner, *Chem. Rev.* 118 (2018) 434–504.
- [2] W. Li, H. Wang, X. Jiang, J. Zhu, Z. Liu, X. Guo, C. Song, *RSC Adv.* 8 (2018) 7651–7669.
- [3] R. Mutschler, E. Moiola, W. Luo, N. Gallandat, A. Züttel, *J. Catal.* 366 (2018) 139–149.
- [4] F. Marques Mota, D.H. Kim, *Chem. Soc. Rev.* 48 (2019) 205–259.
- [5] E. Moiola, A. Züttel, *Sustain. Energy Fuels* 4 (2020) 1396–1408.
- [6] R.W. Dorner, D.R. Hardy, F.W. Williams, H.D. Willauer, *Energy Environ. Sci.* 3 (2010) 884–890.
- [7] E.V. Kondratenko, G. Mul, J. Baltrusaitis, G.O. Larrazabal, J. Perez-Ramirez, *Energy Environ. Sci.* 6 (2013) 3112–3135.
- [8] I.A. Fisher, A.T. Bell, *J. Catal.* 172 (1997) 222–237.
- [9] I.A. Fisher, A.T. Bell, *J. Catal.* 178 (1998) 153–173.
- [10] X.-M. Liu, G.Q. Lu, Z.-F. Yan, J. Beltramini, *Ind. Eng. Chem. Res.* 42 (2003) 6518–6530.
- [11] S. Kattel, B. Yan, Y. Yang, J.G. Chen, P. Liu, *J. Am. Chem. Soc.* 138 (2016) 12440–12450.
- [12] S. Kattel, P.J. Ramírez, J.G. Chen, J.A. Rodriguez, P. Liu, *Science* 355 (2017) 1296–1299.
- [13] T. Chen, J. Su, Z. Zhang, C. Cao, X. Wang, R. Si, X. Liu, B. Shi, J. Xu, Y.-F. Han, *ACS Catal.* 8 (2018) 8606–8617.
- [14] G. Melaet, W.T. Ralston, C.-S. Li, S. Alayoglu, K. An, N. Musselwhite, B. Kalkan, G.A. Somorjai, *J. Am. Chem. Soc.* 136 (2014) 2260–2263.
- [15] A. Boffa, C. Lin, A.T. Bell, G.A. Somorjai, *J. Catal.* 149 (1994) 149–158.
- [16] G. Prieto, M.I.S. De Mello, P. Concepción, R. Murciano, S.B.C. Pergher, A. Martínez, *ACS Catal.* 5 (2015) 3323–3335.
- [17] K. Zhao, L. Wang, M. Calizzi, E. Moiola, A. Züttel, *J. Phys. Chem. C* 122 (2018) 20888–20893.
- [18] K. Zhao, L. Wang, E. Moiola, M. Calizzi, A. Züttel, *J. Phys. Chem. C* 123 (2019) 8785–8792.
- [19] S. Yoon, K. Oh, F. Liu, J.H. Seo, G.A. Somorjai, J.H. Lee, K. An, *ACS Catal.* 8 (2018) 5391–5398.
- [20] C.K. Vance, C.H. Bartholomew, *Appl. Catal.* 7 (1983) 169–177.
- [21] S. Kattel, W. Yu, X. Yang, B. Yan, Y. Huang, W. Wan, P. Liu, J.G. Chen, *Angew. Chem.* 55 (2016) 7968–7973.
- [22] S. Kuld, M. Thorhauge, H. Falsig, C.F. Elkjær, S. Helveg, I. Chorkendorff, J. Sehested, *Science* 352 (2016) 969.
- [23] K. Zhao, J. Zhang, W. Luo, E. Moiola, M. Spodaryk, A. Züttel, submitted, (2020).
- [24] A.M. Karim, Y. Su, M.H. Engelhard, D.L. King, Y. Wang, *ACS Catal.* 1 (2011) 279–286.

-
- [25] K.C. Sabat, R.K. Paramguru, S. Pradhan, B.K. Mishra, *Plasma Chem. Plasma Process* 35 (2015) 387–399.
- [26] W. Luo, S. Zafeiratos, *J. Phys. Chem. C* 120 (2016) 14130–14139.
- [27] L.J. Garces, B. Hincapie, R. Zerger, S.L. Suib, *J. Phys. Chem. C* 119 (2015) 5484–5490.
- [28] G. Garbarino, D. Bellotti, P. Riani, L. Magistri, G. Busca, *Inter. J. Hydrog. Energy* 40 (2015) 9171–9182.
- [29] G. Garbarino, D. Bellotti, E. Finocchio, L. Magistri, G. Busca, *Catal. Today* 277 (2016) 21–28.
- [30] M.S. Duyar, A. Ramachandran, C. Wang, R.J. Farrauto, *J. CO₂ Util.* 12 (2015) 27–33.
- [31] G.D. Weatherbee, C.H. Bartholomew, *J. Catal.* 77 (1982) 460–472.
- [32] A. Karelavic, P. Ruiz, *ACS Catal.* 3 (2013) 2799–2812.
- [33] G.L. Bezemer, J.H. Bitter, H.P.C.E. Kuipers, H. Oosterbeek, J.E. Holewijn, X. Xu, F. Kapteijn, A.J. van Dillen, K.P. de Jong, *J. Am. Chem. Soc.* 128 (2006) 3956–3964.
- [34] Y. Pan, D. Mei, C. Liu, Q. Ge, *J. Phys. Chem. C* 115 (2011) 10140–10146.
- [35] S. Kato, S.K. Matam, P. Kerger, L. Bernard, C. Battaglia, D. Vogel, M. Rohwerder, A. Züttel, *Angew. Chem.* 55 (2016) 1–6.
- [36] Y. Pan, C. Liu, Q. Ge, *Langmuir* 24 (2008) 12410–12419.
- [37] Y. Pan, C. Liu, D. Mei, Q. Ge, *Langmuir* 26 (2010) 5551–5558.
- [38] O. Seiferth, K. Wolter, B. Dillmann, G. Klivenyi, H.J. Freund, D. Scarano, A. Zecchina, *Surf. Sci.* 421 (1999) 176–190.
- [39] A. Hakim, T.S. Marliza, N.M. Abu Tahari, R.W.N. Wan Isahak, R.M. Yusop, W.M. Mohamed Hisham, A.M. Yarmo, *Ind. Eng. Chem. Res.* 55 (2016) 7888–7897.
- [40] G. Krenn, J. Schoiswohl, S. Surnev, F.P. Netzer, R. Schennach, *Top Catal* 46 (2007) 231–238.
- [41] R. Bal, B.B. Tope, T.K. Das, S.G. Hegde, S. Sivasanker, *J. Catal.* 204 (2001) 358–363.
- [42] K. Pokrovski, K.T. Jung, A.T. Bell, *Langmuir* 17 (2001) 4297–4303.
- [43] J. Wang, B. Hokkanen, U. Burghaus, *Surf. Sci.* 577 (2005) 158–166.
- [44] S. Wohlrab, D. Ehrlich, J. Wambach, H. Kuhlenbeck, H.-J. Freund, *Surf. Sci.* 220 (1989) 243–252.
- [45] H.J. Freund, H. Behner, B. Bartos, G. Wedler, H. Kuhlenbeck, M. Neumann, *Surf. Sci.* 180 (1987) 550–564.
- [46] J. Wambach, G. Illing, H.J. Freund, *Chem. Phys. Lett.* 184 (1991) 239–244.
- [47] W.N.R.W. Isahak, Z.A.C. Ramli, M.W. Ismail, K. Ismail, R.M. Yusop, M.W.M. Hisham, M.A. Yarmo, *J CO₂ Util.* 2 (2013) 8–15.
- [48] P. Kuśtrowski, L. Chmielarz, E. Bożek, M. Sawalha, F. Roessner, *Mater. Res. Bull.* 39 (2004) 263–281.
- [49] H.E. Kissinger, *Anal. Chem.* 29 (1957) 1702–1706.
- [50] G. Munteanu, E. Segal, *Thermochimica. Acta.* 89 (1985) 187–194.

-
- [51] U. Burghaus, *Prog. Surf. Sci.* 89 (2014) 161–217.
- [52] U. Burghaus, in: S.L. Suib (Eds.), *New and Future Developments in Catalysis*, Elsevier, Amsterdam, 2013, pp. 27–47.
- [53] M. Marwood, R. Doepper, A. Renken, *Appl. Catal. A: General* 151 (1997) 223–246.
- [54] V.A. Saveleva, L. Wang, W. Luo, S. Zafeiratos, C. Ulhaq-Bouillet, A.S. Gago, K. A. Friedrich, E. R. Savinova, J. *Phys. Chem. Lett.* 7 (2016) 3240–3245.
- [55] J.H. Kwak, L. Kovarik, J. Szanyi, *ACS Catal.* 3 (2013) 2449–2455.

Supporting Information

Unraveling and Optimizing the Metal–Metal Oxide Synergetic Effect in a Highly Active $\text{Co}_x(\text{CoO})_{1-x}$ Catalyst for CO_2 Hydrogenation

Kun Zhao^{a,b,*}, Marco Calizzi^{a,b}, Emanuele Moioli^{a,b}, Mo Li^{a,b}, Alexandre Borsay^{a,b}, Loris Lombardo^{a,b}, Robin Mutschler^{a,b}, Wen Luo^{a,b,*}, Andreas Züttel^{a,b}

^a Laboratory of Materials for Renewable Energy, Institute of Chemical Sciences and Engineering, École Polytechnique Fédérale de Lausanne (EPFL), 1951 Sion, Switzerland

^b Swiss Federal Laboratories for Materials Science and Technology (EMPA), 8600 Dübendorf, Switzerland

Table of Contents

Section S5.1. Determination of the molar ratio of metallic cobalt from H_2 consumption using MS

Figure S5.1. H_2 consumption of $\text{Co}_x(\text{CoO})_{1-x}$

Figure S5.2. The removed ratio of O atom (R_O) in each repeated synthesis of $\text{Co}_x(\text{CoO})_{1-x}$

Table S5.1. Specific surface area and CO_2 adsorption amount

Section S5.2. Other characterizations

Figure S5.3. XRD

Section S5.3. Activity of CO_2 to CH_4 conversion

Figure S5.4. CH_4 yield

Figure S5.5. CO_2 conversion and CH_4 production at different temperatures

Figure S5.6. The CO_2 hydrogenation reaction at 350 °C for 3 days on $\text{Co}_{0.2}$ sample

Section S5.4. The selectivity of CO and C_2H_6

Figure S5.7. The yield of CO and C_2H_6

Figure S5.8. The maximum yield of C_2H_6

Section S5.5. The stability of samples

Figure S5.9. The XPS of $\text{Co}_{0.2}$, $\text{Co}_{0.5}$ and $\text{Co}_{0.8}$ samples after CO_2 hydrogenation reaction

Section S5.6. Surface reaction mechanisms

Figure S5.10. H_2 and CH_4 desorption

Figure S5.11. Calculation of activation energy of CO_2 desorption

Figure S5.12. Co 2p_{3/2} and 2p_{1/2} peaks

Section S1. Determination of the molar ratio of metallic cobalt using H₂ consumption recorded using MS

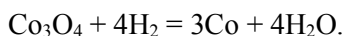
The calculation method for removed O atom by H₂ reduction:

I. Determine the H₂ consumption amount

- 1) normalize H₂ intensity by He intensity;
- 2) integrate H₂ depletion area (A);
- 3) make a sum of overall H₂ supplied (A₀);
- 4) divide the H₂ depletion area by the overall H₂ to obtain ratio of consumed H₂ ($R_H = A/A_0$);
- 5) calculate total molar number of supplied H₂ ($N_H = \text{flow (mL min}^{-1}) \times \text{time (min)} \div 24.5 \text{ (mL mmol}^{-1})$);
- 6) molar number of consumed H₂ is to multiply ratio of consumed H₂ by total molar number of supplied H₂: $n_H = R_H \times N_H$.

II. Determine the removed amount of O atoms

According to the stoichiometric reaction:



To remove all the O atoms from a certain weight of Co₃O₄ (m (g)), the theoretical molar number (n₀) of H₂ is:

$$n_0 = m \text{ (g)} \div 241 \text{ (g mol}^{-1}) \times 4.$$

As one mole of H₂ molecule takes away one mole of O atom, the molar ratio of consumed H₂ molecules equals to the molar ratio of removed O atoms. Therein,

$$R_O = n_H/n_0.$$

R_O is the molar ratio of removed O atoms.

III. Determine the molar ratio of metallic cobalt

The remained molar number of O atoms per molecular unit of cobalt oxide is:

$$n_O = 4 \times (1 - R_O).$$

The molar ratio of metallic cobalt is:

$$Co\% = \frac{Co}{Co + CoO} = \frac{3 - n_o}{(3 - n_o) + n_o} = \frac{3 - n_o}{3}$$

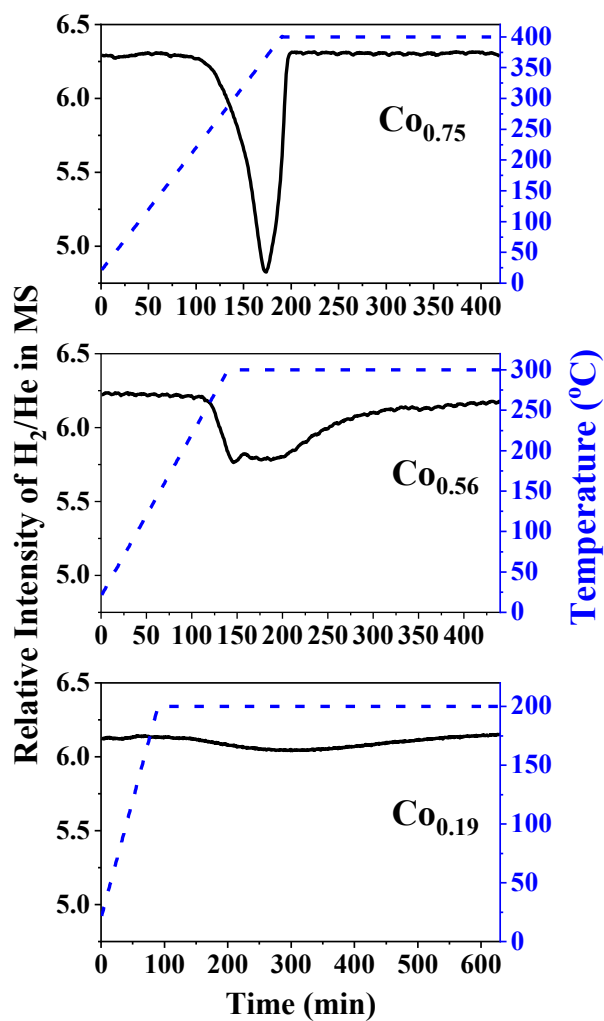


Figure S5.1. H_2 consumption of $Co_x(CoO)_{1-x}$ samples by in situ reduction from Co_3O_4 and detected by mass spectrometry.

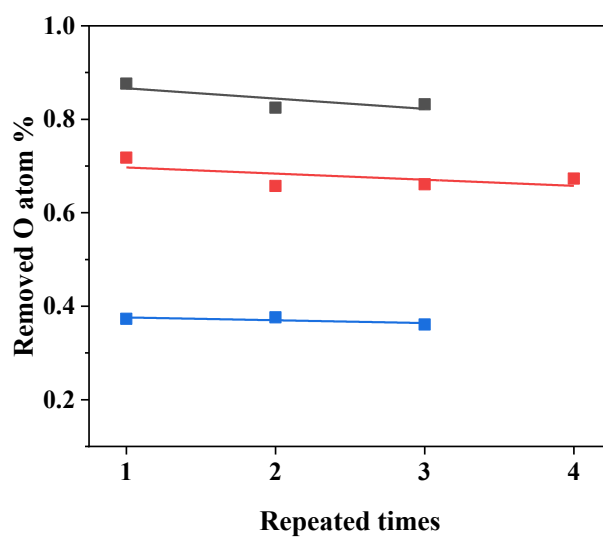


Figure S5.2. The removed ratio of O atom (R_O) in each repeated synthesis of $Co_x(CoO)_{1-x}$ samples.

Table S5.1. Specific surface area and CO_2 adsorption amount of $Co_x(CoO)_{(1-x)}$ samples measured using Micromeritics Tristar 3000 instrument

Sample name	BET surface area ($m^2 g^{-1}$)	CO_2 adsorbed at 1 bar ($mmol g^{-1}$)
Co_3O_4	12.58	0.107
$Co_{0.2}$	13.75	0.075
$Co_{0.5}$	4.04	0.025
$Co_{0.8}$	1.12	0.023

Section S5.2. Other characterizations

XRD. The crystal structures of all the samples were determined via powder X-ray diffractometer (PXRD, Bruker D8 Discover) using a Cu K α source. The samples were loaded in the glovebox in an airtight sample holder. Specifically, we used cling film and an aluminum ring to cover the top of sample holder during the sample transfer and measurement. This air-free condition is not rigorous for long-time operation.

We measured the 2θ range from 20 to 80°, which took around 1~1.5 hours for each measurement. During this transfer and measurement hour, the sample may be partially oxidized by oxygen. As CoO can be easily oxidized to Co₃O₄, the less reduced Co_{0.2} sample show higher peak intensity of Co₃O₄. Moreover, the CoO peaks of these samples did not show obvious differences in the Co_x(CoO)_{1-x} samples, which must be caused by the imperfect protection of the samples during the transfer and measurement. However, from our XPS measurements which were performed through rigorously air-free transfer of the samples, we confirm that the surface of the Co_{0.2} catalyst has only Co and CoO, and the certain ratios of the Co to CoO in all the samples.

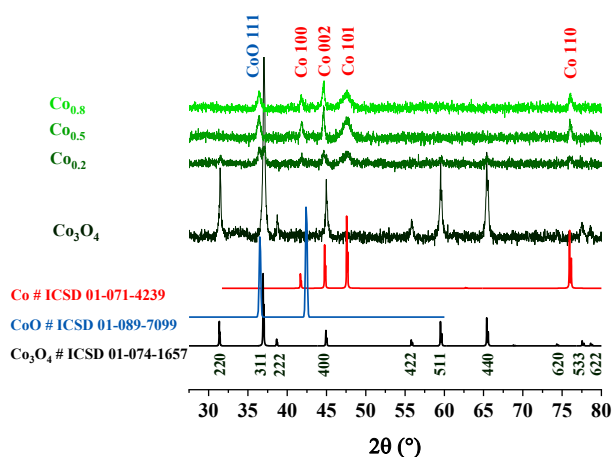


Figure S5.3. XRD of the Co₃O₄, Co_{0.2}, Co_{0.5} and Co_{0.8} samples.

Section S5.3. Activity of CO₂ to CH₄ conversion

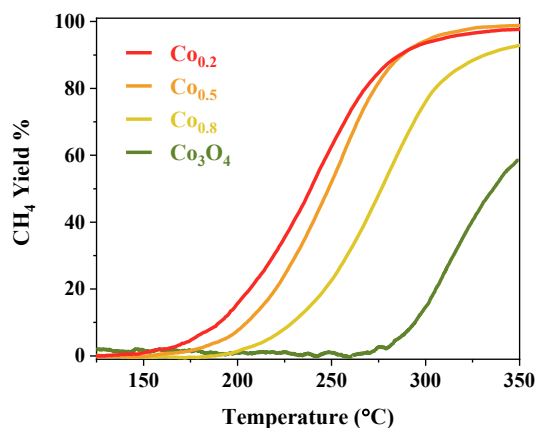


Figure S5.4. CH₄ yield of Co₃O₄, Co_{0.2}, Co_{0.5} and Co_{0.8} samples.

As shown in Figure S5.5(a) and (b), CO₂ conversion and CH₄ yield showed the same developments throughout the temperatures. The selectivity of CH₄ formation was provided above the onset reaction temperature on each sample to reduce the calculation errors. As shown in Figure S5.5(c), the selectivity of CH₄ also showed the similar trend as CH₄ yield over these samples below 275 °C, and was generally high, above 92% on Co_{0.2}, Co_{0.5} and Co_{0.8} samples. Above 275 °C, the selectivity of CH₄ on these samples reached the maximum 98%. The CH₄ production rate per surface area scattered out above 225 °C when the CH₄ production on the Co_{0.2}, Co_{0.5} and Co_{0.8} samples were above the onset temperature (Figure S5.5(d)).

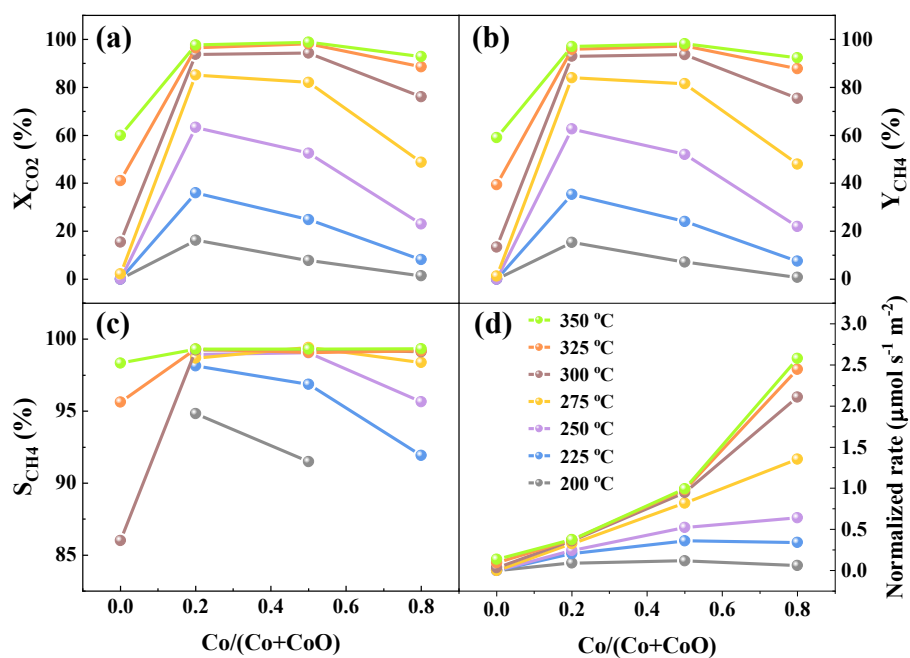


Figure S5.5. (a) CO₂ conversion, (b) CH₄ yield, (c) CH₄ selectivity, and (d) CH₄ production rate per surface area of N₂ adsorption at 200, 225, 250, 275, 300, 325, and 350 °C.

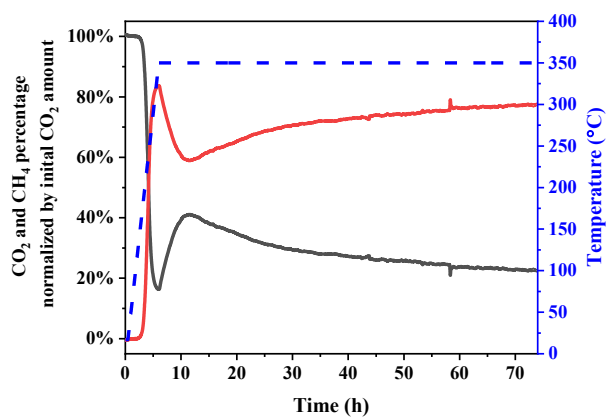


Figure S5.6. The CO₂ hydrogenation reaction at 350 °C for 3 days on Co_{0.2} sample.

Section S5.4. The selectivity of CO and C₂H₆

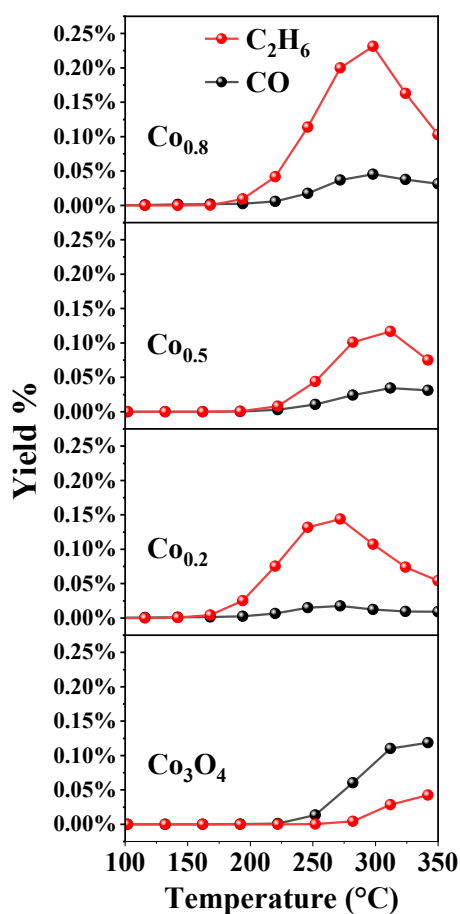


Figure S5.7. The yield of CO and C₂H₆ on Co₃O₄, Co_{0.2}, Co_{0.5} and Co_{0.8} samples.

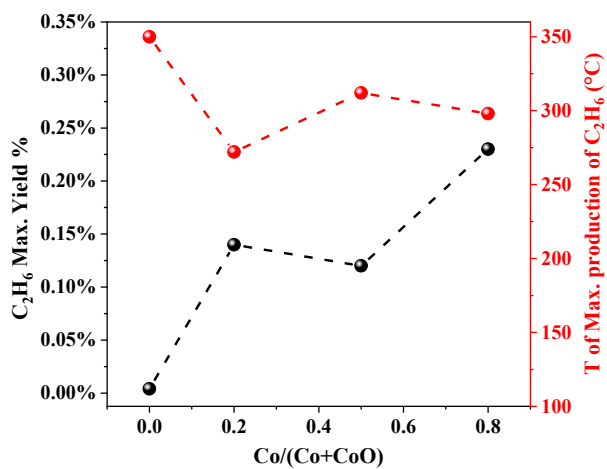


Figure S5.8. The maximum yield of C₂H₆ (left axis) and the temperature of the maximum yield of C₂H₆ (right axis) over the Co₃O₄, Co_{0.2}, Co_{0.5} and Co_{0.8} samples.

Section S5.5. The stability of samples

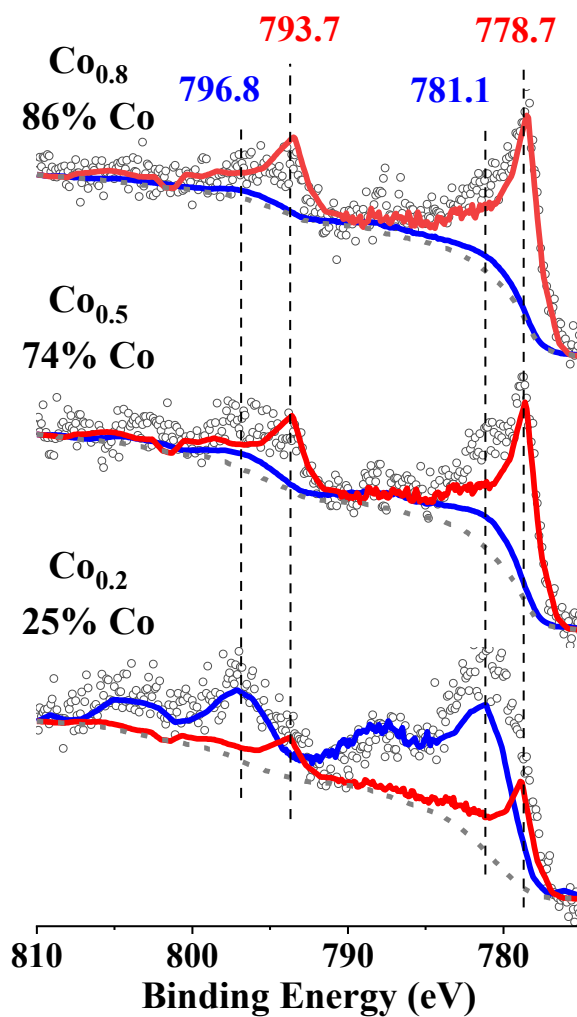


Figure S5.9. The XPS of Co_{0.2}, Co_{0.5} and Co_{0.8} samples after CO₂ hydrogenation reaction. These three samples are further reduced to have 25%, 74%, and 86% Co, respectively.

Section S5.6. Surface reaction mechanisms

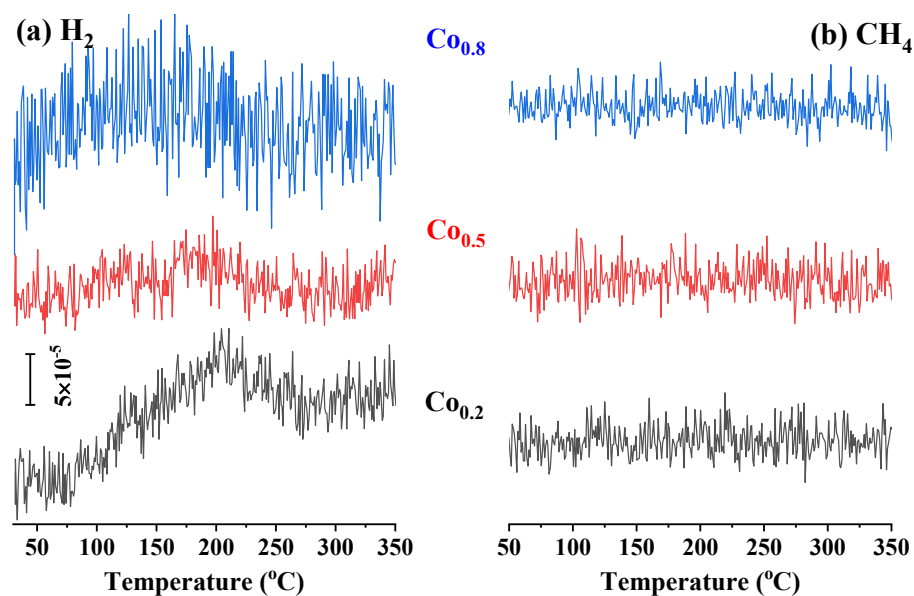


Figure S5.10. (a) H_2 with $m/z = 2$ and (b) CH_4 with $m/z = 15$ from $\text{CO}_2 + \text{H}_2$ co-adsorption in TPD-MS with a heating rate of $15^\circ\text{C min}^{-1}$. The intensities are normalized with He intensity.

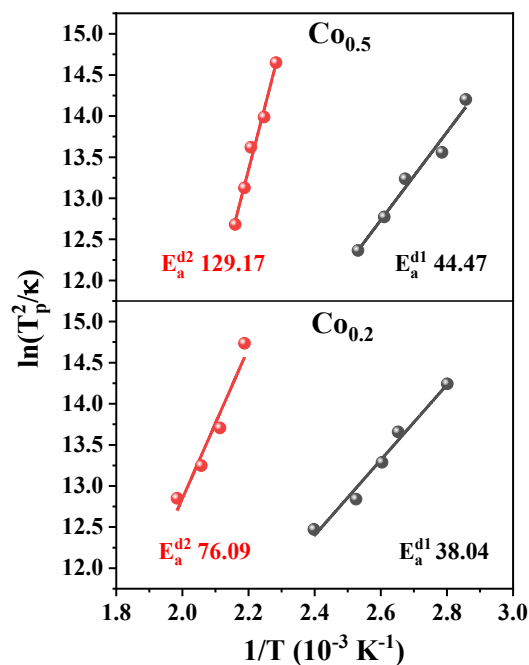


Figure S5.11. Calculation of activation energy of CO_2 desorption from $\text{CO}_2 + \text{H}_2$ co-adsorption in TPD-MS by varying the heating rate 5, 10, 15, 25, and $40^\circ\text{C min}^{-1}$. The black plot is from the first desorption peak at Figure 6(b) in the main manuscript, and the red plot is from the second desorption peaks.

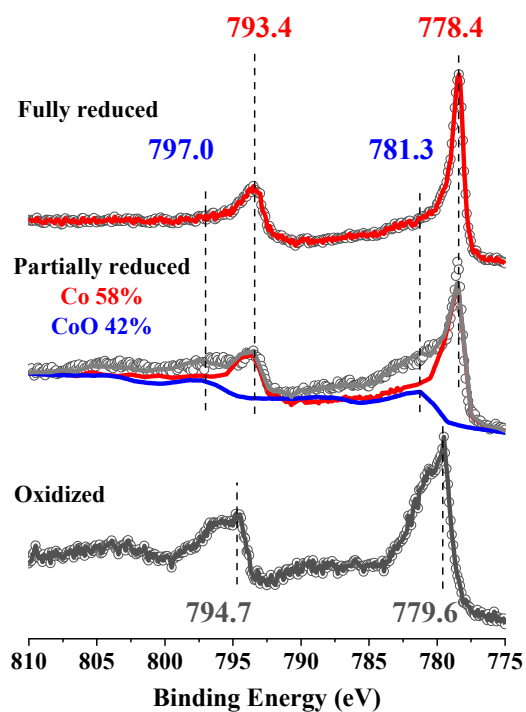


Figure S5.12. Co 2p_{3/2} and 2p_{1/2} peaks of not reduced, reduced after 1h (partially reduced) and 2h (fully reduced) in H₂, respectively in situ NAP-XPS. Black, blue and red lines represent the deconvoluted signals of Co₃O₄, CoO and Co states, respectively. Gray line is the total fitted spectra.

Conclusions

In this thesis, we focused on disclosing the reaction mechanisms of CO₂ hydrogenation on the catalyst surface. The project was accomplished through four sub-projects.

Firstly, we built up an in situ DRIFTS and investigated the spectroscopy of CO₂ gas as functions of pressure and temperature. The pristine metals, Fe, Co, Ni, and Cu were utilized to study the CO₂ adsorption behavior and their properties in CO₂ activation. CO₂ reduction by H₂ were carried out on these metal surfaces under constant volume conditions to understand the reactivities of these metals. The results showed Fe is the most active in CO₂ activation that dissociate CO₂ to CO gas at temperature above 350 °C. Co and Ni rank the second. Cu is not active in CO₂ activation reaction. While in CO₂ hydrogenation reaction at mild temperature (200 °C), Co is the most active to convert CO₂ to CH₄; Ni produced four times less yield of CH₄ than Co; Fe and Cu are not active at this temperature. We conceived that formation of metal hydride could improve the CO₂ methanation profited from H₂ pre-storage in the material. Therefore, we employed the classical metal hydride, LaNi₄Cu alloy, for CO₂ reduction. CH₄ produces only above 300 °C. Unfortunately, at this temperature the stored H₂ was desorbed already. Hence, H₂ pre-storage might be not the key to trigger CO₂ methanation. Besides, there are no adsorption species observed on these pure metal surfaces. However, on the metal-oxide Co-CoO catalysts, CO₂ methanation exhibits lower onset temperature and higher conversion than those pristine and alloyed metals. Moreover, there are adsorption species on the surface detected by IR. Therefore, we start to change the catalyst category from pure metals to metal-oxide. Also, we upgraded the in situ DRIFTS to operando DRIFTS-MS-GC, where the gases were detected by MS and GC, the liquid products were detected by ex-situ NMR, and the surface adsorbates were detected by IR.

Secondly, we developed an analysis program, bilevel evolutionary Gaussian fitting (BEGF) program. This program deconvolutes the overlapping IR bands of the similar bond vibrations in spectral sets automatically and efficiently. The standard chemicals, including carbonate and bicarbonate salts, formic acid, acetic acid, methanol, and ethanol adsorbed on the catalyst surface, were measured by IR for assigning the peaks generated from CO₂ hydrogenation. Isotopic spectra of ¹³CO₂+H₂ and CO₂+D₂ reactions were employed for assisting the peak assignments also. In addition, the reactivity of formate adsorbed on the Ru/Al₂O₃ surface by H₂ reduction was examined for the purpose of clarifying whether it is intermediate or byproduct. As a result, we resolved the peak positions of O-C-O asymmetric and symmetric stretching of different adsorption structures: HCO₃^{-*}, CO₃^{2-*}, HCOO^{-*},

and CO*, as well as the C-H stretching and bending of HCOO*, on both Ru/Al₂O₃ and Al₂O₃ surfaces. What is more, the HCO₃*, HCOO*, and CO* on the Ru site and the interface of Ru/Al₂O₃ were reducible by H₂.

Thirdly, in order to understand the reaction steps of CO₂ methanation, we in situ controlled the individual formation and hydrogenation of each adsorption species appears in the CO₂ methanation reaction on Ru/Al₂O₃. The results showed that the first step is CO₂ adsorbed as HCO₃* at the interface of Ru and Al₂O₃ no matter if there is H₂ in the system or not. Surface hydroxyl groups provide the acceptance sites for CO₂. The second step is HCO₃* dissociating into *CO. The dissociation temperature is high (130 °C) in H₂ depletion condition but at room temperature in H₂ rich environment. The third step is *CO hydrogenation to CH₄ starting at 100 °C, through transition states, without detectable intermediates. If in H₂-rich condition at the beginning, HCOO* at the interface also forms as the first step of CO₂ activation, and infuse with the CO* formation and hydrogenation step.

Fourthly, since we discovered the important function of the oxide support in the CO₂ hydrogenation reaction, we designed Co/(Co+CoO) catalysts with different ratios to investigate the relationship of the metal/oxide ratio and their reactivities. The results showed more composition of CoO in the catalysts facilitates higher activity in the CO₂ conversion (98%). CH₄ is the main product on these samples. Trace C₂H₆ is preferentially produced on the sample with a high concentration of metallic cobalt, while the trace CO production is favored on the pure oxide. The origin of the distinct reactivity comes from the CO₂ chemisorption on the CoO surface. The CO₂ chemisorption is the rate determining step of the overall hydrogenation reaction. High CoO concentration surface not only enhanced the adsorption amount but lowered down the binding strength of CO₂. However, CoO did not create catalytic center, the CO₂ reduction center is still on Co atom. These results elucidate the optimal composition of metal and metal oxide for achieving the highest catalytic reactivity, and clarified the different active functions of the metal and metal oxide in the CO₂ hydrogenation reaction.

These results established mature and sensitive methods for operando study of heterogeneous catalysis over gas/solid interface, accompanied by analysis program of IR dataset and the database of IR peak positions of the adsorbates from CO₂ methanation on the metal-oxide surfaces. The systematic and progressive investigations present the performances of pristine metals, metal hydride alloy, and metal-oxide catalysts in CO₂ adsorption and methanation reactions. CO₂ activation initiates on the interface of metal-oxide, and is reduced to CH₄ through converting to multiple intermediate species, such as HCO₃*, HCOO*, CO* on Ru/Al₂O₃ catalyst surface, or HCOO* and CO₃* on Co_x(CoO)_{1-x}.

x catalyst surface. Concurrent exist of metal and metal oxide is vital for efficient CO₂ methanation. The metal oxide is not just supporting the metal nanoparticles, more importantly it functions as CO₂ adsorption site, which is the initial step of the catalytic reaction. Therefore, the design of the catalyst should consider the concentration of oxides for optimizing the CO₂ conversion.

Perspectives

We have established a powerful DRIFTS-MS-GC setup and analysis program for operando study of CO₂ hydrogenation process on gas/solid interface. The CO₂ methanation mechanisms and their relation with the different transition metal-based catalysts have been elaborated using IR, MS, XPS, GC, NMR, etc. techniques. Three continuous work are envisioned for the future.

First, CO₂ methanation reaction occurs through one step, or passing through CO* or HCOO* as intermediates, according to the literature and this thesis. However, the observation of the intermediate steps from CO* or HCOO* to CH₄ are limited by the current experimental research. Therefore, which intermediate determines the reaction ending with CH₄ or continuing with carbon chain growth remains mystery. Relative coverage of CO*/H*, H₂ pressure, binding energies of the possible transitional adsorbates, and surface structure are discussed in the literature. Therefore, controlling experiments of adjusting CO* and H* coverage on model catalyst, e.g. Ru/Al₂O₃, could be helpful to understand the CO* hydrogenation step. Especially, carrying out the controlling experiments in vacuum would enable the observation of transitional adsorbates, such as COH* and CHO* using DRIFTS.

Second, synthetic methanol is much more valuable than synthetic methane. The disadvantage of methanol production is the requirement of high pressure (> 20bar). The working pressure of our apparatus is limited to 10 bar. However, this limit is because of the commercial DRIFTS chamber where the dome consists of 4mm thick windows for the IR beam passing. It is possible to change the dome to allow thicker glass window for holding higher pressure. Then we can study the methanol processes on the catalyst surface using the developed methods in this thesis. C-C coupling also occurs under high pressure reaction, hence, C-C coupling mechanisms in long chain hydrocarbons could also be investigated.

Third, numerous researches investigate the active sites of the catalysts. The effects from size, support, interface, alloy, and so on, are well presented. However, plenty of the reports are limited at explanation of the phenomena. The intrinsic causes of those effects are still less proved. Therefore, we suggest further investigations of specific design of catalysts together with comprehensive characterizations under reaction conditions.

Appendix – BEGF Program

Execution file 1 and Execution file 2

The code structure is given in Table A.1 with all detailed description of each matrix involved given directly in the code comments.

Table A.1. Code structure.

File name	Function	Calling	Called by
main.m	Execution file with all input specifications and solving options. This file calls preprocess.m first to process input spectra and then executes a genetic algorithm (the upper-level algorithm) for global optimization.	preprocess.m	–
preprocess.m	Customized processing of given spectrum files. This needs to be adapted for specific format of recorded data to return the required data to be used in main.m.	Input source experimental spectra	main.m
gafitness.m	Lower-level algorithm: multi-peak Gaussian fitting with the calculation of objective function and file writing to record the evolution information. This file also activates a monitoring plot to illustrate the evolution progress. This file is called by genetic algorithm for each low-level evaluation.	gfparser.m	Genetic algorithm executed in main.m
gfparser.m	Parse the results returned by the original multi-peak Gaussian fitting algorithm from MATLAB and update the monitoring plots of each spectrum. This file is called by gafitness.m.	gfparser.m	gafitness.m
gaussian.m	Formulation of Gaussian function	–	gfparser.m

Execution file 1 main.m:

Note: the initial values in Pini, Plbd, Pubd, olbd and oubd were what we used for the spectra set of CO₂ hydrogenation reaction on Ru/Al₂O₃ catalyst surface.

```
% Clear and clean matlab and prepare pathes
clear all;
clc;
format compact
global fsep curdir
fsep = filesep;
curdir = pwd;

% Input and output folder
global inpdire outdire
inpdire = [curdir fsep 'sources'];
outdire = [curdir fsep 'results'];
disp(['sources path: ' inpdire]);
disp(['results path: ' outdire]);

%% -----
% Automatic iterative Gaussian fitting with evolutionary algorithms
%
% Only for inhouse use by Kun Zhao. Distribution of the code should be
% authorized by Dr. Ligang Wang, since it is based on inhouse evolutionary
% algorithms developed in IPESE-STI-FM.
%
% Key features:
% 1. Automatic iterative Gaussian fitting without manual interfere
% 2. Automatic decision on the number of peaks
% 3. No manual initialization needed for each peak due to global search
% 4. Global optimization with less risk of local optimum
% 5. Every run handles one wavelength, due to complexity of figure display
%-----

%% Global setup
% Control display
% fsrc : plot source data? (0: no plot; 1: do plot)
% fres : plot results? (0: no plot; 1: do plot)
global fres
fsrc = 0;
```

```

fres = 1;

% Problem setup
% rngs : wavelength ranges considered, rngs = [[l1,u1];[l2,u2];];
% nitm : Number of peaks considered
% npar : Number of parameters for each peak formulation
%      3-parameter Gaussian fitting: height,center,deviation;
% Pini : Initialization of npar-parameter peak
% Plbd : Lower-bound of npar-parameter peak
% Pubd : Upper-bound of npar-parameter peak
% olbd : Global lower-bound for Plbd
% oubd : Global upper-bound for Pubd
% doGA : Whether do GA to iteratively find peaks
% yini : 0 - GA use olbd,oubd as bound; 1 - GA use Plbd,Pubd as bound
% x      : Wavelength range considered of each file
% y      : The corresponding Absorbance of each file
% rng1   : Starting wavelength
% rng2   : End wavelength
% fnames : All file names
global npar doGA rngs nitm
global x y rng1 rng2 fnames temp lb
doGA = 1;
yini = 1;
rngs = [1535,1780];
npars = 3;
nitm = 5;
Pini = [0.041 1560 10 0.057 1591 10 0.1 1620 15 0.1 1650 20 0.01 1690 30 0.01 1690 30 0.01 1690 30 0.01 1690 30];
Plbd = [0.01 1555 16 0.01 1589 12 0.00 1616 25 0.0 1650 20 0.0 1680 0 0 1535 0 0 1535 0 0 1535 0];
Pubd = [0.08 1571 25 0.20 1593 16 0.20 1635 32 0.5 1655 30 0.3 1705 50 50 1780 60 50 1780 60 50 1780 60];
% Global initialization for optimization (centroids are important)
olbd = [0 1540 16 0 1580 12 0 1620 25 0 1650 20 0 1670 0 0 1535 0 0 1535 0 0 1535 0];
oubd = [50 1580 60 50 1620 60 50 1650 60 50 1670 60 50 1710 60 50 1780 60 50 1780 60 50 1780 60];

% data preprocessing
rng1 = rngs(1,1); % Starting wavelength
rng2 = rngs(1,2); % Ending wavelength
[x,y,temp,fnames] = preprocess(rngs,fsep,inpdir,fsrc);

%% Close all figures first
if fres == 1 || doGA == 1
    close all;

```

```

end
% remove results folder
if isdir(outdir)
    rmdir results s
end
mkdir(outdir)

% Reduce the size of Pini, Plbd and Pubd with npar and nitm
% Check size, warning and resize arrays
if isequal(size(Pini),size(Plbd)) && isequal(size(Pini),size(Pubd))
    nnum = size(Pini,2);
    if nnum < npar*nitm
        disp('Error: Sizes of Pini & Plbd & Pubd less than npar * nitm!');
    else
        % Now reduce Pini, Plbd and Pubd sizes
        Pini = Pini(1,1:npar*nitm);
        Plbd = Plbd(1,1:npar*nitm);
        Pubd = Pubd(1,1:npar*nitm);
    end
else
    disp('Error: Sizes of Pini, Plbd, Pubd inequal!');
    return
end

%%% GA setup
% Form input
if doGA == 0
    % Perform Gaussian fitting
    gafitness([Pini,Plbd,Pubd]);
else
    % Prepare GA
    % Set bounds
    galb = [];
    gaub = [];
    lb = [];

    for i = 1:nitm
        galb = [galb [0.01 0.01 0.01]];
        gaub = [gaub [0.99 0.99 0.99]];
    end
    for i = 1:nitm

```

```

    galb = [galb [0.01 0.01 0.01]];
    gaub = [gaub [0.99 0.99 0.99]];
end
if yini == 0
    olbd = olbd(1,1:npar*nitm);
    oubd = oubd(1,1:npar*nitm);
    galb = [galb olbd];
    gaub = [gaub oubd];
    lb = [lb olbd];
else
    Plbd = Plbd(1,1:npar*nitm);
    Pubd = Pubd(1,1:npar*nitm);
    galb = [galb Plbd];
    gaub = [gaub Pubd];
    lb = [lb Plbd];
end
%disp('Lowerbound, upperbound: ')
%format long g
%[galb' gaub']

GAoptions = optimoptions('ga');
%GAoptions.OutputFcn = @gaoutput;
%GAoptions.PlotFcn = @gaplotbestf;
GAoptions.CreationFcn = @gacreationlinearfeasible;
GAoptions.MutationFcn = @mutationadaptfeasible;
GAoptions.CrossoverFcn = {@crossoverintermediate, 0.5};
GAoptions.CrossoverFraction = 0.5;
%GAoptions.Display = 'iter'; % 'off' | 'iter' | 'diagnose' | {'final'}

fobj = @gafitness;
%[gax,gay] = ga(fobj,3*npar*nitm,A,b,[],[],lb,ub,[],[],GAoptions)
fprintf('Current time %s\n', datestr(now,'HH:MM:SS.FFF'))
disp('Start GA:');
[gax,gay] = ga(fobj,3*npar*nitm,[],[],[],[],lb,gaub,[],[],GAoptions)
end

disp('*****');
disp(['Run completed, wavelength [' num2str(rng1) ' ' num2str(rng2) ']']);
disp('*****');
rmpath(genpath([curdir fsep 'moo']));

```

Execution file 2 preprocess.m:

```
%% Customized source-data preprocessing
% File name related to read txt or csv file generated from experiment
% nsrt : Starting text file
% nint : This is added to avoid
% nend : End text file
% tsrt : Starting temperature, C
% tint : Temperature interval, C
% temp : Temperature range, C
function [x,y,temp,fnames] = preprocess(rngs,fsep,inpdir,showfig)
nsrt = 12;
nint = 1;
nend = 40;
tsrt = 19;
tint = 10;

x = [];
y = [];
temp = [];
fnames = [];
% Process experimental source data
rng1 = rngs(1,1); % Starting wavelength
rng2 = rngs(1,2); % Ending wavelength
id = 0; % Index of active spectrum
for i = nsrt : nend
    if mod((i-nsrt),nint) == 0
        id = id + 1;
        % Current temperature
        tcur = tsrt + tint * (i - nsrt);
        temp = [temp;tcur];
        % Form and display file name
        if i < 10
            fname = [num2str(tcur) ' C.000' num2str(i)];
        else
            fname = [num2str(tcur) ' C.00' num2str(i)];
        end
        fnames{id} = fname;
        disp(['File to be read: ' fname '.txt']);

        % Read the file indicated above and store contents into a matrix (dat)
```

```

fid = fopen([inpdire fsep fname '.txt']);
txt = textscan(fid,'%f','delimiter',' ');
fclose(fid);
mat = txt{:};
nrow = size(mat,1);
dat = [];
for j = 1 : nrow/2
    dat = [dat; [mat(2*j-1) mat(2*j)]];
end

% All data read can be plotted below to check if data is correct
if showfig == 1
    figname = 'Source data all';
    hall = findobj('Type', 'Figure', 'Name', figname);
    if isempty(hall)
        hall = figure('NumberTitle','off','Name',figname);
        set(gcf,'Name',figname,'NumberTitle', 'off');
        movegui('west');
    else
        figure(hall);
    end
    plot(dat(:,1),dat(:,2));
    xlabel('Wavelength (cm^{-1})');
    ylabel('Absorbance (a.u.)');
    ax = gca;
    ax.Title.String = 'Original source: total range';
    hold on
end

% Find the wavelength expected from the data read
index_wl = dat(:,1) >= rng1 & dat(:,1) <= rng2;
reduced_dat = dat(index_wl,:);

% Put the interested data in X-Y format in a local matrix
xloc = reduced_dat(:,1);
yloc = reduced_dat(:,2);
%plot(xloc,yloc,'linewidth',1.5);
%hold on

% Smooth measurement first to reduce noise
yloc = smooth(xloc,yloc,0.1,'loess');
```

```

%plot(xloc,yloc_new,'linewidth',1.5);

% Wavelength size
nxloc = size(xloc,1);

% Baseline processing to be added
slope  = (yloc(nxloc) - yloc(1)) / (xloc(nxloc) - xloc(1));
base   = yloc(1);
for ip = 1 : nxloc
    yloc(ip) = yloc(ip) - (base + slope * (xloc(ip)-xloc(1)));
end

% Remove negative numbers
yloc(yloc < 0) = 0;


% Store xloc and yloc into x, y
x(:,id) = xloc;
y(:,id) = yloc;

% All data read can be plotted below to check if data is correct
if showfig == 1
    figname = 'Source data range';
    hrng = findobj('Type','Figure','Name',figname);
    if isempty(hrng)
        hrng = figure('NumberTitle','off','Name',figname);
        set(gcf,'Name',figname,'NumberTitle','off');
        movegui('east');
    else
        figure(hrng);
    end
    plot(xloc,yloc);
    xlabel('Wavelength (cm^{-1})');
    ylabel('Absorbance (a.u.)');
    ax = gca;
    ax.Title.String = ['Original source: [' num2str(rng1) ', ' num2str(rng2) ']];
    hold on
end
end
end

```

Life Story

Carrying the strong curiosity about the origin of modern science and about the western life, I arrived in Switzerland for PhD from a village in Wuhan, China after all the endeavors. EPFL is famous as a leadership university, especially in photo(electric) energy field. I knew it because there are many large groups researching on photo(electric) energies at top 15 universities in Wuhan. I appreciate very much that I study here. The challenge in my study here was starting over: facing new research topic; switching from theoretical calculations to experiments; and all my previous achievements became no relation here no matter how proud I was and what fame I obtained. Also, the research topic of CO₂ hydrogenation was new in this group. I had no sense of feasibilities of the instruments in this research. When searching the investigation methods and the catalysts, I had an impression that everything was investigated because so many techniques, catalysts, and mechanisms were reported. Therefore, it was a long and lonely journey to pass through countless up and down and to get the novel results finally. I worked the most intense on the last three months of thesis preparation: working 12-16 hours per day, taking one day as two days. Afterwards, I managed to finish two more articles and the thesis. That was ever most efficient time. At the end I am proud of my skills in experiment, the methods I developed, the scientific discoveries of the CO₂ hydrogenation mechanisms on the catalyst surfaces, and the life in Switzerland.

Before starting the PhD, some PhDs at the last year warned me that these four years would develop as this curve “”. I was doubting it would happen on me, especially I had super nice supervisor and colleagues. However, I did not escape from this curve. I expected very high for the achievements at the beginning, then dropped into depression in the reality. It is said misfortunes never come singly. Truly, there were continuous pressures and anxieties joined from other sides: the relationships, the cultural conflicts, and the increasing competition from China. Four years passed like a blink. But every year was so different to me. I did not want to admit, but the real challenge was going through the overwhelming conflicts of the differences between the Chinese and European sides: the cultures, the political bias, the social communications, the way of thinking, and so on. It was totally a battle in the minds and the battle crashed my beliefs. I have been searching the answer and myself in this battle.

Now I can understand more or less why the battle and crash happened. It consumed my enormous energies to go through and figure out, because the new things I met here challenged my past life and belief. Therefore, I must record it.

About the nation

China is a country with really long and heavy history. Chinese people have to learn the poems and ancient articles from those dynasties throughout the educational periods. Those poems carry poignant and beautiful souls. One of the most famous books reflecting the life and minds in one dynasty is “Dream of the Red Chamber”

("Le Rêve dans le Pavillon Rouge" in French), which was written around 270 years ago. It tells highly complex stories about love, the rise and fall of a representative noble family, and wonderful descriptions about Chinese women under that time background. It writes with very delicate ancient words and poems. There is a big official group studying this book exclusively since from 1980s in China. When my landlord here, an elder Swiss couple, showed me that they had been reading this book in French for ten years, I was shocked and gratified.

After revolutions of thousands of years, this nation survives. The recent over a hundred years of wars opened the decayed door of the dynasty, also subverted its sacred image established over the dynasties. However, the culture, humanity, and spirit implanted into Chinese people's characters and consciousness. Along with the development in the recent one century, the traditional and modern cultures clash all the time. Besides, the magnificence China had and the humiliation the invasion wars brought formed the complicated sensations to Chinese people.

World today is a political world. Chinese communist is more famous than Chinese culture. When I say I love my country, people reflect immediately that I must love the communist party. This is sad to me. Because people put almost the full emotions to the communist, not really seeing the culture and life there. As for the Chinese communist party, on one hand, it indeed builds the new China very well; on the other hand, its bureaucracy, fawning the superior and disrespect the subordinates/normal people, and tight control are hateful. Not until I have life in Switzerland did I understand what freedom and respect are. However, China has a very complex society and history. It might become more transparent and trustable after the development arrives a higher level.

About the mentality

Generally, Chinese people are used to be led by one power as in the history. In personality, Chinese people suppress the needs of oneself, even deny the selves, have deep sense of conservative morality and fame, and easily feel shamed for a manner or a failure. The speaking is often serious and playing around instead of relaxed and straightforward, especially speaking with superiors. We have to guess the meaning carefully. Speaking about the government is a very sensitive topic, except saying good or constructive but not aggressive words. I did not know that talking about the governments, including Chinese government, is a daily chat in Europe. That made me very nervous, shamed and angry at the beginning. After I learned the international relations and the developing processes of many countries, I started to understand the natural processes of a country grow and the political measures and bias, being calmer and more aware.

Chinese way of thinking originated from two major philosophies: Confucianism and Taoism, which developed around 2500 years ago. Confucius teaches the relationships of the person with the family, friends, society, and government in a kindness and respect manner. Confucianism flourishes and widespread the most after traversing so long history, having the strongest influence ubiquitous in China. However, it carries conservative

minds and too many restrictions, and tends to educate the communication regarding to people's title, not the person him/herself. Tao imparts the connection of the person with the inner energy and the universe, and suggests freedom in the spirit.

Influenced by the conservative rules, Chinese normally connect the spirit and flesh mentally strongly, which might be comparable to the old Christian style. We easily live in sin or shame: when we did not get good performance in the school, drank/smoked/dated at high school, did not follow various rules, not married above 30 years old especially for woman, no car or apartment/house before marriage especially for man, being disagreed by others' opinions, etc. The society is filled with rushes, competitions, comparisons, and the Chinese communist. Although I realize the contradictory parts after the comparison with the life in Switzerland, I have to burden these pressures as long as I live in this society.

Society in Switzerland is so open. People live comfortably, weathily, confidently, and can develop their interests freely. There are so many greetings in the mornings, evenings, holidays, before and after meals, and so on, while Chinese usually do not have. How enviable the life is! However, men and women are unbelievably open with funs, having no struggles with separating the "spirit and flesh". When people say he/she likes someone, it does not mean the same "like" in China. In China, saying "like" to a girl/boy between friends means pursuing a relationship. And the relationship here is independent from the aim of marriage. While in China, relationship usually aims at marriage, although it could fizzle out. So, when we judge things based on our backgrounds, a lot of contradictions and misunderstandings could be created, which is miserable.

About the life experiences

This is a personal case. When I was in China, I was lost because of no sense of the physical life. Actually, the students were commented as having eyes high and hands low by the society. I did not know the basic living skills: how to use vacuum cleaner, how to cut meat, how to cook, and so on. I never thought one day I had to find apartment, furniture, and health insurance alone, because in China the dormitory, food, insurances, etc. are provided by the schools or universities. It was impossible to live off campus for me.

The worst was to live in the expectations from the family, friend, and society due to the social sense of fame and competition. Those expectations pointed to me only one road to Rome, which was "good good study, day day up" – getting good performance in the school and entering one of the top universities. There were 9 to 11 million students competing the universities every year. I had to use high scores or grades to convince my family that I am a promising person, to draw teachers' attention, and to be confident among friends and neighborhoods. I had also to be very careful with my behavior and speaking when I was a child because I was the unexpected second girl in the family under the "one child" policy. To obtain good judgements from others, I put myself in all kinds of "behavior templates". That was choking time.

Luckily, I became more or less free after attending the university. I could finally read and study a lot of knowledges that I was interested, participate various activities, and travel. Abandoning all the templates and people's eyes, suddenly I felt nothing was really important, nearly "the unbearable lightness of being". I lived in a spiritual world, seeming like free, but with invisible cage. The older I grew, the deeper I felt. But I did not know what the cage was. Until I lived four years in Switzerland, I understood it was because of the ubiquitous competition, the hateful part of the social circumstance, and the harsh education originated from the family. What was more, there was no balance between work and life. Work was at everywhere and anytime except when sleeping. What poor Chinese! Everyone was in a rush of supporting the life. I felt stronger the competition from China when I am in Switzerland due to the fast movements in China and the slow progress in Europe. Without time to enjoy life, Chinese people generally were not really happy, and easily to be serious, angry and shouting.

In Switzerland, the social environment, people's minds, and working styles are open, kind and flexible. The natures are well protected; having the real seasons and countless stars; energy sources are abundant; roads are well built; infrastructures are well established; shops have selected the optimal products for the consumers and not varied the prices very much between different shops; people are polite, quiet, well educated and respectful..... Here, people can stop working on weekends and take vacations without worrying about the work, can even relax without worrying about the job and the career. The society is so harmonic even without "fixed" president. Living here is like living in the heaven with freedom, equality, wealth, peace, and incredibly beautiful nature. I not only love and enjoy living here very much, but also feel the connection of the environment here to my soul. I could not imagine elsewhere would have better environment. However, at the starting two years, the differences in living style, way of thinking, and some contradictions in the senses of morality of people's behaviors described above created terrible loneliness, misunderstandings and spiritual crash.

As a consequence, these two spirits – Chinese tradition and western opening – in me struggled in fierce battle for three and half years. I remember I arrived in Switzerland naive, innocent, enthusiastic, curious, unworldly, loving, and high-expectation. Under so many strong conflicts, I became miserable, aggressive in words, and antipathetic for all the things opposed to my Chinese spirit. I was exhausted mentally in the years of spiritual battle. But at the end, I break through these difficulties and found out the compromise. I become comfortable, confident and certain, and understand the nations, international relations and the politics more. This was a journey from sorrow to happiness, a journey full of harsh philosophy of life, which took me three quarters of my PhD time to pass. This is indeed a doctorate of PHILOSOPHY! "What does not kill us makes us stronger."

Overall, PhD is harsh. In addition to the difficult research work, PhD time is also the first state of handling independent life, dealing with colleague relationships, facing all kinds of conflicts, all the time trying to calm down from the pressures and to solve the problems. Passing the PhD exam is a rebirth. Thankfully, I found what life I want at the end.

Curriculum Vitae

I Profile

Name: Kun ZHAO 赵焜

Gender: Female

Nationality: Chinese

Date of Birth: Oct. 4th 1988

e-mail: kun.zhao@epfl.ch

Mobile: +41 779951177



OrCID : 0000-0002-7182-8089

Address: Rue de Condémines 30, 1950 Sion, Switzerland

Summary: I am a highly motivated, persistent and hard-working young scientist. I am specialized and enthusiastic in the investigations of the reaction mechanisms of surface catalysis and the relation between surface structure and reactivity for energy conversion and storage. In my eight years of research study since from the last year of undergraduate, I have found the facets structure-dependent molecular oxygen activation of bismuth oxychloride by means of experiments and theoretical simulations, discovered the reaction pathways of CO₂ hydrogenation on metal/support interface by finely controlling the surface intermediates in in situ spectroscopic apparatus, and elaborated the support effect in CO₂ hydrogenation reaction. I have fourteen high-quality publications and been cited more than 2000 times, at the same time acquired multiple instrumental skills listed below. I am always looking forward to expanding my knowledge and improving my skills in the fields of surface catalysis and materials at advanced platforms with passionate and intelligent people.

II Education

- | | |
|-----------------|--|
| 2/2016 – 6/2020 | PhD in École Polytechnique Fédérale de Lausanne (EPFL), 1015 Lausanne, Switzerland. |
| 9/2012 – 6/2015 | M.S. in Physical Chemistry, Key Laboratory of Pesticide & Chemical Biology of Ministry of Education, College of Chemistry, Central China Normal University, Wuhan 430079, P. R. China. |
| 9/2008 – 6/2012 | B.S. in Applied Chemistry, Central China Normal University, Wuhan 430079, P. R. China. |
| 9/2008 – 6/2012 | B.S. in Physics, Central China Normal University, Wuhan 430079, P. R. China. |

III Research Experience

- | | |
|-----------------|---|
| 7/2020 – 8/2020 | Internship in Prof. Dr. Hannes Jónsson's group at University of Iceland, working on DFT calculations of facet-dependent CO ₂ hydrogenation on copper. |
| 2/2016 – 6/2020 | PhD in Laboratory of Materials for Renewable Energy (LMER), EPFL, working on catalysis of CO ₂ hydrogenation on gas/solid interface utilizing spectroscopic methods under supervision of Prof. Dr. Andreas Züttel. |

7/2015 – 9/2015	Internship in Laboratory of Nanostructures at Surface (LNS), EPFL, working on catalysis of substrate-supported clusters utilizing STM and DFT calculations.
9/2012 – 6/2015	Master's thesis of Surface Structure-Dependent Photocatalysis of BiOCl Single Crystalline Surfaces under supervision of Prof. Dr. Lizhi Zhang.
11/2011 – 12/2012	Visiting student in Hefei National Laboratory for Physical Sciences at the Microscale, University of Science and Technology of China, Hefei 230026, P. R. China, learning DFT calculations by VASP code under supervision of Prof. Dr. Qunxiang Li.

IV Publications*

1. Zhao, K.; Calizzi, M.; Moioli, E.; Li, M.; Borsay, A.; Lombardo, L.; Mutschler, R.; Luo, W.; Züttel, A. Unraveling and Optimizing the Metal–Metal Oxide Synergetic Effect in a Highly Active $\text{Co}_x(\text{CoO})_{1-x}$ Catalyst for CO_2 Hydrogenation. *J. Energy Chem.* **2020**, in press.
2. Luo, W.; Zhang, Q.; Zhang, J.; Emanuele, M.; Zhao, K.; Züttel, A. Electrochemical reconstruction of ZnO enhances selective reduction of CO_2 to CO. *Appl. Catal. B* **2020**, 273, 119060.
3. Lombardo, L.; Heena, Y.; Zhao, K.; Dyson, P. J.; Züttel, A. Solvent-free and catalyst-free CO_2 capture and reduction to formate with borohydride ionic liquid. *ChemSusChem*. **2020**, 13, 2025.
4. Mutschler, R.; Moioli, E.; Zhao, K.; Lombardo, L.; Oveisi, E.; Porta, A.; Falbo, L.; Visconti, C. G.; Lietti, L.; Züttel, A. Imaging catalysis: Operando investigation of the CO_2 hydrogenation reaction dynamics by means of infrared thermography. *ACS Catal.* **2020**, 10, 1721.
5. Li, M.; Borsay, A.; Dakhchoune, M.; Zhao, K.; Züttel, A. Thermal stability of size-selected copper nanoparticles: effect of size, support and CO_2 hydrogenation atmosphere. *Appl. Sur. Sci.* **2020**, 510, 145439.
6. Zhao, K.; Zhang, J.; Luo, W.; Li, M.; Moioli, E.; Spodaryk, M.; Züttel, A. A Combined Diffuse Reflectance Infrared Fourier Transform Spectroscopy-Mass Spectroscopy-Gas Chromatography for the Operando Study of the Heterogeneously Catalyzed CO_2 Hydrogenation over Transition Metal-Based Catalysts. *Rev. Sci. Instrum.* **2020**, under review.
7. Calizzi, M.; Mutschler, R.; Patellie, N.; Zhao, K.; Züttel, A.; Pasquini, L. CO_2 hydrogenation over unsupported Fe-Co nanoalloy catalysts. *Nanomaterials*. **2020**, under review.
8. Zhao, K.; Wang, L.; Calizzi, M.; Moioli, E.; Züttel, A. Identifying Reaction Species by Evolutionary Fitting and Kinetic Analysis: An Example of CO_2 Hydrogenation in DRIFTS. *J. Phys. Chem. C* **2019**, 123, 8785.
9. Spodaryk, M.; Zhao, K.; Zhang, J.; Oveisi, E.; Züttel, A. The Role of Malachite Nanorods for the Electrochemical Reduction of CO_2 to C_2 Hydrocarbons. *Electrochimica Acta* **2019**, 297, 55.
10. Zhao, K.; Wang, L.; Calizzi, M.; Moioli, E.; Züttel, A. In Situ Control of the Adsorption Species in CO_2 Hydrogenation: Determination of Intermediates and Byproducts. *J. Phys. Chem. C* **2018**, 112, 20888.

11. Li, H.; Shang, J.; Shi, J. G.; Zhao, K.; Zhang, L. Z. Facet-Dependent Solar Ammonia Synthesis of BiOCl Nanosheets via a Proton-Assisted Electron Transfer Pathway. *Nanoscale* **2016**, 8, 1986.
12. Li, J.; Zhao, K.; Yu, Y.; Zhang, L. Z. Facet-Level Mechanistic Insight into General Homogeneous Carbon Doping for Enhanced Solar-to-Hydrogen Conversion. *Adv. Funct. Mater.* **2015**, 25, 2189.
13. Li, H.; Shi, J. G.; Zhao, K.; Zhang, L. Z. Sustainable Molecular Oxygen Activation with Oxygen Vacancies on the {001} Facets of BiOCl Nanosheets under Solar Light. *Nanoscale* **2014**, 6, 14168.
14. Ding, X.; Zhao, K.; Zhang, L. Z. Enhanced Photocatalytic Removal of Sodium Pentachlorophenate with Self doped Bi₂WO₆ under Visible Light by Generating More Superoxide Ions. *Environ. Sci. Technol.* **2014**, 48, 5823.
15. Zhao, K.; Zhang, L. Z.; Wang, J. J.; Li, Q. X.; He, W. W.; Yin, J. J. Surface Structure- Dependent Molecular Oxygen Activation of BiOCl Single-Crystalline Nanosheets. *J. Am. Chem. Soc.* **2013**, 135, 15750.
16. Jiang, J.; Zhao, K.; Xiao, X. Y.; Zhang, L. Z. Synthesis and Facet-Dependent Photoreactivity of BiOCl Single-Crystalline Nanosheets. *J. Am. Chem. Soc.* **2012**, 134, 4473.
17. Dong, G. H.; Zhao, K.; Zhang, L. Z. Carbon Self Doping Induced High Electronic Conductivity and Photoreactivity of g-C₃N₄. *Chem. Commun.* **2012**, 48, 6178.

* Google scholar citations more than 2000 times in total, increasing on average 300 times per year.

V Laboratory skills

Experimental: Diffuse Reflectance Infrared Fourier Transform Spectroscopy (DRIFTS), Raman, Tip-Enhanced Raman Spectroscopy (TERS), Thermal Desorption Spectroscopy (TDS), Differential Scanning Calorimetry (DSC), Transmission Electron Microscopy (TEM), X-ray Photoelectron Spectroscopy (XPS), Scanning tunneling microscope (STM), UV-vis spectroscopy, Photoluminescence, X-ray Powder Diffraction (XRD), Swagelok connections, glove box.

Theoretical: Density Functionary Theory (DFT) by Vienna Ab-initio Simulation Package (VASP) and Materials Studio.

VI Teaching

1. Teaching assistant of Lecturer Guido Rothenberger for the course “Chimie Physique des Interfaces”, 09, 2016 – 01, 2017, Undergraduate student course of Chemistry and Chemical Engineering, EPFL, Lausanne.
2. Teaching assistant of Prof. Andreas Züttel for the course “Thermodynamics of Energy Conversion and Storage”, 02 – 06, 2017, Master Program of Chemistry and Chemical Engineering, EPFL, Lausanne.
3. Supervision of for two master students, Mr. Adrien Depallens and Mr. Matthieu Porchet, on research of

“Spectroscopic study of CO₂ reduction on Ru/Al₂O₃ surface”, 09 – 12, 2017, Interdisciplinary / Disciplinary Project of Chemical master, EPFL, Sion.

4. Teaching assistant of Prof. Andreas Züttel for the course “Thermodynamics of energy conversion and storage”, 02 – 06 2018, Master Program of Chemistry and Chemical Engineering, EPFL, Lausanne.
5. Raman training and service for EPFL Sion users on Renishaw Raman instrument, 02 – 12, 2016, EPFL Sion.

VII Language

Chinese (mother tongue), English (second language), French (B1).

VIII Conferences

1. Kun Zhao, “Hydrogen Storage with CO₂ as Synthetic Hydrocarbons”, **invited speaker**. Hydrogen-Metal Systems Gordon Research Seminar (GRS), June 29th – 30th, 2019, Castelldefels, Spain.
2. Kun Zhao, *et al.* “In Situ Control of the Adsorption Species in CO₂ Hydrogenation: Determination of Intermediates and Byproducts”, **oral presentation**. 16th International Symposium on Metal-Hydrogen Systems, October 28th – November 2nd, 2018, Guangzhou, China.
3. Kun Zhao, *et al.* “Evolution of Adsorption species during CO₂ hydrogenation on Ru/Al₂O₃: Intermediates or Byproducts?”, poster. The Fourteenth International Conference on Electronic Spectroscopy and Structure, October 8th – 12th, 2018, Shanghai, China.
4. Kun Zhao. “H₂ Storage in Hydrocarbon by CO₂ Hydrogenation: Surfaces Interaction Studies”, **oral presentation**. 12th Int. Symposium Hydrogen & Energy, February 11th – 16th, 2018, Lausanne, Switzerland.
5. Kun Zhao, Andreas Züttel. “CO₂ interactions with Fe, Co, Ni, and Cu powder surface”, poster. Gordon Research Conference Carbon Capture, Utilization & Storage, June 11th – 16th, 2017, Colby-Sawyer College, USA.
6. Kun Zhao, Andreas Züttel. “CO₂ adsorption reaction on Ni and Cu powder surface”, poster, 11th Int. Symposium Hydrogen & Energy, February 26th – March 3rd, 2017, Hawaii, USA.
7. Kun Zhao, Andreas Züttel. “Spectroscopic Characterizations of CO₂ Reduction”, poster, Summer School on Interfaces and Energy, September 4th – 9th, 2016, Göttingen, Germany.
8. Kun Zhao, Andreas Züttel. “CO₂ Adsorption and Reduction in DRIFT and Raman”, poster, International Summer School on CO₂ Conversion: From Fundamentals towards Applications, August 29th – September 2nd, 2016, Villars, Switzerland.
9. Kun Zhao, Andreas Züttel. “FT-IR Spectroscopy of CO₂ Adsorption and Reduction”, poster, 15th International Symposium on Metal-Hydrogen Systems, August 7th – 12th, 2016, Interlaken, Switzerland.

-
10. Kun Zhao, Andreas Züttel. “Spectroscopy of CO₂ Electrocatalytic Reduction”, poster, Hydrides as Energy Materials, June 1st – 3rd, 2016, Aarhus, Denmark.

IX Life Hobbies

Ski (good), Via Ferrata (good), Cycling (good), Fitness (intermediate), Chinese Ancient Music Instrument GuZheng (intermediate)